# The Synthesis and Evaluation of Proton Conducting Electrolytes for High Temperature Steam Electrolysers

by

Paul Anthony Stuart

A thesis submitted to

Imperial College London

Department of Materials

for the degree of

Doctor of Philosophy

**Abstract**

Proton conducting ceramics based on acceptor doped perovskites are the subject of investigation as candidate electrolyte materials for Solid Oxide Electrolyser Cells (SOECs). Specifically, $BaCe_{0.9}Y_{0.1}O_{3-\delta}$ (BCY10) and $BaZr_{0.9}Y_{0.1}O_{3-\delta}$ (BZY10) were investigated. Samples with greater than 95% of the maximum theoretical density were successfully prepared using a BCY10 commercial powder. It was found that when small additions of ZnO were added to a BZY10 commercial powder, a density of greater than 95% of the theoretical maximum was achievable whereas without ZnO addition, the maximum achievable density was 85%. BCY10 was found to have a total conductivity approximately one order of magnitude greater than Zn-doped BZY10 over the entire temperature range studied. Spray pyrolysis and sol-gel methods were used successfully to prepare single phase pure BZY10 powders. The sintering behaviours of the powders produced by spray pyrolysis were found to alter significantly with changes in powder processing parameters. BCY10 and Zn-doped BZY10 cells were tested in electrolysis and fuel cell modes and the effects of varying operating conditions on cell performances were studied. At $750^oC$, the Area Specific Resistances (ASR) of a BCY10 cell in electrolysis mode was found to be lower when the anode compartment was humidified to $\approx$83% than to $\approx$3%. Below this temperature, ASR values were greater when using increased humidity levels. It was concluded that a degree of oxide ion conduction may be beneficial to the operation of proton conducting electrolysers. Post-test, BCY10 cell cross-sections were imaged using scanning electron microscopy and analysed using Energy Dispersive X-ray (EDX) spectroscopy. Significant erosion of grain boundaries regions close the electrode-electrolyte interfaces was observed and EDX spectroscopy results suggested the formation of a secondary phase in these regions, possibly Y:$CeO_2$. Had testing continued over an extended period of time it is probable that BCY10 cells would have undergone mechanical failure.

## Acknowledgements

I would like to thank my supervisors and colleagues for their guidance throughout my studies. In particular, Stephen Skinner has provided me with once in a lifetime experiences and has always endeavoured to further my personal development throughout my PhD. He has been my mentor for many years and his considerable knowledge, understanding and kindness has made him an outstanding supervisor. I am also very thankful to John Kilner for applying his considerable wisdom to my work.

Miguel Laguna tirelessly assisted me with experiments and theory for which I shall forever be indebted to him. Richard Sweeney, Robert Rudkin, Mahmoud Ardakani and Richard Chater have all assisted me with my experiments and I would like to thank them all for their time and expertise. I would also like to thank Sehban Husain, Alex Jasper, Fatos Derguti and Ruth Sayers for their companionship and support throughout my studies. Without their friendship, producing this thesis would have been that much more difficult.

My parents have given me unwavering support and encouragement throughout my education, for which I am deeply grateful. They have invested their time and effort in furthering my knowledge and understanding of the world and their devotion for me has contributed greatly towards my achievements.

This thesis is dedicated to my doting wife Rebecca. Without her support, encouragement and love, it would have been impossible for me to finish this work.

# List of Figures

1.1 Graph showing heat (Q), electrical ($\Delta$G) and total ($\Delta$H) energy demand change with temperature [1]. As electrolyser operating temperature increases, $\Delta$G decreases, reducing the cost of the hydrogen produced. This is assuming that the additional heat energy required is provided from an external source. . . . . 29

1.2 Schematics representing the operation of; (a) an oxide ion conducting SOFC, and (b) an oxide ion conducting SOEC . . . . . 30

1.3 Schematic showing the basic operation of a proton conducting SOEC supplied with steam . . . . . 32

1.4 Schematic showing the basic operation of a proton conducting SOFC with pure hydrogen as a fuel source . . . . . 33

2.1 BCY10 conductivity plot comparing literature by Ma *et al.* [2], Slade and Singh [3], Coors and Readey [4] and Bonanos *et al.* [5] . . . . . 49

2.2 Proton transport number of $BaCe_{0.9}M_{0.1}O_{3-\delta}$ against ionic radius of dopant M under fuel cell conditions [6] . . . . . 50

2.3 Lattice parameters of $BaCe_{0.9}M_{0.1}O_{3-\delta}$ calculated from XRD against ionic radius of dopant M [6] . . . . . 51

2.4 Ion transport number against temperature for BCY10 (circles) and BCY25 (triangles) [7] . . . . . 52

2.5 Proton conductivities of various oxides as calculated from data on proton concentrations and mobilities, according to Norby and Larring [8]. This data led to conclusions by Kreuer *et al.* [9] stated in the text. . . . . 58

2.6 Comparison of BZY10 total conductivities in air with ambient humidity from the literature [10–13] . . . . . 59

2.7 Conductivity data for $BaCe_{0.9-x}Zr_xY_{0.1}O_{3-\delta}$ with $0.0 \leq x \leq 0.9$ at 600, 800 and 1000$^o$C. Conductivity values can be seen to decrease with increasing zirconium content [13]. . . . . 62

2.8 Temperature for the onset of BCY10 carbonation upon cooling versus $CO_2$ concentration (line indicates best fit) [14] . . . . . 67

3.1 A schematic of the spray pyrolysis experimental setup. Red arrows indicate direction of flow of carrier gas. . . . . 71

3.2 Example of an AC impedance spectrum with markers indicating frequencies at maximum loss ($\omega_{max}$) in the spectrum . . . . . 79

3.3 A schematic of the improved SOEC-SOFC experimental test rig . . . . . 83

4.1 X-ray diffraction pattern of BCY10 as-supplied commercial powder . . . . . 88

4.2 X-ray diffraction pattern of BCY10 as measured by Zakowsky *et al.* [14] . . . . . 88

4.3 X-ray diffraction pattern of $BaCO_3$ as measured by Holl *et al.* [15] . . . . . 89

4.4 X-ray diffraction patterns of BCY10 as-supplied powder (black) and BCY10 commercial powder that was calcined at 1500$^o$C (red). Comparison shows that anomalous peak positions have been eradicated by the calcination process . . . . . 90

4.5 X-ray diffraction pattern of BZY10 as-supplied commercial powder . . . . . 91

4.6 X-ray diffraction pattern of BZY10 as measured by Snijkers *et al.* [10] . . . . . 91

4.7 X-ray diffraction patterns of BZY10 as-supplied powder (black) and BZY10 commercial powder that was fired at 1500$^o$C (red). Comparison shows that anomalous peak positions have been eradicated by the firing process . . . . . 92

4.8 Particle size distribution data for (a) as supplied and (b) 120 hour milled powders 93

4.9 SEM image of a BCY10 fracture surface displaying the grain structure of the material . . . . . 95

4.10 (a) Particle size distribution and equivalent particle diameter values for the as-supplied BZY10 commercial powder. (b) Particle size distribution and equivalent particle diameter values for the 120 hour milled BZY10 commercial powder . . . 97

4.11 SEM image of a polished and thermally etched Zn doped BZY10 surface displaying the grain structure of the material . . . . . 99

4.12 Section of an AC impedance spectrum of BCY10 at measured at 200$^o$C in air . 100

4.13 An example of an equivalent circuit model used to determine grain bulk and grain boundary resistances from AC impedance data . . . . . 101

4.14 Conductivity results of a BCY10 sample measured on heating from 300$^o$C to 800$^o$C and subsequently on cooling, in an atmosphere of flowing air with approximately ≈3% humidity . . . . . 104

4.15 Arrhenius plot comparing BCY10 data from the current work with BCY10 literature conductivity data . . . . . 105

4.16 Arrhenius plot comparing BCY10 data collected using a 5%$H_2$-Ar atmosphere with nominally 'dry' conditions and with a ≈20% humidity . . . . . 108

4.17 Section of an AC impedance spectrum of BZY10 measured at 200$^o$C in air . . . 108

4.18 Arrhenius plot comparing Zn-doped BZY10 data from the current work with BZY10 literature conductivity data . . . . . 109

4.19 Arrhenius plot of BZY10 data collected using a 5%$H_2$-Ar atmosphere with nominally 'dry' conditions and with a ≈20% humidity . . . . . 110

4.20 Arrhenius plot of BZY10 and BCY10 data collected using a 5%$H_2$-Ar atmosphere with a ≈20% humidity . . . . . 111

4.21 XRD powder diffraction pattern of a sample produced by spray pyrolysis at 600$^o$C - Markers below diffraction pattern indicate $Ba(NO_3)_2$ peak positions [16] . . . . 112

4.22 Graph of DTA signal against temperature showing decomposition of the $Ba(NO_3)_2$ precursor occurring just below 600$^o$C . . . . . 113

4.23 XRD powder diffraction pattern of a sample produced by spray pyrolysis at a furnace temperature of 800$^o$C showing single phase BZY10. Markers below diffraction pattern indicate $BaZrO_3$ peak positions [17] . . . . . 113

4.24 Particle size distribution of 120 hour milled commercial powder. Equivalent particle diameter values are also shown. . . . . 114

4.25 Particle size distribution of powder synthesised by spray pyrolysis with parameters; concentration; 2.5 x $10^{-3}$ mol.l$^{-1}$, nebuliser frequency; 2.5 MHz and furnace temperature; 800$^o$C. Equivalent particle diameter values are also shown. . . . . 115

4.26 SEM Micrographs of (a) powder showing typical particle agglomeration and faceted particles that are present in all samples and (b), powder prepared by pyrosol synthesis, 2.5 x $10^{-3}$ mol.l$^{-1}$, 2.5 MHz, 800$^o$C showing particle size distribution and varied particle morphologies . . . . . 116

4.27 TEM micrographs of (a) powder showing an agglomeration of particles less than 250 nm in diameter and (b), powder exhibiting the presence of dense particles . 117

4.28 Dilatometric curves of samples produced using a range of conditions. Red line is the time-temperature profile and corresponds to the right hand axis. . . . . 118

4.29 SEM image of powder produced in experiment 4 after ultrasound treatment showing particulate fracture . . . . . 121

4.30 Dilatometric curves of samples from experiment 4 before and after ultrasound treatment. The red line is the time-temperature profile and corresponds to the right hand axis. . . . . 122

4.31 X-Ray diffraction pattern of powder synthesised using a sol-gel technique. Peaks at 30, 43 and 53.5 °2$\Theta$ indicate that BZY10 perovskite phase was partially formed at this stage. Other peaks correspond to unreacted precursors. . . . . 123

4.32 X-Ray diffraction pattern of powder synthesised using a sol-gel technique after calcination at 1250$^o$C for 10 hours . . . . . 124

4.33 Particle size distributions of (a) as-prepared and (b) 120 hour milled powders synthesised using a sol-gel technique . . . . . 126

4.34 SEM micrograph of sol-gel 120 hour milled powder . . . . . 127

5.1 Preliminary characterisation of BCY10 cell in fuel cell mode over a range of temperatures and comparison with 750$^o$C data from Suksamai and Metcalfe [7] . 132

5.2 Initial characterisation of BCY10 cell in electrolysis cell mode over a range of temperatures . . . . . 134

5.3 Characterisation of developed BCY10 system in fuel cell mode over a range of temperatures. Suksamai and Metcalfe data plotted for comparative purposes [7]. 135

5.4 Characterisation of developed BCY10 system in electrolysis mode over a range of temperatures . . . . . 136

5.5 Fuel cell data collected using an anode atmosphere with elevated $H_2$ concentration and comparison with 750$^o$C data from Suksamai and Metcalfe [7] . . . . . 138

5.6 Electrolysis Data Collected using an Anode Atmosphere with Elevated $H_2$ Concentration . . . . . 140

5.7 Electrolysis data collected using a gas feed of 5%$H_2$-$N_2$, with ≈83% humidity over a range of temperatures . . . . . 142

5.8 Change in current density measured at 2 V applied with temperature, comparing data collected using either ≈3% or ≈83% humidity in the anode compartment. . 143

5.9 Potentiodynamic measurements made at 500$^o$C using a 100% $N_2$ gas supply that was either nominally dry or humidified to ≈83% . . . . . 144

5.10 Potentiodynamic measurements made at 600$^o$C using a 100% $N_2$ gas supply that was either nominally dry or humidified to ≈83% . . . . . 144

5.11 Potentiodynamic measurements made at 750$^o$C using a 100% $N_2$ gas supply that was either nominally dry or humidified to ≈83% . . . . . 146

5.12 Potentiodynamic measurements made using a 100% $N_2$ gas supply humidified to ≈83% at 500$^o$C. Red symbols are data collected with increasing voltage and blue symbols are data collected with decreasing voltage. . . . . 147

5.13 Potentiodynamic measurements made using a 100% $N_2$ gas supply humidified to ≈83% at 600$^o$C. Red symbols are data collected with increasing voltage and blue symbols are data collected with decreasing voltage. . . . . 147

5.14 Potentiodynamic measurements made using a 100% $N_2$ gas supply humidified to ≈83% at 750$^o$C. Red symbols are data collected with increasing voltage and blue symbols are data collected with decreasing voltage. . . . . 149

5.15 Zn doped BZY10 fuel cell data, collected using a gas feed of 10%$H_2$-$N_2$, with ≈3% humidity at 750$^o$C . . . . . 150

5.16 Zn doped BZY10 electrolysis cell data, collected using a gas feed of 10%$H_2$-$N_2$, with ≈3% humidity at 750$^o$C . . . . . 150

6.1 Galvanodynamic data recorded at 600$^o$C before and after galvanostatic measurements in (a) SOFC and (b) SOEC mode . . . . . 156

6.2 SEM image of preliminary sample fracture surface: Pt electrode-electrolyte $H_2$-$H_20$ interfacial region. Grain boundary regions can be seen to have been altered by SOEC/SOFC testing . . . . . 157

6.3 FEGSEM images of (a) Control sample and (b) SOEC/SOFC sample at Pt electrode-electrolyte interfacial region - Interfacial layer and corrosion of grains visible in SOEC/SOFC sample . . . . . 158

6.4 FEGSEM image of SOEC/SOFC sample polished surface and EDX line scan data. Line on FEGSEM image shows where EDX line scan data was acquired and (a) and (b) refer to grain boundary locations . . . . . 159

6.5 SEM image of SOEC/SOFC sample fracture surface, 250 $\mu$m from the $H_2$-$H_2O$ electrode (middle of the sample) . . . . . 159

6.6 FEGSEM images of grain boundary triple points in (a) SOEC/SOFC and (b) control samples. Distinct grain boundary region and crystallites on the surface of grains can be seen in SOEC/SOFC sample. . . . . 160

6.7 Focused ion beam electron image of the trench created using focused ion beam milling. The area displayed is at the anode-electrolyte interfacial region in the preliminary sample. Grain contrast and secondary phase located at the grain boundaries are clearly visible. Inset; schematic of the cross-section of the sample after milling, showing surface geometry and viewing angle. . . . . 161

6.8 FEGSEM images of interfacial regions at (a) the cathode and (b) the anode. Secondary phase at grain boundaries can be seen to be much more abundant at the cathode side than the anode side of the cell . . . . . 162

6.9 FEGSEM image of the cathode-electrolyte interfacial region with example EDX spectra measurement locations indicated as follows; (a) interfacial layer, (b) and (e) grain bulk, (c) and (d) grain boundary triple points. Circle diameters roughly indicate the area of primary electron interaction at the surface of the sample, however, it should be noted that the maximum cross sectional area of the primary electron interaction volume parallel with the surface of the sample is greater than this area. . . . . 163

6.10 Change in current density over 24 hours with 1.75 V applied (SOEC mode) . . . 166

6.11 SEM image of the cathode-electrolyte interface showing 'spots' at sites (a) and (b) that were analysed using EDX spectroscopy. Sites in locations such as (c) and (d) were also analysed using EDX for comparison. . . . . 167

6.12 Potentiodynamic measurements made at the beginning and end of a test cycle, conducted using an anode gas supply feed of 5% $H_2$ balanced with $N_2$, humidified to ≈83%. Results show a slight change in SOEC performance during approximately 18 hours of testing at various temperatures and applied voltages. . . . . 168

6.13 SEM image of the cathode-electrolyte interface of a sample after operation with approximately ≈83% humidity in the anode gas chamber . . . . . 169

6.14 SEM image of the anode-electrolyte interface after 18 hours of operation in SOEC with an ≈83% humidity in anode gas feed . . . . . 171

6.15 A high magnification SEM image of the anode-electrolyte interface showing detail of the interfacial layer containing nanoscopic particulates . . . . . 171

# List of Tables


1.1 Electrode and total reactions of an oxide ion conducting device in SOFC and SOEC modes. Kröger-Vink notation is used to describe the interactions between fluids and the device components . . . . . 31

1.2 Specific energy and energy density values for various energy storage technologies also with targets set by the United States Department of Energy . . . . . 34

2.1 Reported lattice parameter values for BCY10 [18] and SCY10 [19]. Also presented are activation energies for BCY10 in the temperature range 300-900$^o$C [4] and SCY10 in the temperature range 300-510$^o$C [20] . . . . . 47

2.2 Reported % maximum theoretical density values of BZY20 under various sintering conditions and corresponding protonic conductivity values at 500$^o$C [21, 22] . . . 57

2.3 Reported % maximum theoretical density values of $BaCe_{0.9-x}Zr_xY_{0.1}O_{3-\delta}$ and $BaZrO_3$ under various sintering conditions [23] . . . . . 63

2.4 Reported peak power density values for the cell; $H_2$ (3% $H_2O$), Ni-BCZY7 $\|$ BCZY7 $\|$ layered $GdBaCo_2O_{5-x}$, air [24] . . . . . 65

2.5 Reported % maximum theoretical density values of $BaCe_{0.8-x}Zr_xY_{0.2}O_{3-\delta}$ under various sintering conditions and corresponding peak power density values at 700$^o$C [25] . . . . . 65

3.1 Characteristics of Praxair powders (as-supplied) . . . . . 70

3.2 A list of experimental parameter sets for spray pyrolysis powder synthesis. experiments numbered 1-6 were conducted using a carrier gas flow rate of 6 l.min$^{-1}$ 71

3.3 AC Impedance Response Capacitance Values and Corresponding Possible Phenomenon Responsible [26] . . . . . 79

4.1 Average sintered densities of BCY10 pellets sintered using BCY10 regime 1. Table includes data for as-supplied and milled powders. . . . . 93

4.2 Average sintered densities of BZY10 pellets sintered using BZY10 regime 1. Table includes data for as-supplied and milled powders. . . . . 96

4.3 Average sintered densities of BZY10 pellets sintered using a ZnO dopant in a range of 0.1 to 0.5 wt% and sintering temperatures in the range 1300 to 1400$^o$C. A 200$^o$Chr$^{-1}$ heating / cooling rate and a sintering time of 10 hours were used for all experiments. . . . . 98

4.4 AC impedance response capacitance values and corresponding possible phenomenon responsible [26] . . . . . 100

4.5 Green and sintered densities of dilatometry samples. Green density values quoted here should be considered when analysing figure 4.28. Experiments 2 and 3 were conducted using a furnace temperature of 600$^o$C and therefore, were not comparable and omitted from figure 4.28. . . . . 118

4.6 Sintered densities (%TD) of as-prepared and 120 hour milled powders made using a sol-gel technique . . . . . 125

4.7 Sintered densities of milled sol-gel synthesised powders using various sintering conditions . . . . . 128

5.1 Peak power densities for a preliminary BCY10 cell and experimental setup over a range of temperatures, including 750$^o$C value from Suksamai and Metcalfe data [7] 133

5.2 Peak power densities for developed BCY10 cell and experimental setup over a range of temperatures, including 750$^o$C value from Suksamai and Metcalfe data [7] 136

5.3 Comparison of peak power densities over a range of temperatures for 5% and 66% $H_2$ concentration (by flow rate) in the supplied gas feed . . . . . 138

5.4 ASR values for 5% and 66% $H_2$ concentrations measured in fuel cell mode over a range of temperatures and the % difference between values . . . . . 139

5.5 ASR values for 5% and 66% $H_2$ concentrations measured in electrolysis mode over a range of temperatures and the % difference between values . . . . . 140

5.6 ASR values for ≈3% and ≈83% humidified 5%$H_2$-$N_2$ measured in electrolysis mode over a range of temperatures and the % difference between values . . . . . 142

5.7 Comparison of thermal expansion coefficients (TECs) of candidate electrolyte and test rig tube materials . . . . . 149

6.1 Average atomic % of elements detected using EDX spectroscopy measured at various locations corresponding with figure 6.9. Standard deviation values are quoted in brackets. . . . . 163

6.2 Ce:Ba ratios at various locations within the developed cell, calculated from average atomic % presented in table 6.1 . . . . . 164

6.3 Average atomic % of elements detected using EDX spectroscopy, measured in dark 'spot' regions (eg: (a) and (b) figure 6.11) and grain bulk regions (eg: (c) and (d) figure 6.11). Standard deviation values are quoted in brackets. . . . . 167

6.4 Atomic % of elements detected using EDX spectroscopy measured at various points corresponding with figure 6.13 . . . . . 169

6.5 Atomic % of elements detected using EDX spectroscopy measured at various points corresponding with figure 6.13 . . . . . 170

# Table of Contents

**List of Figures** **4**

**List of Tables** **11**

**1 Electrolysers** **18**

1.1 Review of Hydrogen Production Methods . . . . . 18

1.1.1 Introduction . . . . . 18

1.1.2 Hydrocarbons . . . . . 20

1.1.3 Sulphur-Iodine Process . . . . . 23

1.1.4 Biological . . . . . 24

1.1.5 Photo-electrochemical . . . . . 25

1.2 An Introduction to Electrolysers . . . . . 26

1.2.1 The Role of Electrolysers in the Energy Landscape . . . . . 26

1.2.2 Low or High Temperature Electrolysers? . . . . . 28

1.2.3 Basic Operation of Solid Oxide Systems . . . . . 29

1.3 Hydrogen Storage for use with Fuel Cells . . . . . 34

1.3.1 Pressurisation of Hydrogen . . . . . 35

1.3.2 Absorption in Metal Hydrides . . . . . 35

1.3.3 Adsorption/Absorption on/in Carbon Based Materials . . . . . 36

1.3.4 Liquefaction of Hydrogen . . . . . 36

1.4 Summary . . . 37

**2 Review of Proton Conducting Materials for SOEC and SOFC Devices 38**

2.1 Introduction . . . 38

2.2 Proton Conducting SOFCs . . . 39

2.3 Proton Conducting SOECs . . . 39

2.4 Formation of Protonic Defects . . . 42

2.5 Proton Conducting Mechanism . . . 44

2.6 Introduction to the Materials under Investigation . . . 47

2.7 Y:$BaCeO_{3-\delta}$ . . . 48

2.7.1 Synthesis, Conductivity, and Ionic Transport Number . . . 48

2.7.2 Cell Fabrication and Testing . . . 52

2.8 Y:$BaZrO_{3-\delta}$ . . . 55

2.8.1 Synthesis . . . 55

2.8.2 Conductivity . . . 58

2.8.3 Cell Fabrication and Testing . . . 60

2.9 Y:$BaCe_xZr_{(1-x)}O_{3-\delta}$ . . . 61

2.9.1 Synthesis and Conductivity . . . 61

2.9.2 Cell Fabrication and Testing . . . 64

2.10 Chemical Stability of Y:$BaCeO_3$ and Y:$BaZrO_3$ . . . 66

2.10.1 $CO_2$ Containing Atmospheres . . . 66

2.10.2 $H_2O$ Containing Atmospheres . . . 68

2.11 Summary . . . 69

**3 Experimental Methods and Technique Development 70**

3.1 Commercial Powders . . . 70

3.2 Synthesis of BZY10 by Spray Pyrolysis . . . . . 71
3.3 Sol-Gel Synthesis of BZY10 . . . . . 72
3.4 Powder Characterisation . . . . . 72
3.4.1 X-Ray Diffraction (XRD) . . . . . 72
3.4.2 Particle Size Distribution . . . . . 73
3.4.3 Electron Microscopy . . . . . 73
3.5 Pellet Sample Preparation and Sintering . . . . . 74
3.5.1 Commercial Powder . . . . . 74
3.5.2 Spray Pyrolysis Powder . . . . . 75
3.5.3 Sol-Gel Powder . . . . . 75
3.5.4 Dilatometry . . . . . 76
3.5.5 Density Measurements . . . . . 76
3.6 AC Impedance Spectroscopy . . . . . 77
3.7 SOEC-SOFC Testing . . . . . 81
3.8 SOEC/SOFC Post-Test Sample Analysis . . . . . 85
3.8.1 Electron Microscopy . . . . . 85
3.8.2 Focused Ion Beam (FIB) . . . . . 86

**4 Synthesis and Conductivities of Yttrium Doped Barium Cerate and Barium Zirconate 87**

4.1 Commercial Powder . . . . . 87
4.1.1 Powder Characterisation . . . . . 87
4.1.2 Pellet Sintering . . . . . 92
4.2 Conductivity . . . . . 100
4.2.1 AC Impedance Spectroscopy Measurement Technique . . . . . 100
4.2.2 BCY10 . . . . . 104

4.2.3 BZY10 . . . 108
4.3 BZY10 Powder Synthesis . . . 111
4.3.1 Spray Pyrolysis Synthesis of BZY10 . . . 111
4.3.2 Sol-Gel Synthesis of BZY10 . . . 122
4.4 Summary . . . 129

**5 Electrochemical Characterisation 131**

5.1 Preliminary Characterisation of BCY10 Cell Behaviour . . . 131
5.2 Cell Characterisation Using Developed Cell, Test Rig and Apparatus . . . 134
5.3 Effect of Increasing $H_2$ Concentration . . . 137
5.3.1 Fuel Cell Mode . . . 137
5.3.2 Electrolysis Mode . . . 140
5.4 Effect of Increasing the Humidity in Supplied Gas Feed . . . 141
5.5 Effect of Operating without $H_2$ in the Gas Feed . . . 143
5.6 Cell Kinetics . . . 146
5.7 BZY10 Cell . . . 149
5.8 Summary . . . 151

**6 Post-Test Analysis of the Microstructure and Composition of Cells 154**

6.1 Introduction . . . 154
6.2 Analysis of Cells with Anodes Exposed to 5% $H_2$ Humidified to ≈3% . . . 155
6.3 Analysis of Cell with Anode Exposed to 66% $H_2$ Humidified to ≈3% . . . 165
6.4 Effect of Increased Humidity in Supplied Gas Feed on Cell Stability . . . 168
6.5 Summary . . . 172

**7 Conclusions and Further Work 174**

# Chapter 1

# Electrolysers

## 1.1 Review of Hydrogen Production Methods

### 1.1.1 Introduction

Electricity serves as today's most used energy carrier, however, a large proportion of current methods of electricity production rely on fossil fuels. This reliance has resulted in significant environmental damage and puts the world's population's health at risk. Political, social and economic issues also arise due to dependence on oil producing nations. This issue is of critical importance to mankind's continued inhabitation of earth as the consequences of not initiating a rapid change in the way electrical power is produced are potentially cataclysmic. In October 2008, the British Government's independent climate change committee recommended that UK greenhouse gas emissions were to be cut by 80% in comparison to 1990 levels by 2050. This clearly indicates the urgency with which experts on climate change believe action is required to avoid environmental disaster. Thus, a non-polluting renewable fuel is required so that the problems with the burning of fossil fuels may be avoided.

A hydrogen based economy has been identified as having potential economic and environmental benefits and could ultimately lead to an infinitely sustainable fuel source. However, there are a number of issues that need to be addressed before a hydrogen economy can become a reality. One of the most prominent of these is the availability of reliable sources of hydrogen produced in a truly 'clean' manner. Hydrogen gas does not exist naturally in large quantities on earth; therefore, the production of a useful hydrogen fuel involves the separation of hydrogen from

hydrogen containing compounds. Some applications that utilise hydrogen require very high purity levels and in such cases, separation is required to be efficient with additional purification steps undesirable. Traditional methods of hydrogen production damage the environment and are unsustainable as they are based on the separation of hydrogen from hydrocarbons. Water is an abundant, non-carbonaceous resource, and as such, is often used as the hydrogen containing compound in hydrogen production methods currently in development. However, these developing methods must compete with traditional methods economically, and hence, a target 'dollars per unit volume of hydrogen' value must be achievable by developing methods if they are to be employed on a large scale. Hydrogen production methods are judged on their capability to exhibit the following:

- Low environmental impact
- High energy efficiencies and hence, low hydrogen cost
- Good Sustainability

Low environmental impact and good sustainability are now fundamental prerequisites of candidate hydrogen production methods for research and development. Therefore, research and development of hydrogen production methods are generally focused on improving specific efficiencies, with the ultimate goal of decreasing the cost per unit of hydrogen gas produced.

Some hydrogen production methods are only practical for producing relatively large volumes of hydrogen centrally for subsequent distribution whereas others are more suited to producing smaller volumes of hydrogen on-site. Therefore, the development of a range of different hydrogen production processes to suit different end uses is prudent. A fuel cell consumes hydrogen and produces electrical power with the only by-product being water and is one of the most promising uses of hydrogen as a fuel source. These devices are modular systems that can be scaled for a range of applications including transportation and Combined Heat and Power (CHP) for domestic or commercial buildings. Fuel cells are primarily in the research and development stage and are discussed further throughout this thesis.

Brief reviews of hydrogen production methods that account for significant proportions of current production and research activity follow.

### 1.1.2 Hydrocarbons

#### 1.1.2.1 Steam Methane Reformation

The majority of the hydrogen produced in the world today is formed by Steam Methane Reformation (SMR) (95% [27]). Currently the most mature hydrogen production technology, SMR is also the least expensive method of hydrogen production. This process sets the target '$ per unit hydrogen value' that other processes must strive to compete with. This will be discussed further in section 1.2.

The SMR process begins with the reaction 1.1 occurring, commonly using a nickel based catalyst, at temperatures ranging from 700 to 1000$^o$C [28].

$$CH_4 + H_2O \rightleftharpoons CO + 3H_2 \qquad \Delta H_{298K} = 206 kJmol^{-1} \tag{1.1}$$

$$CO + H_2O \rightleftharpoons CO_2 + H_2 \qquad \Delta H_{298K} = -46 kJmol^{-1} \tag{1.2}$$

The carbon monoxide produced can then be combined with more steam to produce more hydrogen in the water gas shift reaction (reaction 1.2). The byproduct of this reaction is carbon dioxide ($CO_2$). Although $CO_2$ is essential for photosynthesis in plants, it is the predominant scientific opinion that excessive build up of $CO_2$ in the Earth's atmosphere has led to global warming by the greenhouse effect. Continued global warming will cause an increase in ocean temperatures, resulting in glacial retreat and consequently sea levels will rise. Further implications could include; an increase in the intensity of extreme weather events, extinction of species and changes in agricultural yields. The greenhouse effect is caused by the presence of 'greenhouse gases', such as $CO_2$, that absorb and emit infrared radiation in the Earth's atmosphere. Sunlight transmits heat energy to the Earth via radiation with wavelengths close to or within the visible spectrum. The Earth then emits infrared radiation which is absorbed by the greenhouse gases in the atmosphere. Some of this radiation is then safely emitted by greenhouse gases into space, however, the remaining radiation is emitted back towards the Earth, thereby resulting in global warming.

One solution that has been proposed to prevent the release of carbon dioxide into the atmosphere is to sequester unwanted carbon dioxide into geologic or oceanic sinks. Considerable research and development is required to bring down the costs of the process, to elucidate the environmental effects of storage and to ensure that carbon dioxide will not escape from stores in unacceptably short timescales [29]. Rice [30] discussed the various ideas for carbon dioxide sequestration in the sea and sea beds and comes to the conclusion that the best method is yet to be defined.

Hydrogen produced by SMR will contain residual carbon monoxide, sulfur and chlorine unless the product is purified. Ultra-high purity $H_2$ is required for systems such as low temperature Proton Exchange Membrane (PEM) fuel cells due to poisoning of electrodes by carbon monoxide. In such instances, the additional expense required to purify hydrogen produced by SMR, means that other hydrogen production methods should be considered [31].

Hydrocarbon reformation may be integrated into Solid Oxide Fuel Cell (SOFC) technology so that hydrocarbon based fuels such as natural gas and naphtha can be internally reformed to produce hydrogen. Internal reformation simplifies the design of SOFCs and their efficiency is increased by utilising the heat generated from the electrochemical reaction of the fuel cell in the hydrocarbon reformation process [32] (equation 1.1). SOFCs operating in this manner could play an important role in the commercialisation of SOFC technology and may act as a stepping stone towards a hydrogen economy. For environmental reasons, it is desirable to ultimately run an SOFC on pure hydrogen produced ecologically, but until a sufficient infrastructure for hydrogen production, storage and distribution is developed, SOFCs with integrated hydrocarbon reformation capability can offer efficient power production from readily available fuel sources.

#### 1.1.2.2 Catalytic Cracking of Methane

Catalytic cracking of methane may represent an attractive alternative to SMR [33]. During the process the following reaction takes place at temperatures between 500 and 800$^o$C;

$$CH_{4(g)} \rightarrow C_{(s)} + 2H_{2(g)} \qquad \Delta H_{298K} = 75kJmol^{-1} \tag{1.3}$$

The advantages of this process over SMR are;

- The hydrogen gas product is not contaminated by carbon monoxide

- Catalytic cracking of methane is an inherently simpler, one step, process
- The SMR reaction is approximately twice as endothermic, or in other words, requires twice the amount of heat energy per mole of hydrogen produced

Catalytic methane cracking does, however, have problems that are yet to be resolved. Currently, the catalysts degenerate with use and its activity decreases as a result. In order to regenerate the catalyst so that its activity is restored, full or partial gasification of carbon in the catalyst is required. There are currently various different materials that are being investigated for use as catalysts in this process such as $NiO_xCuO_{1-x}/MgAl_2O_4$ [31] and $Ni/CeO_2$ [34] in an attempt to improve the deactivation issue and lower the process temperature. The alternatives to these transition metal catalysts are activated carbon catalysts [35, 36]. These materials have the advantage of not requiring separation from the carbon produced but are at the early developmental stage of research.

#### 1.1.2.3 Sorption-Enhanced Hydrogen Production from Methane

Sorption-enhanced hydrogen production is another process involving hydrogen separation from methane and was reviewed by Harrison [37]. During this process, reactions in equations (1.1), (1.2) and carbon dioxide separation reactions take place simultaneously at around $700^oC$ over a mixture of reforming catalyst and carbon dioxide sorbent to give the following overall reaction:

$$CH_{4(g)} + 2H_2O_{(g)} + Sorbent_{(s)} \rightarrow 4H_{2(g)} + Sorbent{\bullet}CO_{2(s)} \tag{1.4}$$

Experimental results reported that in practice, the product may contain 98% $H_2$ and only ppmv levels of CO and $CO_2$, thereby minimizing the final $H_2$ purification step or even eliminating it for some applications. The process has potential advantages in comparison to the standard steam-$CH_4$ reforming process including improved energy efficiency and capital cost reduction through process simplification. However, as with methane cracking, the sorbent must be regenerated using increased temperature and/or pressure and as a result produces carbon dioxide. Variants of calcium-based oxides and potassium promoted hydrotalcite are the materials that have been most intensively researched as potential carbon dioxide sorbents.

These methods of hydrogen separation from hydrocarbons inherently require fossil fuels; therefore, the hydrogen produced is not a truly clean or sustainable fuel. Many other methods of

hydrogen production are currently under research that are promising in terms of long term sustainability and environmental impact, which separate hydrogen from compounds that are not sourced from fossil fuels.

### 1.1.3 Sulphur-Iodine Process

Vitart *et al.* [38] state that the sulphur-iodine thermo-chemical cycle is considered to be one of the most promising methods for producing massive amounts of hydrogen, and uses heat energy from a very high temperature reactor. Thermo-chemical cycles use only heat energy to separate hydrogen from water through a number of chemical reactions that also produce recyclable by-products. The sulphur-iodine cycle proceeds as follows:

$$9I_{2(l)} + SO_{2(g)} + 16H_2O_{(l)} \rightarrow (2HI + 10H_2O + 8I_2)_{(l)} + (H_2SO_4 + 4H_2O)_{(l)} \tag{1.5}$$

[proceeding at $120^oC$]

The two liquids produced during this first reaction are separated and then heated to different temperatures. The first of these, once heated, will produce HI gas that can be heated further to produce hydrogen gas.

$$(2HI + 10H_2O + 8I_2)_{(l)} \rightarrow 2HI_{(g)} + (10H_2O + 8I_2)_{(l)} \tag{1.6}$$

[proceeding at $230^oC$]

$$2HI_{(g)} \rightarrow H_{2(g)} + I_{2(l)} \tag{1.7}$$

[proceeding at $330^oC$]

The second liquid is processed in the following way, so that $SO_2$ and $H_2O$ reactants are produced and can be recycled;

$$(H_2SO_4 + 4H_2O)_{(l)} \rightarrow H_2SO_{4(l)} + 4H_2O_{(l)} \tag{1.8}$$

[proceeding at $300^oC$]

$$H_2SO_{4(l)} \rightarrow H_2SO_{4(g)} \tag{1.9}$$

[proceeding at $360^oC$]

$$H_2SO_{4(g)} \rightarrow SO_{3(g)} + H_2O_{(g)} \tag{1.10}$$

[proceeding at $400^oC$]

$$SO_{3(g)} \rightarrow SO_{2(g)} + \frac{1}{2}O_{2(g)} \tag{1.11}$$

[proceeding at $870^oC$]

Vitart *et al.* report that the current achievable efficiency for the sulphur-iodine process is 34-37% when the efficiencies of components such as pumps and compressors are taken into account. However, hydrogen produced centrally using this method would be required to be stored and distributed. Current issues related to hydrogen storge are discussed in section 1.3 and the infrastructure for hydrogen distribution also requires significant thought and investment for such central hydrogen production methods to become viable.

### 1.1.4 Biological

Currently, there is a significant amount of study of hydrogen production by biological methods. The use of either photosynthetic micro-organisms [39] or non-photosynthetic anaerobic bacteria [40] in hydrogen production processes is attracting attention as environmentally friendly and energy saving alternatives. Biomass gasification is another method of hydrogen production and normally emits low levels of $CO_2$ [27] that could be sequestered. As previously discussed, the cost and environmental implications of $CO_2$ sequestration must be carefully considered [41]. Das *et al.* [42] recently reported in a review of biological hydrogen production methods, specific problems that have been found with producing hydrogen from crops or biological waste and identified where further understanding and improvement is required. These included:

- Costly processing methods of some biomass feed stock
- A lack of an outstanding candidate for a robust, industrially capable micro-organism that can be metabolically engineered to produce a sufficiently favourable hydrogen gas to glucose molar ratio
- Sustenance of a steady $H_2$ production rate
- Scalability

- Prevention of interspecies $H_2$ transfer in non sterile conditions and separation/purification of $H_2$
- Sensitivity of hydrogenase to $O_2$ and $H_2$ partial pressure severely lowers the process efficiency, resulting in a lower yield
- Insufficient knowledge on the metabolism of $H_2$ producing bacteria and the levels of $H_2$ concentration tolerance of these bacteria.

### 1.1.5 Photo-electrochemical

Hydrogen production from the hydrolysis of water by using solar energy, or other sources of optical energy, has been studied since the HondaFujishima effect was first reported in 1972 [43, 44]. $TiO_2$ was found to hydrolyse water with the efficiency of the process greatly improved by doping the material with carbon and has since been studied in great depth [45–48]. Materials with similar capabilities such as $KTaO_3$, $BaTiO_3$, $SrTiO_3$ and ZnO have also been studied [49–51]. Devices have been designed that incorporate these materials into arrays of photo-eletrochemical cells that can be placed onto roofs or other suitably sunlit areas. Hydrogen Solar are a company researching devices of this type and are working on reducing the cost of cell components [52]. Currently, the problems with photo-electrochemical cells reported in the literature include finding materials:

- With band gaps that better match the solar spectrum
- Whose band edges are located at potentials that allow the direct photo-induced evolution of $H_2$ and $O_2$, and
- Materials that exhibit a high level of chemical stability against photo-anodic dissolution

These fundamental requirements are yet to be resolved for a single system, and therefore, the application of this process as an efficient and practical method for hydrogen production is presently not possible [49].

The hydrogen production methods that have been discussed here will compete with electrolysers to become the most efficient, inexpensive, ecologically sound and practical solution to hydrogen production. Socio-economic and scientific issues with electrolysers will now be discussed in depth and their potential benefits highlighted.

## 1.2 An Introduction to Electrolysers

### 1.2.1 The Role of Electrolysers in the Energy Landscape

High temperature electrolysers are in the early stages of R&D and therefore, when considering the role of electrolysers in the energy landscape, the economic situation must first be assessed. There must be an enabling target value for the cost of manufacturing a device that allows for capital investment to be realistic. Reductions in device manufacturing costs can be achieved by research into less expensive materials and development of manufacturing processes. In a report made by the Electric Power Research Institute (EPRI) to the United States Department of Energy (DoE), estimates of electrolyser capital cost and the direct cost of electrolytic hydrogen were made. However, manufacturing costs of electrolysers are uncertain and depend on a vast number of parameters such as; stack size/voltage, operating pressure, number of units made per year, installation and materials costs. Comparing capital costs of an electrolyser with the costs of other methods of hydrogen production should therefore be approached with caution. A further essential target value must also be set for the cost of electrolytic hydrogen per unit, which must be competitive with other methods of hydrogen production for electrolysers to become economically viable. The improvement of various system efficiencies, as well as the catalysis of the reactions that occur within the cells themselves, is required in order to reduce the cost of electrolytic hydrogen. A reasonable comparison of the direct cost of hydrogen production by electrolysis with SMR can be made based on current obtainable efficiencies and resource costs. Raissi and Block [53] reported that the cost of hydrogen produced by SMR is roughly 3 times the cost of the feedstock. The commercial price of natural gas in June 2009 was on average \$2 per gge (based on higher heating value), where gge is the amount of alternative fuel it takes to equal the energy content of one liquid gallon of gasoline. Therefore, the cost of hydrogen produced by SMR would be approximately \$6 per gge, although this value is likely to rise in the future based on projected supply and demand. The EPRI report considered an electricity cost of 0.035 $\$kWh^{-1}$ and calculated the cost of electrolytic hydrogen to be \$14, \$8 or \$4 per gge including maintenance and gas compression costs, but not storage, for an electrolsyer producing 10, 100 and 1000 kg of hydrogen per day respectively [54]. Details on the operating temperature of the system and how heat energy should be supplied to the system were not stated in the report. Based on these calculations, electrolysers would need to be made to a large scale in order to

compete with SMR on an economic basis. A clearer target for the cost of electrolytic hydrogen was set by the US DoE in 2005 when they announced a new hydrogen cost goal of $2-$3 per gge (delivered, untaxed, 2005$, by 2015). Should indirect costs be discounted and an electricity cost of 0.035 $\$kWh^{-1}$ be assumed, this would relate to a power cost of 28500-43000 moles of hydrogen gas per kWh.

A reliable hydrogen infrastructure is essential in building the foundations of a hydrogen economy and an important part of this infrastructure is the development of more efficient hydrogen production systems [55]. Electrolysers enable on site and on demand production of hydrogen and will play an important role in the future energy landscape. Steam electrolysis using electricity from renewable sources such as solar or wind power, allows clean and sustainable fuel to be produced with negligible local air pollutants and greenhouse gas emissions. When installed in refueling stations a reliable supply of hydrogen gas for fuel cell vehicles can be provided by electrolysers. Levene *et al.* [56] analysed the capability of electrolysers to provide hydrogen fuel for fuel cell vehicles. It was concluded that ample solar and wind resources exist to meet the transportation fuel needs of the United States, but renewable energy systems face challenges to reduce the cost of electricity and to independently meet the energy requirements of distributed fueling stations.

Alternatively, electrolytic hydrogen produced centrally has advantages. Due to continued interest in nuclear power and the potential benefits, the coupling of electrolysers with nuclear reactors was assessed by Shin *et al.*and Fujiwara *et al.* [57, 58]. By utilising the heat and off-peak electricity from a nuclear reactor, the cost of hydrogen produced can be dramatically reduced (see section 1.2.2). In this configuration electrolysers would produce $H_2$ centrally for distribution via either tankers or pipelines. Nuclear power is an alternative source of energy that is growing in popularity with governments seeking a solution to securing future energy sources. The rise in oil prices and the increased concern about $CO_2$ emissions have promoted the use of nuclear power as an economically viable and secure energy source for power generation. Also, technological advancements have improved reactor safety and waste management. However, the disposal of spent nuclear fuel, consisting of transuranic elements and highly enriched uranium, represents a major problem and is under investigation by the international scientific community to identify the most promising solutions [59]. However, as with the sulphur-iodine process, the problems of

hydrogen storage must be emphasised when considering centrally distributed hydrogen production and this topic will be discussed in section 1.3.

### 1.2.2 Low or High Temperature Electrolysers?

There are two distinct subcategories of electrolysers: High and low temperature. Electrolysers that use High Temperature Electrolysis of Steam (HTES) and Low Temperature Electrolysis of Steam (LTES) differ greatly in design. LTES devices incorporating a solid polymer electrolyte have been tested at temperatures between 80 and 400$^o$C [60, 61]. Systems operating at the higher end of the temperature range were not stable; however systems operating between 80 and 200$^o$C were shown to have sufficient stability to warrant further study. Alkaline based low temperature electrolysis cells have also been investigated at temperatures around 25$^o$C [62, 63]. It was commented that high electric energy consumption is the biggest problem with alkaline systems and this degrades the competitiveness of the process. LTES is a more mature technology than HTES with companies such as ITM Power currently commercialising a polymer electrolyte based LTES device [64]. However, there are many factors that support the arguement that HTES has greater potential than LTES:

- The electrolysis of $H_2O$ is increasingly endothermic with increasing temperature and therefore requires more heat energy supplied to maintain operation. However, the electrical power need is reduced at higher temperatures (600-1000$^o$C) because the joule heating of an electrolysis cell can be utilised to supply this additional heat energy [65].
- High temperature helps to reduce electrode overpotentials which cause power losses in the electrolysis cell [1].
- Low temperature electrolysis cells have corrosion problems on electrodes, whereas high temperature electrolysers (ceramic solid oxide) are almost corrosion free [1].

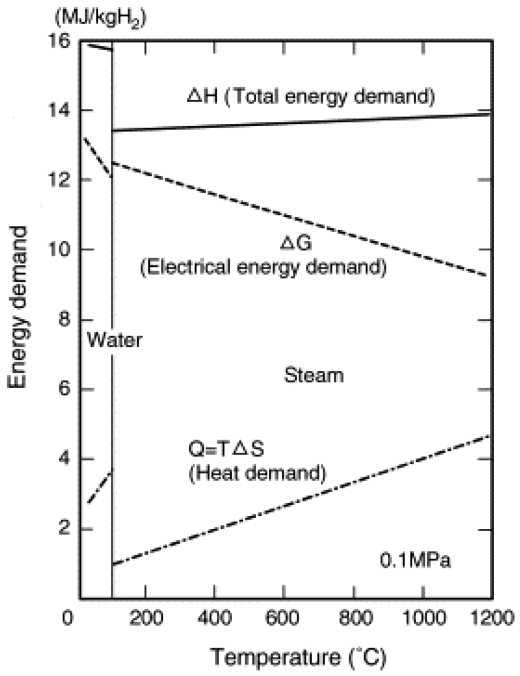



Figure 1.1: Graph showing heat (Q), electrical ($\Delta$G) and total ($\Delta$H) energy demand change with temperature [1]. As electrolyser operating temperature increases, $\Delta$G decreases, reducing the cost of the hydrogen produced. This is assuming that the additional heat energy required is provided from an external source.

Figure 1.1 shows how electrical energy demand ($\Delta$G) decreases and heat energy demand (Q) increases with increasing temperature at a steam pressure of 0.1 MPa. The combination of these two effects ($\Delta$H) is also displayed in figure 1.1, showing a slight increase in total energy with temperature. Even though total energy demand is increasing, the important factor to consider is the decrease in electrical energy demand as over two thirds of the cost of electrolytic hydrogen arises from electricity usage. Operating at higher temperature can therefore effectively decrease the cost of the hydrogen produced if the increase in heat energy demand can be fulfilled by an external heat source. Also, by using solid oxide ionic conductors, high temperature electrolysis systems benefit from their high levels of ionic conductivity at elevated temperatures which reduces the power required to electrolyse steam.

### 1.2.3 Basic Operation of Solid Oxide Systems

Conventionally, solid oxide systems are based on oxide ion conducting materials. Figure 1.2(b) displays the processes occurring during the operation of an oxide ion conducting Solid Oxide Electrolysis Cell (SOEC). An electrolysis cell operates by using electrical power to dissociate

$H_2O$ and produce $H_2$ gas. In SOEC mode, the anode is the positive electrode and the cathode is the negative electrode. Electrons combine with $H_2O$ at the cathode forming hydrogen gas and oxygen ions. The hydrogen gas flows away from the cathode and oxygen ions migrate through the electrolyte and reduce at the electrolyte-anode interface, producing oxygen gas.

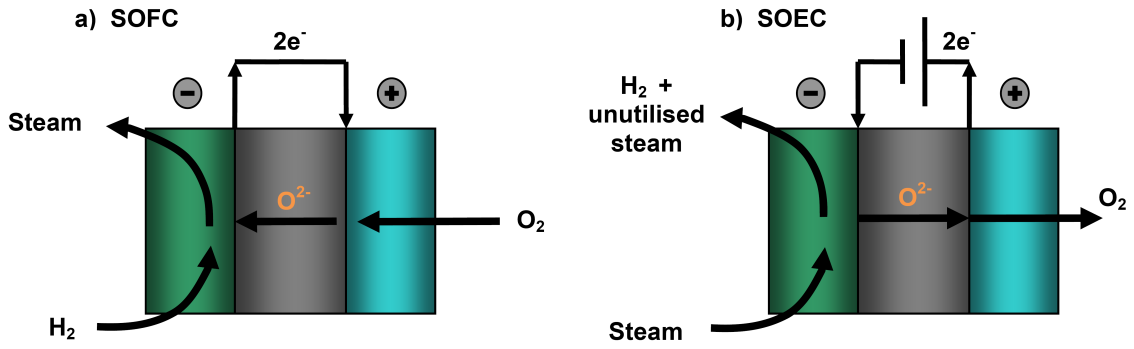



Figure 1.2: Schematics representing the operation of; (a) an oxide ion conducting SOFC, and (b) an oxide ion conducting SOEC

Figure 1.2(a) displays the processes occurring during the operation of an oxide ion conducting SOFC. Oxidant flows across the cathode (positive) surface and is reduced and fuel (in this case hydrogen) flows across the anode (negative) and is oxidised. Electrons liberated from the fuel travel to the external circuit. Oxygen gas combines with electrons from the external circuit to create oxygen ions at the cathode. These oxygen ions then migrate through the gas impermeable electrolyte and react with fuel at the anode to complete the circuit. Examples of possible electrode reactions in both SOFC and SOEC modes and resultant overall reactions are shown in table 1.1.

It is possible, and potentially beneficial, for electrolysers to be able to be reversed to act as a fuel cell. Savings on space and manufacturing costs make reversible SOECs practical if sufficient catalysis of appropriate reactions can be achieved in both electrolysis and fuel cell modes. Since SOFC technology has had a very large amount of dedicated research, a starting point for SOEC designs are often based on reversing SOFCs. Eguchi *et al.* investigated the implications of testing SOFC designs in SOEC mode [66]. This study found that because of the differing electrode reactions occurring in each mode (SOFC and SOEC), simply reversing the operation of an efficient SOFC did not create an efficient SOEC. It was also found that when a cell incorporating a ceria based electrolyte was operated in SOEC mode, the applied potential caused the reduction

of $Ce^{4+}$ to $Ce^{3+}$. This reduction lowered the ionic transference number and promoted electronic conductivity in the electrolyte, thus causing SOEC efficiency to deteriorate. The conclusion was made that a bare ceria based electrolyte cannot be used for SOEC applications. A suggested solution to this was to coat the surfaces of the ceria based electrolyte with thin Yttria Stabilised Zirconia (YSZ) layers. The mixed electrolyte cell achieved low internal resistance and theoretical Open Circuit Voltage (OCV) and hence was an encouraging result for the investigation of reversible cells.

| SOFC | SOEC |
|---|---|
| Anode (-) | Anode (+) |
| $H_{2(g)} + O_o^x \rightarrow H_2O_{(g)} + V_o^{\bullet\bullet} + 2e'$ (1.12) | $O_o^x \rightarrow 2e' + \frac{1}{2}O_{2(g)} + V_o^{\bullet\bullet}$ (1.13) |
| Cathode (+) | Cathode (-) |
| $\frac{1}{2}O_{2(g)} + V_o^{\bullet\bullet} + 2e' \rightarrow O_o^x$ (1.14) | $H_2O_{(g)} + V_o^{\bullet\bullet} + 2e' \rightarrow H_{2(g)} + O_o^x$ (1.15) |
| Total | |
| $H_{2(g)} + \frac{1}{2}O_{2(g)} \rightarrow H_2O_{(g)}$ (1.16) | $H_2O_{(g)} \rightarrow H_{2(g)} + \frac{1}{2}O_{2(g)}$ (1.17) |

Table 1.1: Electrode and total reactions of an oxide ion conducting device in SOFC and SOEC modes. Kröger-Vink notation is used to describe the interactions between fluids and the device components

This thesis is focused on the development of a proton conducting system that operates in a different manner to systems based on oxide ion conductors. An inherent advantage of a proton conducting SOEC over an oxide ion conducting SOEC, is that these systems produce pure, dry hydrogen gas at the cathode, as shown in figure 1.3. In an oxide ion conducting device, non-utilised steam is mixed with the hydrogen produced and these gases require separation which requires additional energy and components. This also means that proton conducting SOECs are able to be coupled directly with a high temperature reactor steam cycle whereas an oxide ion conducting system are not.

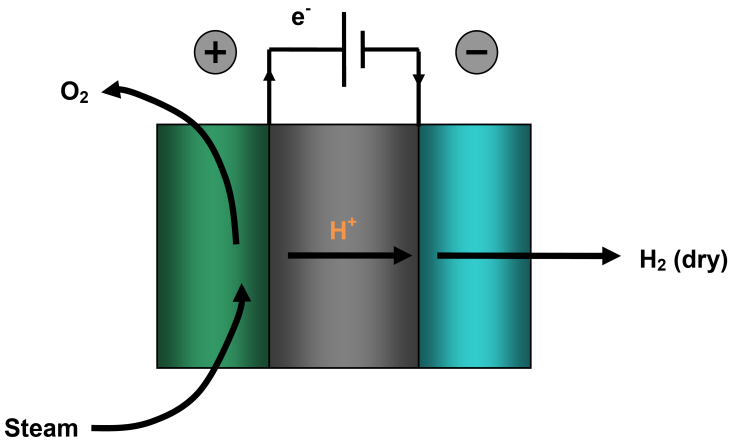



Figure 1.3: Schematic showing the basic operation of a proton conducting SOEC supplied with steam

The following are possible proton conducting SOEC electrode reactions using Kröger-Vink notation to describe interactions between fluids and the electrolyser components;

$$\textbf{Anode (+)} \qquad H_2O_{(g)} + V_o^{\bullet\bullet} + O_o^x \rightarrow 2OH_o^{\bullet} \tag{1.18}$$

$$\textbf{Cathode (-)} \qquad 2OH_o^{\bullet} + 2e' \rightarrow H_{2(g)} + 2O_o^x \tag{1.19}$$

Steam is dissociated at the cathode by the application of power to the cell where protons become associated with filled oxygen ion sites in the electrolyte to form a protonic defect. Protons are then able to be transported across the electrolyte by using filled oxygen ions sites as pivots. The mechanism of protonic defect formation and protonic transport in the electrolyte for both SOEC and SOFC modes and will be discussed in depth in sections 2.4 and 2.5.

Proton conducting SOFC systems have a fundamental advantage over oxide ion conducting systems. Steam and fuel do not need to be separated at the anode (-) (see figure 1.4), whereas in oxide ion conducting based SOFCs, steam dilutes the fuel at the anode. This causes cell performance deterioration in the oxide ion conducting system unless the fuel gas is circulated to remove the water vapour [67] (see figure 1.2(a)).

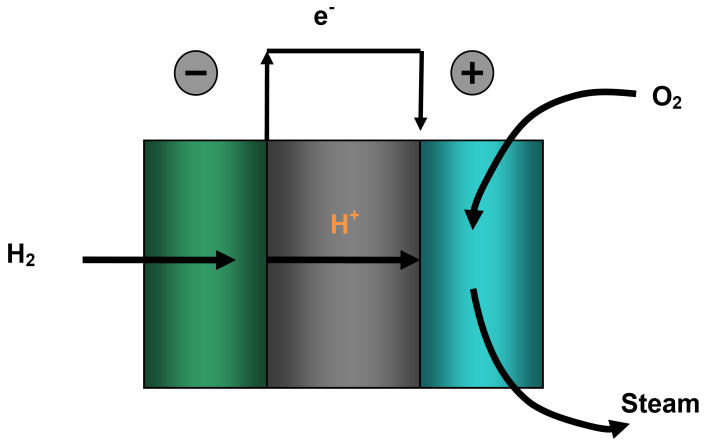



Figure 1.4: Schematic showing the basic operation of a proton conducting SOFC with pure hydrogen as a fuel source

The following are possible proton SOFC electrode reactions using Kröger-Vink notation to describe interactions between fluids and the fuel cell components;

$$\textbf{Anode (-)} \qquad H_{2(g)} + 2O_o^x \rightarrow 2OH_o^\bullet + 2e' \tag{1.20}$$

$$\textbf{Cathode (+)} \qquad 2OH_o^\bullet + \frac{1}{2}O_{2(g)} + 2e' \rightarrow H_2O_{(g)} + 2O_o^x \tag{1.21}$$

It is interesting to note that the direction of electronic and ionic current flow when changing from SOEC to SOFC mode does not change in proton conducting systems but does change in oxide ion conducting systems. Current reversal may have a detrimental impact on reversible SOEC durabilities although there is currently no evidence to support this theory.

Proton conductors have been proven to be able to conduct oxide ions as well as protons at higher temperatures [7]. This complicates the operation of these devices greatly but could potentially be beneficial to the device performances. Should mixed ionic conduction occur, the number of possible electrode reactions increases. Consequentially, the manner of reaction completion and the status of the resultant products in relation to the components of the SOEC/SOFC, could lead to a major change in the performance of the device. This issue, as well as a more detailed account of the mechanisms of device operation, are discussed at length in the following chapters.

Once hydrogen has been produced it is required to be stored before use. A brief review of current

issues and technologies in the hydrogen storage research field follows.

## 1.3 Hydrogen Storage for use with Fuel Cells

With the use of electrolysers, hydrogen can be used as a storage medium for electricity generated from renewable resources. For example, the electricity generated by solar power during the day could be used to electrolyse water and produce hydrogen which can be stored. This stored hydrogen could then be used to create electrical power using fuel cells during times when the solar cells cannot, for instance, at night, or on board a vehicle. The energy storage capacity of hydrogen can therefore be the solution to one of the most crucial issues with renewable energy sources by allowing a typical renewable, intermittent supply of power, to indirectly supply power on demand, reliably. However, one of the crucial technological barriers to the widespread use of hydrogen as an effective energy carrier is the lack of a safe, low-weight and low-cost hydrogen storage method. Currently there are four main technologies for hydrogen storage:

- Hydrogen pressurisation
- Hydrogen absorption in metal hydrides
- Hydrogen adsorption on/in carbon based materials
- Liquefaction of hydrogen

Pressurisation of hydrogen gas and hydrogen adsorption in metal hydrides, are considered to be the two most mature hydrogen storage technologies of these four [71]. The storage of hydrogen

| Energy Source | Specific Energy ($kWh.kg^{-1}$) | Energy Density ($kWh.dm^{-3}$) |
|---|---|---|
| Liquid Hydrogen [68] | 1.2 | 1.7 |
| Compressed Hydrogen (350 bar - 35MPa) [68] | 0.5 | 1.9 |
| Compressed Hydrogen (700 bar - 70MPa) [68] | 0.8 | 1.6 |
| Carbon Materials | undetermined | undetermined |
| Complex Metal Hydrides [68] | 0.6 | 0.8 |
| Chemical Hydrides [68] | 1 | 1.4 |
| Li-ion Batteries [69] | 0.16 | 0.165 |
| U.S. DOE Target 2010 [70] | 2 | 1.5 |
| U.S. DOE Target 2015 [70] | 3 | 2.7 |

Table 1.2: Specific energy and energy density values for various energy storage technologies also with targets set by the United States Department of Energy

for mobile applications remains a barrier to the implementation of fuel cell vehicles. Therefore, research has concentrated on achieving solutions that give high specific energy ($kWh.kg^{-1}$) and energy density values ($kWh.dm^{-3}$). Current achievable specific energy and energy density values for various hydrogen storage technologies are compared with United States Department of Energy (U.S. DOE) targets and competing energy storage technologies in Table 1.2. An assessment of the potential of each of these four technologies to achieve the properties and levels of performance required to operate in conjunction with fuel cells follows.

### 1.3.1 Pressurisation of Hydrogen

Containers used to store compressed hydrogen gas are made from carbon fibre composites that have high strength and low weight. A potential issue with the pressurisation of hydrogen gas is cost, as up to 20% of the energy content of hydrogen can be required to compress the gas from ambient conditions [72]. However, a unique advantage of electrolysis over other methods of hydrogen production is that electrolysers can be used as electrochemical compressors and can require as little as an additional 100 mV of applied potential to pressurise hydrogen from ambient pressure to 34.5 MPa (345 bar) [55]. A major disadvantage of storing hydrogen in compressed cylinders is that only a very low energy density can be achieved. Pressurisation technology is therefore highly unlikely to be employed in mobile applications but may be the most economically viable option for stationary applications.

### 1.3.2 Absorption in Metal Hydrides

The criteria for metal hydride materials for hydrogen storage are very demanding. The material must have a high storage capacity (wt% hydrogen) with the potential for a high degree of dehydrogenation. Fast hydrogen uptake and release kinetics are also required to reduce refueling times and allow a sufficient fuel delivery rate to the fuel cell. Furthermore, good durability with respect to cycling and exposure to various atmospheres and contaminants is also crucial. When considering suitable metal hydrides as a storage medium for hydrogen, the pressure at which the hydrogen is required to be delivered to the fuel cell and the potential waste heat from the fuel cell that can be utilised for hydrogen release from the metal hydride, must be evaluated and a match found. The dehydrogenation temperature of the material then becomes another crucial material property to consider. Commercially available $LaNi_5H_6$ can function in the required

pressure and temperature window for a typical PEM fuel cell, but its energy density is too low and it is too expensive for mobile applications [70]. Sodium alanates doped with titanium have the potential to offer higher energy density values, but these complex metal hydrides have a low hydrogen storage capacity (max. potential 5.5 wt%) and slow hydrogen uptake and release kinetics [70]. Development of materials with potential to meet the stringent requirements is ongiong.

### 1.3.3 Adsorption/Absorption on/in Carbon Based Materials

Carbon based materials are high surface area sorbents that offer the advantages of fast hydrogen kinetics and low hydrogen binding energies and, hence, potentially fewer thermal management issues during hydrogen charging and discharging than with metal hydrides [70]. A comprehensive review of research on hydrogen storage by carbon based materials was conducted by Ströbel *et al.* and reported on a wide range of materials, including; activated carbon, graphite, graphene, fullerene and carbon or graphite nanofibres [73]. The authors commented that research was focused on maximising the hydrogen storage capacity, measured in weight% hydrogen, of these materials. Theoretical studies have indicated that stable scandium-based organometallic buckyball" fullerenes might adsorb and desorb as many as 11 hydrogen atoms per scandium atom, leading to a theoretical maximum reversible hydrogen storage density of close to 9 wt% [74]. Research into these materials is at an early stage and much more work is required in order to fully establish their capability to fulfill the requirements of a hydrogen storage medium.

### 1.3.4 Liquefaction of Hydrogen

Liquefaction offers higher specific energy and energy density values than pressurisation, although a similar, more acute disadvantage with this option exists, as up to 30% of the energy content of hydrogen may be required to liquefy ambient gas by cooling to 20 K [75]. A method circumventing such a large energy penalty for liquefaction has not been established, hence this method of hydrogen storage is unlikely to play a significant role in the future energy landscape.

## 1.4 Summary

There are many different ways to separate hydrogen from various compounds in order to create a fuel source for power devices such as fuel cells. Some of these methods have the potential to provide a reliable source of hydrogen at a lower cost than steam methane reformation to the mass market. Considering a remote location where the use of grid power is not possible or is undesirable, electrolysers coupled with wind or solar power can produce hydrogen on site and on demand, a capability that is currently unrivaled. Large scale SOEC operation for the centralised production of hydrogen is also a viable option since SOEC devices are modular and could be scaled with relative ease to application specifications. For example, integrating electrolysers into a nuclear power facility is an attractive application because heat energy from the nuclear power source can be utilised to reduce the electrical power demand of electrolysis at no extra cost. Furthermore, SOEC electrical power demand can be satisfied during the off-peak hours for the nuclear power source when the electricity cost is lower. However, issues with hydrogen storage and distribution must be addressed.

The advantages of high temperature proton conducting SOECs in comparison to oxide ion conducting systems and low temperature polymeric cells have been discussed. A high temperature proton conducting SOEC provides a pure dry source of hydrogen, whereas oxide ion systems do not. Also, the cost of electrolytic hydrogen produced at high temperature is lower than that produced using low temperature polymer electrolysers due to a lower electrical power demand. We have therefore focused on the development and analysis of these devices and the materials required.

The following chapter details and discusses the status of research on proton conducting materials and their implementation as electrolytes in SOECs and SOFCs.

# Chapter 2

# Review of Proton Conducting Materials for SOEC and SOFC Devices

## 2.1 Introduction

It was first found in the 1960s that protons existed in some oxides as minority charge carriers [76]. The prominent oxides were found to be $ABO_3$ - type perovskites mainly based on $SrCeO_3$, $SrZrO_3$, $BaCeO_3$ and $BaZrO_3$. To achieve proton conduction, a certain fraction of the B atoms are replaced by trivalent cations such as Y, Yb or Nd resulting in the formation of oxygen ion vacancies due to the charge neutrality condition (see equation 2.2). These oxygen ion vacancies have been proven to play a pivotal role in the uptake of water vapour [77]. When considering materials for the electrolyte in a proton conducting SOEC, it is crucial that sufficient proportions of protons and hydroxide ions created from the dissociation of water at the anode can be absorbed, so that the electrolysis reaction may occur efficiently.

The combination of high protonic conductivity and chemical stability is generally considered to be a key problem in utilising proton conducting oxides in SOEC/SOFC designs [78]. For example, doped $BaCeO_3$ has a high conductivity but a poor chemical stability and is only slightly thermodynamically stabilised with respect to decomposition into its binary oxides [9, 79]. This instability could lead to a reduction in the lifetime of the device should the material be exposed

to certain atmospheric conditions. Alternatively, a material such as In-doped $CaZrO_3$ exhibits good chemical stability, but its low conductivity means that it cannot be used in high drain applications such as SOECs or SOFCs [80]. A balance between these two properties is therefore required when selecting electrolyte materials for a proton conducting SOEC or SOFC device.

A review of previous work on proton conducting SOFC and SOEC devices and comments on the methods of sample synthesis follows. The mechanisms of protonic defect formation and protonic conduction are also discussed in this chapter.

## 2.2 Proton Conducting SOFCs

The use of proton conductors as electrolytes in SOFCs has been widely investigated by several authors [6,67,81–88]. Previous investigations into SOFC systems based on $BaZrO_3$, for example, have provided lower peak power density values than conventional SOFC systems based on oxide ion conducting electrolytes [9]. A large contribution to this finding can be attributed to the fact that there has been much more research into oxide ion conducting systems than proton conducting systems. Hence, when potential improvements to systems through, for example, reduction of electrode polarisation or grain boundary impedance are considered, there is scope for proton conducting SOFCs to become competitive. Examples of proton conducting SOFC systems are discussed in more detail in later sections in this chapter.

## 2.3 Proton Conducting SOECs

As mentioned in section 1.2.3, a significant advantage of proton conducting SOECs over oxide ion conducting SOECs is that proton conducting SOECs produce pure hydrogen at the cathode (see figure 1.3), whereas oxide ion conducting SOECs produce a mixture of hydrogen and un-utilised steam at the cathode [67] (see figure 1.2(b)). Incorporation of an additional system to separate hydrogen and water increases the cost and size of the electrolyser. In addition to this, proton conductors have been reported to have higher ionic conductivities than oxide ion conductors at intermediate temperatures (400-700$^o$C) [89, 90]. Operation in this temperature range, lower than currently required for optimal oxide ion based system operation, could enable the use of materials that might otherwise be prohibited, allowing SOEC systems to become more affordable, robust, and practical.

Proton conducting perovskites containing cerium may not be suitable as fuel cell electrolytes due to stability limits in $CO_2$ containing atmospheres as outlined in section 2.2. Carbonaceous gases are not anticipated to exist in an electrolyser cell in practice, and therefore, these materials are promising electrolyte candidates for proton conducting SOECs due to their generally high protonic conductivity. One of the first attempts to electrolyse steam at high temperature using a proton conducting electrolyte was made by Iwahara *et al.* [86] in 1981. Cells made from $SrCe_{0.9}Sc_{0.1}O_{3-\delta}$ and $SrCe_{0.95}Sc_{0.05}O_{3-\delta}$ electrolytes coated with Pt electrodes were operated in electrolyser mode. Steam at 1 atm was supplied to the anode and argon was passed through the cathode compartment. It was commented that a high voltage was necessary to electrolyse steam due to insufficient conductivity of the proton conducting electrolyte. However, overvoltage (except ohmic loss) was less than 0.3 V at a current density of 0.4 $Acm^{-2}$. We may conclude from this work that the conductivity of Sc-doped $SrCeO_3$ is insufficient and that perhaps platinum is a suitable candidate for the initial electrode material. Although the platinum has a prohibitively high cost for implementation in a commercial product, the use of platinum electrodes would allow convenient comparison at this early research stage since alot of the work on proton conducting SOECs has utilised platinum as electrodes. Furthermore, platinum electrodes are easily applied to the surfaces of candidate electrode materials without extensive research into processing methods. Detailed results such as IV curves were not published in Iwahara's work, nor indeed were such results published previous to this work at all. The study of proton conducting SOEC systems is therefore very much in its infancy.

Iwahara *et al.* [67, 87] subsequently carried out further steam electrolysis experiments at temperatures of between 700-900$^oC$ using similar cells as previously. Current efficiencies for $H_2$ evolution were reported to be about 90% in the current density range 0.1-0.8 $Acm^{-2}$. It should be noted that the proton transport number is related to the current efficiency. Any current that causes electron - electron hole recombination, arising from electronic conduction in the electrolyte, will reduce the value of current efficiency for $H_2$ evolution. A considerably high applied voltage was found to be necessary to produce hydrogen and it was concluded that losses were largely due to ohmic losses. It was commented that proton conducting oxides are promising candidate electrolyte materials for fuel cells and electrolysers if they can be used as thin films to reduce the required voltage. The cell thicknesses were not reported, however, this argument is probably valid since there are significant processing challenges involved in creating thin ceramic

layers and at that stage, no work had been carried out on the creation of thin layers using such materials. Matsumoto *et al.* [91] also found that ohmic loss was the main contributor to the overall losses during their experiments. Steam was electrolysed at 800$^o$C with a cell made from $SrCe_{0.95}Yb_{0.05}O_{3-\delta}$ electrolyte and Pt electrodes. Hydrogen evolution was less than the theoretical maximum with the proton transport number measured to be as low as 0.6. At 800$^o$C it is likely that oxide ion transport occurred in the electrolyte which would have contributed to the low proton transport number measured and impacted the hydrogen evolution rate. Throughout these works, current losses were ascribed to electronic conduction [67, 87, 91]. In atmospheres with a low partial pressure of oxygen, electron liberation may have resulted from the reduction of $Ce^{4+}$ to $Ce^{3+}$ in these materials due to the charge neutrality condition;

$$Ce_{Ce}^{x} + O_{o}^{x} \rightarrow Ce_{Ce}^{'} + e^{'} + V_{o}^{\bullet\bullet} + \frac{1}{2}O_2 \tag{2.1}$$

A comprehensive study of proton conducting SOECs has since been conducted by Kobayashi *et al.* [92]. Steam electrolysis was carried out at temperatures between 460 and 600$^o$C, using a cell with a $SrZr_{0.9}Yb_{0.1}O_{3-\delta}$ electrolyte and Pt (56 vol%) - $SrZr_{0.9}Yb_{0.1}O_{3-\delta}$ (44 vol%) cermet electrodes. A current density of 2.4 mA cm$^{-2}$ was applied to the cell and immediately afterwards the $H_2$ production rate was close to the maximum theoretical rate. The $H_2$ production rate decreased with time and became almost constant after about 100 minutes. At the anode, the $O_2$ production rate was only 25% of the theoretical value just after direct current was applied and this rose to 38% after 100 minutes when steady state had been reached. Because of this, the $H_2$:$O_2$ production rate ratio at the start of electrolysis was much greater than the expected 2:1. The $H_2$:$O_2$ ratio only approached 2:1 after approximately 100 minutes. Just after direct current was applied, $H_2$ production was thought to have commenced at an increased rate because of the evolution of $H_2$ from a pre-existing concentration of protons. Once this initial proton concentration had been exhausted, the $H_2$:$O_2$ production ratio approached 2:1 as the hydrogen evolved at the cathode could only be produced from protons originating from the decomposition of water at the anode. Therefore, it can be said that the reaction rate of producing $H_2$ from protons and electrons at the cathode was found to be faster than that of oxidising water vapour into protons and $O_2$ at the anode. From this result, it can be said that research into the catalysis of the rate determining step or steps involved in the dissociation of steam at the anode should

take priorty over cathode development.

A patent has been published on steam electrolysers using a proton conducting electrolyte [93]. Many proton conducting materials were suggested for use as the electrolyte material in the document including BCY10, BZY10 and $BaCe_{0.9-x}Zr_xY_{0.1}O_{3-\delta}$ (BZCY). In the case of using BCY10, it was stated that a material with high chemical stability in $CO_2$ containing atmospheres such as $Sr_3CaZr_{0.5}Ta_{1.5}O_{2.95}$ should be used to coat the cathode side of the electrolyte to prevent degradation. Similarly, a material stable in atmospheres with high steam content should be used to coat the anode side of the electrolyte such as SCZTO or BZY10. The device was stated to operate between 500 and 700$^o$C with an electrolyte thickness of no more than 25 $\mu$m. A porous platinum cathode was suggested, however there is no suggestion of any specific material for the anode. It was proposed that the anode is deposited onto a $La_{0.8}Sr_{0.2}MnO_3$ substrate and then the electrolyte deposited onto the anode, followed by the cathode. Although the patent is not a scientific document, it does have a high importance since many ideas and thoughts on the composition and operation of a proton conducting SOEC are stated. These include a relevant discussion on the method of producing Y:$BaZrO_3$, a matter that is discussed further in section 2.8.

## 2.4 Formation of Protonic Defects

The most important reaction leading to the formation of protonic defects ($OH_o^{\bullet}$) in perovskites at intermediate temperatures is the dissociative absorption of water, which requires the presence of oxygen ions and oxygen ion vacancies ($V_o^{\bullet\bullet}$) [9] (see equation 2.4). Vacancies may be formed:

- By varying the ratio of the main constituents (e.g. complex perovskites such as $Ba_3Ca_{1+x}Nb_{2-x}O_{9-\delta}$ [94] or $BaY_{0.5}Sn_{0.5}O_{3-\delta}$ [95])
- Extrinsically, to compensate for an acceptor dopant M. In the case of perovskite type oxides, substitution of up to 30% of the B-site cation by a lower-valent cation (i.e., $A(B_{1-x}M_x)O_{3-\delta}$; denoted M:$ABO_3$)

An example of the latter of these two methods of vacancy formation is a trivalent dopant incorporated into a perovskite. The incorporation reaction in this example is written as follows;

$$M_2O_3 + 2B_B^x + O_o^x \rightarrow 2M_B^{'} + V_o^{\bullet\bullet} + 2BO_2 \tag{2.2}$$

Where; M = Trivalent metal ion, B = B-site perovskite ion.

Iwahara *et al.* [96] doped $BaCeO_3$ with trivalent and divalent cations to produce oxygen ion vacancies. When the dopant was changed from Y (trivalent) to Ca (divalent), both protonic and oxide ion conduction decreased. It was suggested that the larger difference in electronic charge between Ca and Ce caused a stronger interaction between Ca and oxide ion vacancies to be formed within the lattice. As a result, the accommodation and migration of protons in the oxide was hindered. It was concluded that better conduction can be achieved by doping prospective proton conducting perovskite-type materials with trivalent cations instead of divalent cations.

Once oxygen ion vacancies have been formed, the material can become hydrated by the dissociative absorption of water;

$$H_2O_{(g)} + V_o^{\bullet\bullet} + O_o^x \rightarrow 2OH_o^{\bullet} \tag{2.3}$$

Assuming;

- Ideal behaviour of all species involved in the hydration reaction
- That this leads to the formation of two protonic defects
- One crystallographic site exists for A, B, and O

the equilibrium condition is written [97]:

$$K = [OH_o^{\bullet}]^2 \left([V_o^{\bullet\bullet}][O_o^x]\, p_{H_2O}\right)^{-1} \tag{2.4}$$

Munch *et al.* [98] find that protonic defect concentration is lower in $Y:SrCeO_{3-\delta}$ than $Y:BaCeO_{3-\delta}$ for the same yttrium concentration and conclude that the number of the oxygen sites able to form protonic defects is less in $Y:SrCeO_{3-\delta}$ than $Y:BaCeO_{3-\delta}$. They find that oxygen sites in both materials decay into two types with differing degrees of electron density (basicity) and

that only the most electronegative type is involved in the formation of protonic defects. The proportion of oxygen ion sites with higher electron density in Y:$SrCeO_{3-\delta}$ was lower than in Y:$BaCeO_{3-\delta}$. Varying electronegativity of the oxygen ion site also has an impact on proton transport within the electrolyte and this will discussed further in the following section.

## 2.5 Proton Conducting Mechanism

Once protonic defects have been formed within the electrolyte in a proton conducting SOEC, protons must be transported from the anode to the cathode before combining with electrons so that $H_2$ is evolved. According to Kreuer [80], from one $H_2O$ molecule, two charged defects are formed at the anode that can diffuse into the bulk of the oxide, but only when accompanied by the counter diffusion of oxide ion vacancies $V_o^{\bullet\bullet}$. Kreuer *et al.* [99] reported in a detailed study of diffusion and water uptake for Gd:$BaCeO_{3-\delta}$, that ambipolar diffusion of $V_o^{\bullet\bullet}$ and $OH_o^{\bullet}$ occurs within the material when exposed to a water containing atmosphere (see figure 1.3). Protons attached to hydroxide ions produced in equation 4.9 were considered to be interstitials and migrate by 'hopping' from one filled oxygen site to an adjacent filled oxygen site [94, 99]. Ma *et al.* [100] proved that non-doped $BaCeO_3$ can exhibit proton conductivity in $H_2$, but not in wet air. This finding supports the conclusion of Kreuer *et al.* [9], that the presence of oxygen ion vacancies in perovskites is critical to the uptake of water and hence their protonic conductivity in wet atmospheres.

Hydroxide ions were considered to be able to migrate via oxygen ion vacancies in Nd:$BaCeO_{3-\delta}$ by Iwahara *et al.* [101] and Yb:$SrCeO_{3-\delta}$ by Bonanos *et al.* [5], although no firm evidence was presented. Kreuer *et al.*'s work [99] details why this was not the case with their samples of $BaCe_{0.9}Gd_{0.1}O_{3-\delta}$. The oxygen (tracer) diffusion coefficient at $640^oC$ for a specimen exposed to an atmosphere with a $pH_2O$ of 3.5 kPa was found to be an order of magnitude lower than for a specimen exposed to a dry atmosphere. The work directly proved that in this material;

- Oxygen (tracer) diffusion takes place via oxygen ion vacancies
- $OH_o^{\bullet}$ defects are 'blocking' the oxygen ion vacancies
- At $640^oC$, about 90% of the oxygen-ion vacancies in $BaCe_{0.9}Gd_{0.1}O_{3-\delta}$ that were unoccupied in the dry state became occupied by protonic defects ($OH_o^{\bullet}$) when the material was

exposed to a humidified atmosphere

Therefore, diffusion of protons must have involved proton transfer from $OH_o^\bullet$ to $O_o^x$ sites in $BaCe_{0.9}Gd_{0.1}O_{3-\delta}$ under these conditions. Under different conditions, the oxygen ion vacancy concentration may have remained relatively high whilst retaining a significant protonic defect concentration. Kreuer *et al.*'s work does not directly prove $OH_o^\bullet$ diffusion to be impossible under such circumstances. Protonic defect concentration can be measured by thermal gravimetric analysis (TGA) as $OH_o^\bullet$ formation is accompanied by a significant weight increase [9]. As part of the investigation by Kreuer *et al.* [99], the $OH_o^\bullet$ concentration was found to be 2.2 mol% in $BaCe_{0.9}Gd_{0.1}O_{3-\delta}$ under humidified conditions. Since under humidified conditions protonic defects were proven to occupy 90% of the oxygen ion vacancies present in the dry state, the upper limit for the concentration of oxygen vacancies in the dry state is then around 2.4 mol%, much lower than the assumed 5 mol% when considering: $2Gd_{Ce}^{'} = [V_o^{\bullet\bullet}]$. The low concentration of oxygen ion vacancies was explained by:

- A distribution of the Gd dopant over both cation ($Ba^{2+}$ and $Ce^{4+}$) sites
- Defect association

It is possible for the following defect associations to occur in Gd:$BaCeO_{3-\delta}$:

$$Gd_{Ce}^{'} + V_o^{\bullet\bullet} = (Gd_{Ce}^{'} V_o^{\bullet\bullet})^\bullet \tag{2.5}$$

$$2Gd_{Ce}^{'} + V_o^{\bullet\bullet} = (Gd_{Ce}^{'} V_o^{\bullet\bullet} Gd_{Ce}^{'}) \tag{2.6}$$

Such defect association occurs at a critical concentration of dopant and lowers the concentration of mobile oxygen ion vacancies. Also, when in a water containing atmosphere the following association could also occur:

$$Gd_{Ce}^{'} + OH_o^\bullet = (Gd_{Ce}^{'} OH_o^\bullet) \tag{2.7}$$

Davies *et al.* [102] note that an increase in dopant-hydroxyl defect association can increase the activation energy for conduction. Therefore, defect association is undesirable and because the likelihood of dopant-hydroxyl defect association increases with increasing dopant concentration,

the dopant concentration must be carefully chosen, as well as the dopant element. A contributory factor that the authors did not consider was the possibility of anion contaminants such as F or Cl forming $F_o^{\bullet}$ or $Cl_o^{\bullet}$ [103]. However, relatively high levels of impurities would have had to be present to account for the 2.6 mol% discrepency in its entirity.

Kreuer *et al.* [80] have conducted a comprehensive review of proton conducting oxides in which they have calculated activation energies for conduction for both $BaCeO_3$ and $BaZrO_3$ incorporating various concentrations of the following dopants: $Gd^{3+}$, $Y^{3+}$, $Sc^{3+}$ and $In^{3+}$. They found that proton mobility decreased with increasing dopant concentration in *most* cases and that the activation energy increased with the pre-exponential factor remaining unchanged. However, this was not attributed to defect association, but instead it was suggested that dopants such as Y in $BaCeO_3$ cause an increase in electron density (basicity) of all oxygens in the lattice, thus increasing the binding energy between protons and oxygens and decreasing proton mobility. On the other hand, it was found that the proton mobility and activation energy of $Y:BaZrO_{3-\delta}$ was largely unaffected by variation in dopant concentrations (for $0 \leq x \leq 0.2$). Kreuer *et al.* [104] suggested that substituting Zr with Y in $BaZrO_3$ caused a lattice expansion, but left the basicity of oxygens unchanged. It was also commented by Kreuer *et al.* [9] that mobilities of protonic defects in perovskites with structures strongly deviating from cubic symmetry (mostly orthorhombic) are significantly lower, eg; $Y:SrCeO_{3-\delta}$. Kreuer argued that the large orthorhombic distortion of $Y:SrCeO_{3-\delta}$ affects the activation enthalpy [9]. As briefly mentioned previously, the oxygen sites in cubic structures such as $Y:SrCeO_{3-\delta}$ degenerate into two sites with probabilities $\frac{1}{3}$ (O1) and $\frac{2}{3}$ (O2). Oxygen ions on these sites show distinctly different electron densities (basicity) due to their altered interactions with cations (especially A site) and therefore, have different binding energies with protons. The most electro-negative oxygen site in $Y:SrCeO_{3-\delta}$ was thought to be O1. Kreuer argued that since $Y:SrCeO_{3-\delta}$ has an orthorhombic distortion in comparison with $Y:BaCeO_{3-\delta}$ the difference in electro-negativity between the two oxygen sites is much greater. Table 2.1 shows the lattice parameters and c/a ratios measured for BCY10 and SCY10 by other authors. C/a ratios were only found to be very slightly lower in BCY10 than SCY10. Although this could have some effect on the differences in oxygen site electro-negativity as described by Kreuer, such a minor difference in distortion is perhaps not sufficient to explain the large differences in activation energies (also shown in table 2.1). A more plausible and significant cause for the observed activation energy difference was

also put forward by Kreuer. The most electro-negative oxygen site in Y:$BaCeO_{3-\delta}$ was thought to be O2 [9]. Assuming that protons are associated with the most electronegative oxygen sites most of the time, they may show long-range proton transport via O2 sites alone in $BaCeO_3$, whereas long-range proton transport in $SrCeO_3$ must involve transfer between chemically differing oxygen ion sites, O1 and O2. This would therefore explain why Y:$SrCeO_{3-\delta}$ has a larger activation enthalpy than Y:$BaCeO_{3-\delta}$.

| Material | Lattice Parameters Å(a, b, c) | c/a Ratio | Activation Enthalpy(eV) |
|---|---|---|---|
| BCY10 | 6.211, 6.233, 8.764 | 1.41 | 0.408 |
| SCY10 | 6.005, 6.143, 8.587 | 1.43 | 0.697 |

Table 2.1: Reported lattice parameter values for BCY10 [18] and SCY10 [19]. Also presented are activation energies for BCY10 in the temperature range 300-900$^o$C [4] and SCY10 in the temperature range 300-510$^o$C [20]

Kreuer *et al.* [9] further commented that thermodynamics predict the activation enthalpy of long range proton diffusion to be less than 0.15 eV, provided that the O-H-O bond configuration is linear when the proton is in the transient state. Later, however, Kreuer [80] found that activation enthalpies are in the order of 0.4-0.6 eV for proton conduction. During atomic simulations work by Munch *et al.* [105] the proton was not found on the edge of the octahedron but outside the $BO_6$ octahedron as part of a strongly bent hydrogen bond, which still has some barrier to proton transfer. This explains the higher than initially predicted activation enthalpies found by Kreuer [80]. The hydrogen bond was found to be strongly bent because of a strong repulsion between protons and the highly charged B site cation. The importance of this repulsion is emphasised by the finding that pentavalent B-site cation perovskites (I-V), such as $LiNbO_3$ and iron doped $KTaO_3$, have significantly higher activation enthalpies for proton transfer than tetravalent B-site cation perovskites (II-IV) [106].

## 2.6 Introduction to the Materials under Investigation

Proton conducting materials were selected for investigation from candidate materials discussed in the literature based on their suitability as electrolytes in an SOEC device. Y:$BaZrO_{3-\delta}$ and Y:$BaCeO_{3-\delta}$ were amongst the most researched materials although each of the these have their advantages and disadvantages. As mentioned previously, when utilising proton conductors based on simple perovskites as electrolytes in SOFC/SOECs, a compromise must be made between

conductivity and stability. Ryu *et al.* [79] found that Y:$BaCeO_{3-\delta}$ had a rather poor chemical stability in $CO_2$ containing atmospheres. Both Ryu *et al.* and Kreuer *et al.* [9] concluded that the chemical stability of all cerates are particularly poor with regard to $CO_2$ presence because of their reactivity. For example, $BaCeO_3$ can form insulating $BaCO_3$ and $CeO_2$ layers when exposed to $CO_2$ containing atmospheres. Formation of such insulating layers in the electrolyte of an SOEC/SOFC would be very detrimental to the performance [107]. Therefore, cerate reactivity prevents hydrocarbon containing fuels being used in conjunction with cerate based SOFCs [9]. This does not necessarily rule out the use of Y:$BaCeO_{3-\delta}$, since the electrolyte in an SOEC device is unexpected to be exposed to significant levels of carbonaceous species. Should a Y:$BaCeO_{3-\delta}$ electrolyte be used in an SOFC, either a protective layer, or a non-carbonaceous fuel would be required to be used. There have been no reports of Y:$BaZrO_{3-\delta}$ instability in $CO_2$ containing atmospheres but Iwahara *et al.* [77] reported that Y:$BaZrO_{3-\delta}$ had a significant but lower protonic conductivity than Y:$BaCeO_{3-\delta}$. A higher conductivity is desirable because this will lead to a reduction in the amount of power required to produce a unit of hydrogen when the material is utilised in an SOEC. Therefore, the use of Y:$BaCeO_{3-\delta}$ can not be discounted at this stage. Previous work on the synthesis of Y:$BaZrO_{3-\delta}$ and Y:$BaCeO_{3-\delta}$ samples and their use as electrolytes is discussed in the following sections.

## 2.7 Y:$BaCeO_{3-\delta}$

### 2.7.1 Synthesis, Conductivity, and Ionic Transport Number

After surveying the literature, it was found that Y:$BaCeO_{3-\delta}$ was most commonly synthesised using the solid state reaction method. Dense samples were able to be produced, although a high sintering temperature was found to be required. There has been some discussion on how powder preparation methods can be optimised in order to reduce sintering temperatures, often by milling processes, however, there has been very little focus on Y:$BaCeO_{3-\delta}$ powder preparation techniques in comparison with Y:$BaZrO_{3-\delta}$.

There have been several thorough investigations into the fundamental properties of Y:$BaCeO_{3-\delta}$ [2, 4, 6, 13, 18, 108–112]. Coors and Readey have compiled the most comprehensive review of work on the total conductivity of BCY10 to date and have generated conductivity data across the widest range of temperatures [4]. This data, presented in figure 2.1, shows a decrease in

activation energy for conduction ($E_a$) above 300$^o$C from 0.53 eV 0.41 eV. Coors and Readey concluded that a phase transition induced change in the bulk transport mechanism may explain this increase. Knight studied the structure of $BaCeO_3$ using neutron diffraction and found that the material underwent a second order phase transition at approximately 290$^o$C from Pmcn to Incn [113]. This may well be related to the change in activation energy observed by Coors and Readey but requires further investigation to ascertain whether BCY10 undergoes a similar transition and if the bulk transport mechanism is effected as a result.

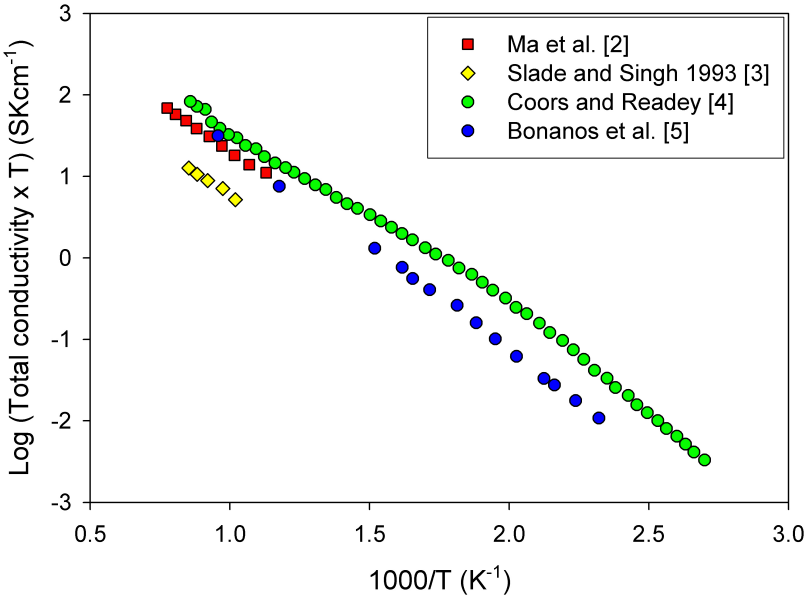



Figure 2.1: BCY10 conductivity plot comparing literature by Ma *et al.* [2], Slade and Singh [3], Coors and Readey [4] and Bonanos *et al.* [5]

BCY10 conductivity data from other authors, Ma *et al.* [2], Bonanos *et al.* [5], and Slade and Singh [3] are also shown in figure 2.1. In each of the studies listed above, samples were prepared by high temperature solid state reaction between $CeO_2$, $Y_2O_3$ and $Ba(CH_3COO)_2$. There were slight variations in processing and conductivity measurement conditions and these differences caused the observed discrepancies in the conductivity data sets, although it is unknown whether processing or measurement conditions had the greater impact.

Iwahara *et al.* [6] tested $BaCe_{0.9}M_{0.1}O_3$ under fuel cell conditions ($H_2$-Air) with M = Nd, Sm, Gd, Dy, Y and Yb all having stable trivalent cations. Water evolution rates were measured at both anode and cathode during cell discharge using a thermo-hygrometer to estimate proton and

oxygen ion conductivities from 700 to 1000$^o$C. The results, shown in figure 2.2, confirm that a transition from predominantly proton conduction to predominantly oxide ion conduction occurs as the temperature is increased (assuming an ionic transport number of 1). Generally, proton transport numbers were found to decrease with increasing ionic radius of dopant. However, at 700 and 800$^o$C, Y doped samples had the highest proton transport number. This did not fit the trend as Yb has a smaller ionic radius than Y. Indeed, at 700$^o$C Nd doped samples also had a higher proton transport number than trend predicted.

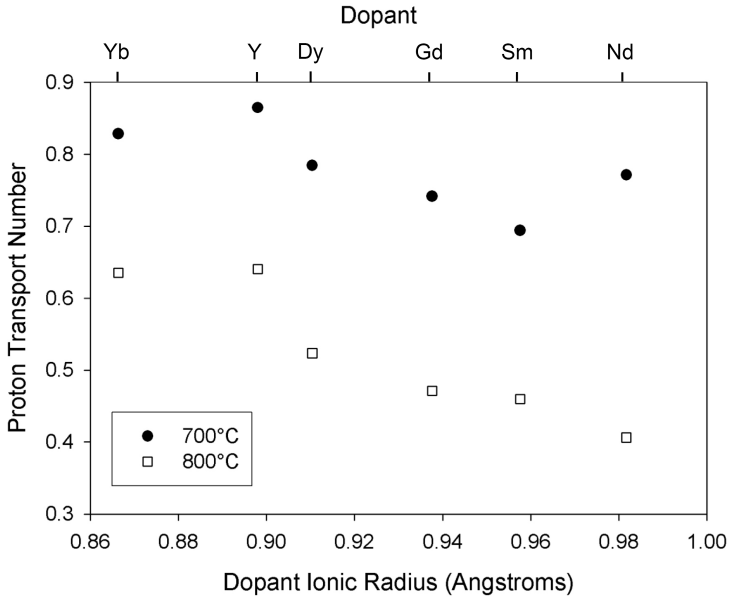



Figure 2.2: Proton transport number of $BaCe_{0.9}M_{0.1}O_{3-\delta}$ against ionic radius of dopant M under fuel cell conditions [6]

The authors correlated this data with lattice spacings measured using XRD (figure 2.3). They found that as ionic radius of dopant increased so did the lattice spacing in the a-axis increasing the orthorhombic distortion of the unit cell. It was therefore concluded, that the contribution of oxide ions to the total conduction increased as the spacing along the a-axis becomes longer. However, yttrium and neodynium doped samples, again, did not fit the trend. The situation is complicated by the fact that lattice parameters were measured at room temperature and it is possible to have phase transformations occurring at higher temperatures causing lattice parameters to change. Scherban *et al.* [114] reported phase transformations of non-doped $BaCeO_3$ from orthorhombic to cubic just above 800$^o$C via a tetragonal phase, although crystal form varied with dopant as shown in their later work [115]. High temperature studies of BCY10 crystal

structure have not been carried out, although it is probable that phase transformations occur with increasing temperature as with un-doped $BaCeO_3$. The inferred dependence of proton transport numbers measured at high temperature on correlating lattice parameters measured at room temperature must therefore be considered with caution. However, the evidence presented by Iwahara *et al.* [6] does imply that yttrium is the most suitable dopant of $BaCeO_3$ for the formation of a proton conducting material.

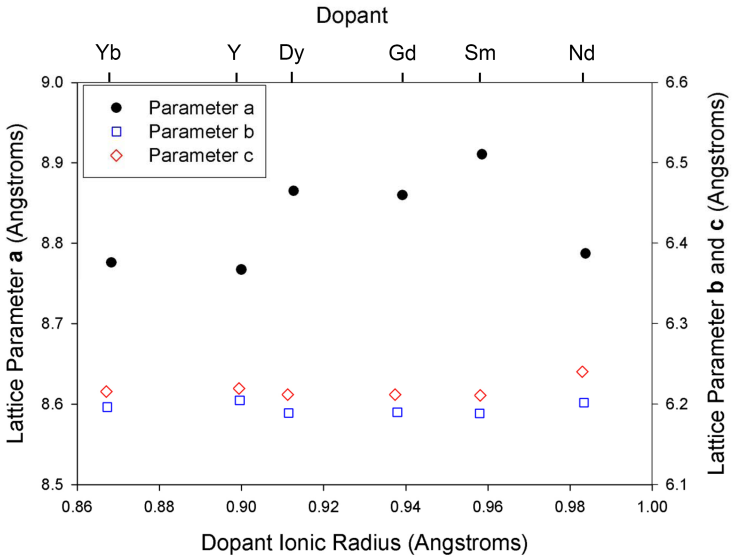



Figure 2.3: Lattice parameters of $BaCe_{0.9}M_{0.1}O_{3-\delta}$ calculated from XRD against ionic radius of dopant M [6]

The ionic transport numbers of BCY10 and BCY25 were measured by Suksamai and Metcalfe [7] in further detail and the results are displayed in figure 2.4. The proton transport number of BCY10 at 700$^o$C was found to be a little higher in Iwahara *et al.*'s work, 0.95 instead of 0.88, but a good agreement of proton transport numbers between the two works was found at 800$^o$C. Any differences were due to the method of transport number measurement or sample synthesis methods. By studying two different dopant concentrations, the dependence of proton transport number on dopant concentration was investigated by Suksamai and Metcalfe [7]. At and below 550$^o$C the proton transport numbers were found to be 1 in each materials. As temperature was increased, the proton transport number for BCY10 remained greater than for BCY25. BCY25 became predominantly oxide ion conducting at around 680$^o$C whereas BCY10 did not become predominantly oxide ion conducting below 800$^o$C. By extrapolating the trend from these results, BCY10 becomes predominantly oxide ion conducting at around 825$^o$C. Therefore, BCY10 is a

more suitable composition than BCY25 for the maximisation of proton conductivity at high temperatures (above 550$^o$C) where SOEC devices benefit from improved thermodynamics that reduce the power requirements of the device. Reasoning behind this behaviour was not given by the authors, however, a possible explanation is that protonic defect concentration may have been reduced by defect association in BCY25. A more plausible explanation is that the crystal structure of BCY25 differs from BCY10 at these temperatures. Takeuchi *et al.* and Loong *et al.* [18,116] found the crystal structure of BCY10 to be orthorhombic whereas BCY25 was found to be rhombohedral at room temperature. The crystal structures of these compositions at high temperature have not yet been established, however, based on this information it is probable that a difference in crystal structure existed.

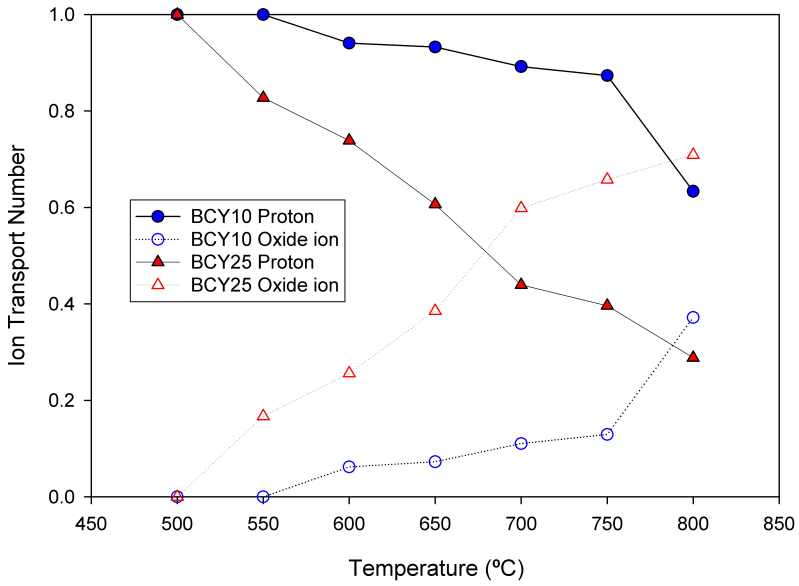



Figure 2.4: Ion transport number against temperature for BCY10 (circles) and BCY25 (triangles) [7]

### 2.7.2 Cell Fabrication and Testing

Methods of Y:$BaCeO_{3-\delta}$ based cell fabrication and results from testing reported in the literature are reviewed in this section. Many examples of SOFC testing were found, however, no detailed results have been reported on SOEC cells based on this material nor indeed using Y:$BaZrO_{3-\delta}$ electrolytes. Hence, this thesis will report detailed results on such devices for the first time.

Suksamai and Metcalfe [7] operated BCY10 and a BCY25 cells in fuel cell mode with platinum electrodes using 5%$H_2$-Ar as a fuel. Peak power densities of 11.7 and 20.5 mWcm$^{-2}$ were found

respectively. This work is discussed in greater depth in chapter 5 as data achieved provided a useful comparison with SOFC data collected in this study. Indeed, this proved to be the only IV curve data reported in the literature for such a system. Other investigations into the use of Y:$BaCeO_{3-\delta}$ as an SOFC electrolyte material was carried out but with only very brief initial findings reported [3, 6, 14, 117]. Hibino *et al.* [90] developed a cell with the following configuration: 3 wt% Pd-loaded FeO ‖ $BaCe_{0.75}Y_{0.25}O_{3-\delta}$ (BCY25) ‖ $Ba_{0.5}Pr_{0.5}CoO_3$. $H_2$ saturated with room temperature $H_2O$ and air were used as anode and cathode gases respectively. This work represented a significant development on that previously reported because both anode and cathode materials have been specifically implemented in order to catalyse fuel cell reactions rather than simply platinum electrodes. Methods of cell fabrication can have a significant effect on the resultant fuel cell performance and hence must be considered carefully. The authors coated dense electrolyte pellets on one face with a thin layer of cathode slurry and fired at 1100$^o$C. Subsequently, the other face of the electrolyte was coated in anode slurry and fired at 900$^o$C. Samples were then sandwiched between two alumina tubes and glass seal gaskets were melted at 800$^o$C in place to create two separate gas chambers. Performance of the BCY25 based cell was compared with 8 mol% Yttria Stabilised Zirconia (YSZ) and 20 mol% Samarium Doped Cerium (SDC20) cells, each with Ni-SDC anodes and $Sm_{0.5}Sr_{0.5}CoO_3$ cathodes. The peak power density of the BCY25 based cell was 135 $mWcm^{-2}$ at 600$^o$C. This value exceeded the peak power density measured for the YSZ and SDC based systems at the same temperature and under the same conditions. YSZ cells would perhaps have out performed the BCY25 cell at higher temperatures as the ionic conductivity of YSZ is not maximised at 600$^o$C. Still, this result is important because it suggests that the performance of proton conducting based SOFCs can be competitive with devices based on established oxide ion conducting materials.

Zhu *et al.* [118] developed a 75 wt% SDC20 and 25 wt% $BaCe_{0.8}Y_{0.2}O_{3-\delta}$ (BCY20) composite electrolyte. Thin electrolyte layers, 0.3-0.5 mm in thickness, were able to be prepared and assisted in the achievement of a low Area Specific Resistance (ASR) value (see section 3.7). Cells were fabricated by loading a mould with anode powder followed by electrolyte powder and subsequently hot-pressed. The exposed electrolyte face was coated with a silver paste before a final firing step. Further details of cell fabrication were not stated although it was commented that the hot-pressing technique allows for a higher density to be achieved. Fuel cell measurements were carried out using the BCY20-SDC composite with a nickel-composite anode

and silver-based cathode. With pure hydrogen as fuel and air as oxidant, a power density of 250 $mWcm^{-2}$ was measured at $550^oC$ for the composite cell. In stark contrast, a cell consisting of a nickel-BCY20 anode, BCY20 electrolyte and silver cathode achieved a power density of less than 50 $mWcm^{-2}$ at $550^oC$. Similarly, a SDC only based cell achieved a power density of less than 70 $mWcm^{-2}$ at $550^oC$. The authors reasoned that the observed improvement in fuel cell power density in the composite based cell was due to hybrid conduction combining the advantages of oxygen ion conduction from the SDC phase and proton conduction from the BCY20 phase. This is an interesting hypothesis and result because a similar improvment in fuel cell performance may be induced by operating a cell based on a pure Y:$BaCeO_{3-\delta}$ electrolyte at a higher temperature where the material has been proven to exhibit similar oxide ion and proton transport numbers (see figure 2.4).

The selection and implementation of electrode materials in fuel cells can be a difficult task to successfully accomplish. It is therefore desirable to simplify cell fabrication techniques where possible. Tomita *et al.* [119,120] developed a cell based on the following arrangement; no anode $\|$ BCY20 $\|$ Pt. A novel method of catalysing reactions at the anode that greatly simplifies the cell fabrication process was developed that also delivered good results. Two cell types were produced, one with, and one without a heat treatment of the electrolyte material at $1700^oC$ for 10 hours in air, prior to cathode deposition. $H_2$ saturated with $H_2O$ at $25^oC$ was supplied to the anode and atmospheric air to the cathode. Peak power densities at $750^oC$ of 52.0 $mWcm^{-2}$ for the heat treated electrolyte cells, and 25 $mWcm^{-2}$ for the non-heat treated electrolyte cells were reported. The authors found that the surface of the heat treated samples had a 10 $\mu$m thick porous layer of $Ce_{0.8}Y_{0.2}O_{1.9}$ that was created by the volatilisation of BaO during the heat treatment. An increase in effective surface area combined with an increase in electrocatalytic activity from the presence of the cerium rich phase was stated to be the cause of an observed decrease in the anodic polarisation in the heat treated electrolyte cells and resulted in a greater peak power density. The cerium rich phase was able to catalyse the oxidation of hydrogen gas, and therefore, speed up the kinetics of the following reaction;

$$H_2 \rightarrow 2H^+ + 2e^- \tag{2.8}$$

The authors found that this resulted in a higher proton transport number to be measured for the

heat treated electrolyte cells (0.79 at 750$^o$C) in comparison to the non-heat treated electrolyte cells (0.52 at 750$^o$C). A further finding of this work, was that when the heat treated electrolyte cells were tested with hydrocarbon fuels, or exposed to $CO_2$ or $H_2S$ containing atmospheres, the cerium rich layer was found to protect the BCY20 electrolyte and prevent degradation and assisted in preventing the formation of carbonates at the anode surface.

## 2.8 Y:BaZrO$_{3-\delta}$

### 2.8.1 Synthesis

BZY10 is notoriously difficult to produce with high density and is quoted as requiring extreme conditions such as sintering at 1700$^o$C for 24h [79, 121, 122] to achieve a density of >95%TD (TD = 6.16 g cm$^{-3}$). Snijkers *et al.* [10] synthesised BZY10 by solid-state reaction. In this work, pellets of BZY10 were iso-statically pressed at 400 MPa and subsequently sintered in air for 4 hours at temperatures between 1500$^o$C and 1700$^o$C. They report a final sintered density of 94.96%TD, although it was not clearly stated in the paper which sintering temperature this value corresponded to. We assume that this was the maximum density achieved and therefore, that this value corresponded to a 1700$^o$C sintering temperature. Such high sintering temperatures are undesirable, as these materials are required to be co-sintered with electrode materials to form cells. The sintering temperatures of typical electrode materials are much lower than 1700$^o$C and as electrodes are also required to have a certain amount of porosity, a sintering temperature much lower than 1700$^o$C is required. Babilo *et al.* [123] studied BZY20 and were able to produce samples with a density >95%TD, by sintering at 1600$^o$C for 10 hours. This remains one of the least severe conditions found to be required to produce dense pure sample of Y:BaZrO$_3$.

Irvine *et al.* [93] state that a 1 wt% addition of ZnO to BZY10 enables the sintering temperature of the material to be reduced from 1700$^o$C to 1350$^o$C with densities of the order of 96% of the theoretical density achievable. The authors consider 1 wt% to be an optimum level of ZnO addition as the conductivity of the material decreases as the amount of ZnO addition increases, however 1 wt% is required for the sintering temperature to be decreased sufficiently. It is also mentioned that the addition of ZnO enables the reduction of the sintering temperature of BCY10. Babilo and Haile [121] have worked on the reduction of the sintering temperature of $BaZr_{0.85}Y_{0.15}O_{3-\delta}$ (BZY15) by the addition of ZnO. They have found that the addition of 4

mol% ZnO introduced as a dispersed oxide to a BZY15 nitrate solution allows the material to become >93% dense when sintered at 1300$^o$C for 4 hours in static air. Both Irvine *et al.* and Babilo and Haile speculate that the $Zn^{2+}$ ion replaces some of the B-site ($Zr^{4+}$) ions. It is further suggested by Babilo and Haile that oxygen ion and barium ion vacancies are created within the lattice as a result of ZnO addition according to;

$$ZnO \; + \; Ba_{Ba}^{x} \; + \; Zr_{Zr}^{x} \; + \; 2O_{o}^{x} \; \rightarrow \; Zn_{Zr}^{''} \; + V_{Ba}^{''} + \; 2V_{o}^{\bullet\bullet} \; + BaO + ZrO_2 \qquad (2.9)$$

BZY15 with 4 mol% ZnO was analysed by Babilo and Haile and up to 5 mol% Zn was detected at grain boundaries coinciding with a decrease of about 3 mol% Y with respect to the bulk. Zn was found to be absent in the grain interiors indicating Zn segregation to grain boundaries. An additional finding was that the mean grain size in Zn doped samples was larger than in undoped BZY15 samples. Hence, the substitution of a small number of $Zr^{4+}$ sites with $Zn^{2+}$ creating barium ion vacancies may enhance the mobility of cations within the material and be responsible for an increase in grain boundary mobility, grain growth and densification. The effect of Zn addition to Y:$BaZrO_3$ on the properties of the material is unclear and this needs to be investigated further. Other authors have concentrated their efforts on sol-gel synthesis routes for the production of pure BZY10 in an attempt to produce dense samples.

Sol-gel synthesis is an established method of producing ceramic oxide materials. There are many parameters that can be altered to optimise the characteristics of the resultant powder. D'Epifanio *et al.* [124] synthesised $BaZr_{0.8}Y_{0.2}O_{3-\delta}$ (BZY20) powders using a sol-gel technique from $Ba(NO_3)_2$, $(CH_3CO_2)_xZr(OH)_y$ and $Y(NO_3)_3 \bullet 6H_2O$ precursors. Ethylene Glycol (EG) or water were used as solvents with citric acid as a chelating agent. When water was used as a solvent, a barium carbonate phase was formed and when EG was used as a solvent, a perovskite phase was formed. The authors explained that metal ions were well distributed in a polymeric network when citric acid underwent a polyesterification reaction in the presence of EG. Such a network was not formed with water as a solvent, and this caused a rise in the oxide formation temperature. The molar ratio of citric acid to total metal ions (in this case 2) was varied. A ratio of 1:1 resulted in a non-uniform distribution of metal ions, whereas a 3:1 ratio caused an excessive amount of organic compound to remain in the powder after calcination. In both of these circumstances barium carbonate was detected in the resultant powders. It was found that a citric

acid to total metal ion molar ratio of 2:1 with an ethylene glycol solvent, gave the best results. Using these conditions, a pure perovskite phase was formed by heating the solution to form a gel, followed by further heating to form a powder, and calcination at 1100$^o$C for 5 hours. Despite these optimisations, sintering BZY20 pellets at 1600$^o$C for 8 hours in air only achieved a density of approximately 80%TD. Cervera *et al.* [21, 22] also synthesised BZY20 powder using a sol-gel method but with metal alkoxide precursors and a 2-methoxyethanol solvent. A crystallised perovskite phase with a grain size of 3-5 nm was produced that contained traces of hydroxides. This powder was pressed at 4 GPa using a cubic anvil technique to produce samples at room temperature. Samples were then annealed at various temperatures and the resultant density values and protonic conductivity values (measured at 500$^o$C in humidified argon) are shown in table 2.2. It can be seen that as the annealing temperature is increased both density and conductivity values increase.

| Annealing Regime | Average Grain Size (nm) | % Maximum Theoretical Density | Protonic Conductivity at 500$^o$C (Scm$^{-1}$) |
|---|---|---|---|
| 800$^o$C 10h | 10 | 90.3 | 8.7 x 10$^{-6}$ |
| 1250$^o$C 10h | 50 | 98.1 | 0.002 |
| 1500$^o$C 20h | 200 | 99.4 | 0.004 |

Table 2.2: Reported % maximum theoretical density values of BZY20 under various sintering conditions and corresponding protonic conductivity values at 500$^o$C [21, 22]

Cervera *et al.* [21, 22] have shown that it is possible to produce highly dense samples of BZY10 without exposure to temperatures in excess of 1250$^o$C. The increase in protonic conductivity observed by increasing the annealing temperature from 800 to 1250$^o$C was attributed to better grain boundary contacts and a more structurally ordered bulk. Also, grain boundary regions in samples annealed at 1250$^o$C and 1500$^o$C were found to have a slightly higher concentration of yttrium in comparison to the bulk by using high resolution TEM/EDX analysis. Oxygen vacancy depletion in this region was therefore decreased in the space charge layer and led to an increase in grain boundary conductivity. These effects were enhanced by increasing the annealing temperature from 1250 to 1500$^o$C and accounted for the observed increase in protonic conductivity. Additionally, electron diffraction and XRD patterns of the 1500$^o$C annealed sample suggest the presence of a superstructure in the lattice. There was evidence to suggest a $Ba_3Zr_2YO_{8.5}$ composition for the second phase. These results were achieved using equipment that is not readily available, a cubic anvil. Other examples of investigators using such apparatus does not occur in

the literature. Therefore, since solid state and sol-gel routes have been proven to have difficulties in achieving high densities at low sintering temperatures other techniques should be explored. Alternative techniques exist, such as the glycine-nitrate combustion method were developed by Chick *et al.* [125]. They reported that powders produced in this way had greater compositional uniformity, lower residual carbon levels and smaller particle sizes than similar compositions synthesised using the amorphous citrate method. Also, nano-crystalline oxide powders have previously been synthesised by spray pyrolysis [124, 126–129]. These powders typically have a sub-micron average particle size and are formed of dense spheres which would perhaps enable the powder to sinter at relatively low temperatures.

### 2.8.2 Conductivity

Controversially, Kreuer *et al.* [9] reported conductivity results that show $BaZrO_3$ has a higher conductivity than $BaCeO_3$, and further comment that the conductivity of $Y{:}BaZrO_{3-\delta}$ is greater than that of doped $BaCeO_3$ (see figure 2.5).

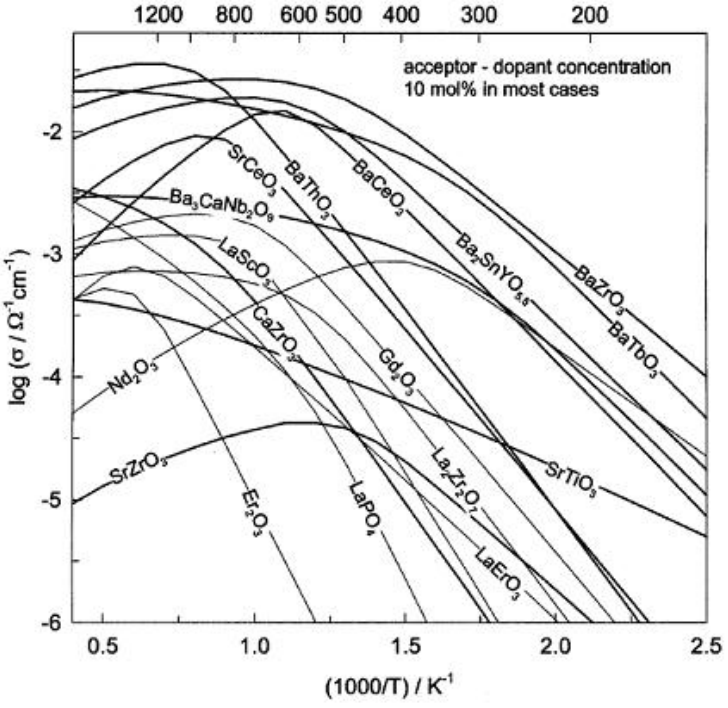



Figure 2.5: Proton conductivities of various oxides as calculated from data on proton concentrations and mobilities, according to Norby and Larring [8]. This data led to conclusions by Kreuer *et al.* [9] stated in the text.

However, the data for $BaZrO_3$ and $BaCeO_3$ in figure 2.5 originated from Norby and Larring [8] and were used by Kreuer *et al.* to deduce these conclusions. The data for $BaZrO_3$ are from calculated values with no dopant concentration specified. The high temperature $BaCeO_3$ data shown in figure 2.5 were extrapolated from results of experiments using $BaCe_{0.95}Y_{0.1}O_{3-\delta}$ (BCY10) single crystals conducted at lower temperatures [108]. Therefore, the statements made by Kreuer *et al.* were flawed due to the data they were based on. Indeed, both Iwahara *et al.* [77] and Ryu *et al.* [79] contradicted Kreuer's findings reporting that $Y:BaZrO_{3-\delta}$ has a lower protonic conductivity than $Y:BaCeO_{3-\delta}$. Ryu *et al.* [79] added that it is difficult to make dense samples of $Y:BaZrO_{3-\delta}$ and that this could cause a deceptively low protonic conductivity of $Y:BaZrO_{3-\delta}$ to be measured. Snijkers *et al.* [10], Katahira *et al.* [13] and Bohn *et al.* [11] measured the conductivity of BZY10 with impedance spectroscopy in air with ambient humidity and their findings are depicted in figure 2.6.

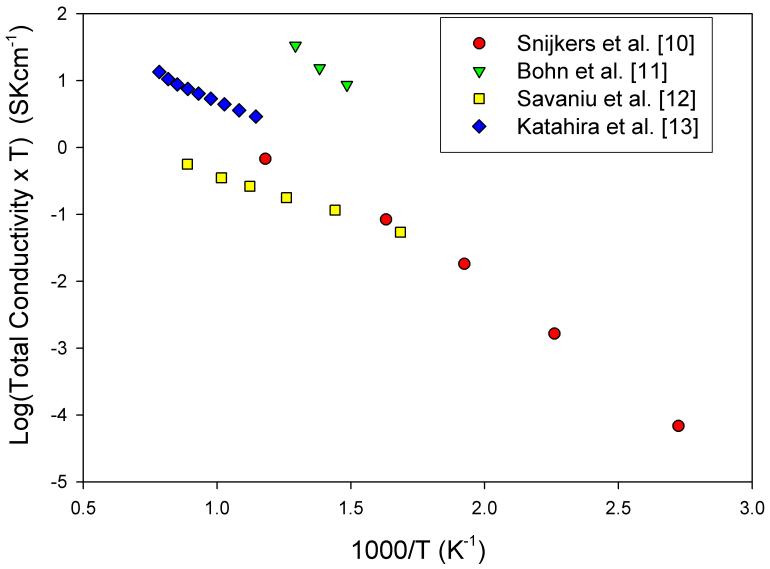



Figure 2.6: Comparison of BZY10 total conductivities in air with ambient humidity from the literature [10–13]

Snijkers *et al.* [10] state that the conductivity of BZY10 can be significantly affected by alterations in the processing route. For example, a surface layer stoichiometrically deficient in BaO was found in samples processed using a stoichiometric BZY10 powder. This was found to be due to volatilisation during the sintering process causing a layer containing $ZrO_2$ precipitates to be formed, that acted as a sink for yttrium. Samples produced with an initial excess of barium

were found to not contain such a layer and have a greater conductivity as a result. Results shown in figure 2.6 are varied as a result of different sintering regimes and powder processing methods used by the authors. Activation energies were found to vary between 0.25 and 0.52 eV (discounting Bohn *et al.* due to lack of data points) and at some temperatures, conductivities were found to be over an order of magnitude apart. Therefore, the importance of BZY10 sample processing details can not be underestimated due to the dramatic effect they have been proven to have on the material's properties.

### 2.8.3 Cell Fabrication and Testing

As with Y:$BaCeO_3$, no detailed results on SOEC operation using Y:$BaZrO_3$ as an electrolyte material have been reported but here SOFC results are discussed. D'Epifanio *et al.* [124] developed cells based on a BZY20 electrolyte with Pt electrodes which were tested in fuel cell mode in the temperature range; 500 to 700$^o$C. Samples were attached to the end of an alumina tube with a gas tight ceramic paste seal to create an anode chamber, into which 100% humidified hydrogen was flowed. The cathode side of the cell was simply exposed to laboratory air. An OCV of almost 1 V was measured at 500$^o$C. This is an intruiging result as this demonstrated that the electrolyte was sufficiently dense to prevent gas diffusion across the cell, despite an electrolyte density of only 80%TD. The OCV was found to decrease to approximately 0.85 V at 700$^o$C and the authors commented that this was as a result of an increased contribution of electrons and holes to the total conductivity of the cell. The maximum power density of 3.6 mWcm$^{-2}$ was measured at 700$^o$C and this value decreased to approximately 1.1 mWcm$^{-2}$ as the temperature decreased to 500$^o$C due to a large increase in the ohmic resistance of the electrolyte. The electrolyte thickness was decreased from 1 mm to 0.6 mm with the effect of increasing maximum power density to 7.0 mWcm$^{-2}$ at 700$^o$C. Interestingly, the peak power density at 600$^o$C was only marginally lower than at 700$^o$C in this thinner cell. The authors took this as an indication of an increase in electronic transport number, although no reasoning is given as to why thinning the electrolyte exacerbates this behaviour.

The effect of utilising a NiO-BZY20 anode and a $La_{0.8}Sr_{0.2}Co_{0.8}F_{0.2}O_3$ (LSCF) cathode on cell performances was also investigated by D'Epifanio *et al.* [124]. A cell of configuration; Pt ‖ BZY20 ‖ LSCF, achieved a maximum power density of 3.2 mWcm$^{-2}$ at 700$^o$C and therefore, the LSCF had little effect on the fuel cell performance. A cell of configuration; NiO-BZY20 ‖

BZY20 || LSCF, achieved a maximum power density of 1.6 $mWcm^{-2}$ at 700$^o$C and therefore, the cell performance was significantly affected by the introduction of the NiO-BZY20 material. This was attributed to an increase in anode polarisation. The contact resistance between the anode and electrolyte was also suggested to be a factor due to poor adhesion of the anode onto the electrolyte surface.

To date, D'Epifanio's work remains the only significant work on cells based on electrolytes made purely from Y:$BaZrO_3$. This is mainly due to research focusing on methods of powder and sample synthesis for the material. Another cause is that researchers have chosen to test cells that incorporate zirconium into Y:$BaCeO_3$ instead of testing a pure form of the material. This was thought to enable a control of the materials properties, namely stability and conductivity and will be discussed further in the following section.

## 2.9 Y:$BaCe_xZr_{(1-x)}O_{3-\delta}$

### 2.9.1 Synthesis and Conductivity

In an attempt to find a compromise between the high conductivity of Y:$BaCeO_3$ and the high stability of Y:$BaZrO_3$, previous workers have studied the synthesis and properties of Y:$BaCe_xZr_{(1-x)}O_{3-\delta}$ with varying values of x. Methods of synthesising Y:$BaCe_xZr_{(1-x)}O_{3-\delta}$ powders have received a similar level of attention as the synthesis of Y:$BaZrO_3$ powders because the inclusion of zirconium in solid solution with Y:$BaCeO_3$ was found to increase the difficulty of successfully sintering pure dense samples. Ding *et al.* [130] compared the gel casting and solid state reaction methods of synthesising $BaZr_{0.1}Ce_{0.7}Y_{0.2}O_{3-\delta}$ powders. The gel casting method involved mixing of the metal oxide/carbonate precursors with an organic monomer, cross-linker and dispersant to form a slurry which was ball milled. The slurry was then heated to 80$^o$C and ammonium bisulfate added to initiate the polymerisation process and to ultimately form a gel to be dried. Calcination temperatures of 1100$^o$C and 1200$^o$C were found to be required to eliminate traces of $BaCO_3$ in the gel cast and solid state reaction powders respectively. Thus using the gel casting method decreased the phase formation temperature by 100$^o$C compared to the conventional technique. The authors reasoned that this was because of the presence of a polymeric network, that immobilised precursor particles during gelation and resulted in a homogeneous powder. The median particle size diameter was 0.96 $\mu$m in gel cast samples, smaller

than that achieved using the solid state reaction method. Gel cast powders were pressed into pellet form and sintered at 1550$^o$C for 5 hours, and achieved a density 95% of the maximum theoretical and a conductivity of 5 x $10^{-3}$ Scm$^{-1}$ in $H_2$ (3%$H_2O$) at 500$^o$C. In contrast, pellets made from powders synthesised by the solid state reation method achieved a density of 86%TD and a conductivity of 2 x $10^{-3}$ Scm$^{-1}$ under the same conditions. These results highlight the differences in conductivity that can be achieved by using different processing routes and the main cause for the large variations in conductivity values that are observed in the literature for these materials. The differences in conductivity were attributed to the differences in density. However, if both samples were made equally dense, microstructural differences, arising from a higher sintering temperature, would be likely to cause conductivity differences to remain.

Katahira *et al.* [13] prepared samples by solid state reaction with the following compositions; $BaCe_{0.9-x}Zr_xY_{0.1}O_{3-\delta}$ ($0.0 \leq x \leq 0.9$). The pellet sintering conditions were 1700$^o$C for 10 hours for $0.0 \leq x \leq 0.4$, 1750$^o$C for 5 hours for $0.5 \leq x \leq 0.8$, and 1800$^o$C for 5 hours for $x = 0.9$. These conditions resulted in densities greater than 95% of the maximum theoretical densities. Single phases were obtained with orthorhombic symmetry for $0.0 \leq x \leq 0.2$ and cubic for $0.3 \leq x \leq 0.9$. The conductitivity of the material was found to decrease with increasing zirconium content (see figure 2.7). The benefits of increasing the zirconium content on the chemical stability of the material are discussed in the following section.

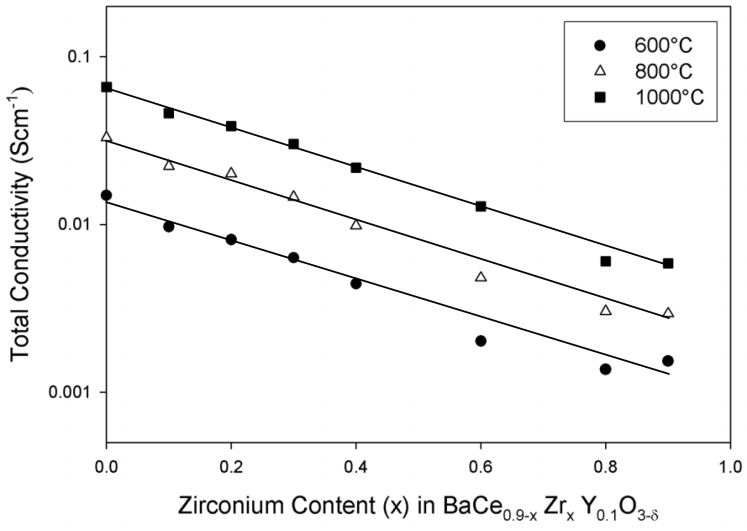



Figure 2.7: Conductivity data for $BaCe_{0.9-x}Zr_xY_{0.1}O_{3-\delta}$ with $0.0 \leq x \leq 0.9$ at 600, 800 and 1000$^o$C. Conductivity values can be seen to decrease with increasing zirconium content [13].

$H_2$ concentration cells were set up for each composition and it was found that, for all samples tested, the voltage values measured were very close to the theoretical calculated from the Nernst equation (3.13). This suggests that although the conductivity is adversely affected by zirconium substitution in Y:$BaCeO_3$, the ionic transport number was unaffected and remained close to unity. Therefore, very little electronic conductivity was detected in either sample and differences in conductivity between cerium rich and zirconium rich samples was purely down to differences in ionic conductivity. However, from these results, any changes to the ratio of proton to oxide ion transport number could not be elucidated.

Zhong *et al.* [23] prepared powders by a co-precipitation and freeze drying method with compositions; $BaCe_{0.9-x}Zr_xY_{0.1}O_{3-\delta}$ ($x$ = 0, 0.2, 0.4, 0.6, or 0.9). A mixture of nitrate precursors with appropriate molar concentration of metal ions was added to a $(NH_4)_2CO_3$ and $NH_4OH$ solution. All metal ions precipitated instantaneously and were freeze dried before calcination. Freeze drying circumvented the coarsening of particulates that could occur by heating the powder, and thus resulted in particle sizes ranging from 50 to 190 nm. By changing the calcination atmosphere from air to argon, hard agglomeration formation was inhibited and final sintered pellet densities were improved (see table 2.3).

| Sample Composition | Sintering Temperature ($^o$C) | % Maximum Theoretical Density |
|---|---|---|
| $x = 0$ (Air calcined) | 1650 | 90 |
| $x = 0$ (Ar calcined) | 1650 | 98 |
| $x = 0.2$ | 1650 | >95 |
| $x = 0.4$ | 1650 | >95 |
| $x = 0.6$ | 1650 | 80 |
| BZY10 | 1650 | 65 |
| $BaZrO_3$ | 1650 | >99 |

Table 2.3: Reported % maximum theoretical density values of $BaCe_{0.9-x}Zr_xY_{0.1}O_{3-\delta}$ and $BaZrO_3$ under various sintering conditions [23]

An unusual method of synthesising Y:$BaCe_xZr_{(1-x)}O_{3-\delta}$ was investigated by Savaniu *et al.* [12]. Initially, they synthesised BZY10 powder from barium acetate, zirconium(IV) acetylacetonate and yttrium 2-ethylhexonoate precursors. Reactants were dissolved in hot acetic acid which also acted as a chelating agent. The resultant gel was heated further to create a powder before a calcination step at 1200$^o$C. The authors reported that pellets of BZY10 were sintered at 1450$^o$C and achieved a density of approximately 98%TD. This is the highest reported density at

this temperature in the literature. In an attempt to reduce the high grain boundary resistance previously observed in Y:$BaZrO_3$, BZY10 particles were coated with a BCY10 shell prior to sintering. BZY10 powder was dispersed ultrasonically into a BCY10 solution, similar to that described above but prepared with a cerium(III) 2-ethylhexanote precursor. Ultrasonic agitation was continued whilst the suspension/solution was heated until a powder was formed. After calcination at 1450$^o$C for 6 hours, particles were found to have a core with approximate composition; $BaZr_{0.85}Ce_{0.05}Y_{0.1}O_{2.95}$, coated with a shell of approximate composition; $BaZr_{0.7}Ce_{0.2}Y_{0.1}O_{2.95}$, 5 to 20 nm in thickness. It was found that the grain boundary resistance of the hybrid BZY-BCY core-shell samples was up to 20 times less than the grain boundary resistance of pure BZY10. The activation energy for conduction was also found to decrease by modifying BZY particles in this way.

### 2.9.2 Cell Fabrication and Testing

Nickel-cermet anodes are commonly used in SOFC designs as anode materials and are often used as a starting point for investigations that are looking at new electrolyte materials. Anode materials based on nickel-electrolyte based cermets, if processed correctly, have been proven to have a good mix of electronic and ionic conductivity and have inherently similar thermal expansion coefficients to the electrolyte material. A more varied selection of cathode materials is present in the literature than anodes and there has been less consistent success with cathode development as a result. Lin *et al.* [24] investigated a $BaCe_{0.7}Zr_{0.1}Y_{0.2}O_{3-\delta}$ (BCZY7) cell with the following arrangement; $H_2$ (3% $H_2O$), Ni-BCZY7 $\|$ BCZY7 $\|$ $GdBaCo_2O_{5-x}$, air. BCZY7 suspension was sprayed onto a green anode before co-firing at 1400$^o$C for 5 hours to create a 10 $\mu$m thick electrolyte. A $GdBaCo_2O_{5-x}$ slurry was then screen printed onto the electrolyte before firing at 975$^o$C. OCV values indicated that this sintering regime was sufficient to create a leak free cell. Information on how the cell was mounted for fuel cell testing was not stated. The peak power density values obtained over the temperature range 550 to 700$^o$C are displayed in table 2.4. These values are unexpectedly low given the thin electrolyte in comparison to others reported in the literature but were still greater than those reported by Fabbri *et al.* [25]. The authors explained these results by suggesting that NiO did not completely reduce to Ni metal, and hence, the anode was dense. SOFC electrodes are required to have a certain degree of porosity to assist the kinetics of reactions that occur at the interface between the electrode

and electrolyte. An electrode with sufficiently high level of porosity will allow gas diffusion to a large number of triple phase boundary sites. Electrode density combined with the large anode thickness and poor conductivity in comparison to the electrolyte would have contributed to lower peak power denisities. Work to establish the individual contributions of the anode and cathode to the total interfacial polarisation resistance was not carried out. Low total interfacial polarisation resistances at 700$^o$C, that accounted for ≈18% of voltage loss, indicated that at 700$^o$C $GdBaCo_2O_{5-x}$ performs well as a cathode material. However, at 550$^o$C, the total interfacial resistance accounted for ≈57% of the total voltage loss. The authors concluded from this work that the development of cathode materials remains a 'grand challenge' in the development of proton conducting SOFCs.

| Temperature ($^o$C) | Peak Power Density (mWcm$^{-2}$) |
|---|---|
| 550 | 84 |
| 600 | 146 |
| 650 | 207 |
| 700 | 266 |

Table 2.4: Reported peak power density values for the cell; $H_2$ (3% $H_2O$), Ni-BCZY7 ‖ BCZY7 ‖ layered $GdBaCo_2O_{5-x}$, air [24]

Fabbri *et al.* [25] prepared powders using a sol gel process with the following compositions; $BaCe_{0.8-x}Zr_xY_{0.2}O_{3-\delta}$ ($0.0 \leq x \leq 0.8$). Pellets, pressed and sintered from these powders, with platinum electrodes were attached to the end of an alumina tube with ceramic paste for hydrogen-air fuel cell tests at 700$^o$C. Hydrogen supplied to the anode compartment was humidified to ≈3%. Elecrolytes were 0.6 mm in thickness, and despite the low density of the zirconium rich samples, OCV values were sufficiently high to suggest that gas did not leak through any sample tested. Reported % maximum theoretical density values under various sintering conditions and corresponding peak power density values are displayed in table 2.5.

| Sample Composition | Sintering Temperature ($^o$C) | % Maximum Theoretical Density | Peak Power Densities (mWcm$^{-2}$) at 700$^o$C |
|---|---|---|---|
| BCY20 | 1500 | 93 | 58 |
| $x = 0.3$ | 1550 | Not Stated | 47 |
| $x = 0.5$ | 1550 | Not Stated | 18 |
| BZY20 | 1650 | 80 | 7 |

Table 2.5: Reported % maximum theoretical density values of $BaCe_{0.8-x}Zr_xY_{0.2}O_{3-\delta}$ under various sintering conditions and corresponding peak power density values at 700$^o$C [25]

It was suggested that the decrease in power densities observed in zirconium rich samples could not be simply explained by lower sample conductivity causing an increased ASR. Electrochemical impedance spectroscopy was performed in-situ to estimate ohmic and electrode polarisation losses. Fabbri *et al.* found that polarisation losses were larger than the ohmic losses for all samples and that they accounted for a increasingly greater proportion of total losses as zirconium content increased. The authors commented that this was due to an increasing mismatch of thermal expansion coefficients between the electrolyte and electrodes with increasing zirconium content, leading to poorer adhesion of the platinum electrode to the electrolyte. It is unclear whether this was the only cause for the larger electrode polarisation observed in the more zirconium rich samples. Results from the experiments conducted on the stabilities of the compositions developed in this work are discussed in the following section.

## 2.10 Chemical Stability of Y:$BaCeO_3$ and Y:$BaZrO_3$

### 2.10.1 $CO_2$ Containing Atmospheres

As mentioned previously, Y:$BaZrO_3$ has been considered to be a more chemically stable compound than Y:$BaCeO_3$ in carbonaceous atmospheres. Work has been carried out by several authors to ascertain the stability limits of these materials. Stability limits of solid solutions of these two materials have also been investigated with the aim of finding a compromise between conductivity and chemical stability. Authors tended to use similar conditions for investigating stability limits, so fair comparisons can be made between different data sets.

D'Epifanio *et al.* [124] exposed both BZY and BCY powders to $CO_2$ at 900$^o$C for 3 hours. It was found by x-ray diffraction and scanning electron microscopy that the BZY powder composition and microstructure was unaffected by this exposure whereas the BCY powder decomposed into $BaCO_3$ and $CeO_2$ (equation 2.10). Therefore, $BaCeO_3$ based materials were found to not be suitable as electrolytes in hydrocarbon fueled SOFCs whereas $BaZrO_3$ based materials were.

$$BaCeO_3 + CO_2 \rightarrow BaCO_3 + CeO_2 \tag{2.10}$$

Zakowsky *et al.* [14] conducted a more extensive study concentrating on the $CO_2$ tolerance limits of BCY10 electrolytes under fuel cell conditions. Figure 2.8 displays the results from TGA and

depicts the temperature at which BCY10 carbonation was detected on cooling at particular $CO_2$ levels. From these results, it can be seen that BCY10 is stable in pure $CO_2$ above 1050$^o$C and stable above 700$^o$C in 9% $CO_2$ balanced with Ar. Under certain conditions, BCY10 can exhibit long term durability and this data suggests that BCY10 may be used successfully as a component in a fuel cell. However, stability in atmospheres containing other likely compounds in hydrocarbon based fuels for SOFCs must also be assessed. It is also important to note that electrolyte stability may also vary with current flow. Therefore, the experiments employed by these authors to test the stability limits of these materials are not entirely conclusive with regard to implementation in SOFC and SOEC devices.

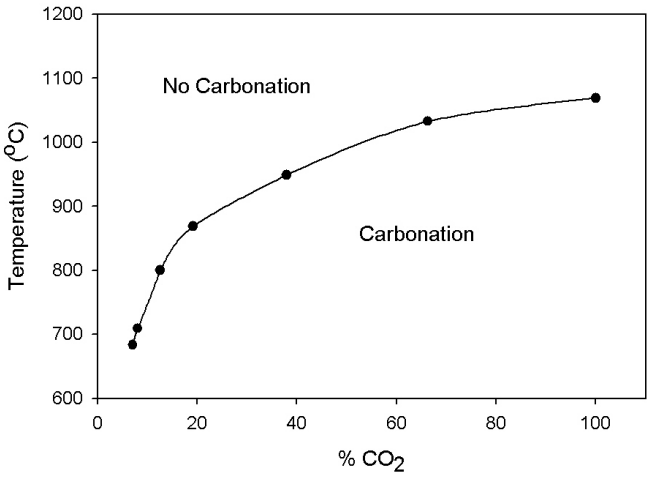



Figure 2.8: Temperature for the onset of BCY10 carbonation upon cooling versus $CO_2$ concentration (line indicates best fit) [14]

Powders of $BaCe_{0.8-x}Zr_xY_{0.2}O_{3-\delta}$, with $0.0 \leq x \leq 0.8$, were exposed to pure $CO_2$ at 900$^o$C for 3 hours by Fabbri *et al.* [25]. It was found that only sample $x = 0.8$ was unaffected by this treatment, with traces of $BaCO_3$ detected in the $x = 0.5$ sample. $BaCO_3$ and $CeO_2$ were clearly identified in samples $x = 0.3$ and 0. Indeed, the perovskite phase was no longer recognisable in the XRD pattern of the $x = 0$ sample after this exposure to $CO_2$. As commented by the authors, these conditions are more severe than can be expected during SOFC operation and are, therefore, somewhat of an erroneous but rapid method of determination of material stability. However, the authors were able to combine these results with the peak power density values observed and concluded that the $x = 0.5$ sample was the optimum composition. They reasoned that this composition exhibited a higher power density than the BZY10 sample without compromising

the stability and was therefore a good candidate electrolyte material for an ITSOFC.

Katahira *et al.* [13] Sintered samples with $0.0 \leq x \leq 0.9$ were exposed to an atmosphere of 100% $CO_2$ at 900$^o$C for 2 hours to investigate the effect of zirconium subsitution in $BaCe_{0.9-x}Zr_xY_{0.1}O_{3-\delta}$ on chemical stability. It was found that samples with $x \geq 0.4$ were unaffected. Samples with $x \leq 0.3$ exhibited decomposition with $BaCO_3$ and $CO_2$ phases detected after exposure to $CO_2$. Therefore, the chemical stability of Y:$BaCeO_3$ in $CO_2$ increased with increasing zirconium substitution of cerium. Zhong *et al.* [23] found very similar results in their work on the same compositions.

### 2.10.2 $H_2O$ Containing Atmospheres

Very little work has been conducted on the stability of Y:$BaCeO_3$ and Y:$BaZrO_3$ in $H_2O$ containing atmospheres. Good chemical stability of a candidate electrolyte material for an SOEC device in such an atmosphere at a given temperature is critical for obvious reasons. Theoretical predictions were made by Fabbri *et al.* [25], who stated that in the temperature range 400-700$^o$C, reaction 2.11 is not significant. Haile *et al.* [131] also commented that reaction 2.11 is not relevant at high temperature citing Kreuer [78].

$$BaCeO_3 + H_2O \rightarrow Ba(OH)_2 + CeO_2 \tag{2.11}$$

Tanner and Virkar [132] exposed Y:$BaCeO_3$ powder and sintered samples to a $H_2O$ pressure of ≈430 Torr (≈57 kPa) in the temperature range 500 to 900$^o$C. All samples decomposed into $CeO_2$ and $Ba(OH)_2$ in relatively short periods of time at temperatures less than 900$^o$C. Doped $BaCeO_3$ decomposed at a faster rate than the undoped $BaCeO_3$ and sintered samples decomposed at a rate comparable to the powder samples. These results established that $BaCeO_3$ is thermodynamically unstable when a critical vapor pressure is exceeded and that the rapid decomposition of both powder and sintered samples is the result of the high solubility of water in doped $BaCeO_3$ which accelerates the kinetics of decomposition. Powders of $BaCe_{0.9-x}Zr_xY_{0.1}O_{3-\delta}$ composition with $x$ values ranging from 0 to 0.9 were exposed to boiling water for 3 hours. It was found that all powders decomposed to varying degrees, including BZY10, although the degree of decomposition decreased with increasing zirconium content. Based on these finding the implementation of Y:$BaCeO_3$ and Y:$BaZrO_3$ as electrolyte in SOECs must be approached with caution.

## 2.11 Summary

Doped perovskites have been established as proton conductors with sufficiently high ionic conductivities in $H_2$ or $H_2O$ containing atmospheres to be considered as electrolyte candidates for SOFC and SOEC devices. Perovskites are required to be doped with aliovalent cations in order for them to be able to absorb significant amounts of $H_2O$. Oxygen ion vacancies are created in this way due to the satisfaction of the lattice charge neutrality condition. Protonic defects can then be formed within the material (see equation 4.9) and this has been backed up by thermogravimetric analysis data. Once dissolved, protons are thought to be mobile by hopping from one filled oxygen ion site to the next. Given the correct electrode material the electrolysis of steam without the application of a prohibitively large voltage may therefore be possible.

Both barium cerate and barium zirconate based materials are promising candidates for proton conducting electrolytes although concerns remain over their stability and conductivity respectively. Some work has been carried out to clarify the stability limits of these materials, but no work has been carried out on testing the durability of SOFC and SOEC devices incorporating these materials. Furthermore, very little detailed SOEC data is present in the literature. There is therefore a need to carry out testing of cells based on these materials to thoroughly establish their performance and durabilities under operating conditions. This may be done by close examination of electrochemical data over long periods of testing and also by post-test microscopy of cell cross-sections combined with analytical techniques such as Energy Dispersive X-ray (EDX) spectroscopy.

# Chapter 3

# Experimental Methods and Technique Development

## 3.1 Commercial Powders

BCY10 and BZY10 commercially available powders were obtained from Praxair and details of the particle size distributions given by the manufacturer are shown in table 3.1. Commercial powders were suspended in acetone and milled using yttria stabilised zirconia (YSZ) milling media for varying periods of time. The milling process was anticipated to decrease the average particle size of the powder. 1 wt% poly-vinyl butaryl (PVB) binder was added to the BCY10 powder so that green compacts would have more mechanical strength. PVB is known to decompose and evaporate during the sintering process and therefore does not remain within the samples post sintering.

| Powder Characteristic | BCY10 | BZY10 |
|---|---|---|
| Purity (%) | 99.9 | 99.9 |
| d10 ($\mu$m) | 0.5 | 0.6 |
| d50 ($\mu$m) | 0.7 | 0.8 |
| d90 ($\mu$m) | 1.2 | 3.6 |
| Surface Area ($m^2g^{-1}$) | 5.87 | 10.41 |

Table 3.1: Characteristics of Praxair powders (as-supplied)

## 3.2 Synthesis of BZY10 by Spray Pyrolysis

Aqueous solutions of $Ba(NO_3)_2$ (R.P. Normapur, 99.5% purity), $ZrO(NO_3)\bullet 6H_2O$ (Fluka, >97%) and $Y(NO_3)_3\bullet 4H_2O$ (Aldrich, 99.999%) were prepared in the cationic proportion 10:9:1, respectively. Solutions were heated at $30^oC$ and stirred for 24 hours to ensure that the salts had fully dissolved. Piezoelectric plates in an ultrasonic atomiser vibrated at frequencies of 1.7 MHz and 2.5 MHz to cause an aerosol to be formed within a chamber. A flow of synthetic air ($N_2$ - $O_2$ mix) was used to transport the aerosol from this chamber through a 2-zone tubular furnace. The first zone of the furnace that the aerosol experienced was $50^oC$ lower than the second. This was so that the aerosol experienced a gradient of heat as the rate at which the aerosol was heated effects particle nucleation and growth. The oxide powder particles formed were collected electrostatically in an extension of the tube outside of the furnace as shown in figure 3.1, a schematic of the spray pyrolysis experimental setup.

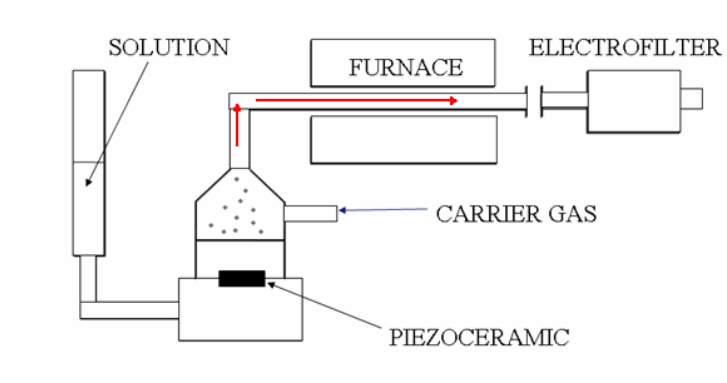



Figure 3.1: A schematic of the spray pyrolysis experimental setup. Red arrows indicate direction of flow of carrier gas.

| Experiment Number | Solution Concentration ($mol.l^{-1}$) | Nebuliser Frequency (MHz) | Furnace Temperature (2nd Zone, $^oC$) |
|---|---|---|---|
| 1 | $2.5 \times 10^{-2}$ | 1.7 | 800 |
| 2 | $2.5 \times 10^{-2}$ | 1.7 | 600 |
| 3 | $2.5 \times 10^{-2}$ | 2.5 | 600 |
| 4 | $2.5 \times 10^{-2}$ | 2.5 | 800 |
| 5 | $2.5 \times 10^{-3}$ | 1.7 | 800 |
| 6 | $2.5 \times 10^{-3}$ | 2.5 | 800 |

Table 3.2: A list of experimental parameter sets for spray pyrolysis powder synthesis. experiments numbered 1-6 were conducted using a carrier gas flow rate of 6 $l.min^{-1}$

The effects of varying solution concentration, nebulisation frequency, carrier gas flow rate and furnace temperature were explored. Experimental parameter sets are listed in table 3.2. Powder yield rates were deemed to be insufficiently high using carrier gas flow rates of 3 $l.min^{-1}$, therefore, all experiments listed here were conducted using a carrier gas flow rate of 6 $l.min^{-1}$. However, as carrier gas flow rate is directly proportional to the aerosol furnace residence time, some interesting results were discovered by using a flow rate of 3 $l.min^{-1}$ as discussed in section 4.3.1.

## 3.3 Sol-Gel Synthesis of BZY10

Aqueous solutions of $Ba(NO_3)_2$, $ZrO(NO_3)\bullet 6H_2O$ and $Y(NO_3)_3\bullet 4H_2O$ (all Aldrich) were prepared individually. Solutions were heated at $30^oC$ and stirred for 24 hours to ensure that the salts had fully dissolved. Precise volumes were made of each solution so that when mixed together, a Ba:Zr:Y cationic molar ratio of 10:9:1 was achieved. The solution was then stirred and heated up to $80^oC$ on a hotplate. Amounts of polyethylene glycol and citric acid were added when the solution had reached this temperature. The citric acid to metal ion molar ratio to be added to the solution in order to obtain optimum powder characteristics, as well as the optimum citric acid to polyethylene glycol molar ratio, is dependent on the system. Since such details of BZY10 synthesis by the sol-gel method had been reported previously, initial values were selected based on literature findings. A citric acid to metal ion molar ratio of 1:1, and a citric acid to polyethylene glycol molar ratio of 2:1 were chosen. Variation of these ratios can effect the resultant powder characteristics and this topic is discussed in further detail in section 4.3.2. Once the citric acid and polyethylene glycol had been added, the solution temperature was maintained at $80^oC$ until a thick gel was created. This typically took 7 hours of heating to occur. After drying at $120^oC$ for 24 hours the gel became a solid. This was then heated in a furnace up to $625^oC$ for 6 hours to remove the organic compounds.

## 3.4 Powder Characterisation

### 3.4.1 X-Ray Diffraction (XRD)

Samples of BCY10 and BZY10, powder and pellets, were characterised using a Philips PW1700 series x-ray diffractometer. Pellets were analysed as whole samples to investigate near surface

crystallographic structures and in some cases ground into a fine powder using pestle and mortar to give a fair representation of the bulk. The x-ray diffractometer had a $CuK_\alpha$ source with a wavelength of 1.5418 $\mathring{A}$ and current and voltage were set to 40 mA and 40 kV respectively. The instrument was routinely calibrated using a silicon standard. Whole pellet samples were continuously rotated during scanning to give a fair representation of surface crystallographic structures. Powder samples were mounted on single crystal silicon plates by scattering the surface with powder before the application of ethanol to allow the formation of an even layer of powder. Initial sample scans covered a $2\Theta$ range from 5 to 105° in steps of 0.04° $2\Theta$ with 1 second scan time per step. Scan ranges, step increments and step times were altered to investigate sections of some sample patterns more closely. Step increments were decreased and step times increased to clarify peak shoulders or ascertain the presence of two or more peaks in close proximity on the $2\Theta$ scale.

### 3.4.2 Particle Size Distribution

The particle size distributions of powders were determined using a Malvern Mastersizer 2000 series laser diffractometers. Small amounts of powder were added to an ultrasonic bath containing de-ionisied water to create a suspension. The suspension was then fed into the diffractometer for analysis. Particles were passed through a laser beam that scattered at an angle that is directly related to the particle size. Large particles scatter light at narrow angles with high intensity, whereas small particles scatter at wider angles but with low intensity. A newer model of diffractometer allowed a particle diameter range of 0.1 $\mu$m to 2 mm to be detected at once. At times, when only an older model of diffractometer was available, only a smaller particle diameter range of 0.1 $\mu$m to 80 $\mu$m was detectable using a single lens. For the new model, an error of $\pm 1\%$ on the d50 value is quoted by the manufacturer. Laser diffractometry particle size analysis assumes spherical particles and hence, should samples contain non-spherical particle morphologies, a much greater degree of error could result.

### 3.4.3 Electron Microscopy

Pellet and powder samples were analysed using a high-resolution field emission scanning electron microscope (FE-SEM), ZEISS ultra 55. Further SEM images were acquired using a JEOL JSM 5610 microscope generally with an accelerating voltage of 20 keV and a spot size of 25 mm.

In some circumstances these parameters were altered in order to optimise captured images. Fragments of fractured pellets were mounted onto aluminium stubs so that fracture surfaces could be examined. This was done by filing the cylindrical stubs down to form a flat vertical surface. Double sided carbon sticky tape could then be used to attach fragments to this vertical surface. Polished cross sections of pellets were achieved by mounting samples in epoxy resin. Glass slides and labels were held in place either side of the samples using metallic clips so that during the curing process, fragments would remain vertical and could be identified easily. Samples could then be ground using silicon carbide paper grades from 250 grit to 1200 grit to reveal the pellet cross section. Diamond suspensions with a range of particle sizes were used, from 6 microns to 0.25 microns, in conjunction with polishing cloths and an automatic rotating wheel to create a highly flat sample. Polished Zn doped BZY10 pellet samples were required to be thermally etched at 1500$^o$C for 30 min before SEM imaging to enhance the visualisation of grain boundary regions.

Powder samples were deposited onto a carbon grid for TEM imaging. Suspensions of powder synthesised by spray pyrolysis were created using an IPA solvent. Carbon grids were then coated in powder by submersion into the suspension, before being removed and dried. A JEOL FX2000 transmission electron microscope (TEM) with a tungsten filament was operated in bright field mode at an accelerating voltage of 200 kV to obtain TEM micrographs.

## 3.5 Pellet Sample Preparation and Sintering

### 3.5.1 Commercial Powder

Milled and non-milled commercial powders of both BCY10 and BZY10 samples were uni-axially pressed for 1 minute into pellet form at a pressure of 1 ton for 13 mm pellets and 2 tons for 30 mm pellets. This was followed by iso-static pressing at 300 MPa prior to sintering to increase the green density. Pellets were sintered over the temperature range; 1300$^o$C to 1660$^o$C and isotherm times ranging from 5 to 10 hours in order to investigate the conditions required to produce sufficiently dense samples. Samples were submerged in the relevant as-supplied commercial powder during sintering to prevent a reaction occurring between the alumina crucible and the sample. This was also done in an attempt to protect the sample from furnace debris and to retard the potential evaporation of BaO [133].

ZnO, $Cr_2O_3$ were used as sintering aids in an attempt to decrease the sintering temperature and time required to produce a dense BZY10 sample. ZnO and $Cr_2O_3$ powders were calcined in air at $1000^oC$ for 2 hours prior to mixing by manual grinding with the BZY10 commercial powder to create a homogeneous powder. After initial results revealed that a $Cr_2O_3$ additive had very little effect on the final density of samples, whereas ZnO did, the addition of ZnO was investigated in depth. The amount of ZnO added to the BZY10 powder was varied from 0.1 to 5 wt%. The milled powder was pressed uni-axially using a hand press with 1 ton of pressure and a 13 mm die to form a green compact pellet.

Sample densities were determined using the Archimedes method, discussed in section 3.5.5, and were verified by combining geometrical and weight measurements. A value of 95% of maximum theoretical density is recognised as being the minimum required measured density for samples that should be used as an electrolyte material in SOEC/SOFC experiments. This is to remove doubt that connected porosity is present within the sample which would lead to an unfair representation of the cell performance. Porosity will also effect results from AC impedance spectroscopy. Green pellet sample diameters were 13 mm for general investigative purposes including samples for density investigation and AC impedance spectroscopy. Larger samples with a green diameter of 30 mm were prepared for SOFC and SOEC experiments (see section 3.7) as larger pellets were required to fit the test rig.

### 3.5.2 Spray Pyrolysis Powder

Due to the small amount of powder synthesised during spray pyrolysis experiments, only a single 6 mm diameter pellet could be produced for most parameter sets. Pellets were formed using a uni-axial press and were not iso-statically pressed. The sintering behaviour of these pellets was studied using dilatometry (see section 3.5.4).

### 3.5.3 Sol-Gel Powder

Powder synthesised using the sol-gel method was treated in a similar manner to the commercial powder. Milled and non-milled samples were uni-axially pressed into pellet form and were generally followed by iso-static pressing at 300 MPa prior to sintering. Pellets were sintered using various regimes to investigate the conditions required to produce samples with the maximum possible density from the powder produced.

### 3.5.4 Dilatometry

Green density pellet samples, 6 mm in diameter, were formed by uni-axial pressing of the powders at half a ton. The powders used to form these samples included powders synthesised by spray pyrolysis as well as milled BZY10 commercial powder, with and without a 1 wt% ZnO additive. Samples were loaded into a Netzsch DIL 402 dilatometer and were in contact with alumina push rods. Samples were heated to $1500^oC$ using a heating rate of $10^oCmin^{-1}$. A flowing air atmosphere was used to prevent any build up of gases within the dilatometry chamber during the experiments. A 1 hour isotherm at $1500^oC$ was used to allow densification before subsequent cooling at a natural rate.

### 3.5.5 Density Measurements

An established technique called the Archimedes method was used to determine final sintered densities. Dry, wet and submerged sample weights were measured using specialised scales and from these values the density could be determined using the following equation;

$$\frac{\rho_w Wt_{dry}}{Wt_{wet} - Wt_{sub}} \tag{3.1}$$

Where;

$\rho_w$ = Density of water at a given temperature ($gcm^{-3}$)

$Wt_{dry}$ = Weight of dry sample (g)

$Wt_{wet}$ = Weight of wet sample (g)

$Wt_{sub}$ = Weight of submerged sample (g)

Obtained values were verified by measuring sample dimensions and weight followed by a simple calculation. Measured values were compared to maximum theoretical densities calculated using the following equation:

$$\frac{mz}{VN_A} \tag{3.2}$$

Where;

m = Molar mass ($gmol^{-1}$)

z = Unit cell contents number

V = Volume of unit cell ($cm^3$) (detected by XRD)

$N_A$ = Avogadro's constant 6.022 x $10^{23}$ ($mol^{-1}$)

## 3.6 AC Impedance Spectroscopy

AC impedance spectroscopy was used to elucidate the contributions from constituent elements to the resistance of samples by utilising their different frequency dependences. The impedance was determined by applying an alternating voltage across a sample and measuring the current response. The excitation signal expressed as a function of time is given as;

$$E(t) = E_o cos(\omega t) \tag{3.3}$$

Where;

E(t) = Potential at time t (V)

$E_o$ = Amplitude of the signal (V)

$\omega$ = Radial frequency ($rads^{-1}$)

The current response is shifted in phase by $\phi$ in comparison to the excitation voltage and is given by;

$$I(t) = I_o cos(\omega t - \phi) \tag{3.4}$$

Where;

I(t) = Current at time t (A)

$I_o$ = Current response (A)

Since impedance is analogous with resistance, a similar equation to that stated in Ohm's law can then be used to calculate the impedance;

$$Z = \frac{E(t)}{I(t)} = \frac{E(t) = E_o cos(\omega t)}{I(t) = I_o cos(\omega t - \phi)} = Z_o \frac{cos(\omega t)}{cos(\omega t - \phi)} \tag{3.5}$$

Impedance is therefore expressed in terms of magnitude ($Z_o$) and phase shift ($\phi$). Using Eulers relationship;

$$exp(j\phi) = cos\phi + jsin\phi \tag{3.6}$$

it is possible to express impedance as a complex function;

$$Z = \frac{E}{I} = Z_o exp(j\phi) = Z_o(cos\phi + jsin\phi) \tag{3.7}$$

Therefore, the expression for complex impedance contains real (resistance) and imaginary (reactance) parts. Frequency response analysers (FRAs) are able to measure impedance and distinguish between the real and imaginary parts. Measurements were carried out using applied AC voltage frequencies over a range of 0.1 to 1 x $10^6$ Hz in steps increasing logarithmically. This was the optimum frequency range that could be applied by the FRA in order to detect sample responses at each temperature and condition. Different elements, such as the grain boundary and grain bulk in a polycrystalline ceramic material, are characterised by a resistance (R) and capacitance (C) placed in parallel (RC element). RC elements are separable due to the relation shown in equation 3.8 which holds at the frequency of maximum loss, $\omega_{max}$.

$$\omega_{max} RC = 1 \tag{3.8}$$

Each parallel RC element was represented as a semi circle on a plot of imaginary impedance (Z") against real impedance (Z'), also known as a Nyquist plot. An example of a Nyquist plot is shown in figure 3.2.

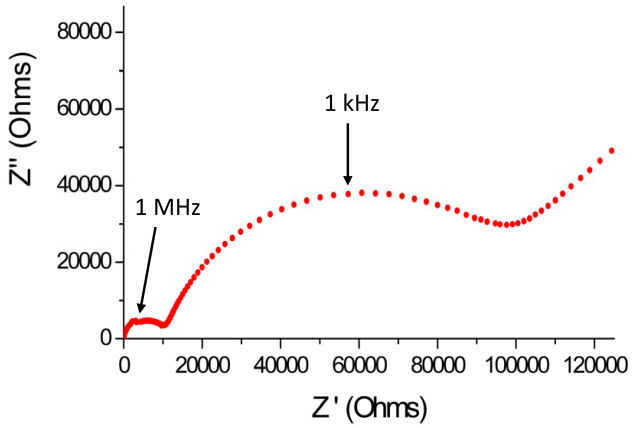



Figure 3.2: Example of an AC impedance spectrum with markers indicating frequencies at maximum loss ($\omega_{max}$) in the spectrum

Resistance values of sample responses were calculated from the intercepts of the semi circles with the Z' (real) axis. Capacitance values were calculated by applying equation 3.8 to the maximum of each semi circle. Sample responses could then be assigned elements based on the magnitude of capacitance in accordance with the literature once the dimensions of the sample have been taken into account (table 4.4) [26].

AC impedance spectra of dense doped ZnO BZY10 and BCY10 pellets were obtained. The conductivity of insufficiently dense pellets was not carried out as these sample types should not be used as an electrolyte in an SOEC/SOFC. Platinum electrodes were used in all experiments. Pellets were coated on each circular face with platinum paste (Metalor 6082A) and subsequently sintered at 900$^o$C for 3 hours. AC impedance spectroscopy scans were carried out using a Solartron SI 1260 impedance/gain-phase analyser connected to a PC running Zplot/Zview 2$^{TM}$ [134].

| **Capacitance (F)** | **Phenomenon Responsible** |
|---|---|
| $10^{-12}$ | Grain Bulk |
| $10^{-11}$ | Minor, Second Phase |
| $10^{-11}$ to $10^{-8}$ | Grain Boundary |
| $10^{-10}$ to $10^{-9}$ | Bulk Ferroelectric |
| $10^{-9}$ to $10^{-7}$ | Surface Layer |
| $10^{-7}$ to $10^{-5}$ | Sample-Electrode Interface |
| $10^{-4}$ | Electrochemical Reactions |

Table 3.3: AC Impedance Response Capacitance Values and Corresponding Possible Phenomenon Responsible [26]

Measurements were taken in either 50 or 100$^o$C intervals in the temperature range; room temperature to 850$^o$C. Both heating and cooling data were collected. Samples were exposed to various atmospheres during measurements to discover the effect on conductivity. Some samples were pre-conditioned at 600$^o$C by exposing the sample to atmospheres containing 5% hydrogen and/or humidified using a water bubbler at room temperature (≈3%). This was done to load the sample with protons prior to impedance measurements. The effect of varying exposure times and atmospheric conditions during pre-conditioning on impedance results was investigated. Gas flow rates were constant during pre-conditioning and measurement at around 9-10 $cm^3min^{-1}$. ≈3% atmospheric humidity was achieved by flowing gas through a water bubbler at room temperature. A higher humidity of ≈20% was achieved by flowing gas through a water bubbler at 60$^o$C. These humidity values were calculated using equations in the literature and assuming ambient atmospheric pressure within the chamber [135]. The equations used to estimate humidity in the gas feed were as follows, where T is water temperature:

For 0$^o$C < T < 63$^o$C

$$\%Humidity = 9.8692\ x\ 10^{-4}(610.78\ x\ e^{((17.269xT)/(237.3+T))}) \tag{3.9}$$

For 63$^o$C < T < 110$^o$C

$$\%Humidity = 9.8692\ x\ 10^{-4}(610.78\ x\ e^{((17.269xT)/(236.3+(1.01585xT)))}) \tag{3.10}$$

To prevent condensation of water onto the apparatus so that the sample does not experience a lower humidity than desired, and so that reservoirs of water do no build up that may present a hazard, the AC impedance test rig had to be modified. Inlet and outlet tubes were insulated using heating tapes, insulation wool and tin foil. Gases were attempted to be dried by passing the gas through columns containing dried out silica, However, no differences in conductivity were detected between 'dried' and ambient atmospheres so this was deemed to be superfluous and ineffectual.

## 3.7 SOEC-SOFC Testing

An amount of electrical energy is required to be applied to the cell to induce the electrolysis of steam. This value is based on the Gibbs free energy differences between the dissociation of water reaction and the formation of hydrogen reaction at a given temperature and is calculated by using the following equation;

$$\Delta G = \Delta H - T\Delta S \tag{3.11}$$

Where;

$\Delta$ G = Change in Gibbs free energy (J)

$\Delta$ H = Change in Enthalpy (J) (or total energy required in order for the electrolysis reaction to occur)

T = Temperature (K)

$\Delta$ S = Change in Entropy ($JK^{-1}$)

The relation between the change in Gibbs free energy and the open circuit voltage for the cell is given by the following equation;

$$\Delta G = nFE \tag{3.12}$$

Where;

n = The number of moles of electrons involved in the reaction (mol)

F = Faraday's constant: 9.64853399 x $10^4$ ($Cmol^{-1}$)

E = Cell potential at open circuit (V)

The open circuit voltage is dependent upon the partial pressures of gases as described by the Nernst equation;

$$E = \frac{\Delta G^{\circ}}{nF} - \frac{RT}{nF} ln(\frac{P_{O_2}^{\frac{1}{2}} P_{H_2}}{P_{H_2O}}) \tag{3.13}$$

Where;

$\Delta G^{\circ}$ = Gibbs free energy at standard pressure (J)

$P_{O_2}$ = Partial pressure of oxygen at the cathode (Pa)

$P_{H_2}$ = Partial pressure of hydrogen at the anode (Pa)

$P_{H_2O}$ = Partial pressure of steam at the anode (Pa)

R = The ideal gas constant (8.314 $JK^{-1}$ $mol^{-1}$)

Theoretically, any voltage applied to the cell greater than E will result in the electrolysis of steam. However, practically, additional electrical energy must be applied to the cell in order to overcome activation polarisation losses. These activation polarisation losses can be minimised by careful consideration of materials selection, as well as the manner in which these materials are processed. The causes and effects of cell losses are discussed in greater depth in chapter 5.

Dense BCY10 samples, approximately 25 mm in diameter and 2 mm in thickness were ground using silicon carbide paper of grades from 250 grit to 800 grit to a thickness of ≈500 $\mu$m. It is desirable to reduce the electrolyte thickness as much as possible to reduce ohmic losses, however, samples could not be processed to thickness <2 mm with this diameter as samples become warped during the pressing and sintering process. Thinning the sample to ≈500 $\mu$m decreased the mechanical stability of the sample and increased the probability of mechanical failure during the sealing of the cell. BCY10 samples were attached to a zirconia tube using a glass sealant (Encapsulant 8190, Du Pont) to create a gas tight seal. This was done by heating the assembly to 810$^{o}$C at very slow rates (1-2$^{o}$C per minute) before cooling to operation temperature. Slow heating and cooling rates were required because during this process, stresses built up in the sample due to mismatches in thermal expansion coefficients between the sample, sealant and zirconia tube. Slow changes in temperature helped prevent mechanical failure of the sample. Indeed, the mechanical failure rate of samples of ≈500 $\mu$m thickness was excessively high, although a sample of 450 $\mu$m thickness was successfully sealed and tested. This cell is referred to in chapter 5 as the preliminary cell. All other data presented in chapter 5 was collected using cells that were ground to an approximate thickness of 1 mm as standard to ensure a low mechanical failure rate.

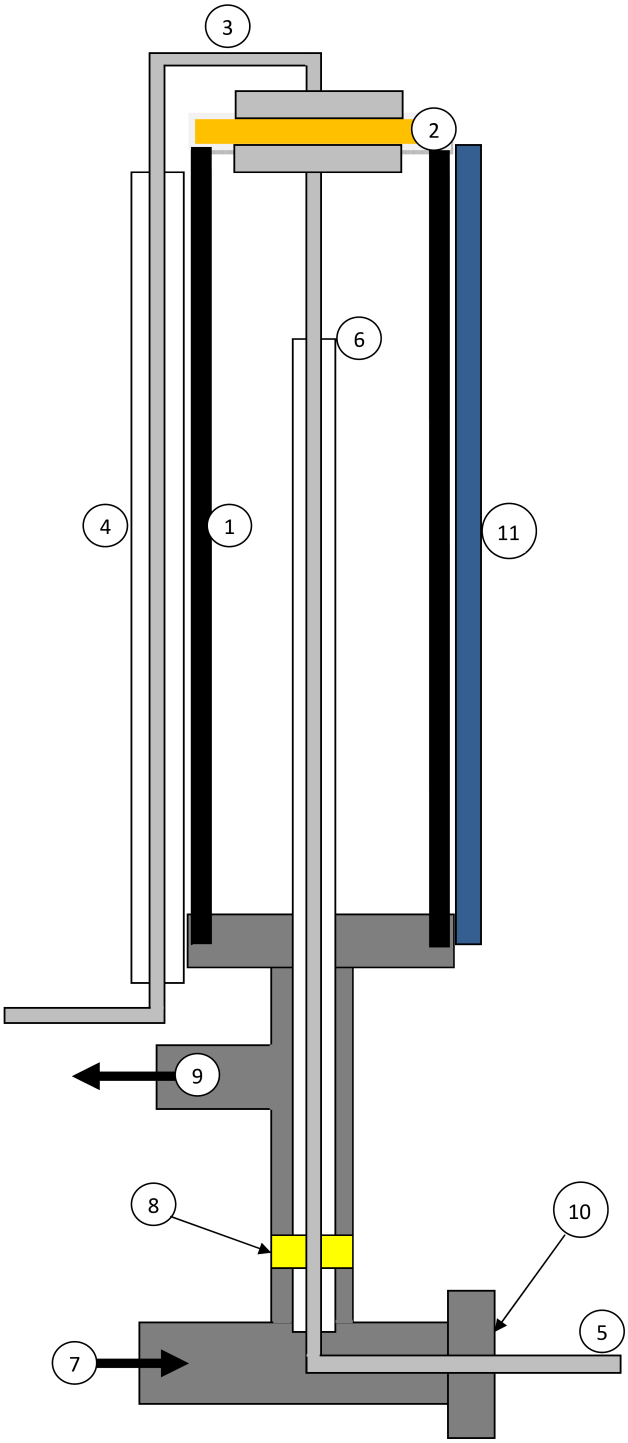



Figure 3.3: A schematic of the improved SOEC-SOFC experimental test rig

Key:

1. Main alumina or zirconia tube. O-ring present at tub base to ensure gas tight seal.

2. Sample with electrodes attached, sealed onto the main tube with glass sealant
3. Air side electrical connection. Pt wire guided by item 4.
4. Air side alumina Pt wire guide tube
5. Controlled atmosphere side electrical connection. Pt wire guided by item 6 and insulated from T-junction fitting using a series of alumina rings. Insulation between wire and end cap (item 10) provided by silicon based glue.
6. Point of gas feed entry to chamber. Also alumina tube for Pt wire guide.
7. Gas supply feed
8. Air tight silicon rubber seal
9. Supplied gas exit point
10. End cap
11. Thermocouple

A test rig was inherited from a previous researcher which after preliminary experiments was found to have flaws. An error in this design was that the electrical connection of the SOEC cathode was pressed up against metal fittings. A schematic of the improved design is displayed in figure 3.3. It can be seen that in this design, all electrical connections to the sample were not in contact with any metallic components of the test rig. A seal, labeled 8 in figure 3.3, ensures that the only exit point for the gas is at location number 9. SOEC and SOFC testing was carried out in the temperature range 500-750$^o$C. Open Circuit Voltage (OCV), galvanostatic, galvanodynamic, potentiostatic and potentiodynamic measurements were made using a Solartron 1286 potentiostat. This allowed I-V curves of both electrolysis cell and fuel cell data to be plotted. Cware/Cview $^{TM}$ software [136] was used to collect and analyse results. Peak power density is a value used to gauge fuel cell performance and is the maximum power a cell can produce per square centimetre. As current density increases, voltage losses in the cell accumulate and this leads to a maximum in the product of current density and voltage. Greater voltage losses result in lower peak power densities and therefore, peak power densities are a good measure of the efficiency of the cell. Another useful figure of merit when comparing the efficiency of cells

operating in either fuel cell or electrolysis mode is the area specific resistance (ASR). ASR is a measure of the resistance to the flow of ions in the electrolyte added to the resistance to flow of electrons through the electrodes to the electrolyte interface. It can be measured by finding the gradient of the linear portion of an I-V curve. A steeper gradient means that for each additional volt applied, the current density increased by a lesser amount, and is therefore, indicative of a higher cell resistance. ASR has units $\Omega cm^2$, and is calculated using the following equation;

$$\text{ASR} = \frac{\text{Voltage}}{\text{Current Density}} \tag{3.14}$$

Half cell arrangements were deployed with one side of the sample exposed to air and the other side exposed to a controlled atmosphere. Initially a humidified 5%$H_2$ balanced with argon was used as the controlled atmosphere. The supply gas was humidified by flowing gas through a water bubbler at room temperature. As the experimental setup was developed and mass flow controllers could be deployed, mixtures of $H_2$ and $N_2$ in various proportions could be used as the controlled atmosphere. A water bath heated to $95^oC$ and heated gas lines allowed a humidity of $\approx$83% to be achieved in the supplied gases. Some experiments were conducted using nominally dry supply gases. By observing differences in electrochemical responses from using differing levels of humidity, some indication of SOEC operation mechanisms could be investigated.

## 3.8 SOEC/SOFC Post-Test Sample Analysis

### 3.8.1 Electron Microscopy

After testing, cells were removed from the test rig occasionally causing fracture, however, cells that did not fracture on removal underwent a forced controlled fracture. Platinum grids were required to be forcibly removed with as much care as possible so as to prevent damage to the electrode surface. Samples for electron microscopy were created in a similar manner to that explained in section 3.4.3. Fractured fragments from cell were mounted onto aluminium stubs for observation. Larger fragments, preferably with a fracture surface across the entire width of the cell and the current collection region, were mounted in epoxy resin. Glass slides and labels were held in place either side of the fragments using metallic clips so that during the curing process, fragments would remain vertical and could be identified easily. Samples were

ground and polished to achieve highly flat samples so that Energy Dispersive X-ray (EDX) spectroscopy could be used to quantitatively assess the distribution of elements throughout the cell cross-section. Control samples that were not tested were created using the same procedure as tested samples. Analysis of control samples assisted in the determination of compositional and microstructural changes that cells experienced during testing.

### 3.8.2 Focused Ion Beam (FIB)

In an attempt to obtain improved FE-SEM images, a polished cross section of a tested cell was mounted in an FEI Focused Ion Beam (FIB) instrument using an angled stage (see section 3.8.1). The angled stage allowed the sample surface to be positioned at a $<5^{\circ}$ angle with reference to the incident $Ga^{+}$ ion beam. When normal to the incident beam, a 100 $\mu$m wide, 30 micron long trench was milled across the electrolyte - $H_2$ platinum electrode interface using a 5 nA beam current. The deep end of the trench coincided with the electrode end of the trench. The sample was then rotated and angled at various angles ranging from 2 to $5^{\circ}$ with respect to the incident beam. Following accurate positioning, a 3 nA beam current was used to polish an exposed section of the trench surface which could eventually be polished using a 1 nA beam current to create a surface suitable for SEM observations and EDX spectroscopy analysis.

# Chapter 4

# Synthesis and Conductivities of Yttrium Doped Barium Cerate and Barium Zirconate

## 4.1 Commercial Powder

### 4.1.1 Powder Characterisation

The XRD pattern of a sample of as-supplied $BaCe_{0.9}Y_{0.1}O_{3-\delta}$ Praxair powder is displayed in figure 4.1. XRD data measured by Zakowsky *et al.* [14] is presented in figure 4.2 for comparative purposes. When figure 4.1 is cross referenced with figure 4.2, it can be seen that peaks with low intensity at 2Θ values: 24, 34, 42, 45 and 47° exist in the sample data that do not appear in the literature data, the most intense being at 24° 2Θ.

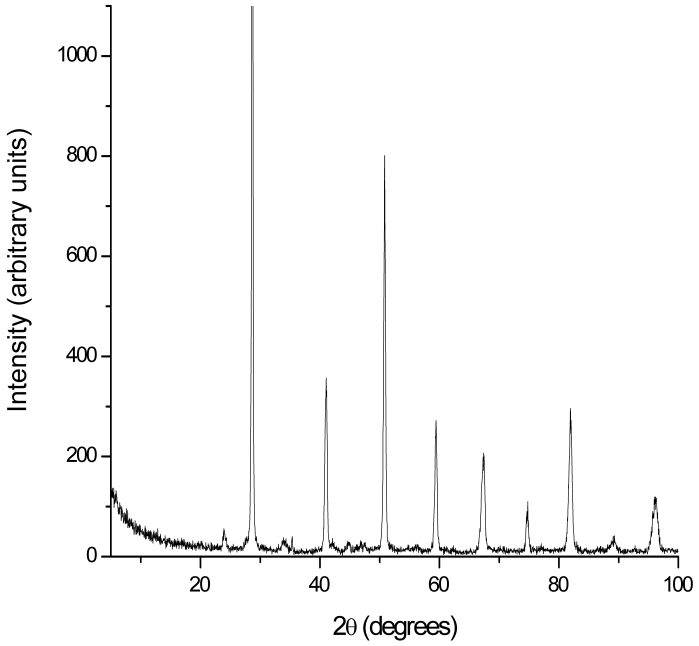



Figure 4.1: X-ray diffraction pattern of BCY10 as-supplied commercial powder

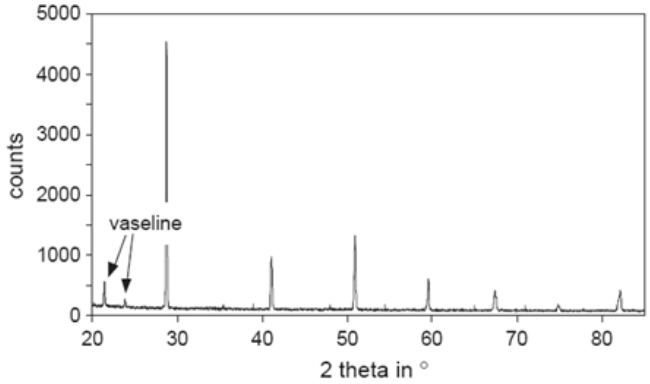



Figure 4.2: X-ray diffraction pattern of BCY10 as measured by Zakowsky *et al.* [14]

A crystallographic database was searched for potential pattern matches with these impurity peaks [137]. Figure 4.3 is the diffraction pattern of $BaCO_3$ measured by Holl *et al.* [15] and it can be seen that the most intense peaks of this pattern are at 24, 34, 42, 45 and 47° 2Θ and that these peaks clearly coincide with the impurity peaks observed in figure 4.1. Impurity peaks observed in figure 4.1 were therefore attributed to the presence of a $BaCO_3$ impurity phase in the as-supplied BCY powder from Praxair. The presence of an impurity phase is undesirable in

an electrolyte material as the conductivity or durability of the sample may be affected.

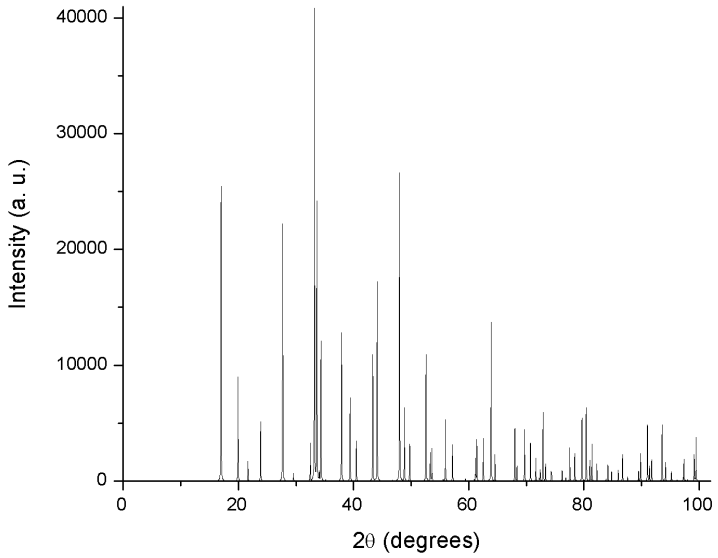



Figure 4.3: X-ray diffraction pattern of $BaCO_3$ as measured by Holl *et al.* [15]

Materials safety data sheets quote $BaCO_3$ as having a decomposition temperature of $1300^oC$. After the as-supplied powder was calcined at $1500^oC$ for 6 hours it was found that the $BaCO_3$ had fully decomposed leaving a pure perovskite phase of $BaCe_{0.9}Y_{0.1}O_{3-\delta}$. This is highlighted by figure 4.4 that compares sections of the as-supplied powder and the calcined powder XRD patterns. The fired powder XRD pattern matched the literature data well and the impurity phase had fully decomposed.

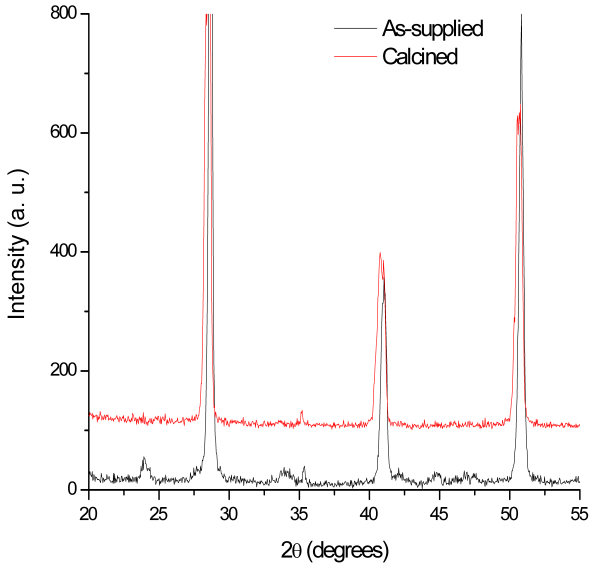



Figure 4.4: X-ray diffraction patterns of BCY10 as-supplied powder (black) and BCY10 commercial powder that was calcined at 1500$^o$C (red). Comparison shows that anomalous peak positions have been eradicated by the calcination process

It is prudent to consider the decomposition mechanism of the $BaCO_3$ and hence the stoichiometry of the BCY10 phase remaining as variations in stoichiometry may effect the electrochemical behaviour of the material [100]. Assuming $BaCO_3$ decomposed into BaO and $CO_2$ [138], it is possible for the BaO produced to have either evaporated, or entered the perovskite phase. The exact stoichiometry of the barium site in the Praxair powder after firing was unknown. Indeed, as XRD is unable to detect subtle variations in the barium stoichiometry, the barium stoichiometry of the as-supplied powder may not have been equal to one. It is necessary to use a technique such as neutron diffraction to accurately detect the stoichiometry of the barium site. This experimental route was not pursued as it was deemed beyond the scope of this thesis.

As with the BCY10 powder, the as-supplied BZY10 Praxair powder XRD pattern shown in figure 4.5, contains peaks at 24, 34, 45 and 47° 2Θ that do not appear in the XRD patterns of $BaZr_{0.9}Y_{0.1}O_{3-\delta}$ from the literature [10] (figure 4.6). A peak from the impurity phase at 42° 2Θ is somewhat masked in figure 4.5 and appears as a shoulder on a BZY10 peak. We find that a $BaCO_3$ impurity phase was also present in the BZY10 Praxair powder. Firing the BZY10 powder at 1500$^o$C for 6 hours caused $BaCO_3$ to decompose and is shown in figure 4.7, a comparison of XRD patterns of as-supplied and fired BZY10 commercial powders.

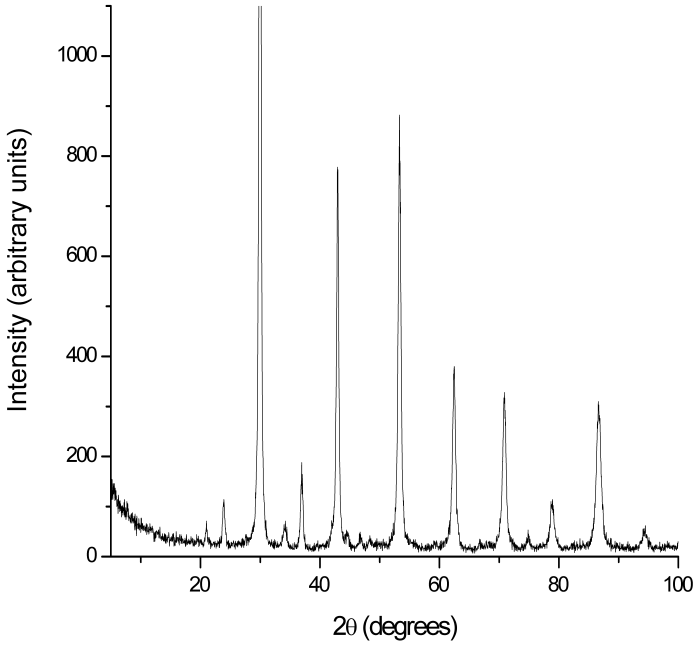



Figure 4.5: X-ray diffraction pattern of BZY10 as-supplied commercial powder

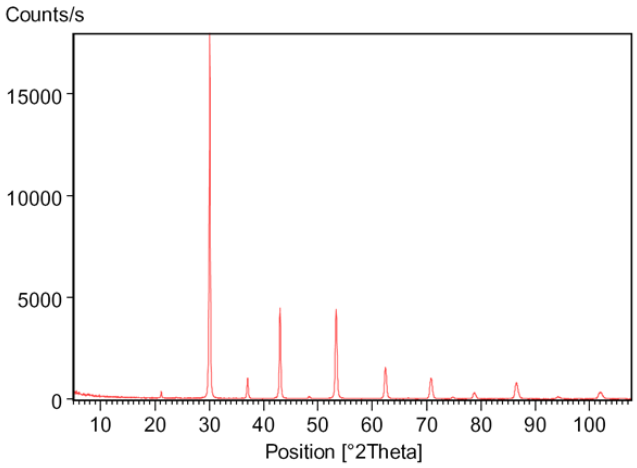



Figure 4.6: X-ray diffraction pattern of BZY10 as measured by Snijkers *et al.* [10]

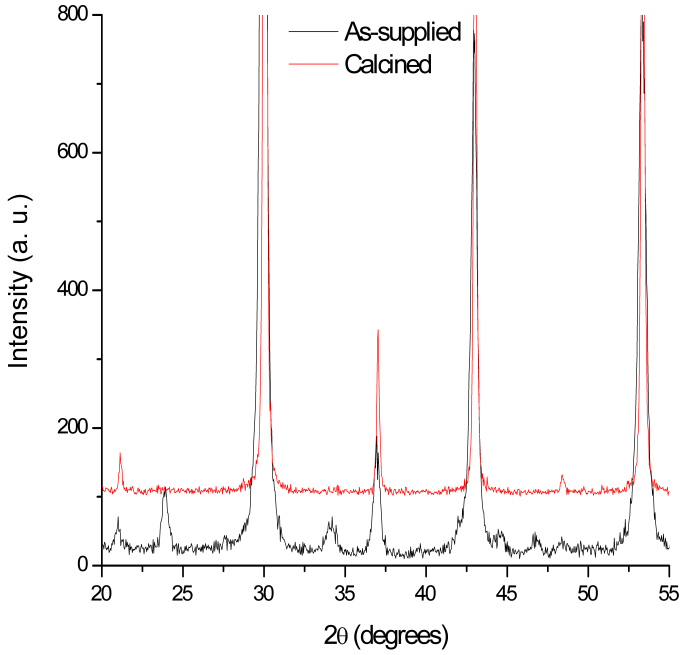



Figure 4.7: X-ray diffraction patterns of BZY10 as-supplied powder (black) and BZY10 commercial powder that was fired at 1500$^o$C (red). Comparison shows that anomalous peak positions have been eradicated by the firing process

### 4.1.2 Pellet Sintering

#### 4.1.2.1 BCY10

As commented on in sections 2.7 and 2.8, both BCY10 and BZY10 have been found to require comparatively extreme sintering conditions in order to form sufficiently dense samples for SOEC/SOFC testing. The sintering conditions required to create dense samples using the powders and equipment available were investigated, so that satisfactory SOEC/SOFC test samples could be manufactured. A furnace with a quoted maximum temperature of 1700$^o$C was available and used for all sintering of pellets, however, set temperatures did not exceed 1660$^o$C for element preservation purposes.

A sintering study of BCY10 powders supplied by Praxair commenced using a sintering temperature of 1660$^o$C to ascertain the maximum density achievable for a given sintering time. From initial experiments using as-supplied, 30 hour milled and 120 hour milled powders, it was found that a sintering time of 6 hours was sufficient to create dense samples. Therefore, BCY10 sin-

tering experiments proceeded with the following regime:

**BCY10 Regime 1**

Heating rate / cooling rate: $300^oChr^{-1}$

Set temperature: $1660^oC$

Sintering time: 6 hours

For each powder type, 10 samples were sintered using these conditions and the resultant average sintered densities of pellets are shown in table 4.1.

| Powder | Average Sintered Density (%TD) | Standard Deviation |
|---|---|---|
| BCY10 as-supplied | 93.44 | ±1.60 |
| BCY10 30 hour mill | 94.90 | ±1.62 |
| BCY10 120 hour mill | 97.03 | ±1.56 |

Table 4.1: Average sintered densities of BCY10 pellets sintered using BCY10 regime 1. Table includes data for as-supplied and milled powders.

Average sintered densities were found to increase with increasing milling time. In order to investigate the cause of this result, the particle size distributions of the three powder were measured using laser diffractometry. Particle size distributions and equivalent particle diameter values for the as-supplied and 120 hour milled powders are presented in figure 4.8.

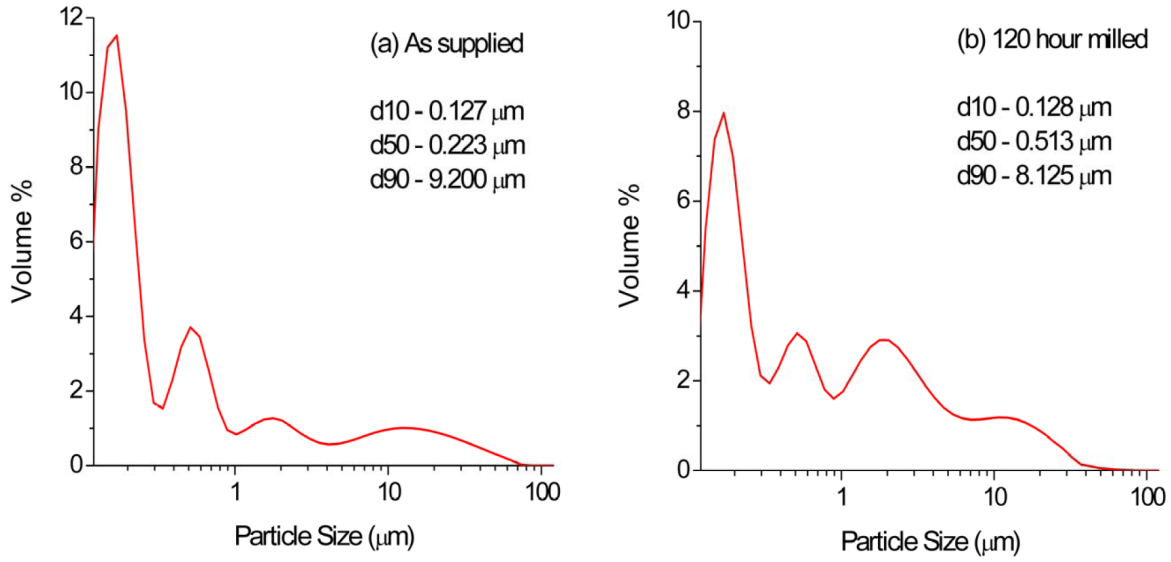



Figure 4.8: Particle size distribution data for (a) as supplied and (b) 120 hour milled powders

It can be seen that 4 modes are present in both the as supplied and milled powder particle size distributions. Peak locations on the particle size axis were not effected by the milling process. However, the proportions of contributions to the total volume % by each mode were significntly effected. This resulted in a greater d50 value, but a smaller d90 value in the milled powder. The width of the peak relating to the largest particle size mode was reduced during the milling process, with fewer particles contributing to total volume % above a size of 30 $\mu$m. Simultaneously, the volume % contribution from the peak relating to the smallest particle size mode decreased due to agglomeration of smaller particles. This resulted in the detection of more particles in the particle size range 1 to 4 $\mu$m in the milled powder sample than in the as-supplied powder. Particle size distribution can significantly effect the manner in which particles pack together during the pressing of pellets and consequently, the ability of the powder to sinter. By levelling out the modes of particle sizes in the distribution, as seen in figure 4.8, a higher green density was achieved. Green density measurements of samples prior to sintering, found that average green density value increased from 45.86%TD for the as supplied powder to 53.12%TD for the 120 hour milled powder. Therefore, the cause of the observed increase in average sintered density with increasing milling time is likely to be due to the formation of a beneficial distribution of particle sizes created during the milling process.

It is desirable to decrease the sintering temperature to a temperature as close as possible to the sintering temperatures of candidate electrode materials. This is because during the cell fabrication, co-firing of electrode and electrolyte materials are often required. High sintering temperatures can also lead to barium evaporation which could lead to a reduction in ionic conductivity. BCY10 regime 1 also often resulted in sample fracture during the sintering process. Crack initiation sites were located at the circumferential edges of the samples. It was possible that the outer section of pellets were experiencing high temperatures before the centre, causing a build up of stresses and crack initiation. Based on these considerations, the following sintering regime was implemented;

**BCY10 Regime 2**

Heating rate / Cooling Rate: $200^{o}\text{Chr}^{-1}$

Set temperature: $1500^{o}$C

Sintering time: 10 hours

By decreasing the heating and cooling ramp rates, the proportion of fractured samples decreased. Samples sintered using the 120 hour milled powder and regime 2 achieved an average density of 95.3%TD with a standard deviation of $\pm 1.88$. Initially, the sintering temperature was decreased to $1500^{o}$C without an increase in sintering time, however, an increase in sintering time to 10 hours was found to be required in order to form dense samples. Sintering regime 2 in conjunction with 120 hour milled Praxair BCY10 powder was deemed sufficient to create dense BCY10 samples for SOFC-SOEC testing. At a later date, it may be advantageous to explore increasing the sintering time further, to discover the effects on sintered density, microstructure and conductivity.

Sample conductivities are dependent on microstructure as well as composition because grain bulk and grain boundary conductivities often vary. Therefore, it is important to record sample grain structure and size. It also was important to note sample microstructure before any conductivity measurements or SOEC/SOFC testing was carried out, so that any microstructural changes that may occur during these experiments can be realised. Fracture surfaces of BCY10 samples produced using sintering regime 2 were observed using a scanning electron microscope. Samples were found to be well crystallised, with distinct, clean grain boundaries and an average grain size of $\approx 10$ $\mu$m (figure 4.9).

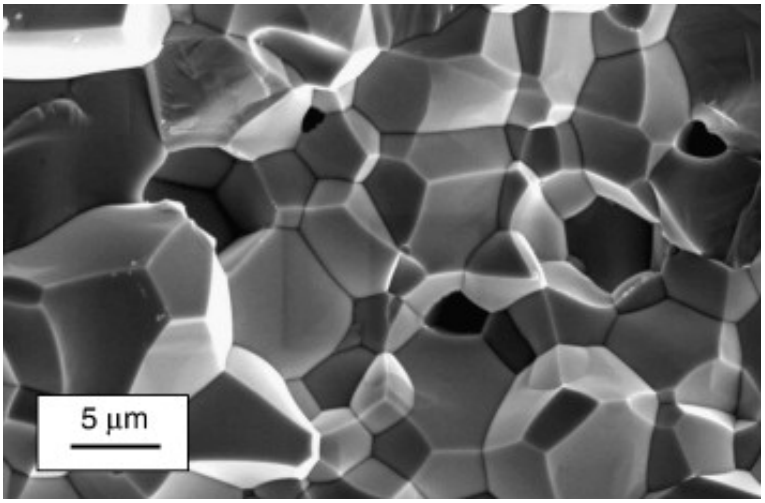



Figure 4.9: SEM image of a BCY10 fracture surface displaying the grain structure of the material

#### 4.1.2.2 BZY10

BZY10 is a promising candidate for an electrolyte material but has been reportedly difficult to sinter to high density. Careful consideration of the powder preparation has been required in order achieve high densities, as discussed in section 2.8. With this in mind, dense BZY10 samples were attempted to be sintered from Praxair commercial powder. Preliminary BZY10 sintering experiments proceeded with the following regime:

**BZY10 Regime 1**

Heating rate / Cooling Rate: $300^oChr^{-1}$

Set temperature: $1660^oC$

Sintering time: 10 hours

| Powder | Average Sintered Density (%TD) | Standard Deviation |
|---|---|---|
| BZY10 as-supplied | 72 | 1.90 |
| BZY10 30 hour mill | 85 | 1.72 |
| BZY10 120 hour mill | 87 | 1.70 |

Table 4.2: Average sintered densities of BZY10 pellets sintered using BZY10 regime 1. Table includes data for as-supplied and milled powders.

Average sintered densities of pellets prepared using this regime are shown in table 4.2. 10 samples were manufactured to achieve average density values. As-supplied powder achieved an average density of 72%TD, far below the target of 95%TD. Therefore, as with BCY10, the powder was milled for 30 hours before sintering and this resulted in an average density of 85%TD. Although this is a significant improvement in density, it was thought that the powder may benefit from an increased milling time to 120 hours. However, this only resulted in a marginal improvement in the average sintered density in comparison with the BCY10 results and may be due to the greater hardness of BZY10 than BCY10.

Particle size distributions and equivalent particle diameter values of the as-supplied and 120 hour milled BZY10 powders, as measured using laser diffractometry, are presented in figures 4.10(a) and 4.10(b) respectively. Data does not continue beyond 0.1 or 80 $\mu$m due to the limitations of the instrument.

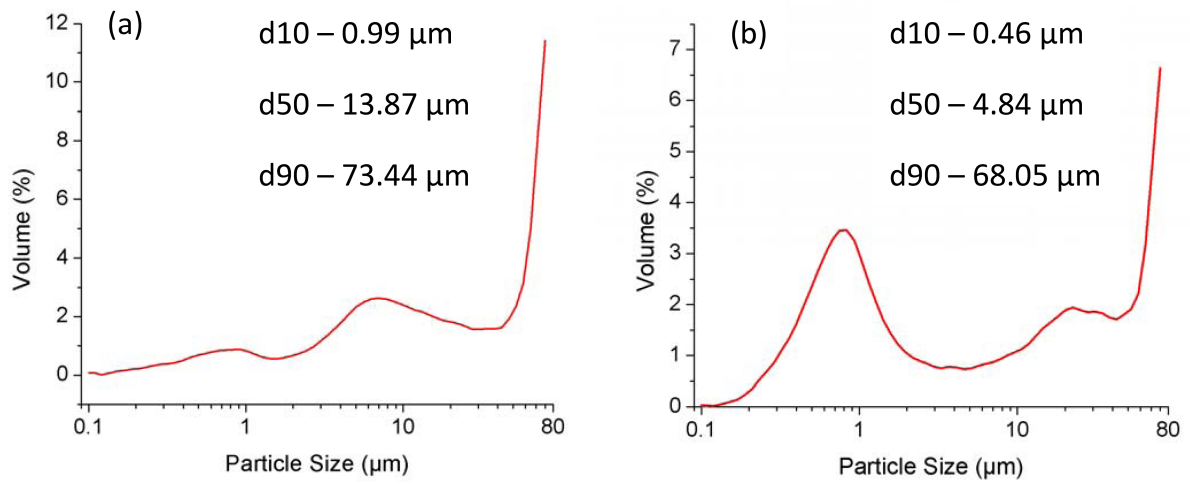



Figure 4.10: (a) Particle size distribution and equivalent particle diameter values for the as-supplied BZY10 commercial powder. (b) Particle size distribution and equivalent particle diameter values for the 120 hour milled BZY10 commercial powder

Measured d90 values were found to be very different to those stated by the manufacturer. Therefore, the peak in both of these distributions at the high end of the particle size scale is most likely due to insufficient de-agglomeration of particles. Results were skewed towards high particle sizes due to the method of measurement and are mis-representative. Sufficient investigation into the solvent and surfactant required to achieve more accurate results would have required significant effort and was beyond the scope of this thesis. However, as both samples were treated in the same manner, it is reasonable to assume that a fair comparison can be made between the data sets. From these results we conclude that a significant decrease in the average particle size occurred by milling the commercial powder. Therefore, average sintered density is believed to have increased because of a decrease particle sizes caused by milling. Smaller particle sizes created a greater total particle surface area which aided the coalescence of particles during the sintering process. An increase in milling time above 120 hours would probably not be advantageous and 87%TD was deemed to be the greatest average density which could be achieved by simply milling the commercial powder and using BZY10 sintering regime 1. This value is well below the target of 95%TD for SOEC-SOFC samples and a new approach was therefore necessary. Literature had stated that ZnO added in small quantities to Y:$BaZrO_{3-\delta}$ aided the sintering process and hence this experimental route was investigated [93,121]. The use of other sintering aids such as $Cr_2O_3$ was investigated without success. ZnO powder was added to the 120 hour milled Praxair powder as a sintering aid in the range of 0.1 to 5 wt%. Sintering

temperatures ranged from 1300$^o$C to 1500$^o$C with sintering isotherm times kept constant at 10 hours. Table 4.3 shows the initial results of the sintering investigation with ZnO added to BZY10.

| **Sintering Temperature ($^o$C)** | **Weight % ZnO** | **Average Sintered Density (%TD)** |
|---|---|---|
| 1300 | 0.1 | 62.5 |
| | 0.2 | 64.4 |
| | 1 | 90.3 |
| | 2 | 92.8 |
| 1350 | 0.1 | 64.6 |
| | 0.2 | 67.0 |
| | 1 | 92.4 |
| | 2 | 94.2 |
| 1400 | 0.1 | 68.9 |
| | 0.2 | 70.7 |
| | 0.4 | 79.9 |
| | 0.6 | 88.5 |
| | 0.8 | 92.5 |
| | 1 | 93.8 |
| | 2 | 95.2 |
| | 5 | 93.3 |
| 1500 | 1 | 96.3 |

Table 4.3: Average sintered densities of BZY10 pellets sintered using a ZnO dopant in a range of 0.1 to 0.5 wt% and sintering temperatures in the range 1300 to 1400$^o$C. A 200$^o$Chr$^{-1}$ heating / cooling rate and a sintering time of 10 hours were used for all experiments.

A sintering temperature of 1300$^o$C and 1 wt% of ZnO additive was sufficient to produce a sample more dense than that achieved with a sintering temperature of 1660$^o$C without any sintering aid. Clearly, the ZnO dopant had a dramatic effect on the sintering behaviour of the BZY10 Praxair powder. However, the effects of Zn on the electrochemical properties of the material are unknown, hence it is desirable to minimise the amount of ZnO additive required to produce a dense BZY10 sample at this stage. When the sintering temperature was raised to 1500$^o$C the average sintered density with a 1 wt% ZnO additive was greater than 96%TD. It was decided that these conditions would be used to create samples for SOEC/SOFC testing because this provided a balance between sintering temperature, wt% ZnO and %TD.

Both Irvine *et al.* [93] and Babilo and Haile [121] speculated that $Zn^{2+}$ ions replace some of the B-site ($Zr^{4+}$) ions. It is further suggested by Babilo and Haile that oxygen ion and barium ion vacancies are created within the lattice as a result of ZnO addition according to equation 4.1. The high final sintered density observed in the Zn doped samples may be explained by

the creation of barium ion vacancies by the substitution of a $Zn^{2+}$ onto a Zr site. Barium ion vacancies may have assisted the diffusion of ions during the sintering process and led to the formation of a highly dense material.

$$ZnO + Ba_{Ba}^{x} + Zr_{Zr}^{x} + 2O_{o}^{x} \rightarrow Zn_{Zr}^{''} + V_{Ba}^{''} + 2V_{o}^{\bullet\bullet} + BaO + ZrO_2 \tag{4.1}$$

As mentioned previously, sample conductivity can vary significantly with variations in microstructure and it is therefore necessary to observe sample fracture surfaces. Initially, the grain structure of the Zn doped BZY10 samples was not visible by observing the fracture surface using SEM imaging. Samples were polished and subsequently thermally etched at 1500$^o$C for 30 minutes and this successfully allowed observations of the microstructure of the material to be made using a field emission SEM. Figure 4.11 is an SEM micrograph of the thermally etched Zn doped BZY10 pellet.

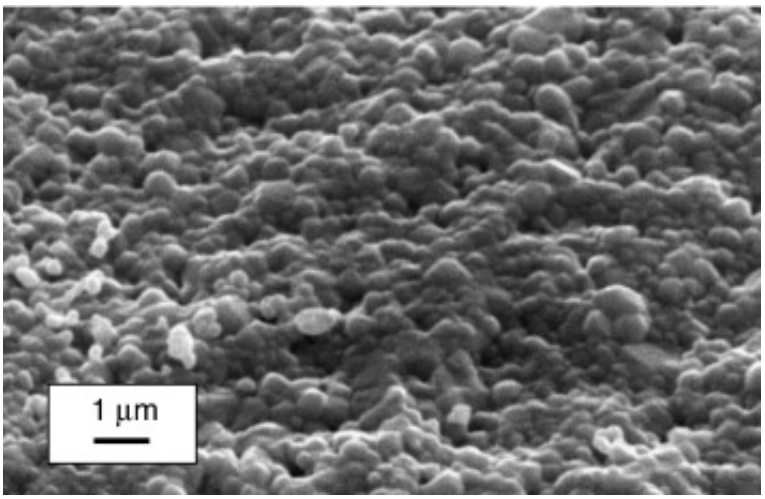



Figure 4.11: SEM image of a polished and thermally etched Zn doped BZY10 surface displaying the grain structure of the material

From this image we can see a sub-micron grain structure is present. A small increase in grain size may have occurred during the thermal etching process although this effect was thought to be minimal. This image is evidence that the particle size distributions in figure 4.10 are indeed skewed to larger particle sizes due to an unsophisticated measurement technique. The manufacturer of the BZY10 powder quote a d50 value of 0.8 $\mu$m which is much more consistent with the observed grain size.

## 4.2 Conductivity

### 4.2.1 AC Impedance Spectroscopy Measurement Technique

AC impedance spectroscopy is a powerful technique that is often used to measure conductivity of ceramic materials. Figure 4.12 is an example of part of an AC impedance spectrum of BCY10 and will be used to demonstrate the methodology behind the acquisition of grain bulk and grain boundary conductivities and conductivity plots presented later in this section and sections 4.2.2 and 4.2.3. These data were collected at 200$^o$C using a 5%$H_2$-Ar atmosphere with ambient humidity, when three responses could be distiguished from one another. The attributions of these responses based upon their capacitances were made in accordance with the literature, as shown in table 4.4 [26]. Also of note is the jump observed at a frequency of 1 MHz in the spectrum. This feature is present on all measured ACI spectra and is instrumentation and not sample related.

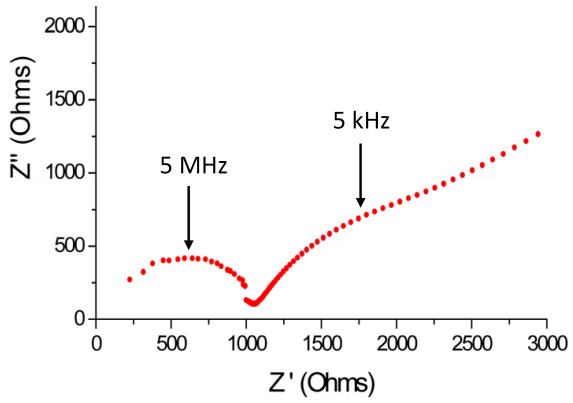



Figure 4.12: Section of an AC impedance spectrum of BCY10 at measured at 200$^o$C in air

| Capacitance (F) | Phenomenon Responsible |
|---|---|
| $10^{-12}$ | Grain Bulk |
| $10^{-11}$ | Minor, Second Phase |
| $10^{-11}$ to $10^{-8}$ | Grain Boundary |
| $10^{-10}$ to $10^{-9}$ | Bulk Ferroelectric |
| $10^{-9}$ to $10^{-7}$ | Surface Layer |
| $10^{-7}$ to $10^{-5}$ | Sample-Electrode Interface |
| $10^{-4}$ | Electrochemical Reactions |

Table 4.4: AC impedance response capacitance values and corresponding possible phenomenon responsible [26]

Capacitances of the responses were determined by the use of equivalent circuit modeling. Classically, ion conducting materials have AC impedance responses that can be modeled by a series of capacitors and resistors in parallel. However, all semi-circle responses relating to the sample that were detected were depressed. When a constant phase element (CPE) is in parallel with a resistor, a Cole element is created which can model depressed semi-circle (or arc) responses, better than simply a capacitor in parallel with a resistor. In figure **??**, the CPE1 and R1 components model the grain bulk response, CPE2 and R2 model the grain boundary response and CPE3 and R3 model the sample-electrode interface response.

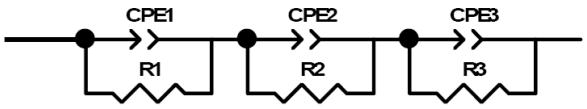



Figure 4.13: An example of an equivalent circuit model used to determine grain bulk and grain boundary resistances from AC impedance data

Common reasons for the need to implement CPEs instead of capacitors in equivalent circuits are surface roughness (electrode) or a distribution of reaction rates. In this case, it is probable that depressed semi-circles were detected because of a distribution of reaction rates, as complex reactions may occur when measuring the conductivity of proton conducting materials such as BZY10 and BCY10. Mathematically, a CPE's impedance is given by;

$$\frac{1}{Z} = Y = (Q_o j\omega)^n \tag{4.2}$$

Where;

Z = Impedance ($\Omega$)

Y = Admittance (S)

$\omega$ = Frequency (rad.s$^{-1}$)

$Q_o$ = Admittance at $\omega = 1$ (S)

The phase angle of the CPE impedance is independent of frequency and has a value of -(90*n) degrees, hence the term constant phase element. Depressed semi circles have their centre below the x axis on a Nyquist plot (such as that shown in figure 4.12) and the greater this depression,

the greater the value of n. As n approaches a value of 1, the CPE resembles a capacitor, whereas as n approaches 0, the CPE resembles a resistor. True capacitance values of responses were able to be calculated using equation 4.3. Responses could then be designated to either grain bulk, grain boundary or to the sample-electrode interface:

$$C = \frac{(Q_o R)^{n-1}}{R} \tag{4.3}$$

Where;

R = Resistance of resistor in parallel with the CPE ($\Omega$)

The equivalent circuit model used to determine grain bulk and grain boundary capacitance and resistances in the temperature range; room temperature to 250$^o$C for BCY10 and room temperature to 350$^o$C for BZY10, is shown in figure 4.13. This equivalent circuit was used to model the example ACI impedance spectrum shown in figure 4.12. The high frequency arc on the left of the figure was attributed to the grain bulk response as the capacitance of this arc was calculated to be of the order of $10^{-11}$F. The second arc was attributed to a grain boundary response as the capacitance of this arc was calculated to be of the order of $10^{-8}$F. An upturn is present on the far right of the spectrum and this was attributed to an electrode-sample interface response with a capacitance of $10^{-5}$F. Components R1 and R2 of the Cole elements shown in figure 4.13 were used directly as measures of the grain bulk and grain boundary resistance values.

In the temperature range 250$^o$C to 500$^o$C for BCY10 and 350$^o$C to 650$^o$C for BZY10, grain bulk semi circle responses were not detected. This was because at these higher temperatures the grain bulk response was beyond the measurable frequency range. The equivalent circuit model shown in figure 4.13 could still be used to model the data, however, the CPE1 component was effectively removed since the grain bulk exhibited no capacitance. R1 in the equivalent circuit is a resistor representative of the grain bulk resistance combined with any resistances associated with wires and contacts. As temperature increased, wire resistance became a greater proportion of the R1 value and is more important to consider. R1 resistance values were adjusted by subtracting the wire and contact resistance at the given temperature, which was measured separately, to obtain an estimate of grain bulk resistance.

At temperatures above 500$^o$C for BCY10 and 650$^o$C for BZY10, grain boundary responses were also not measurable. Above these temperatures, grain bulk and grain boundary responses could no longer be distinguished from one another and only total conductivity could be measured. Resistances calculated using equivalent circuits were corrected using equation 4.4 to find resistivities and in turn, conductivities.

$$\rho = \frac{RA}{l} \tag{4.4}$$

$$\sigma = \frac{1}{\rho} \tag{4.5}$$

Where;

$\rho$ = Resistivity ($\Omega$m)

R = Resistance calculated from equivalent circuit model ($\Omega$)

A = Cross sectional area of sample ($m^2$)

l = Sample thickness (m)

$\sigma$ = conductivity ($Sm^{-1}$)

Under wet conditions the temperatures at and below which the grain boundary responses were directly detectable decreased to 400$^o$C for both BCY10 and BZY10. An interesting finding is that the grain bulk conductivity was found to be greater than the grain boundary conductivity in BCY10 at and below 300$^o$C using an atmosphere of 5%$H_2$-Ar with ≈20% humidity. However, above this temperature, the grain bulk conductivity was found to be lower than the grain boundary conductivity. This is in contrast to BZY10 where, under the same conditions, the grain bulk conductivity is significantly greater than the grain boundary conductivity over the entire temperature range that the two responses were distinguishable from one another. Since the concentration of this thesis is on the creation of samples for SOEC/SOFC testing, further investigation into how the processing of these materials could be adapted to achieve more favourable microstructures in light of these findings was not conducted. Therefore, from here onwards, only total sample conductivities are considered.

It is important to determine if conductivity hysteresis can occur in samples during AC impedance measurements. This is because it is possible for the concentration of mobile species such as protons to become permanently effected on heating so as to produce different conductivity values

on cooling and inaccurate results. The conductivity results of a BCY10 sample, measured on heating and subsequently on cooling in humidified air, are shown in figure 4.14.

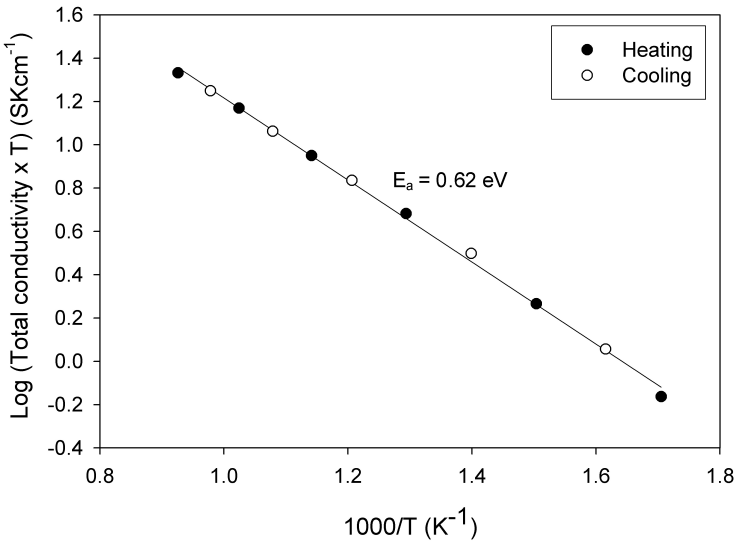



Figure 4.14: Conductivity results of a BCY10 sample measured on heating from 300$^o$C to 800$^o$C and subsequently on cooling, in an atmosphere of flowing air with approximately ≈3% humidity

It can be seen that the sample does not experience hysteresis as it is heated to over 800$^o$C and subsequently cooled. For additional reassurance, measurements were repeated with the same samples and gave identical results. BZY10 samples were subjected to the same analysis also with no hysteresis observed. Further repeats were carried out using a 5%$H_2$-Ar atmosphere without hysteresis observed. We conclude that the concentrations of occupied oxygen ion vacancies and protons were not irreversibly affected by the heating cycle. This is an important finding as a comparison can be made between conductivity data collected in different atmospheres for any one sample with confidence.

### 4.2.2 BCY10

Figure 4.15 is an Arrhenius plot and compares BCY10 data collected in 5%$H_2$-Ar with ≈3% humidity and data reported in the literature. It is important to note the atmospheric and sample preparation conditions when comparing data sets in order for unbiased comparisons to be made (section 2.7.1). A significant finding is that the conductivity data for BCY10 in this study are in agreement with that reported in the literature and bears particular resemblance to data from

Ma *et al.* [2]. Data collected using 5%$H_2$-Ar with ≈3% humidity shows lower conductivities than that of both Ma *et al.* and Coors and Readey [2, 4], whose data were collected in humidified hydrogen, and higher conductivities than Slade and Singh [3], whose data were collected in humidified 8.5%$H_2$-He.

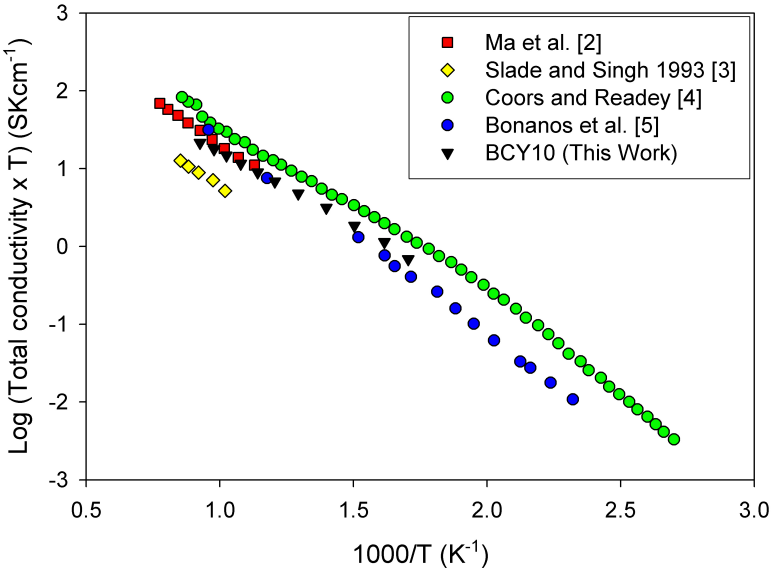



Figure 4.15: Arrhenius plot comparing BCY10 data from the current work with BCY10 literature conductivity data

Linear trends can be applied to Arrhenius plots and the activation energy for conduction can be calculated from the resultant slopes with the aid of the equations 4.6 and 4.7. Activation energy values are indicative of which the mobile species are present within the material, as values for electronic, protonic and oxide ionic conduction have been established.

$$\sigma T \;=\; \sigma_o \, e^{-(\frac{E_a}{RT})} \tag{4.6}$$

$$log(\sigma T) \;=\; log\, \sigma_o \;-\; \frac{E_a}{2.303RT} \tag{4.7}$$

Where;

$\sigma$ = Conductivity (Scm$^{-1}$)

T = Temperature (K)

$\sigma_o$ = Pre-exponential factor (SKcm$^{-1}$)

$E_a$ = Activation energy ($Jmol^{-1}$)

R = Universal gas constant (8.3144 $Jmol^{-1}K^{-1}$)

For all data sets presented in figure 4.15, activation energies were calculated to be in the region of 0.4-0.5 eV above 300$^o$C. This activation energy range is indicative of proton conduction by proton hopping from one oxide ion to the next [139, 140]. Slade and Singh [117] state that their calculated values for activation energies in BCY10 are lower than is likely for a conduction mechanism that involves anion migration ($OH^-$) via vacancies, which would be closer to that for $O^{2-}$ migration in related oxide ion conductors (>0.78 eV). Proton conducting mechanisms were also discussed previously in section 2.5 where other experimental evidence reported in the literature can be found to support the theory that a proton hopping mechanism is the most likely for this material.

If the charge mobilities (indicated by activation energy) are the same, then differences in conductivity data are attributable to differing concentrations of mobile species. The pre-exponential factor, $\sigma_o$, shown in equation 4.7, is indicative of the concentration of mobile species and relates to the intercept of the linear trend with the y axis of the Arrhenius plot. Samples in this study were prepared from a commercial powder, whereas the authors who published the literature data presented in figure 4.15 synthesised their powders by high temperature solid state reaction of constituent oxides and carbonates. Subtle differences in the processing procedure, precursors and atmospheres are likely causes for the disparity observed between data sets. It is possible that these variables affected the oxide ion vacancy concentration due to non-stoichiometry or segregation of dopant ions, which in turn inhibited or promoted the formation of protonic defects within the material. The atmospheric conditions may also contribute to disparity between results as the partial pressure of hydrogen was higher in both Ma *et al.* and Coors and Readey's experiments than reported here. A higher hydrogen partial pressure will increase the concentration of protonic defects within the material according to:

$$\frac{1}{2}H_{2(g)} + O_o^x \rightarrow OH_o^{\bullet} + e' \tag{4.8}$$

Figure 4.16 allows comparison between data collected in a nominally dry 5%$H_2$-Ar atmosphere with a 5%$H_2$-Ar atmosphere that has a humidity of ≈20%. It can be seen that between 300 and 700$^o$C the sample exhibits higher total conductivity in ≈20% humidified 5%$H_2$-Ar. This difference is attributed to additional protonic conductivity occurring using the atmosphere with higher humidity. As the partial pressure of $H_2O$ increased, the concentration of protonic defects within the material increased according to equation 4.9, causing an increase in the protonic contribution to the total conductivity.

$$H_2O_{(g)} + V_o^{\bullet\bullet} + O_o^x \rightarrow 2OH_o^{\bullet} \tag{4.9}$$

Conductivity data collected using an atmosphere with ≈20% humidity shows a decrease in activation energy above 400$^o$C from 0.70 eV to 0.39 eV. An activation energy of 0.70 eV is indicative that significant proton conduction does not occur below 400$^o$C. This is supported by a change in trend at around 300$^o$C that can also be seen in the reported data by Coors and Readey shown in figure 4.15. Although, less severe, an increase in activation from 0.41 eV to 0.53 eV is again indicative of a decrease in proton mobility below this temperature. Another feature of the data shown in figure 4.16 is that above 700$^o$C, conductivity values in the two atmospheres become very similar. Suksamai and Metcalfe [7] find that the proton transport number of BCY10 begins to significantly decrease above 650$^o$C, accompanied by a corresponding increase in oxygen ion transport number (see figure 2.4). Therefore, a likely cause for the convergence of the data above 700$^o$C is that the protonic contribution to the total conductivity decreased with temperature, negating the effect of the humidified atmosphere.

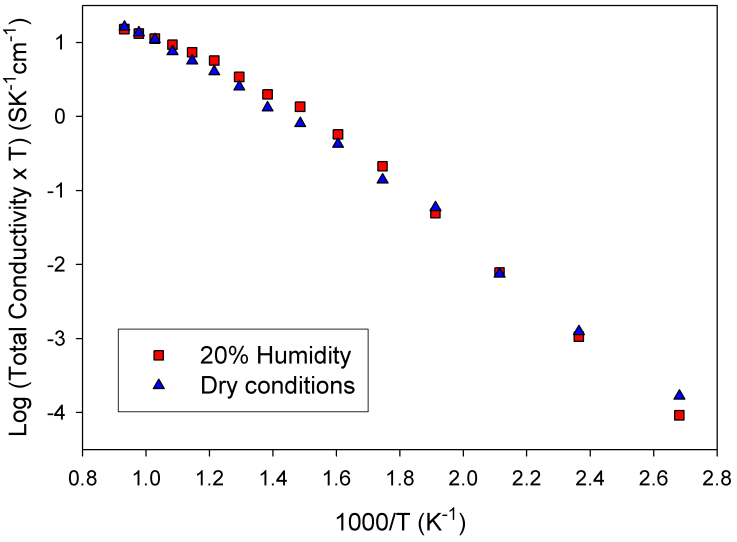



Figure 4.16: Arrhenius plot comparing BCY10 data collected using a 5%$H_2$-Ar atmosphere with nominally 'dry' conditions and with a ≈20% humidity

### 4.2.3 BZY10

Figure 4.17 shows part of an AC impedance spectrum of Zn-doped BZY10 collected at 200$^o$C using nominally dry 5%$H_2$-Ar. The high frequency arc on the left of figure 4.17 was attributed to the grain bulk response as the capacitance of this arc was found to be of the order of $10^{-11}$F after equivalent circuit modeling. The second arc was attributed to a grain boundary response as the capacitance of this arc was found to be of the order of $10^{-9}$F. A third arc was observed with a capactiance of the order of $10^{-7}$F and was attributed to the electrode-sample interface response.

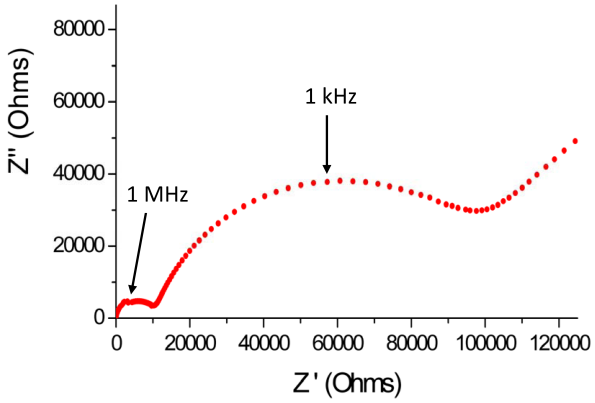



Figure 4.17: Section of an AC impedance spectrum of BZY10 measured at 200$^o$C in air

Figure 4.18 compares Zn-doped BZY10 total conductivity data collected in ≈3% humidified air with BZY10 data reported in the literature. Conductivity data in the literature is within the same order of magnitude as the Zn-doped sample although, activation energies vary significantly. Zn may, therefore, make a significant difference to the manner in which mobile species are transported throughout the material. However, it is impossible to determine whether the ionic transport number of the material has been effected by the addition of ZnO from the AC impedance data. The activation energy of data from Bohn and Schober [11] is most similar to the Zn-doped sample, however, the conductivity data reported is more than one order of magnitude higher than any other data set for BZY10. Furthermore, as only 3 data points were collected in this work, the calculated activation energy is unreliable.

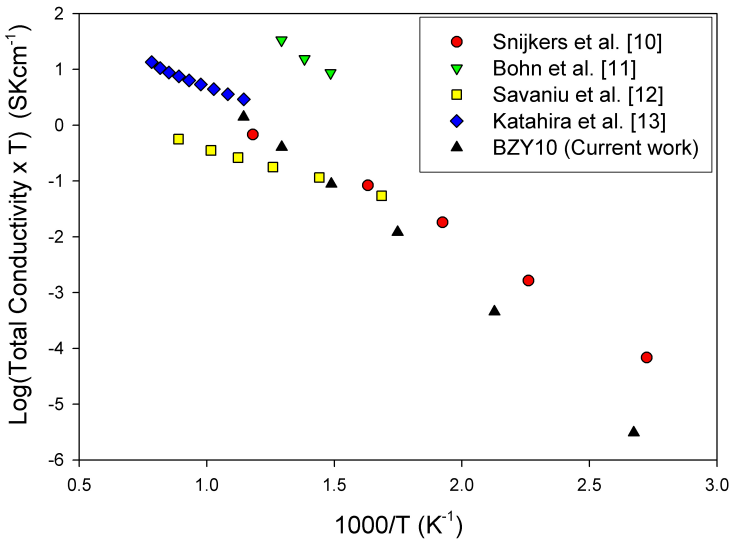



Figure 4.18: Arrhenius plot comparing Zn-doped BZY10 data from the current work with BZY10 literature conductivity data

The same argument applies as with the BCY10 conductivity analysis, that differences in processing and atmospheric conditions effect the conductivity values measured and that these may contribute to the disparity observed between results. Since dense BZY10 samples have been found to be difficult to produce, the techniques used to synthesise BZY10 powders have been more varied than for BCY10 and this is reflected in figure 4.18.

Figure 4.19 allows comparison of conductivity data for a 1 wt% Zn doped BZY10 sample collected using a 5%$H_2$-Ar atmosphere. Data collected using nominally dry and humidified (≈20%)

environments are displayed. Conductivity values were found to be higher in the humidifed atmosphere over the entire temperature range studied. By increasing the humidity, the concentration of protonic defects within the material increased and this is reflected in the Arrhenius plot.

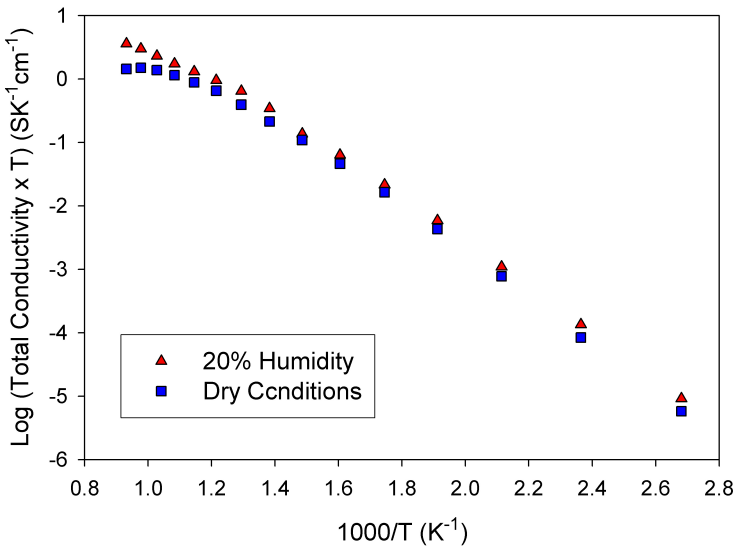



Figure 4.19: Arrhenius plot of BZY10 data collected using a 5%$H_2$-Ar atmosphere with nominally 'dry' conditions and with a ≈20% humidity

Between 100$^o$C and 500$^o$C the activation energy for the humidified data was 0.68 eV. Between 500$^o$C and 800$^o$C the activation energy was 0.41 eV indicating enhanced proton conduction in this temperature range than at lower temperatures. Data collected using a nominally dry atmosphere was found to have an activation energy between 100$^o$C and 550$^o$C of 0.65 eV. Conductivity values collected using a nominally dry atmosphere above 550$^o$C began to diverge from the linear trend established at lower temperatures. The cause for this behaviour is unknown, although this could be due to induced electronic conductivity.

Figure 4.20 displays conductivity data measured over the temperature range of 100 to 800$^o$C in 5%$H_2$-Ar with 20% humidity for both BCY10 and BZY10 samples. It can be seen that over the entire temperature range, BCY10 had a higher total conductivity than the Zn-doped BZY10 under these conditions. This was because BCY10 had both a lower activation energy and a greater charge carrier concentration than the Zn-doped BZY10 material.

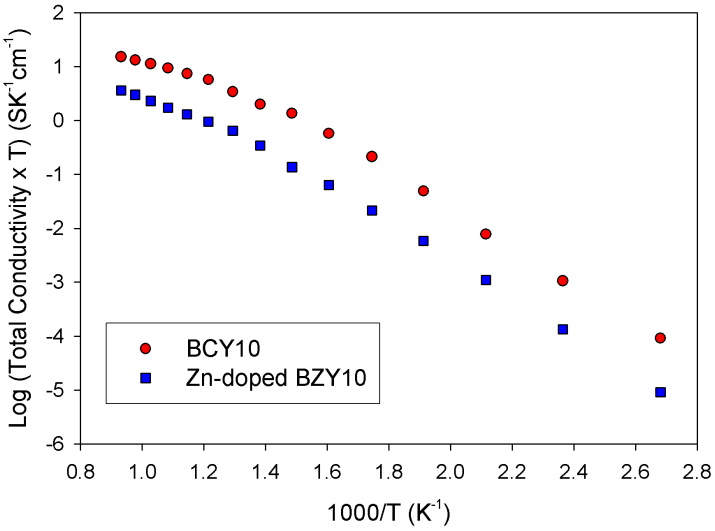



Figure 4.20: Arrhenius plot of BZY10 and BCY10 data collected using a 5%$H_2$-Ar atmosphere with a ≈20% humidity

## 4.3 BZY10 Powder Synthesis

### 4.3.1 Spray Pyrolysis Synthesis of BZY10

#### 4.3.1.1 Synthesis and Characterisation

As reported in the previous section, BZY10 was able to be sintered to a high density at 1500$^o$C, but only when doped with Zn. These samples were shown to have total conductivity values comparable to the literature, although the effect on the ionic transport number was unknown. An alternative method of producing dense pure BZY10 samples at sufficiently low sintering temperatures was investigated as this remains an issue currently unresolved in the literature. Therefore, spray pyrolysis was implemented as a synthesis technique to produce a pure BZY10 powder that will sinter to a high density at the lowest temperature possible. Based on results in the literature, it is reasonable to conclude that BZY10 powders produced by spray pyrolysis may have a particle size distribution and morphology that are beneficial to the sintering behaviour of the material.

The spray pyrolysis method of powder synthesis has several variables which may be altered that could effect the powder produced significantly (see section 3.2). The XRD pattern of the initial powder produced, shown in figure 4.21, revealed the existence of a barium zirconate perovskite

phase with a secondary $Ba(NO_3)_2$ phase present.

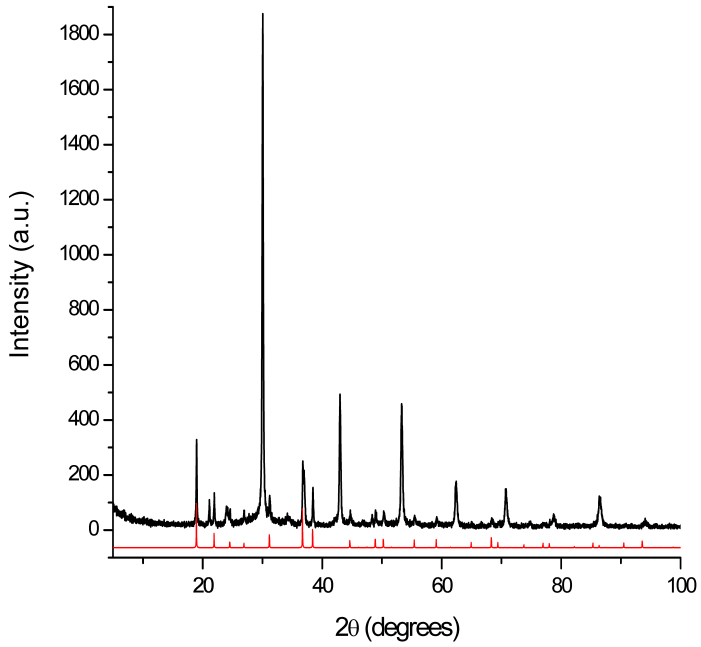



Figure 4.21: XRD powder diffraction pattern of a sample produced by spray pyrolysis at 600$^o$C - Markers below diffraction pattern indicate $Ba(NO_3)_2$ peak positions [16]

In preliminary experiments the furnace temperature (second zone) was set to 600$^o$C which is very close to the decomposition temperature of 599$^o$C for the $Ba(NO_3)_2$ precursor as found by differential thermal analysis (DTA) (see figure 4.22). When the furnace temperature was raised to 800$^o$C, the $Ba(NO_3)_2$ precursor fully decomposed leaving a single barium zirconate perovskite phase (figure 4.23). This is indicative that the production of Y:$BaZrO_3$ by spray pyrolysis is limited by the decomposition temperature of the precursors used. Hence through judicious choice of precursor the BZY phase can be prepared at remarkably low temperatures.

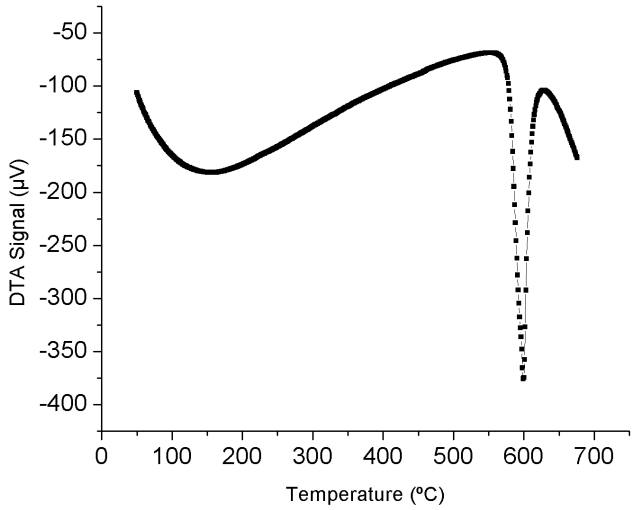



Figure 4.22: Graph of DTA signal against temperature showing decomposition of the $Ba(NO_3)_2$ precursor occurring just below $600^oC$

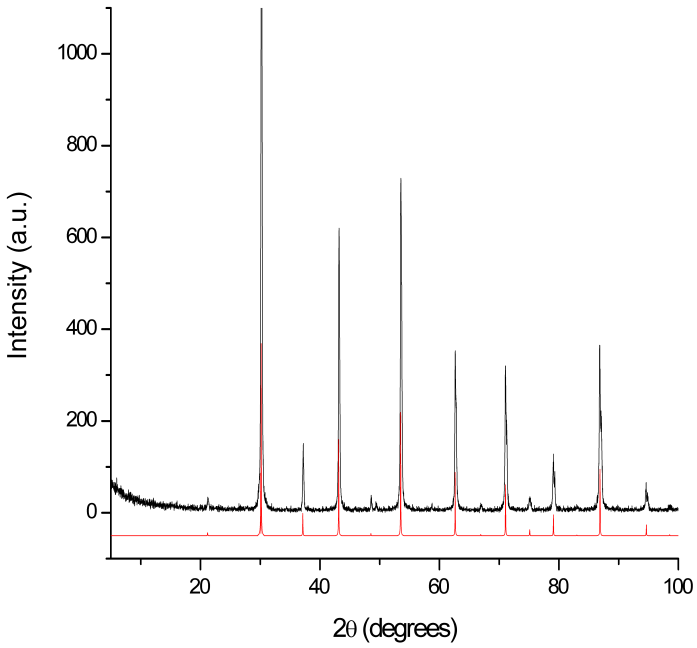



Figure 4.23: XRD powder diffraction pattern of a sample produced by spray pyrolysis at a furnace temperature of $800^oC$ showing single phase BZY10. Markers below diffraction pattern indicate $BaZrO_3$ peak positions [17]

The total residence time of the aerosol within the furnace could be altered by changing the carrier gas flow rate. Therefore, in further experiments, the furnace temperature was maintained at 600$^o$C but the carrier gas flow rate was lowered from 6 l.min$^{-1}$ to 3 l.min$^{-1}$, increasing the aerosol residence time. The resultant powders still contained $Ba(NO_3)_2$ but a reduction in the relative intensity of XRD peaks attributable to $Ba(NO_3)_2$ was observed, suggesting that the longer residence time allowed further decomposition of the nitrates to occur. Whilst this is of note, it should be considered that the spray pyrolysis process produces powder at a relatively slow rate. The powder yield rate is directly proportional to the carrier gas flow rate and therefore it was deemed undesirable to decrease the carrier gas flow rate below 6 l.min$^{-1}$ to produce single phase materials. Therefore, to ensure maximum powder production with full conversion of precursors, a furnace temperature greater than 600$^o$C was required to form a single perovskite phase material. Indeed, a furnace temperature of 800$^o$C was found to be sufficiently high to decompose precursors fully and all powders synthesised using this furnace temperature were found to be single phase perovskite using XRD. The production of BZY10 powders at 800$^o$C is a significant decrease in the synthesis temperature from that recently reported by D'Epifanio et al [124].

The sintering process of ceramic powders is widely recognised to be aided by the presence of small and dense particles. Figures 4.24 and 4.25 display particle size distributions (PSDs) with corresponding d10, d50 and d90 values for the milled commercial BZY10 powder and BZY10 powder produced by spray pyrolysis at a furnace temperature of 800$^o$C, respectively.

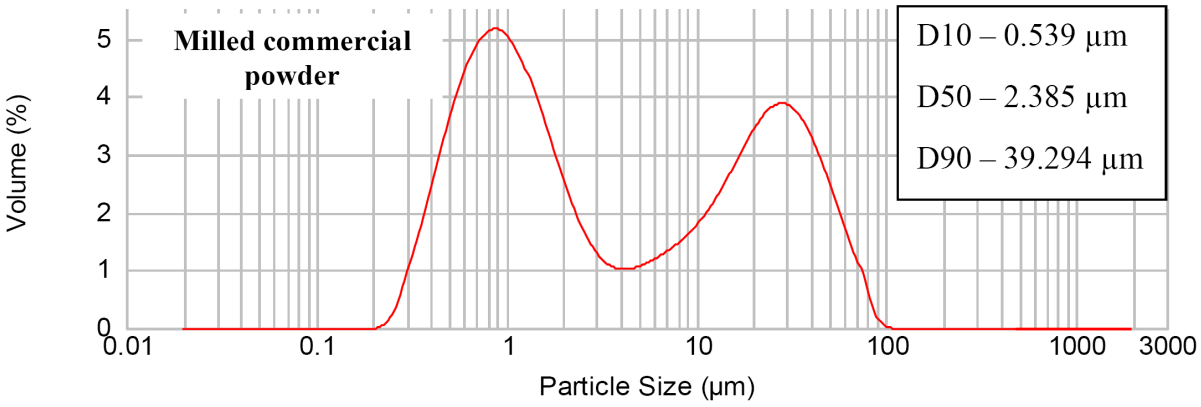



Figure 4.24: Particle size distribution of 120 hour milled commercial powder. Equivalent particle diameter values are also shown.

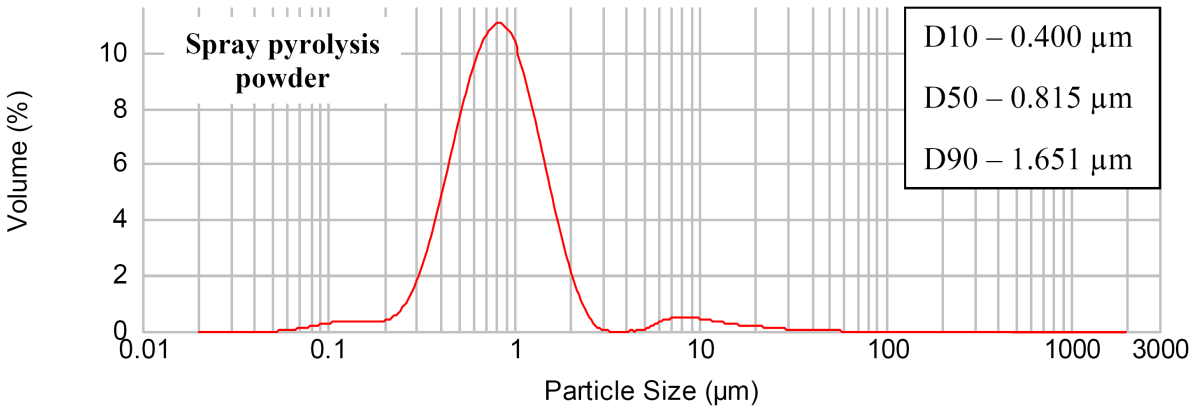



Figure 4.25: Particle size distribution of powder synthesised by spray pyrolysis with parameters; concentration; 2.5 x $10^{-3}$ mol.$l^{-1}$, nebuliser frequency; 2.5 MHz and furnace temperature; 800$^o$C. Equivalent particle diameter values are also shown.

Both PSDs show a peak at around 0.8 to 0.9 $\mu$m although this peak is narrower for the pyrolysis sample, indicating a distribution of smaller particle sizes. A second mode is observed for the PSD of the commercial powder at around 30 $\mu$m that is not observed for the pyrolysis sample and this is reflected in the large difference in d90 values between the two samples. A shoulder present on the main peak in the PSD for the material produced by spray pyrolysis indicated a low volume percent of very small particles, the presence of which was confirmed by electron microscopy. SEM and TEM imaging of spray pyrolysis samples suggested that particles above and around the d50 value in size are in fact agglomerations of smaller particles (figures 4.26(a), 4.26(b) and 4.27(a)). A secondary peak at around 10 $\mu$m in the PSD of the spray pyrolysis sample suggests the presence of larger agglomerates although this could not be verified using SEM imaging. It may be that the particle size analyser was unable to measure the size of particles and agglomerates accurately due to the presence of insufficiently separated clusters of powder. Figures 4.26(a) and 4.26(b) are SEM micrographs of a powder sample produced at 800$^o$C, 2.5 MHz with a solution concentration of 2.5 x $10^3$ mol.$l^{-1}$, and shows the irregular particle morphologies produced.

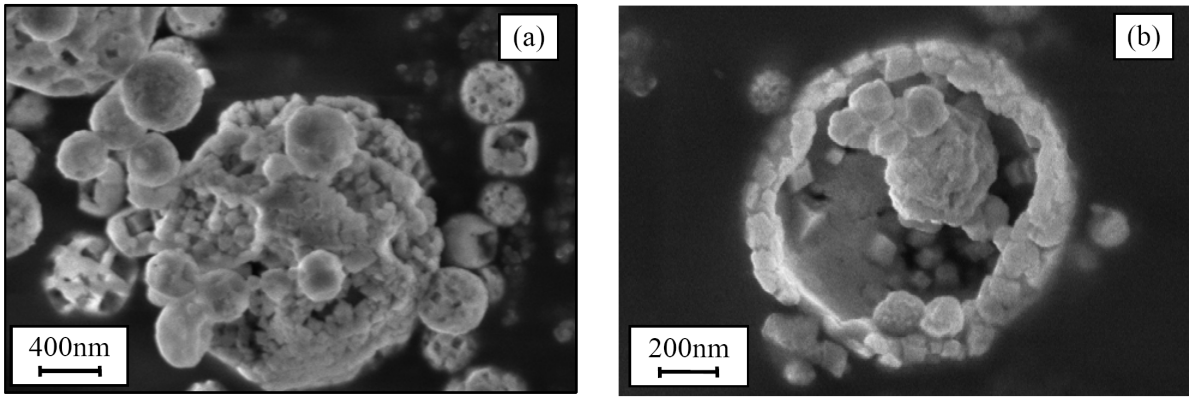



Figure 4.26: SEM Micrographs of (a) powder showing typical particle agglomeration and faceted particles that are present in all samples and (b), powder prepared by pyrosol synthesis, 2.5 x $10^{-3}$ mol.l$^{-1}$, 2.5 MHz, 800$^{o}$C showing particle size distribution and varied particle morphologies

Morphologies of these types were observed in all powders synthesised by spray pyrolysis. Many particles appear to have square facets on their surface with some having adopted a cuboidal shape. It is not known whether the cubic crystal structure of BZY10 was responsible for these morphological features. Possibly, preferential crystal growth occurred after particle nucleation and this caused the formation of cuboidal crystallites. Figures 4.26(a) and 4.26(b) also feature agglomerations of particles that are common within all spray pyrolysis powder samples studied. The agglomerate in figure 4.26(b) appears to be filled with particles, whereas figure 4.26(a) suggests that some agglomerates are hollow. Transmission electron microscopy was therefore used to determine the density of particles and the density of these commonly found agglomerates. A TEM micrograph of the same powder is shown in figure 4.27(a) and is evidence that agglomerates, typically 1 $\mu$m in diameter, are generally a collection of particles of less than 250 nm diameter that form one single hollow sphere. Mass thickness contrast is thought to cause the majority of agglomerates to appear as dark rings encompassing regions of brighter contrast. This indicates that mass is unevenly distributed throughout the cross-section of the agglomerate and that these agglomerates are hollow.

Figure 4.27(b) displays two further types of particle morphology, commonly observed, that are not agglomerates of the type previously mentioned. Particle A in figure 4.27(b) appears to be a dense particle formed from many, very small crystals, less than 10 nm across and may perhaps be classed as an agglomerate. Particle B in figure 4.27(b) appears as a dense particle formed

from several angular crystals, of approximately 70 nm dimension.

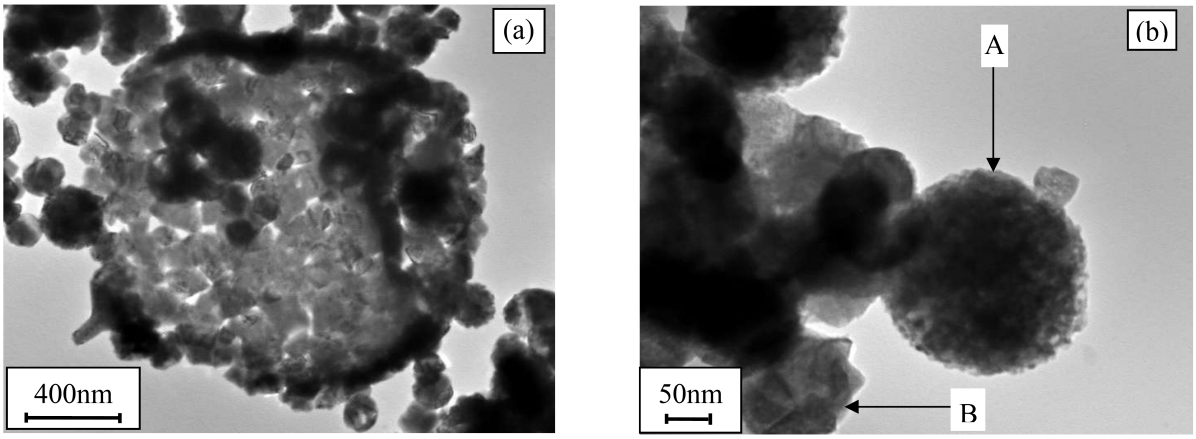



Figure 4.27: TEM micrographs of (a) powder showing an agglomeration of particles less than 250 nm in diameter and (b), powder exhibiting the presence of dense particles

Bucko and Oblakowski [129] found that the crystallite size of $BaZrO_3$ prepared by spray pyrolysis decreased with an increase in furnace temperature. They comment that the kinetics of the formation of the $BaZrO_3$ phase from the precursor salts are the probable cause for this furnace temperature effect. It was argued that the degree of overheating increased with a higher furnace temperature, causing the crystal nucleation process to be more energetically favourable than crystal growth. It may therefore be desirable to increase the synthesis temperature above $800^oC$ to produce a powder with a lower average particle size and could ultimately allow a reduction in sintering temperature of BZY10.

#### 4.3.1.2 Sintering behaviour

Once BZY10 powders had been synthesised using different spray pyrolysis parameter sets, the effects of varying these parameters on the sintering behaviour of these powders was investigated. Dilatometric curves of samples produced under a range of conditions are presented in figure 4.28. It is important to note the green density of the samples (table 4.5) when comparing dilatometric curves as the dilatometer measures change in sample length.

| Experiment Number | Green Density of Dilatometry Sample (%TD) | Sintered Density (%TD) |
|---|---|---|
| 1 | 32.5 | 41.5 |
| 2 | 40.8 | 43.0 |
| 3 | 35.3 | 42.4 |
| 4 | 35.7 | 45.4 |
| 5 | 37.3 | 54.0 |
| 6 | 37.6 | 90.6 |
| 7 - Commercial Powder | 50.1 | 59.0 |
| 8 - Zn doped | 50.7 | 91.5 |

Table 4.5: Green and sintered densities of dilatometry samples. Green density values quoted here should be considered when analysing figure 4.28. Experiments 2 and 3 were conducted using a furnace temperature of 600$^o$C and therefore, were not comparable and omitted from figure 4.28.

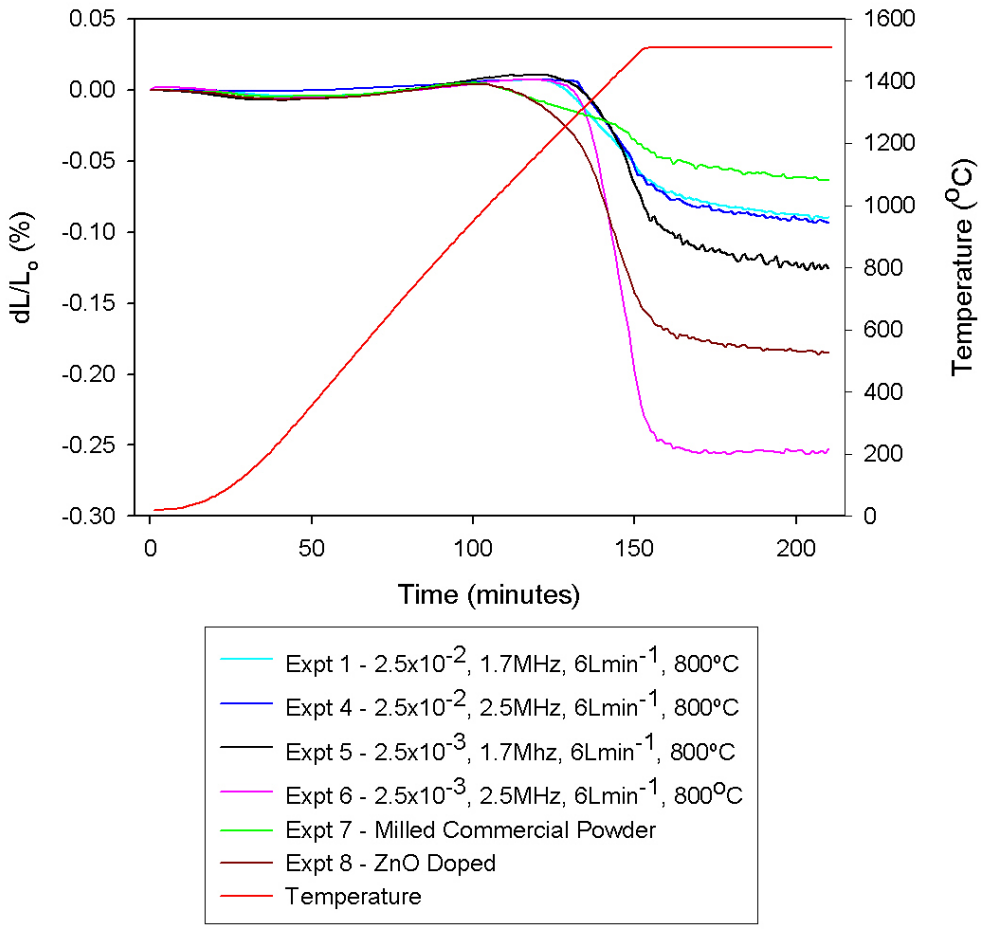



Figure 4.28: Dilatometric curves of samples produced using a range of conditions. Red line is the time-temperature profile and corresponds to the right hand axis.

The onset of sintering occurs at around 1200$^o$C for each spray pyrolysis produced sample, however, small differences in the onset temperature may have been discernible if a slower heating rate (<10$^o$Cmin$^{-1}$) had been used. From a comparison of the dilatometric curves for the samples produced at 1.7 MHz and 2.5 MHz nebulisation frequency, it was observed that increasing the atomising frequency alone did not significantly increase the final sintered density. Details of the influence of spray pyrolysis parameters on the particle morphology and sintering behaviour of yttria stabilised zirconia were reported by Gaudon *et al.* [141]. In this study, it was reported that the PSD widened and the average particle size decreased when the atomising frequency was increased. Furthermore, they state that the atomising frequency is the most influential parameter for control of the droplet size of the aerosol and that ceramic materials will sinter more easily with a wider distribution of particle sizes. We conclude, however, that it is unlikely that the particle size distributions of our powders were significantly effected by an increase in atomising frequency from 1.7 MHz to 2.5 MHz given that the increase in the final sintered density observed was minimal.

Bucko and Oblakowski [129] prepared un-doped $BaZrO_3$ nanopowders by spray pyrolysis and found that the PSD was significantly affected by the solution concentration. In their work, the average particle size varied from 90 nm to 500 nm in powders prepared from solutions of 1 x $10^{-3}$ mol.l$^{-1}$ at 1200$^o$C and 1 x $10^{-2}$ mol.l$^{-1}$ at 800$^o$C, respectively. Based on these literature findings, the effect of varying the solution concentration was investigated. Combinations of two concentrations and two frequencies were investigated (2.5 x $10^{-3}$ mol.l$^{-1}$ and 2.5 x $10^{-2}$ mol.l $^{-1}$ at 1.7 MHz and 2.5 MHz). The powder produced at low concentration and lower frequency achieved a final density of approximately 54%TD, whereas the powder synthesized from higher concentration solution at lower frequency only reached a final sintered density of approximately 41.5%TD. However, powder produced using an atomising frequency of 2.5 MHz and a solution concentration of 2.5 x $10^{-3}$ mol.l$^{-1}$ was found to sinter to a final density of 90.6%TD (experiment 6). Therefore, the combination of a high atomising frequency and a low solution concentration was found to dramatically increase the final sintered density.

Particle morphology, as well as PSD characteristics, may play a major role in the sintering behaviour of BZY10. From observations made using SEM and TEM, all spray pyrolysis powder samples appear to include a variety of particle and agglomeration morphologies. This variation

was perhaps linked to the range of droplet size and shape produced by the ultrasonic nebuliser. For example, particle A in figure 4.27(b) may have been formed by many small droplets agglomerating together before nucleation with little growth subsequently occurring, whereas larger droplets may have experienced a different nucleation and growth mechanism to form particle B in figure 4.27(b). The proportions of these differing morphologies within any one sample were difficult to quantify and hence the influence of a higher proportion of a particular morphology over another on the sintering behaviour is unknown. Djurado and Meunier [126] studied the effect that atomising frequency had on the synthesis of zirconia powders produced by spray pyrolysis. They observed a roughening of particle surfaces when the nebulising frequency was decreased from 1.7 MHz to 850 kHz. This change in particle morphology was attributed to an increase in the rate of solvent evaporation from the aerosol. A variation of parameters in the current study may have also affected the manner in which the aerosol was transformed into oxide powder and altered particle morphology.

The final density for each sample would perhaps be further increased by iso-statically pressing the pellet samples at 300 MPa before the sintering process is carried out. An increase in sintering time would be unlikely to improve the final density of the material significantly as a constant $dL/L_o$ for a period of time was observed during the 1 hour isotherm for all samples. This represents a significant reduction in both sintering temperature and time in comparison with the current literature data [10,121]. Evidently, the microstructure of the material may be altered by increasing the sintering time and this could affect the electrochemical properties of the sample. Due to the technique limitations and access to the spray pyrolysis apparatus, samples for AC impedance or SOEC-SOFC experiments were unable to be produced.

Samples created using milled commercial BZY10 powder reached a final density of about 59%TD and clearly had different sintering behaviour to the spray pyrolysis samples. The onset of sintering occurred at a lower temperature, approximately $1000^oC$, and the sample appeared to have additional phases of sintering. This is indicative of the very different PSD and particle morphology of the powder compared to the spray pyrolysis produced powders. The samples containing a 1 wt% ZnO additive reached a final density of about 91.5%TD and as can be seen in figure 4.28, a density much greater than that achieved by the non-doped commercial powder. This finding is in accordance with results reported in section 4.1.2.2, as well as by Babilo and

Haile [121] and Tao and Irvine [142]. It is of interest to note that the final sintered density of the powder produced by spray pyrolysis and that produced with a ZnO additive are in close agreement, the spray pyrolysis synthesis method outlined in this work can produce powders of suitable particle size and morphology to produce dense samples for ceramic proton conducting devices.

In an attempt to break up agglomerates so that powder may sinter more readily, samples were subjected to an ultrasonic agitation treatment. First, powder was suspended in iso-propanol. A high power ultrasonic probe was then submerged into the suspension and activated using a range of power settings and time periods of agitation. SEM imaging confirmed that the proportion of agglomerates and of large particles was decreased by the ultrasonic agitation treatment. Included in figure 4.29 is an example of a relatively large particle that was fractured by the ultrasound treatment. This is evidence that average particle sizes were decreased by the ultrasonic agitation treatment. The labeled particle can be seen to have approximately halved in size and now resembles a hemisphere. Figure 4.30 displays the dilatometric curves of samples produced from powder using experiment 4 conditions, before and after an ultrasound treatment.

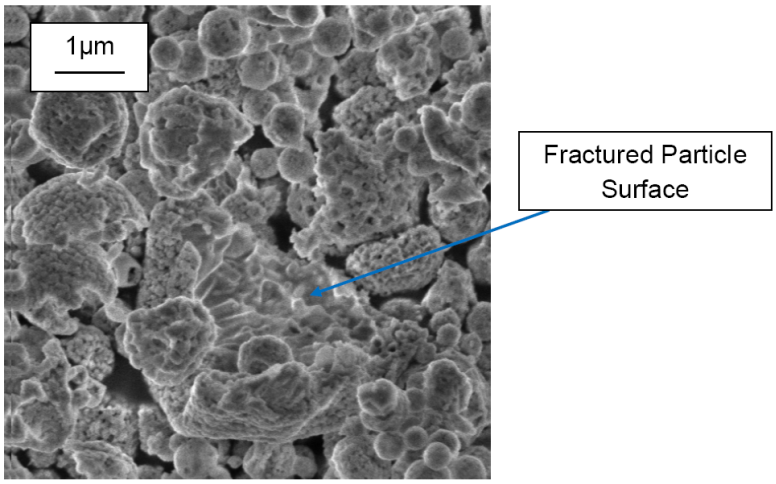



Figure 4.29: SEM image of powder produced in experiment 4 after ultrasound treatment showing particulate fracture

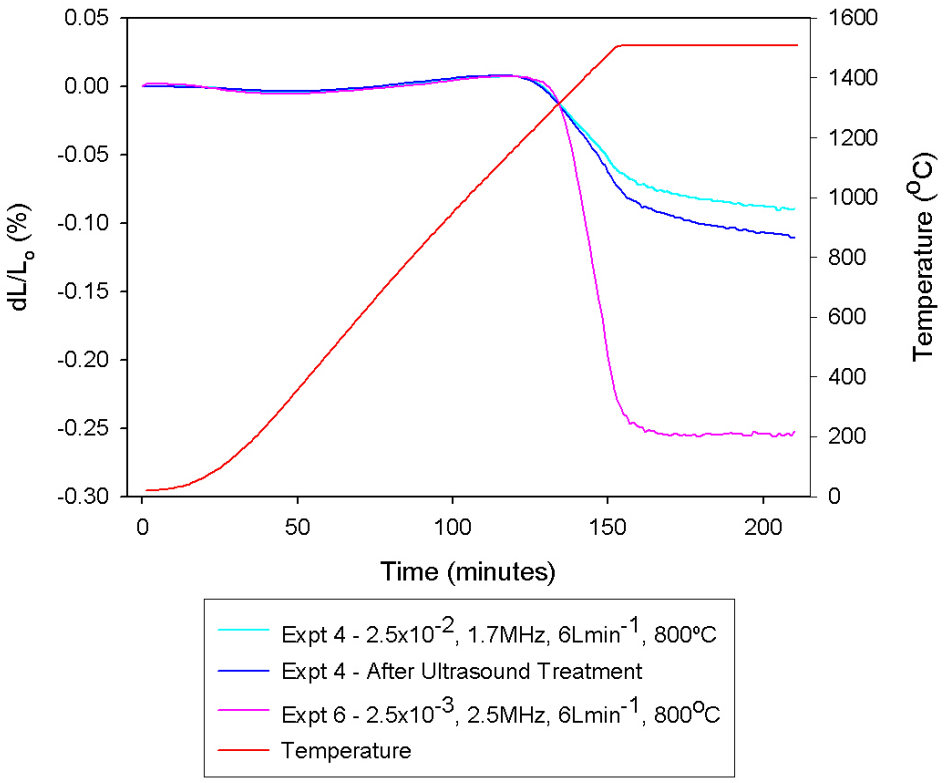



Figure 4.30: Dilatometric curves of samples from experiment 4 before and after ultrasound treatment. The red line is the time-temperature profile and corresponds to the right hand axis.

A small increase in the achieved density was observed in the ultrasonically agitated sample over the untreated sample. This increase was attributed to a greater particle surface area, although the particle morphology as observed in figure 4.29, may well have been detrimental as spherical particles have been proven to aid the sintering process. Ultrasonic agitation may have had a similar or more pronounced effect on samples from other experiments but this could not be investigated due to limited powder and limited access to the ultrasonic probe. Some samples may have benefited more, or less, than powder produced in experiment 4 from ultrasonic agitation since the proportions of large agglomerates and particles varied between experiments.

### 4.3.2 Sol-Gel Synthesis of BZY10

Although we have proven that spray pyrolysis is a technique that can produce pure BZY10 powders able to be sintered to high density at 1500$^o$C, the method was found to have a very low powder yield rate using the laboratory apparatus available. A further method of synthesising

pure BZY10 powder with a higher yield rate, that was able to be sintered at sufficiently low temperatures was therefore investigated. As detailed in section 2.8, there have been previous attempts at synthesising Y:$BaZrO_3$ powder via a sol-gel type processing route with varying success [21, 22, 124, 143]. D'Epifanio *et al.* [124] dissolved precursors in ethylene glycol and used citric acid as a chelating agent. Resultant powders produced samples approximately 80% of the maximum theoretical density when sintered at 1600$^o$C for 8 hours. Precise details of the Pechini method employed by Iguchi *et al.* [143] were not reported but it was stated that >95% of the maximum theoretical density was achieved by sintering samples at 1700$^o$C for 10 hours. Cervera *et al.* [21, 22] used metal alkoxide precursors dissolved in 2-methoxyethanol solvent. Powder was pressed at room temperature to 4 GPa before annealing and allowed a density of 98.1%TD to be achieved using a sintering temperature of only 1250$^o$C. Equipment to press powder samples using these very high pressures was not available, therefore, the more conventional methods of powder preparation employed by D'Epifanio *et al.* and Iguchi *et al.* [124, 143] were used as a guide to synthesise BZY10 using the sol-gel method. Details of the method employed in this work are given in section 3.3. Figure 4.31 is an XRD pattern of the powder produced using this method.

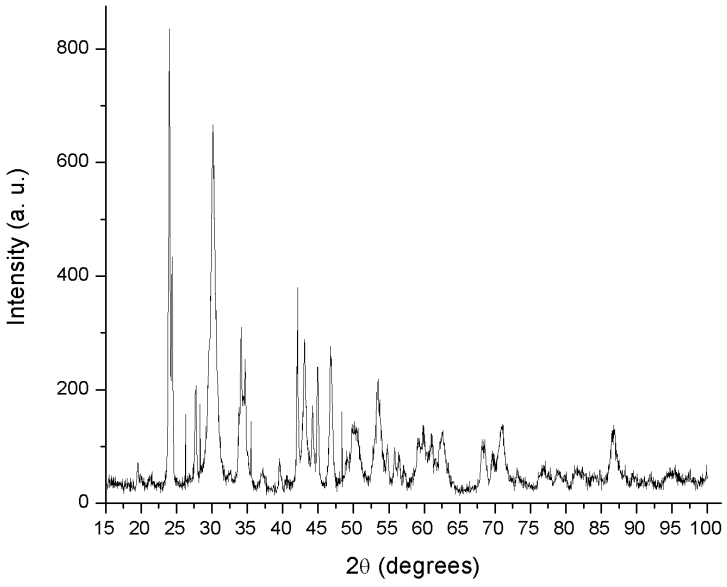



Figure 4.31: X-Ray diffraction pattern of powder synthesised using a sol-gel technique. Peaks at 30, 43 and 53.5 °2Θ indicate that BZY10 perovskite phase was partially formed at this stage. Other peaks correspond to unreacted precursors.

It can be seen that full reaction between the precursors had not completed at this stage and that a further calcination step was required to obtain a single perovskite phase. Literature was consulted when deciding the appropriate calcination temperature and it was concluded that a temperature of 1250$^o$C for 10 hours should ensure the reaction to reach completion [122]. Figure 4.32 is an XRD pattern of the sol-gel synthesised powder after the calcination step.

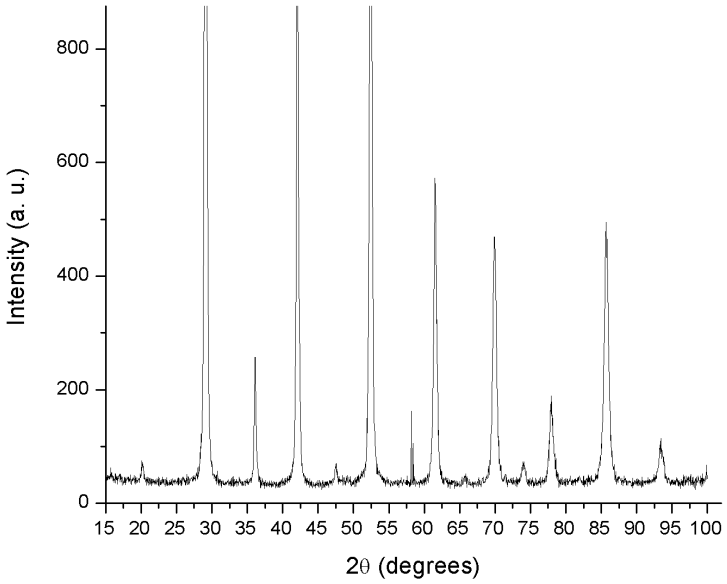



Figure 4.32: X-Ray diffraction pattern of powder synthesised using a sol-gel technique after calcination at 1250$^o$C for 10 hours

When comparing figure 4.32 with the data from the literature shown in figure 4.6 [10], it can be seen that the reaction had reached completion and a single perovskite phase was successfully synthesised. Peak positions and relative intensities match with the literature data for BZY10 with no impurity phases detected. The peak at 57° 2Θ was found to be an instrument artifact and not as a result of X-ray interaction with the sample. Sufficient powder was produced for a sintering study to be conducted to ascertain whether, using these parameters, this technique could yield a BZY10 powder capable of sintering to high density at lower temperatures than the commercial powder. It should be noted that only one set of experimental parameters was used to produce the powder implemented in this sintering study and that no attempt was made to optimise the technique due to time constraints. Table 4.6 shows the sintered densities achieved using as-prepared and 120 hour milled powders using the following sintering regime;

**Sol-Gel Regime 1**

Heating rate / cooling rate: $5^oCmin^{-1}$

Set temperature: $1500^oC$

Sintering time: 10 hours

The sintered density of the as-prepared powder was found to be a disappointingly low 63.2%TD. Particle coarsening during calcination may be partially responsible and the average particle size was attempted to be reduced by milling the powder for 120 hours. Marginal improvement was observed in the sintered density, with a 3.2%TD increase. Figure 4.33 shows the particle size distributions of the non-milled and milled powders.

| Powder | Sintered Density (%TD) |
|---|---|
| As-Prepared | 63.19 |
| 120 Hour Milled | 66.42 |

Table 4.6: Sintered densities (%TD) of as-prepared and 120 hour milled powders made using a sol-gel technique

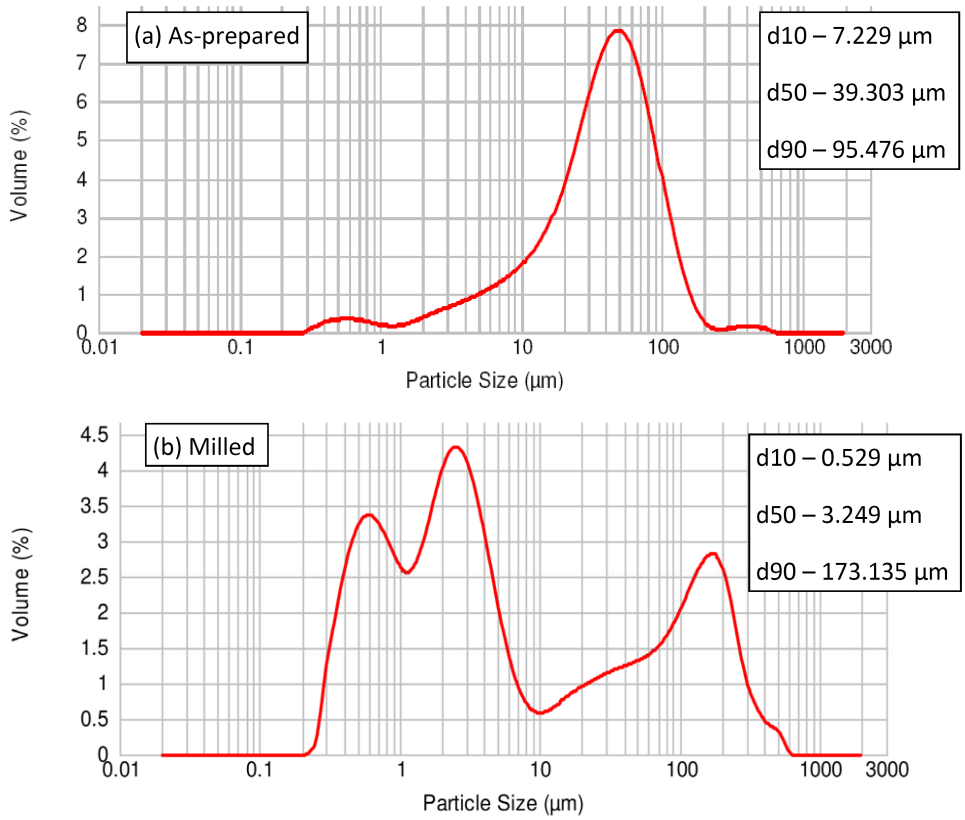



Figure 4.33: Particle size distributions of (a) as-prepared and (b) 120 hour milled powders synthesised using a sol-gel technique

It can be seen that by milling the powder for 120 hours, large particles have been broken down into smaller particles as indicated by a dramatic decrease in d10 and d50 values. This explains the increase in sintered density observed by milling the sol-gel powder. However, also of note is that the d90 value increased by milling the powder for this length of time, indicative that perhaps particle agglomeration had occurred by the milling process. Figure 4.34 is a SEM micrograph of the sol-gel 120 hour milled powder and displays an example of particle plasticisation.

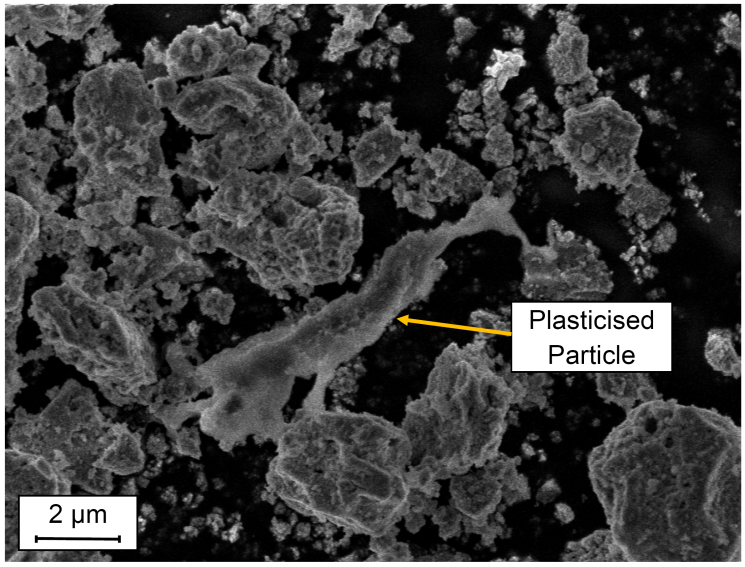



Figure 4.34: SEM micrograph of sol-gel 120 hour milled powder

Particles such as this are likely to have been formed due to excessive milling and do not conform to the ideal spherical morphology for sintering. Hence, improved sintered densities may result from a decreased milling time. Agglomerates of the order of 20-30 $\mu$m were observed but none in the order of >100 $\mu$m. It is possible that plasticised particles, such as that displayed in figure 4.34, skewed the third mode of the particle size distribution towards the larger end due to the assumptions made by the laser diffractometer when analysing the powder. Results from the particle size distribution of the milled powder are therefore thought to be inaccurate based on SEM observations.

Sol-gel sintering regime 1 was modified in an attempt to produce a dense sample for AC Impedance and SOEC-SOFC experiments. Table 4.7 shows the sintered densities achieved using the 120 hour milled powder and various sintering conditions. By increasing the sintering temperature and time, the sintered density increased. However, even when using high temperatures and long sintering times, a sufficiently dense sample for electrochemical testing was not achievable. There is scope for optimisation of the sol-gel synthesis technique as several parameters can be adjusted which may have a significant impact on the particle size and morphology produced and hence, sintering behaviour.

The molar ratio of citric acid to metal ions could be varied which may have an impact on the reaction between precursors as observed by Yang *et al.* [144]. Should the reaction between

| Sintering Temperature ($^o$C) | Sintering Time (hours) | Average Sintered Density (%TD) |
|---|---|---|
| 1600 | 10 | 72.68 |
| 1660 | 10 | 73.19 |
| 1660 | 30 | 77.42 |

Table 4.7: Sintered densities of milled sol-gel synthesised powders using various sintering conditions

precursors be allowed to proceed further at the organics decomposition heating step (625$^o$C) by varying the molar ratio of citric acid to metal ions, or indeed by marginally increasing the temperature, the calcination temperature and time may be reduced, or the calcination step may even be no longer required. Regardless of any variation in this ratio, it may be possible to reduce the calcination temperature and time whilst still synthesising a single phase powder. This would decrease the average particle size and could also affect particle morphology. As we have proved previously in our spray pyrolysis experiments, it is possible to synthesis pure BZY10 from nitrate precursors at 800$^o$C and therefore, there is cause to believe that the calcination temperature could be reduced below 1250$^o$C yet still result in a single phase powder being synthesised.

The molar ratio of citric acid to polyethylene glycol could also be varied. This would have an effect on the organic framework formed and in turn the nucleation and growth of the particles synthesised. Grinding the dried gel whilst still in the form of a porous network, before the organics decomposition step of the synthesis route, could also have a significant impact on the manner in which the reaction occurs and ultimately, on the particle sizes.

## 4.4 Summary

A sintering study was conducted using BCY10 and BZY10 commercial powders. It was found that by sintering milled BCY10 powders 1500$^o$C for 10 hours, sufficiently dense samples for SOEC/SOFC experiments could be manufactured. BZY10 was found to require a 1 wt.% dopant of ZnO in order to achieve similar densities using the same sintering regime.

AC impedance of dense BCY10 and BZY10 samples was conducted. It was found that BCY10 was in close agreement with the reported literature data. Conductivity data reported in the literature for BZY10 was found to be erratic with differing activation energies for conduction quoted. Zn doped samples were found to have conductivities within the bounds of the literature data. However, due to the large variances between these data, the affect of Zn addition on the total conductivity of BZY10 could not be concluded. Under humid conditions, the activation energies for both BCY10 and BZY10 above 400$^o$C, were found to be significantly lower than below 400$^o$C. Therefore, the proton mobilities for these materials were found to be greater above 400$^o$C than below. Also, BCY10 was found to have a conductivity approximately one order of magnitude greater than BZY10 over the entire temperature range studied.

The effects of a Zn dopant in BZY10 on the ionic conductivity were unknown, therefore, it was desirable to find a method of synthesising a pure BZY10 powder capable of sintering to a high density at relatively low temperatures. Spray pyrolysis is an established technique for producing powders with very small particle sizes and hence was a potentially useful method. Various experiments were carried out in order to determine the optimum parameter set. A density of 90.6%TD was found to be achievable using a combination of a high atomising frequency and a low solution concentration. This was in stark contrast to other sets of parameters investigated. It was unclear precisely why such a dramatic increase in final sintered density was found to occur with this parameter set in comparison with others, however, it has been noted in the literature that high atomising frequencies and low solution concentrations can have a significant affect on the particle size distributions achieved. Therefore, smaller, more dense particles beneficial for sintering were achieved using this parameter set in comparison with others.

The sol-gel method of synthesising BZY10 powder was also investigated as an alternative to spray pyrolysis, with the aim of developing a method capable of increased powder yield rates. Average sintered densities above 78%TD were not able to be achieved, even with extreme sintering

conditions. It is probable that the method could have been optimised in order to synthesise powders capable of sintering to higher densities, however, there was insufficient time to conduct such a thorough investigation.

In the following chapter, SOEC and SOFC data collected using BCY10 and Zn-doped BZY10 based cells are presented and discussed.

# Chapter 5

# Electrochemical Characterisation

## 5.1 Preliminary Characterisation of BCY10 Cell Behaviour

Preliminary SOEC/SOFC experiments were carried out over a temperature range of 500-750$^o$C based on literature data on ion transport number [7] and the variation of the electrical energy demand of the electrolysis reaction with temperature. The lower limit of this temperature range was selected to be 500$^o$C because the proton transport number of BCY10 is equal to 1 at and below this temperature. Also, the electrical energy demand for electrolysis decreases with increasing temperature and therefore, it is undesirable to operate at a lower temperature because the cost per unit of hydrogen would increase. Above 750$^o$C, the proton transport number decreases rapidly with temperature and therefore, during any experiments above this temperature, a large contribution from oxygen ion transport would occur. Experiments above 750$^o$C were deemed beyond the scope of this thesis, although the effects of ionic transport being split 50-50 between protons and oxide ions on SOEC/SOFC performance would perhaps yield interesting results.

Open circuit voltage (OCV) is routinely used to determine whether there is a good gas tight seal between the anode and cathode. It was important to determine the OCV values of the cell and compare this with theoretical values. As dictated by the Nernst equation, the OCV value is dependent upon partial pressure differences of gases containing mobile species within the electrolyte and the corresponding ion transport numbers. If there is a leak present, the partial pressure difference will be lowered, directly lowering the OCV. The OCV of the preliminary BCY10 sample and experimental set up was found to vary from 993 to 882 mV between 500

and 750$^o$C respectively. An OCV of 998 mV at 750$^o$C was found by Suksamai and Metcalfe [7] when operating a solid oxide fuel cell incorporating a BCY10 electrolyte with Pt electrodes under similar conditions. The maximum theoretical OCV calculated using the Nernst equation at 750$^o$C was 1110 mV assuming an ionic transport number of 1 [145]. The differences between experimental and theoretical values may therefore be due to excessive electronic conductivity present in the samples. Another possible cause for a lower OCV value is gas leakage originating from either the sample seal or components of the test rig. Also of concern was insufficient delivery of feed gas to the sample and an accurate control of feed gas flow rate, as this could have also effected the results significantly.

Due to the lack of previous work on electrolysers based on BCY10, evaluation of cell performance was carried out by comparison with the literature data for a BCY10 cell operating in fuel cell mode. Suksamai and Metcalfe [7] conducted BCY10 fuel cell testing at 750$^o$C using similar conditions to those used in this work and therefore provided a data set for comparison. Fuel cell data from this work is presented, along with the Suksamai and Metcalfe data, in figure 5.1 in the form of IV curves.

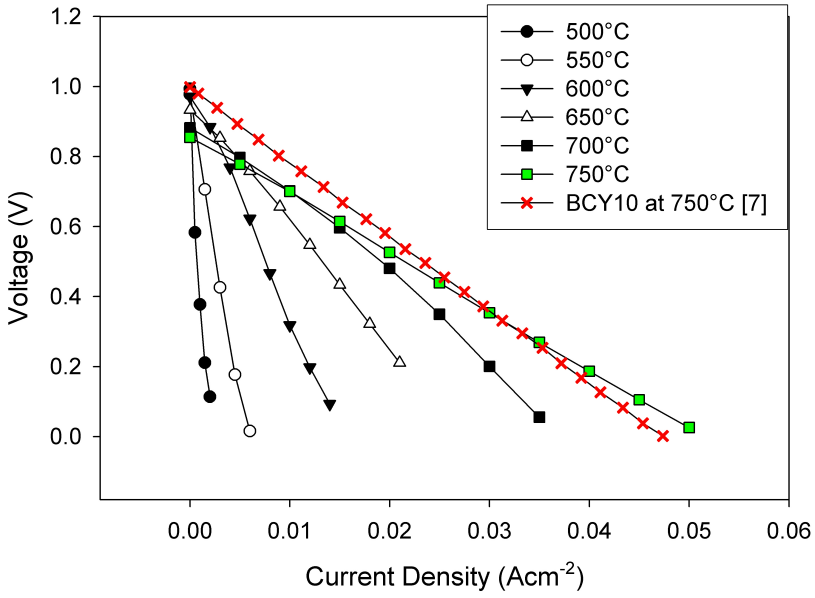



Figure 5.1: Preliminary characterisation of BCY10 cell in fuel cell mode over a range of temperatures and comparison with 750$^o$C data from Suksamai and Metcalfe [7]

Peak power density values provide a useful benchmark for the analysis of the efficiency of a fuel cell. Data presented in figure 5.1 shows that at low current densities, the Suksamai and Metcalfe cell exhibited higher power densities than the preliminary cell (table 5.1). However, the area specific resistance (ASR) value of the Suksamai and Metcalfe cell can be seen to be greater than those found in this work (21.0 $\Omega cm^2$ in comparison to 16.6 $\Omega cm^2$). This meant that above approximately 35 $mAcm^{-2}$, the Suksamai and Metcalfe cell exhibited lower power densities than the preliminary cell. As commented previously, the OCV of the preliminary cell was lower than the maximum theoretical predicted by the Nernst equation. If the OCV was able to be increased, the peak power density value for the preliminary cell should be greater than that reported by Suksamai and Metcalfe. However, it must also be considered that electrolyte thickness influences and is directly proportional to the cell ASR. The cell developed by Suksamai and Metcalfe was approximately 1 mm, whereas the preliminary cell was approximately 450 $\mu$m thick. Therefore, a fair direct comparison of these results cannot be made.

| Temperature ($^o$C) | Peak Power Densities ($mWcm^{-2}$) |
|---|---|
| 500 | 0.4 |
| 550 | 1.3 |
| 600 | 3.8 |
| 650 | 6.5 |
| 700 | 9.5 |
| 750 | 11.0 |
| 750 [7] | 11.7 |

Table 5.1: Peak power densities for a preliminary BCY10 cell and experimental setup over a range of temperatures, including 750$^o$C value from Suksamai and Metcalfe data [7]

Results from the preliminary electrolysis cell measurements are presented in Figure 5.2. At 500, 550 and 600$^o$C, the IV data was non-linear at low applied current densities due to large activation polarisation losses. These losses were attributed to the slow kinetics of reactions at the electrodes and may be reduced by catalysing the electrode reactions. As the temperature of the cell was increased, activation polarisation and ohmic losses of the cell were reduced. However, should the operating temperature be raised to a point were oxide ion conduction dominates, the inherent advantages of a proton conducting SOEC over an oxide ion conducting system would be lost.

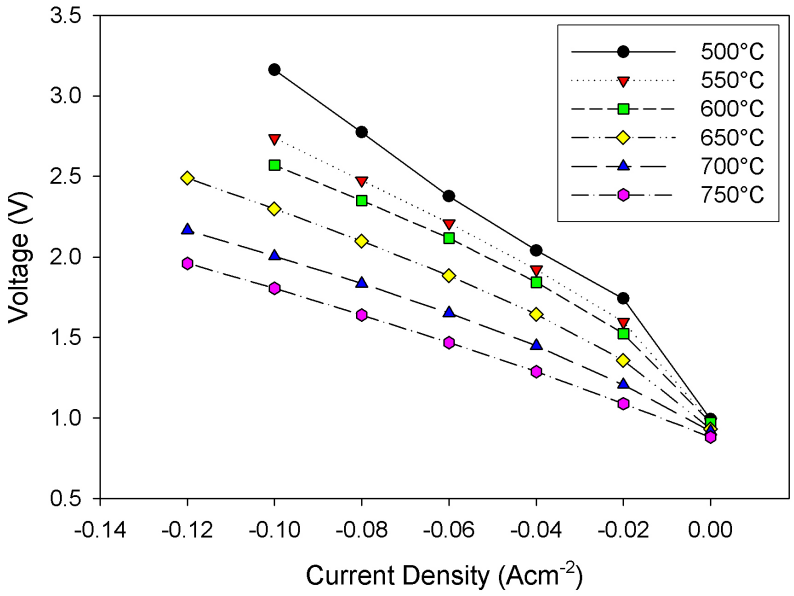



Figure 5.2: Initial characterisation of BCY10 cell in electrolysis cell mode over a range of temperatures

Preliminary experiments discussed in this section were carried out with a sample synthesised using BCY10 sintering regime 1 (section 4.1.2.1) and our original design of test rig. These initial results provided a useful benchmark. Also, this cell test was able to be carried out over a longer time period than any subsequent samples. Therefore, this sample provided information on BCY10 stability under these operating conditions. Further electrochemical data and post test microstructural analysis of this sample will be discussed in detail in the following chapter.

## 5.2 Cell Characterisation Using Developed Cell, Test Rig and Apparatus

Some minor deficiencies were found to be present in the original test design as discussed in section 3.7. All further experiments were conducted using the modified test rig design with additional apparatus. Also, all of the following cells tests were made using electrolyte samples sintered using BCY10 regime 2 and were ≈1 mm in thickness. A cell test was carried out under as similar conditions as possible to the previous test to ascertain any differences caused by making the test rig and sintering alterations as described in sections 3.7 and 4.1.2.1. However, it was concluded that potentiostatic measurements were more suitable than galvanostatic because

it was more desirable to control the voltage range that testing was carried out over. Each of these measurement techniques resulted in identical current values for given voltage values and therefore did not effect the performance observed. By controlling the voltage range, it was easier to control the degree to which the electrolysis reaction was driven. Cell tests at 500$^o$C were not carried out as cell performance at this temperature was deemed to be insufficient in the preliminary testing for further consideration. The results are presented in figures 5.3 and 5.4.

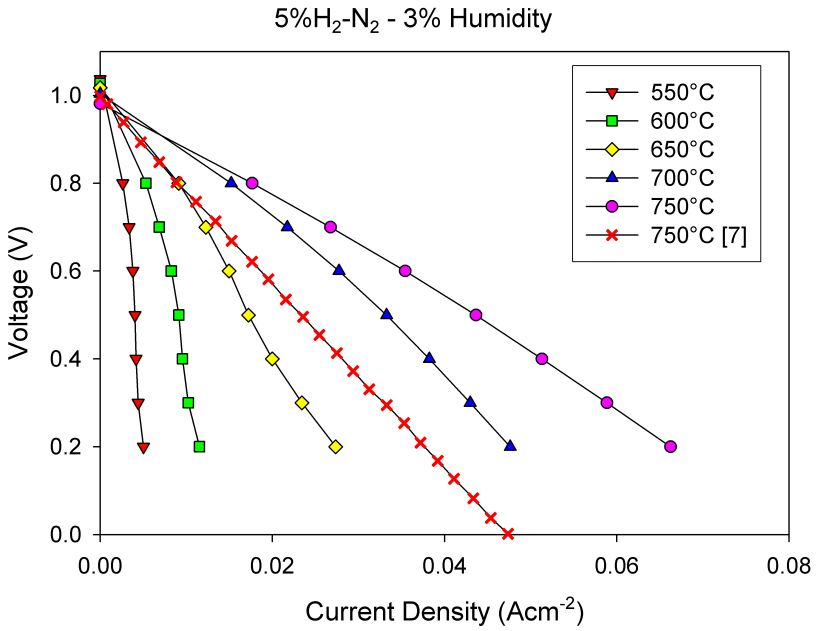



Figure 5.3: Characterisation of developed BCY10 system in fuel cell mode over a range of temperatures. Suksamai and Metcalfe data plotted for comparative purposes [7].

Peak power density values in fuel cell mode were found to be significantly higher than those achieved in the initial system. The peak power density at 750$^o$C was found to be almost double that achieved by Suksamai and Metcalfe under similar conditions. This comparison is fairer than with the preliminary cell since the thicknesses of the electrolytes were both ≈1 mm. Increased OCV values on the preliminary experiments were attributed to improvement in the seal achieved between the cathode and anode compartments and in the delivery of the feed gas to the sample. This aided the increase of peak power density values, but primarily, a reduction of ASR was accountable.

| Temperature ($^o$C) | Peak Power Densities (mWcm$^{-2}$) |
|---|---|
| 550 | 2.4 |
| 600 | 5.0 |
| 650 | 9.0 |
| 700 | 16.8 |
| 750 | 21.9 |
| 750 [7] | 11.7 |

Table 5.2: Peak power densities for developed BCY10 cell and experimental setup over a range of temperatures, including 750$^o$C value from Suksamai and Metcalfe data [7]

The electrolysis IV curves measured using the developed cell and test rig are shown in figure 5.4. Significant activation polarisation losses at lower temperatures were again observed as with the preliminary sample, although the IV gradients at low applied voltages were less than that observed previously. This could be a reflection of the improved supply of feed gas to the sample surface, but could also be due to improved adhesion or catalytic activity of the electrode.

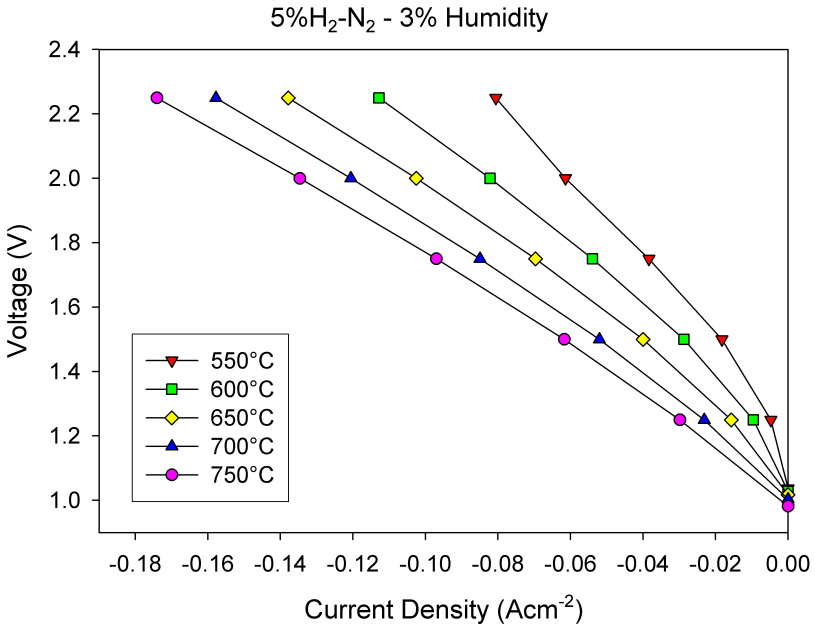



Figure 5.4: Characterisation of developed BCY10 system in electrolysis mode over a range of temperatures

In SOEC modes, at 600$^o$C, the ASR of the developed system was 5.3 $\Omega$cm$^2$ in comparison to 11.3 $\Omega$cm$^2$ for the preliminary system. This result indicates a marked improvement in cell performance, especially when it is considered that the electrolyte in the preliminary cell was less than half the thickness of the developed cell. Improved supply of gas may have been a

contributing factor, however, the contact resistance of the electrodes and the conductivity of the electrolyte may have also improved and contributed to the observed reduction of ASR. Indeed, BCY10 samples sintered using regime 1 (section 4.1.2.1) were found to have lower conductivities than those sintered using regime 2 and this would have contributed towards the disparity between the preliminary and developed cell performances.

An interesting finding when comparing fuel cell and electrolyser operation is that ASR values were lower in electrolysis mode than fuel cell mode at all temperatures. Since sample and atmospheric conditions were identical, the cause for the difference in ASR may be that an application of current to the cell caused electronic conductivity to be promoted in the electrolyte due to the reduction of cerium.

## 5.3 Effect of Increasing $H_2$ Concentration

### 5.3.1 Fuel Cell Mode

Cell data reported previously in this chapter had a 5% hydrogen by flow rate so that cell performance could be compared with the literature. In an attempt to better simulate actual fuel cell operating conditions, the anode was supplied with an increased hydrogen concentration of 66%. Fuel cell data for these conditions are presented in figure 5.5 and peak power density values are presented in table 5.3.

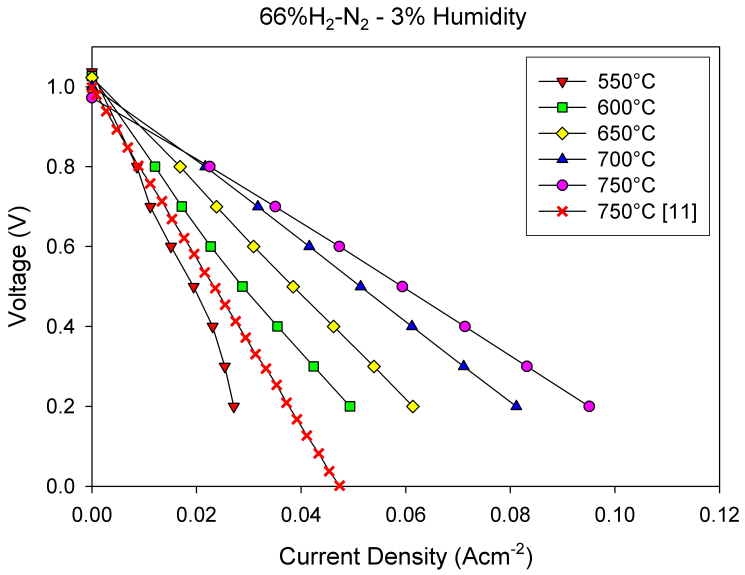



Figure 5.5: Fuel cell data collected using an anode atmosphere with elevated $H_2$ concentration and comparison with 750$^o$C data from Suksamai and Metcalfe [7]

| Temperature ($^o$C) | Peak Power Density 5% $H_2$ (mWcm$^{-2}$) | Peak Power Density 66% $H_2$ (mWcm$^{-2}$) | % Difference |
|---|---|---|---|
| 550 | 2.4 | 9.7 | +304 |
| 600 | 5.0 | 14.5 | +190 |
| 650 | 9.0 | 19.3 | +114 |
| 700 | 16.8 | 25.7 | +53 |
| 750 | 21.9 | 29.7 | +36 |
| 750 [7] | 11.7 | N/A | N/A |

Table 5.3: Comparison of peak power densities over a range of temperatures for 5% and 66% $H_2$ concentration (by flow rate) in the supplied gas feed

By comparing fuel cell data sets using differing $H_2$ concentrations, collected across a range of temperatures where the oxygen ion transport number varied, speculations on the mechanisms of fuel cell operation may be made. Peak power density values were found to be greater when using 66% $H_2$ in the gas supply feed than 5% as shown in table 5.3. The % difference between the peak power density values for 5% and 66% $H_2$ are also shown in table 5.3. % difference values decreased with increasing temperature, suggesting that oxide ion conduction did not benefit the fuel cell operation. By increasing the hydrogen concentration in the gas supply, the peak power density was more than quadrupled at 550$^o$C, whereas at 750$^o$C, the value was only 1.3 times higher using the higher hydrogen concentration. Possible electrode reactions are complicated by the introduction of hydrogen to the cell, rather than simply using an inert carrier gas to supply

moisture. In theory, an increase in $H_2$ concentration allowed the following reaction to occur with greater frequency;

$$H_2 + 2O_o^x \rightarrow 2OH_o^{\bullet} + 2e' \tag{5.1}$$

Literature data suggests that above 550$^o$C the following equation 5.2 will perhaps occur simultaneously with reaction 5.1 [7];

$$H_2 + O_o^x \rightarrow H_2O + V_o^{\bullet\bullet} + 2e' \tag{5.2}$$

With increasing temperature above 550$^o$C, reaction 5.2 may have become more significant due to the emergence of oxygen ion transport and competed with reaction 5.1. As a result, the electrode reactions may have been disrupted, increasing the ASR of the cell and reducing peak power density. Another explanation for this behaviour could be that a limit in the anode/electrolyte catalysis of reaction 5.1 was reached, so that an increase in hydrogen concentration was not able to improve the peak power density at 750$^o$C as it was at 550$^o$C. Such a scenario could occur if there was insufficient proton conduction away from the anode-electrolyte interface so that the concentration of available filled oxygen ion sites was lowered. This would be reflected in the ASR values, shown in table 5.3.2, which correlate with this theory. However, the cause for the observed behaviour cannot be stated with any degree of certainty and further experiments are required to firmly determine the mechanisms of fuel cell operation in mixed ion conducting cells.

| Temperature ($^o$C) | 5% $H_2$ ASR ($\Omega.cm^2$) | 66% $H_2$ ASR ($\Omega.cm^2$) | % Difference |
|---|---|---|---|
| 550 | 250.7 | 32.4 | -674 |
| 600 | 96.8 | 16.1 | -501 |
| 650 | 32.9 | 13.5 | -144 |
| 700 | 18.5 | 10.1 | -84 |
| 750 | 8.8 | 8.3 | -6 |

Table 5.4: ASR values for 5% and 66% $H_2$ concentrations measured in fuel cell mode over a range of temperatures and the % difference between values

### 5.3.2 Electrolysis Mode

Electrolysis data was collected with an elevated concentration of $H_2$ in the gas supply (see figure 5.6). As with the comparison of fuel cell mode data, observing differences in electrolysis data when using differing $H_2$ gas concentrations may be enlightening. ASR values for 5% and 66% $H_2$ (by supplied gas flow rate) over a range of temperatures are displayed in table 5.3.2, with % difference between these ASR values also stated.

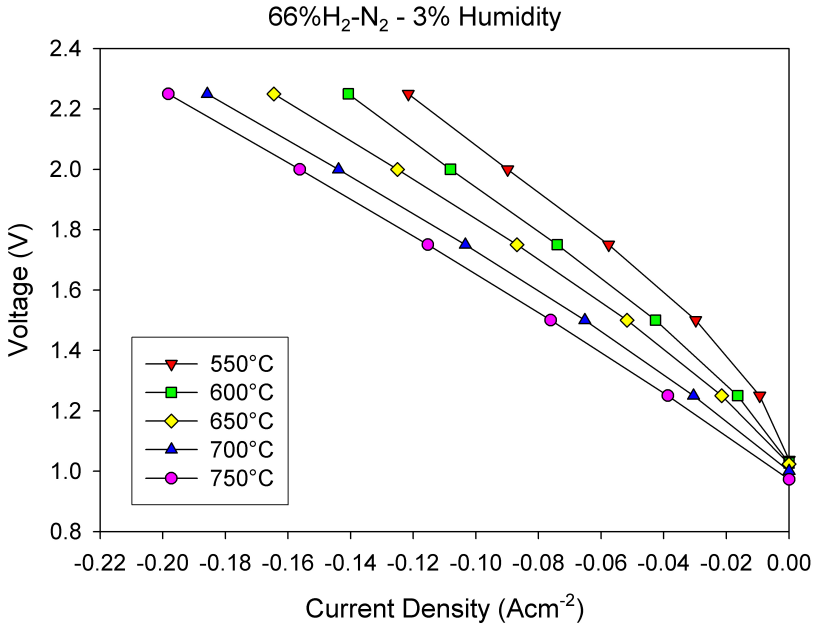



Figure 5.6: Electrolysis Data Collected using an Anode Atmosphere with Elevated $H_2$ Concentration

| Temperature ($^oC$) | 5% $H_2$ ASR ($\Omega.cm^2$) | 66% $H_2$ ASR ($\Omega.cm^2$) | % Difference |
|---|---|---|---|
| 550 | 7.59 | 4.95 | -46 |
| 600 | 5.30 | 4.09 | -29 |
| 650 | 4.22 | 3.47 | -21 |
| 700 | 3.57 | 2.99 | -19 |
| 750 | 3.32 | 2.73 | -19 |

Table 5.5: ASR values for 5% and 66% $H_2$ concentrations measured in electrolysis mode over a range of temperatures and the % difference between values

ASR values were found to be lower when a higher flow rate of $H_2$ was used. It is probable that $H_2$ molecules were preferentially absorbed and reacted with filled oxygen ion sites over $H_2O$ molecules. Reaction 5.1 is therefore likely to have occurred with a greater frequency when a

higher $H_2$ flow rate was used. Under these circumstances, the production of protonic defects did not require oxygen ion vacancies and therefore their concentration in the electrolyte would have improved, causing a reduction in ASR. As can be seen in the % difference values in table , ASR was most improved by the increase in $H_2$ concentration when ionic conduction was purely protonic. It is possible that with increasing oxide ion conduction, reaction 5.2 occurred more frequently than 5.1. Since reaction 5.2 does not result in the formation of $H_2O$ and not protonic defects, this would have caused a greater ASR to be observed. There is a need for measurement of gases produced and the implementation other analysis techniques in order to gain further insight into the mechanisms behind the operation of proton or mixed ion conducting solid oxide electrolysers due to electrode reaction complexities.

## 5.4 Effect of Increasing the Humidity in Supplied Gas Feed

An increased steam concentration was supplied to the anode compartment to deduce the effects on hydrogen production. Electrolysis data measured over a range of temperatures, using a supply gas consisting of 5% $H_2$ balanced with $N_2$, humidified to approximately 83%, is displayed in figure 5.7. Experiments below $600^oC$ were not conducted because cell losses in previous experiments were deemed too great at lower temperatures. ASR values for cells using ≈3% and ≈83% humidity levels are displayed in table 5.6 along with the % difference between the values obtained for each cell. Below $700^oC$, the ASR value was higher when using the greater humidity, but above $700^oC$, the ASR was found to be lower when using the greater humidity. In other words, the ASR of the cell decreased with increasing temperature more rapidly with greater humidity levels in the anode compartment.

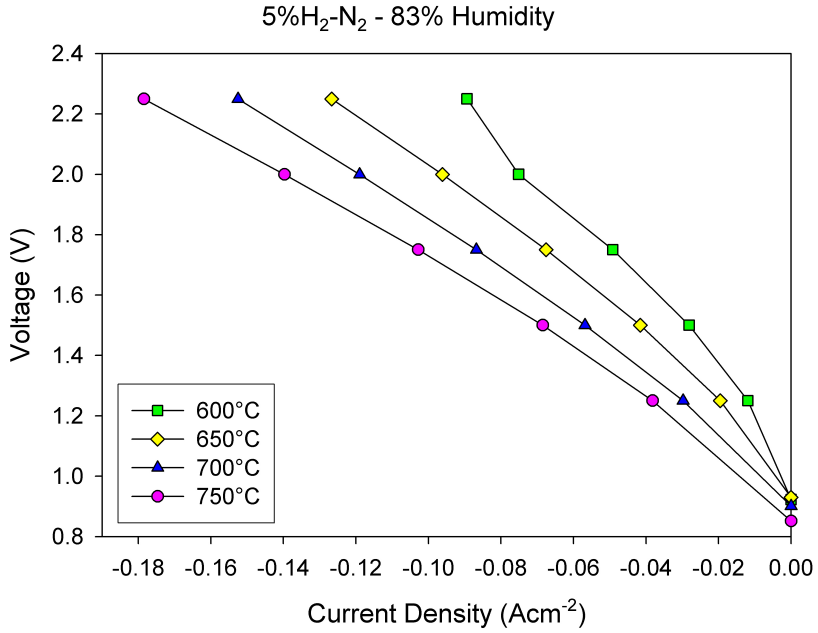



Figure 5.7: Electrolysis data collected using a gas feed of 5%$H_2$-$N_2$, with ≈83% humidity over a range of temperatures

| Temperature ($^o$C) | ≈3% Humidity ASR ($\Omega.cm^2$) | ≈83% Humidity ASR ($\Omega.cm^2$) | % Difference in ASR |
|---|---|---|---|
| 550 | 7.59 | X | X |
| 600 | 5.30 | 6.38 | +20 |
| 650 | 4.22 | 4.45 | +6 |
| 700 | 3.57 | 3.58 | +0 |
| 750 | 3.32 | 3.04 | -9 |

Table 5.6: ASR values for ≈3% and ≈83% humidified 5%$H_2$-$N_2$ measured in electrolysis mode over a range of temperatures and the % difference between values

Figure 5.8 shows the change in current density measured at 2 V with temperature. Below 700$^o$C the current density measured at 2V was lower when using the greater humidity. This suggests that the reactions involving the dissociation of water or the formation of protonic defects (or both) is/are the rate limiting step/s and that an increased amount of energy is required to satisfy the activation energy of one or more of the electrochemical reactions involved. The development of anode materials that can catalyse these reactions and lower the activation polarisation is critical for the production of a competitive hydrogen production system. An alternative explanation is that there could be advantages to operating the device at temperatures where mixed ionic conduction occurs. Oxide ion conduction might facilitate the operation of a proton conducting electrolyser by enabling the mobility of oxide ion vacancies so that protonic

defects may be formed with greater frequency. Indeed, the presence of oxygen ion vacancies has been proven to be essential for the formation of protonic defects in proton conducting oxides [9]. The influence of substantial oxide ion conduction on proton conductivity and protonic defect formation would be an intriguing subject of further investigation.

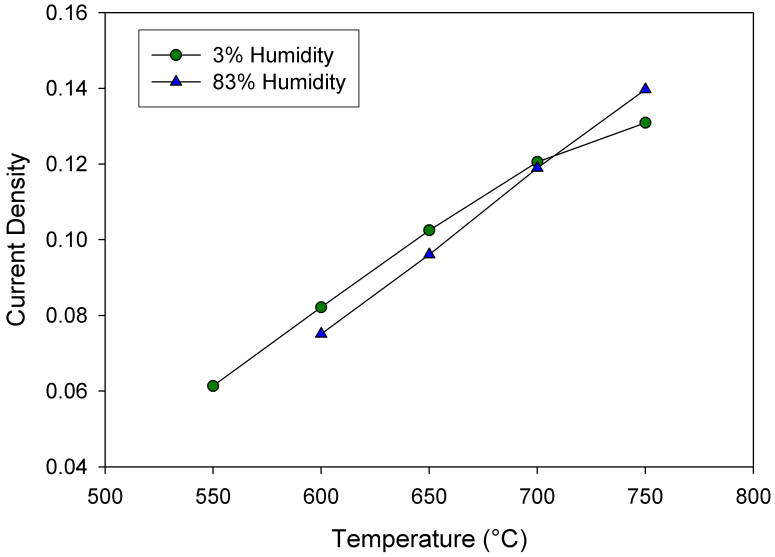



Figure 5.8: Change in current density measured at 2 V applied with temperature, comparing data collected using either ≈3% or ≈83% humidity in the anode compartment.

## 5.5 Effect of Operating without $H_2$ in the Gas Feed

The effect of using a nominally dry supply of 100% $N_2$ was investigated and the results compared with those measured using a gas supply of 100% $N_2$ humidified to ≈83%. Potentiodynamic data is presented because the IV curves obtained during this section of study were more complex. It was useful for potentiodynamic data to be analysed in order to discern the differences between wet and dry conditions since subtleties in IV curves obtained potentiodynamically are more observable than with potentiostatic data with sparse data points. Potentiostatic measurements were carried out to verify the validity of potentiodynamic data at various voltages and under various conditions and, in general, it was found that values were in close agreement with potentiodynamic measurements. This is not all together surprising as during the sweep, the system should be able to reach near steady state operation.

Figures 5.9, 5.10 and 5.11 compare electrolysis data collected in wet and dry conditions at 500, 600 and 750$^o$C respectively. These data were collected using a potentiodynamic sweep from

close to the OCV value and up to an applied voltage of 2.5 V.

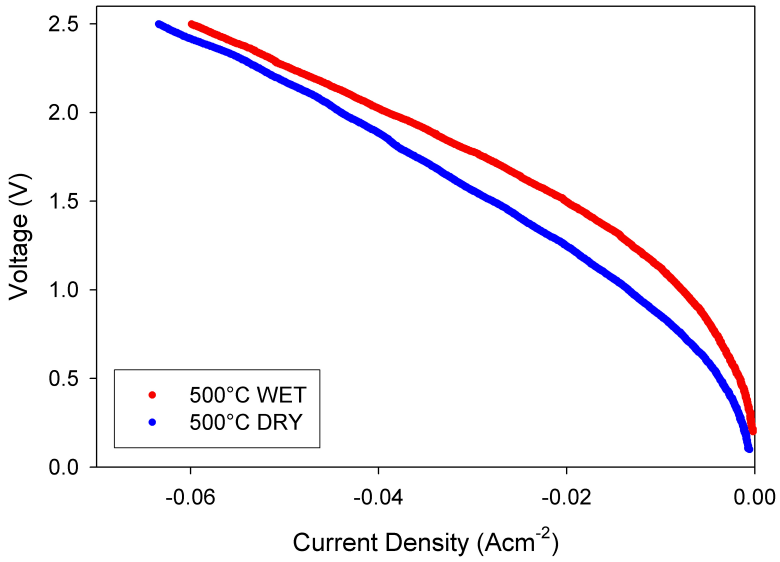



Figure 5.9: Potentiodynamic measurements made at 500$^o$C using a 100% $N_2$ gas supply that was either nominally dry or humidified to ≈83%

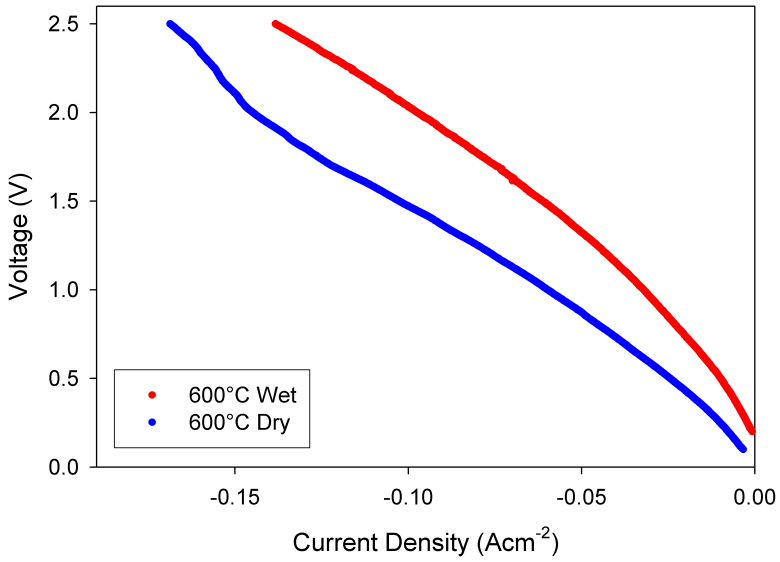



Figure 5.10: Potentiodynamic measurements made at 600$^o$C using a 100% $N_2$ gas supply that was either nominally dry or humidified to ≈83%

At 500$^o$C and 600$^o$C, current density values at a given voltage were greater using dry conditions than using wet conditions across the whole range of voltage values. Clearly, since there is no source of protons to conduct across the electrolyte, hydrogen cannot be produced in dry conditions. A possible explanation for the behaviour exhibited in figures 5.9 and 5.10, is that

cerium in the electrolyte reduced from 4+ to 3+ resulting in the following;

$$Ce_{Ce}^{x} + O_{o}^{x} \rightarrow Ce_{Ce}^{'} + e^{'} + V_{o}^{\bullet\bullet} + \frac{1}{2}O_2 \tag{5.3}$$

Should cerium reduce, electron holes are formed as the charge neutrality condition must be satisfied. An introduction of electronic conductivity in the electrolyte invalidates any assumption that all the current measured was as a result of $H_2$ production processes. Differences in current density values measured at a given voltage between wet and dry data at 500 and 600$^o$C were therefore, probably due to the a significant amount of electronic conduction [67,87]. Lower activation energies for reactions involving purely electronic species in comparison to the electrolysis reaction is thought to be the cause of the differences observed between wet and dry data at these temperatures. Also, ASR values at 500$^o$C were lower when using wet conditions than dry, whereas at 600$^o$C, ASR values were higher when using wet conditions than dry. Additional protonic conductivity, coupled with less electron hole formation at lower temperatures, are potential causes for this difference.

IV curves obtained using the same conditions as for 500$^o$C and 600$^o$C were found to be considerably different to those obtained at 750$^o$C, as shown in figure 5.11. From near OCV to around 0.6 V, similar linear sections are observed in the IV curves of both wet and dry conditions. Such sections were not observed in the IV curves obtained at 500 and 600$^o$C and the cause for this behaviour is unknown. Slower kinetics at lower temperatures may have contributed, however, above 0.6 V the wet and dry data sets began to differ significantly. Under wet conditions, an increase in the IV curve gradient was observed above 0.6 V, thought to be due to the onset of activation polarisation. This increased gradient was maintained until a voltage of around 1.4 V was applied. Above this voltage, the ohmic losses dominated as activation polarisation losses began to increase by negligible amounts with increasing current density. Therefore, above 1.4 V, additional losses were attributed to the resistance of the cell. No concentration polarisation was observed, indicating that steam utilisation was below 100%. Data presented in section 5.4 for the sample operated at 750$^o$C using an atmosphere of 5%$H_2$-$N_2$ humidified to ≈83% does not show such a marked IV gradient difference between the activation polarisation and ohmic loss regions. This resulted in current density values at any given voltage applied being lower when $H_2$ was supplied to the anode compartment than when simply humidified nitrogen. Therefore,

the delivery of $H_2$ to the anode compartment may have disturbed the electrolysis reaction when using high levels of humidity.

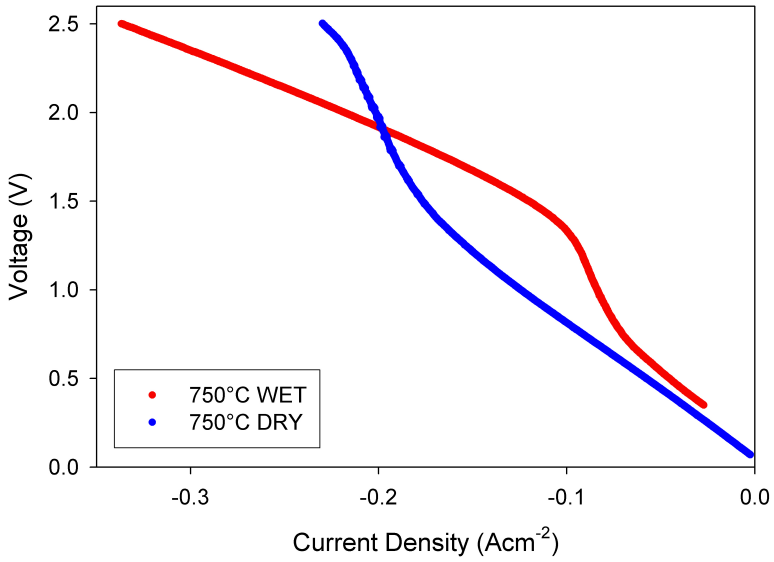



Figure 5.11: Potentiodynamic measurements made at 750$^o$C using a 100% $N_2$ gas supply that was either nominally dry or humidified to ≈83%

Under dry conditions, due to the absence of steam, current density continued to increase linearly with voltage at 0.6 V. At around an applied voltage of 1.5 V, the IV curve gradient became steeper indicating the onset of an electrochemical reaction at this voltage. This may have been due to the instigation of a reaction between oxygen ions, transported from the cathode through the electrolyte to the anode, and nitrogen, to form $NO_x$ gases by the application of a voltage above 1.5 V. At lower temperatures, such behaviour may not have been observed due to insufficient oxygen ion conductivity. However, quantitative gas analysis is required in order to ascertain whether such a reaction occurs under these conditions.

## 5.6 Cell Kinetics

Instantly reversing the voltage change direction during potentiodynamic measurements gave further insight into the cell reaction dynamics. Electrolysis data collected using cyclic potentiodynamic measurements are displayed in figures 5.12 and 5.13, collected at 500 and 600$^o$C respectively using a $N_2$ supply humidified to 83%.

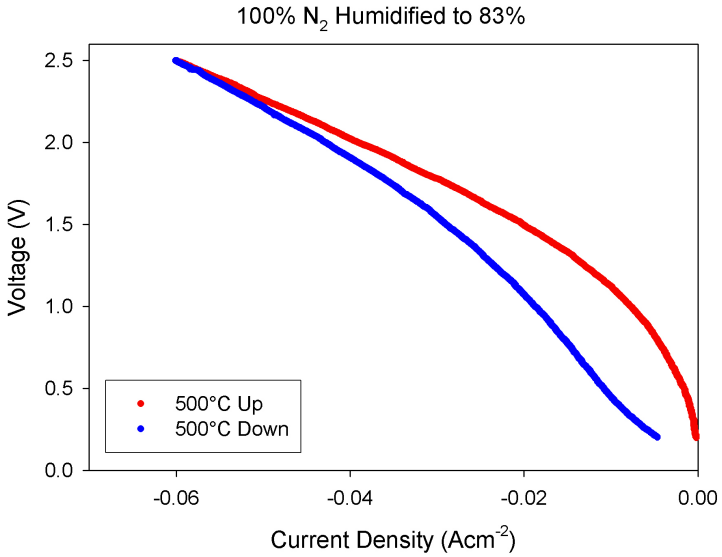



Figure 5.12: Potentiodynamic measurements made using a 100% $N_2$ gas supply humidified to ≈83% at 500$^o$C. Red symbols are data collected with increasing voltage and blue symbols are data collected with decreasing voltage.

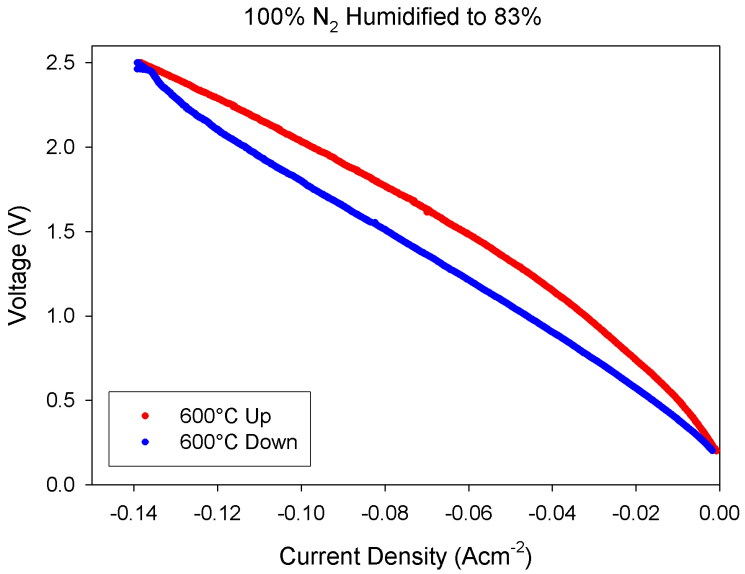



Figure 5.13: Potentiodynamic measurements made using a 100% $N_2$ gas supply humidified to ≈83% at 600$^o$C. Red symbols are data collected with increasing voltage and blue symbols are data collected with decreasing voltage.

It was discovered that when potentiodynamic sweeps were carried out from OCV to 2.5 V and then 2.5 V to OCV immediately afterwards at 500 and 600$^o$C, greater current density values at a given voltage were observed. This was possibly caused by Joule heating. The endothermic nature of electrolysis is counteracted sufficiently for the temperature of the cell to increase when

a voltage above the thermoneutral value is applied to the cell [146] and at 750$^o$C, this value is approximately 1.4 V. Slow kinetics of protonic defect transport and hydrogen evolution may have also contributed towards the observed behaviour. As the voltage increased, protonic defects were created within the electrolyte by the dissociation of water. On measurement with decreasing voltage, a residual concentration of protonic defects may have been present due to the device having been recently operated at a higher voltage. A sweep rate of 3 mVs$^{-1}$ over a voltage range of approximately 2.3 V means that one sweep took around 13 minutes. Over this timescale, the diffusion rate of protons across the cell may have been insufficient for protonic defects, formed at higher applied voltage, to reach the cathode and take part in the hydrogen evolution reaction. A reduction in sweep rate would therefore probably cause the difference between data collected on rising voltage and decreasing voltage to decrease. A final possibility is that an increase in the activation of the electrodes may have taken place when current was passed through the cell. This could have also contributed towards the disparity between the 'up' and 'down' data sets due to improved reaction kinetics.

Minimal differences were observed between potentiodynamic data collected on increasing and decreasing voltage cycles at 750$^o$C (see figure 5.14). In order to investigate why there is so little difference in comparison to experiments at lower temperatures, OCV measurements were taken immediately after potentiostatic measurements using an applied voltage of 2.25 V at 500 and 750$^o$C. It was found that OCV values took almost an hour to return to the original value and stabilise at 500$^o$C, whereas at 750$^o$C, OCV stabilisation was achieved within 1 to 2 minutes. Slow reaction rates are therefore likely to have contributed to the behaviour observed at 500$^o$C and 600$^o$C in the potentiodynamic cycling measurements. It is unclear in what proportions an increase in reaction rates, total ionic conductivity, or specifically oxygen ion conductivity contributed towards the reduction in 'up' and 'down' data differences and increased rate of OCV stabilisation at higher temperatures. However, electrodes are likely to have been better activated at this higher temperature resulting in an improvement in reaction kinetics.

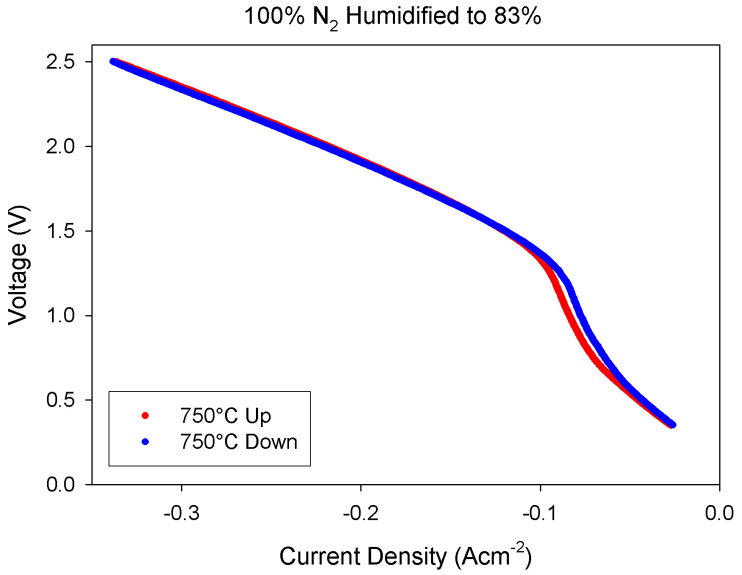



Figure 5.14: Potentiodynamic measurements made using a 100% $N_2$ gas supply humidified to ≈83% at 750$^o$C. Red symbols are data collected with increasing voltage and blue symbols are data collected with decreasing voltage.

## 5.7 BZY10 Cell

SOEC and SOFC experiments using Zn-doped BZY10 cells were carried out using the same test rig as that used for the BCY10 cells. However, when these cells were attempted to be sealed onto the zirconia tube, cells cracked due to a mismatch in the coefficient of thermal expansion between BZY10 and the zirconia tube (see table 5.7). It was possible to adapt the test rig to incorporate an alumina tube instead of a zirconia tube. This, as well as replacing the glass sealant used previously with an 'AREMCO ceramabond 503-T' sealant, successfully enabled the testing of Zn-doped BZY10 cells. the thermal expansion coefficient of alumina is much closer in value to BZY10 than zirconia (table 5.7) and therefore, this component substitution helped to solve the sealing issues that were initially experienced.

| **Material** | **TEC ($10^{-6}$ $K^{-1}$)** | **Reference** |
|---|---|---|
| $BaZrO_3$ (300-1000$^o$C) | 7.13 | [147] |
| YSZ | 10.5 | [148] |
| $BaCeO_3$ (300-1000$^o$C | 10.2 | [147] |
| Alumina | 6 - 8 | [149] |

Table 5.7: Comparison of thermal expansion coefficients (TECs) of candidate electrolyte and test rig tube materials

Zn doped BZY10 cells were tested in fuel cell (figure 5.15) and electrolysis cell (figure 5.16) modes at 750$^o$C. For each of these experiments, 10% $H_2$ balanced with $N_2$, humidified to ≈3%, was supplied to the anode. BCY10 data collected under similar conditions is also presented in figures 5.15 and 5.16.

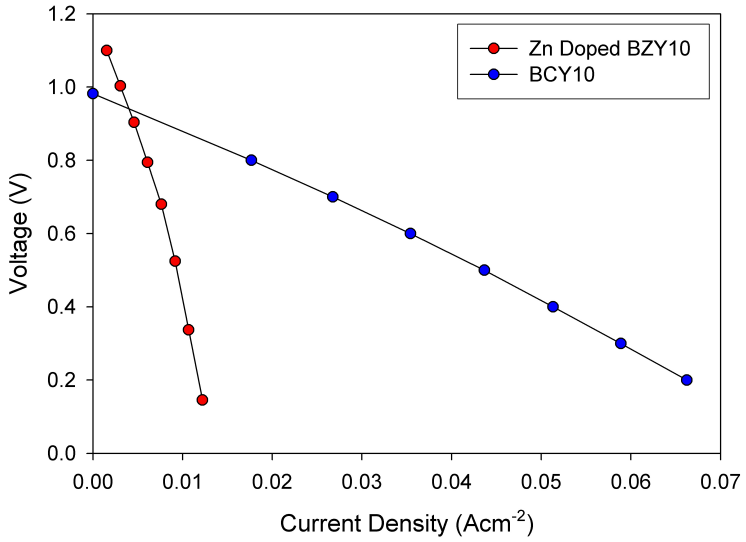



Figure 5.15: Zn doped BZY10 fuel cell data, collected using a gas feed of 10%$H_2$-$N_2$, with ≈3% humidity at 750$^o$C

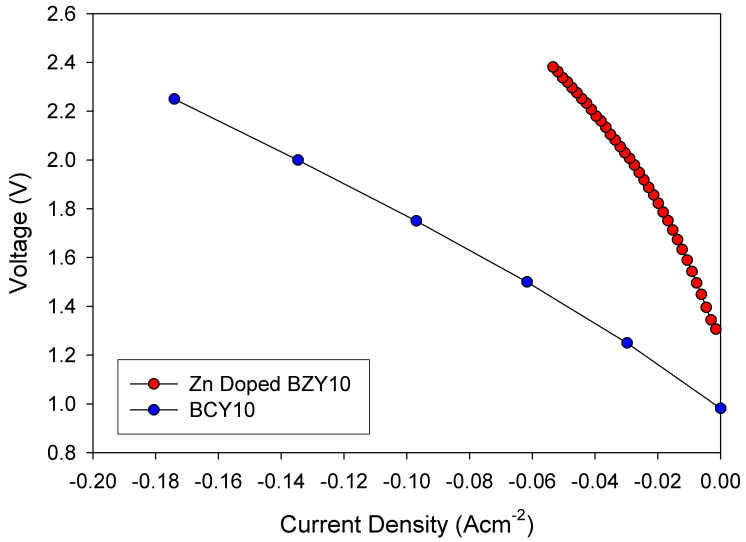



Figure 5.16: Zn doped BZY10 electrolysis cell data, collected using a gas feed of 10%$H_2$-$N_2$, with ≈3% humidity at 750$^o$C

Clearly, the cell losses of BCY10 cells were much lower than for the BZY10 cell. This finding is a reflection of the results presented in the previous chapter that show the conductivity of BCY10 to be greater than Zn doped BZY10. Based on these data, BCY10 would be selected over the Zn doped BZY10 for as an SOEC/SOFC electrolyte, although the chemical stability of BCY10 must also be considered.

OCV values were found to be greater for the Zn doped BZY10 experiments than the BCY10 experiments (1.1 V in comparison to 1.0 V) and were influenced by the slight difference in $H_2$ concentration used. However, the OCV disparity could also be indicative of a difference between the two material's ionic transport numbers. Indeed, this result suggests that either an improved seal was achieved with the BZY10 experimental setup, or that a significant electronic contribution to the the total conductivity existed in the BCY10 samples. These data also suggest that the introduction of Zn to BZY10 did not cause an increase in the electronic contribution to the total conductivity, as previously thought possible.

Cell losses were found to be much lower in electrolysis mode than in fuel cell mode for both BCY10 and Zn doped BZY10. Therefore, these cells are inherently more suitable as electrolysers than fuel cells. Implementation of oxide or cermet electrodes could increase or decrease this bias towards electrolysis mode, however, it may be possible to find electrode materials that allow for an improvement in both modes of operation to be made.

## 5.8 Summary

Results from steam electrolysis experiments using proton conducting solid oxide cells were presented and discussed. IV curves showing the behaviour of solid oxide proton conducting electrolysis cells over a range of temperatures and conditions had not been previously reported in the literature. Preliminary results were improved by developing a test rig, apparatus set up and electrolyte capable of achieving higher power densities in fuel cell mode and lower ASR values in both SOEC and SOFC modes. Furthermore, activation polarisation losses were also reduced. Hydrogen concentration in the anode compartment was found to have significant effects on the electrochemical behaviour of the cell. By using an elevated hydrogen concentration, power densities in fuel cell mode were increased and this effect was more pronounced at lower temperatures. It was reasoned that this behaviour was caused by an increase in oxide ion conduction

in the electrolyte with increasing temperature. A reaction of oxide ions with the additional hydrogen at the anode may have formed steam and competed with the formation of protonic defects, decreasing potential peak power densities at higher temperatures. ASR values were found to decrease in electrolysis mode when a higher concentration of $H_2$ was used, however, it was concluded that further experiments involving the direct measurement of gases were required in order to make substantiated claims on the mechanisms of operation of a proton conducting SOEC device. Although, experiments conducted without $H_2$ supplied to the anode supported the theory that $H_2$ is detrimental to SOEC operation. When the effect of varying humidity was investigated, it was found that oxide ion conduction may be beneficial to the operation of a proton or mixed ion conducting SOEC. When a gas supply of nominally dry 100% $N_2$ was supplied to the anode, it was discovered that it was probable cerium had reduced in the electrolyte and significant electronic conduction had been introduced.

Potentiodynamic measurement cycles were carried out when using an anode supply gas of 100% $N_2$ humidified to ≈83% and a significant system lag was detected at 500 and 600$^o$C. An increasing voltage potentiodynamic measurement was carried out up to an applied voltage of 2.5 V before immediately reversing the direction of the sweep. The current density measured at a given voltage was higher on the decreasing voltage sweep than on the intitial sweep. The effect was less pronounced at 600$^o$C than at 500$^o$C and at 750$^o$C this behaviour was barely observed at all. OCV measurements were made immediately after a potentiostatic measurement at 2.25 V to investigate further. At 500$^o$C, the OCV measurement took almost an hour to stabilise and reach the original value. This is indicative of very slow kinetics of the cell at this temperature and is likely to have contributed towards the potentiodynamic cycling behaviour observed at 500$^o$C and 600$^o$C. A further contributory factor may be that the electrodes were activated at higher voltages so that reaction kinetics were artificially improved on decreasing voltage.

Electrochemical measurements of a ZnO doped BZY10 cell were able to be made by adapting the developed test rig. Mis-matches in thermal expansion coefficients between the cell and the test rig were thought to be responsible for initial cell cracking during sealing. Measurements were enabled by replacing the zirconia tube in the test rig with an alumina tube which matches the coefficient of thermal expansion of BZY10 better than zirconia. BCY10 cell losses were found to be much lower in both SOEC and SOFC modes of operation at 750$^o$C. Based on this

data alone, the Zn-doped material is not conductive enough to compete with BCY10. However, as will be discussed in the following chapter, the durability of BCY10 is questionable.

The following chapter focuses on analysing the microstructure of cells after SOEC/SOFC testing and comments on their degradation and durability under various conditions.

# Chapter 6

# Post-Test Analysis of the Microstructure and Composition of Cells

## 6.1 Introduction

By applying or drawing a current to or from a cell, it is possible for undesirable permanent alterations to occur to the cell microstructure and composition. Durability targets for SOEC/SOFCs are usually in the thousands of hours. Such long term testing was not possible due to the time constraints for this work. However, some signs of alteration in electrochemical behaviour over time were observed during SOEC/SOFC testing. Electrochemical results, together with microstructural and compositional analysis, are reported in this chapter. Such data is currently not present in the literature and may prove to be important in the assessment of the potential of proton conducting SOECs. Information on the status of the cells after operation may assist in the estimation of expected cell lifetime and in the elucidation of the micro-mechanics behind cell operation. When considering the development of a reversible SOEC, the cell must be resistant to degradation caused by switching from SOEC mode to SOFC mode and vice versa. In this work, some cells have been switched between modes and others have only been operated in SOEC mode.

## 6.2 Analysis of Cells with Anodes Exposed to 5% $H_2$ Humidified to ≈3%

The preliminary cell was exposed to laboratory air at the cathode and 5%$H_2$ balanced with argon, humidified to ≈3%, at the anode. Electrochemical data for this sample was reported in the previous chapter and was displayed in figures 5.1 and 5.2. The cell had first undergone SOFC testing followed by SOEC testing before changing temperature, over a period of 20 days. Therefore, this cell had been switched from one mode of operation to the other 11 times. Galvanodynamic measurements conducted before and after sets of galvanostatic measurments for a particular mode at 600$^o$C, gave an indication that alterations in the electrochemical performance had occurred as a result of operation. For example, galvanodynamic data for SOFC and SOEC modes are shown in figures 6.1(a) and 6.1(b) respectively. Data was recorded before and after galvanostatic measurements at 600$^o$C, that totaled 4 hours for SOFC mode and 3 hours for SOEC mode. An interesting feature of these data sets is that the cell resistance decreased with operation in both SOEC and SOFC modes. The cell could have been conditioned in some manner during the galvanostatic measurements and this implies that the combination of atmosphere and applied current effected the composition or microstructure of the cell. However, as discussed in section 5.6, this could also be due to other factors. Further data useful for durability analysis at other temperatures and stages of the experiment were not recorded. Preliminary experiments produced results that were useful indications of how BCY10 cells performed, however BCY10 durability under operating SOFC and SOEC conditions was not investigated in greater detail until later experiments. These data will be discussed later in this chapter.

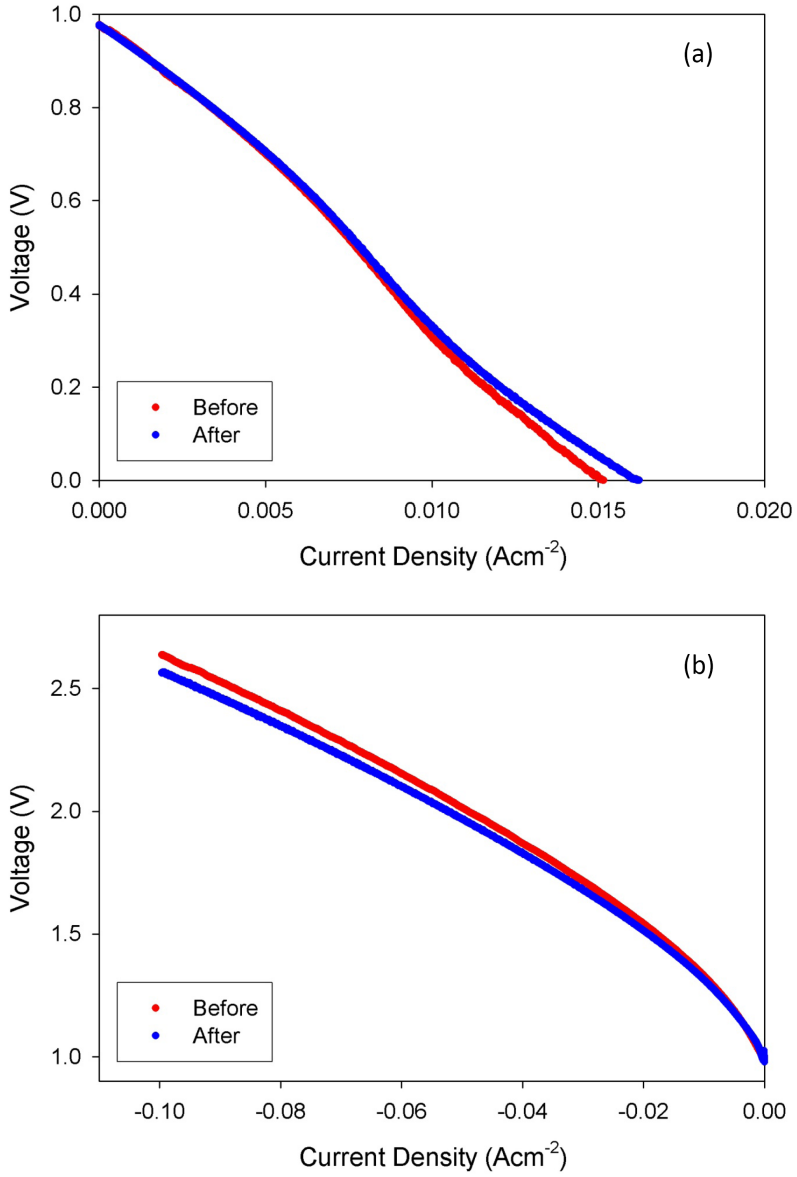



Figure 6.1: Galvanodynamic data recorded at 600$^o$C before and after galvanostatic measurements in (a) SOFC and (b) SOEC mode

Microstructural and compositional analysis of the preliminary cell was carried out using an SEM equipped with Energy Dispersive X-ray (EDX) spectroscopy capability. An SEM image of the fracture surface cross-section of the preliminary BCY10 cell after testing is presented in figure 6.2, in which the anode-electrolyte interfacial region and some delamination of the electrode from the electrolyte can be seen. It is probable that this delamination occurred during the separation of the cell from the current collector mesh after testing and did not impact on the electrochemical data. Electrodes must have good adhesion to the electrolyte so that charge

transfer may take place, however, the reactivity of the electrodes with the electrolyte must be minimal in order to prevent compositional or micro-structural change in the electrolyte that can cause an increase in the cell resistance. Upon close observation, a thin layer approximately one micron in thickness, can be seen in the electrolyte-anode interfacial region. This layer does not appear to be consistent with either the initial state of the electrode or of the electrolyte material. It is likely that this layer formed by a reaction between the $H_2/H_2O$ and the electrolyte that was perhaps catalysed by the platinum in the electrode. Furthermore, it appears this phase was not restricted to the region of contact between the electrolyte and the electrode and also formed between grains in the electrolyte close to the interface.

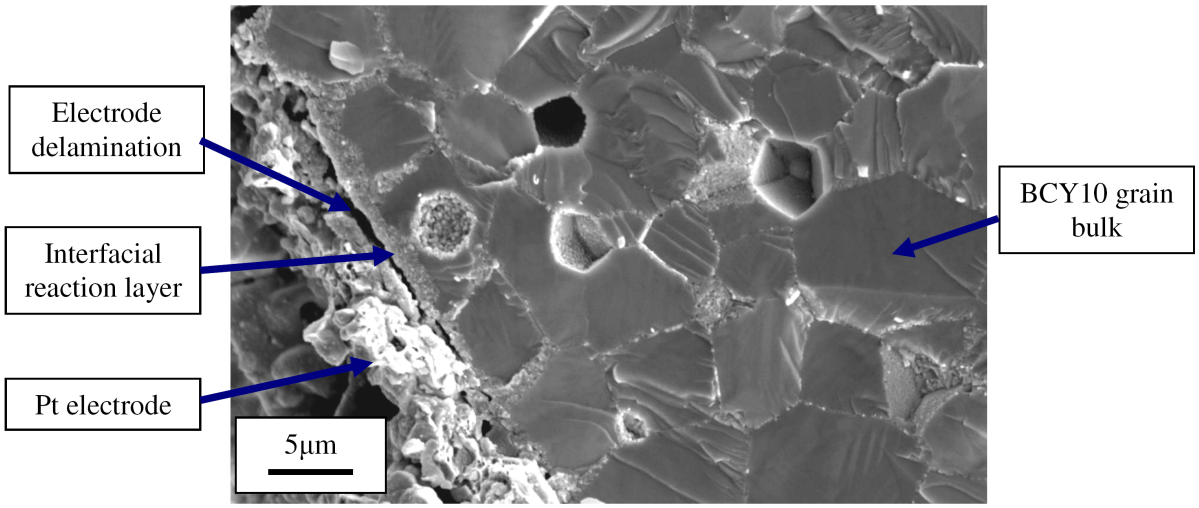



Figure 6.2: SEM image of preliminary sample fracture surface: Pt electrode-electrolyte $H_2$-$H_20$ interfacial region. Grain boundary regions can be seen to have been altered by SOEC/SOFC testing

When the interfacial regions in the control sample and the SOEC/SOFC sample (figure 6.3) are compared it is apparent that during the SOEC and SOFC testing significant microstructural alterations had occurred in the electrolyte material close to the anode. SEM images in figure 6.3 are of polished surfaces and therefore, the grain structure of the electrolyte was not expected to be visible. However, the grain structure in the tested sample can be clearly seen (figure 6.3(b)), but not in the control sample (figure 6.3(a)).

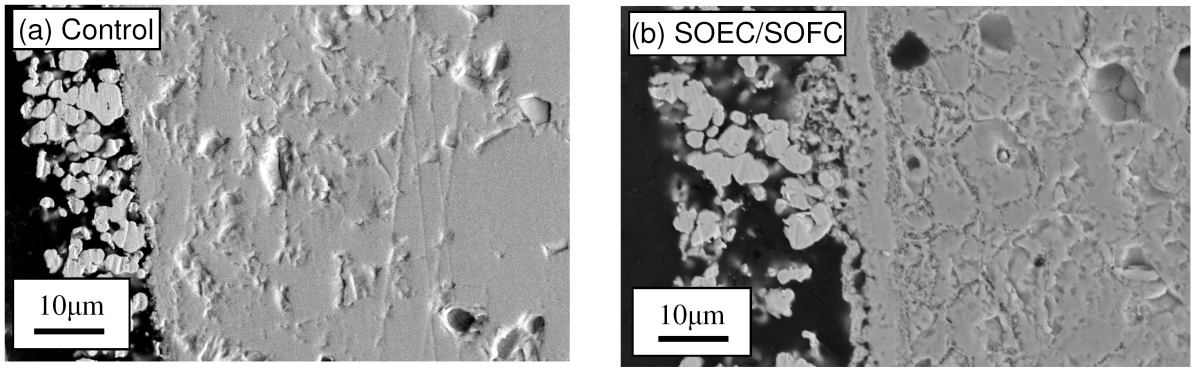



Figure 6.3: FEGSEM images of (a) Control sample and (b) SOEC/SOFC sample at Pt electrode-electrolyte interfacial region - Interfacial layer and corrosion of grains visible in SOEC/SOFC sample

Figure 6.4 is an SEM image of the electrolyte in the preliminary cell after testing with a corresponding graph of EDX spectroscopy line scan data. An indication of where the EDX line scan was taken is shown as a line on the SEM image. It can be seen that the line scan was taken across two grain boundaries, each approximately 1 $\mu$m in thickness, with points (a) and (b) referring to their locations. The image was taken within 50 $\mu$m of the anode-electrolyte interface. Grain boundary regions can be seen to be different to the clear grain boundaries observed towards the middle of the cross-section of the sample (figure 6.5). EDX spectroscopy data suggests a depletion of barium in grain boundary regions close the the anode-electrolyte interface. Relative proportions of cerium, oxygen and yttrium did not fluctuate in the same manner and therefore, it is possible that a secondary phase had been created during SOEC/SOFC operation in these regions. Such line scans were conducted several times across various grain boundary regions similar to those shown in the SEM image in figure 6.4, with similar results. Precise quantitative proportions of the elements present should not be firmly stated because not only is the diameter of the interaction area of the incident electrons larger than 1 $\mu$m, but the microstructure beneath the image plane is unknown. However, grain boundary regions close to the anode-electrolyte interface are deficient in barium, perhaps to the extent to which the perovskite phase was no longer stable. Therefore, a secondary phase may have been formed with a $Ce_{1-x}Y_xO_{2-(x/2)}$ composition. If this were the case, the transport of protons across the electrolyte is likely to have been inhibited and the transport of oxygen ions promoted as a consequence.

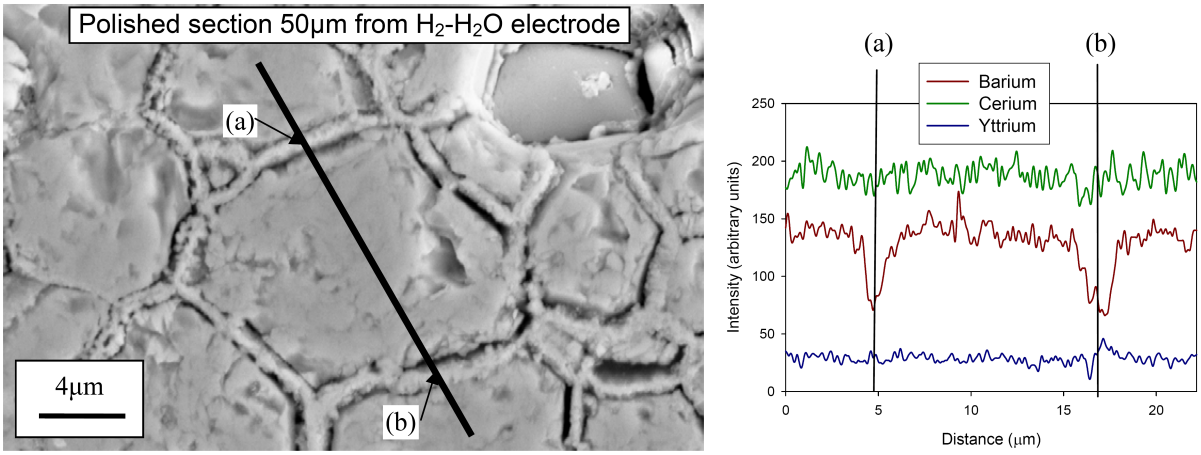



Figure 6.4: FEGSEM image of SOEC/SOFC sample polished surface and EDX line scan data. Line on FEGSEM image shows where EDX line scan data was acquired and (a) and (b) refer to grain boundary locations

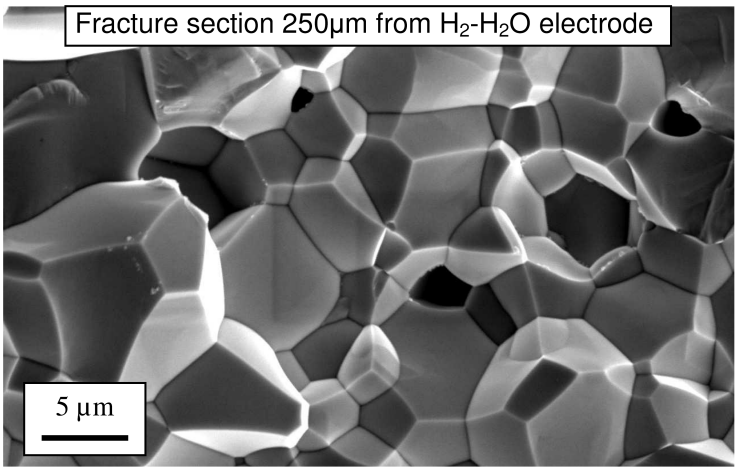



Figure 6.5: SEM image of SOEC/SOFC sample fracture surface, 250 $\mu$m from the $H_2$-$H_2O$ electrode (middle of the sample)

Interesting features were observed on exposed grain surfaces within 50 $\mu$m of the anode-electrolyte interface. Figure 6.6 includes two high magnification SEM images and shows examples of grain surfaces visible in polished samples. Such grain surfaces were visible in this way either because of grain pull out during polishing, or most likely, the presence of pores in the material. Cuboidal or plate like crystallites of unknown composition can be seen on the grain surface in the SOEC/SOFC sample (figure 6.6(a)) ranging from approximately 20 to 200 nm in size. These crystallites formed during SOEC/SOFC operation when the material was exposed to humidified hydrogen as no such artifacts are visible in the control sample (figure 6.6(b)). Therefore, per-

haps the crystallites are a result of $H_2O$ leaching out barium hydroxide species leaving behind an eroded surface. Also visible in figure 6.6(a) is a grain boundary triple point, with distinct regions approximately 200 nm in thickness either side of the boundary itself. This may be further evidence of mass transport along grain boundaries in the material during operation as crystallites have not formed in these areas. Such mass transport was likely to have been activated by the application and drawing of charge and not due to atmospheric conditions alone.

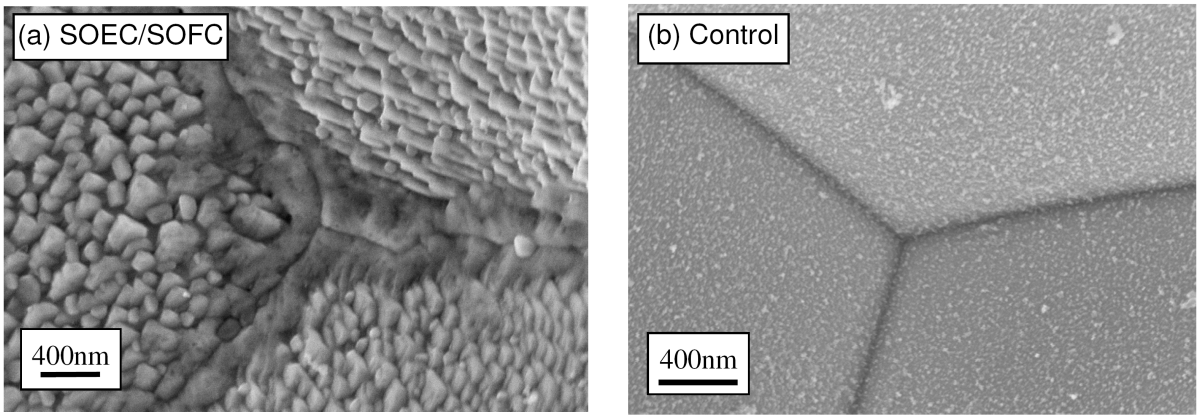



Figure 6.6: FEGSEM images of grain boundary triple points in (a) SOEC/SOFC and (b) control samples. Distinct grain boundary region and crystallites on the surface of grains can be seen in SOEC/SOFC sample.

In an attempt to investigate the microstructure of the tested preliminary sample more closely, a fresh surface on the sample was created using a focused ion beam (FIB). By polishing the sample with a low gallium ion beam current, a better defined surface was created than could be achieved by using mechanical polishing. An image created by the detection of scattered electrons from the surface of the sample as a result of incident gallium ions is shown in figure 6.7. This work is incomplete since 'curtaining' is still visible on the polished surface and the electrode-electrolyte interfacial region had not been fully revealed. Polishing using a lower beam current would create an even clearer surface and the overhang above the electrode also needs to be removed in order to create a finished surface for analysis. However, at this stage, the grain structure can be seen more clearly using this technique than by SEM imaging. Also, grain contrast can be observed using this technique and interestingly, some grains were found to have a similar contrast to the secondary phase at grain boundaries. Compositional variations could be investigated with FIB secondary ion mass spectrometry and also by using the FIB to create transmission electron microscopy samples.

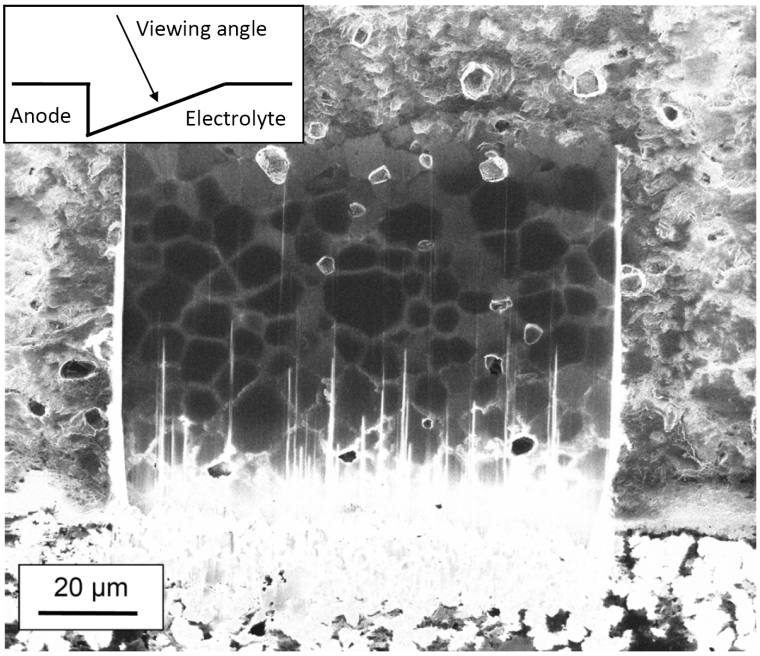



Figure 6.7: Focused ion beam electron image of the trench created using focused ion beam milling. The area displayed is at the anode-electrolyte interfacial region in the preliminary sample. Grain contrast and secondary phase located at the grain boundaries are clearly visible. Inset; schematic of the cross-section of the sample after milling, showing surface geometry and viewing angle.

It is clear that micro-structural and compositional alterations occurred in the BCY10 electrolyte and platinum electrodes during operation. Eventually, significant erosion of grains in grain boundary regions shown in figure 6.4 would have caused an increase in cell resistance. Indeed, if such erosion continued, it is probable that the cell would experience mechanical failure. Exposure to various atmospheric conditions or the application or drawing of current to the cell, individually, may not have caused the observed microstructural alterations, rather a combination of each of these factors may have been required. Furthermore, the switching between SOEC and SOFC modes may have been a contributing factor, but it is also possible for the observed microstructural alterations to have occurred in one of these modes and not the other.

The developed cell discussed in section 5.2 underwent similar testing as the preliminary cell. It was discovered that this caused similar microstructural alterations to those observed in the preliminary cell, but with some significant differences. The interfacial layer between the anode and the electrolyte observed in the preliminary cell, was not observed in the developed cell, as can be seen in figure 6.8. Instead, a thin layer of nanoscopic particulates, apparent as flecks of light contrast, were observed in the anode-electrolyte interfacial region. EDX spectroscopy

could not be used to ascertain the composition of these particulates since the primary electron interaction volume was too large for meaningful results to be obtained. A potential method of resolving this issue is discussed in more depth in chapter 7. A secondary phase was still found to be present at grain boundaries close to the anode as observed in the preliminary cell, but appeared less prominent.

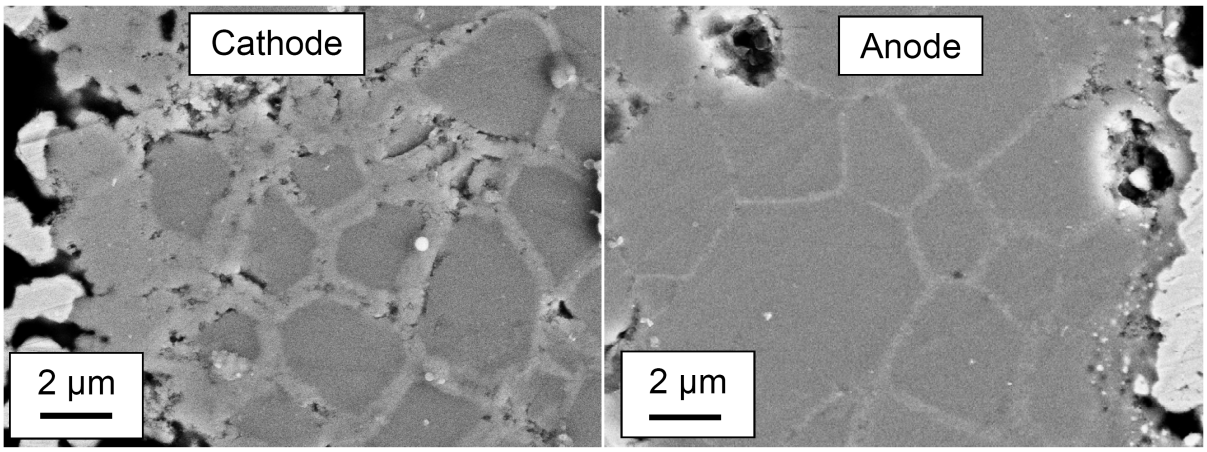



Figure 6.8: FEGSEM images of interfacial regions at (a) the cathode and (b) the anode. Secondary phase at grain boundaries can be seen to be much more abundant at the cathode side than the anode side of the cell

Significant differences were also observed at the cathode-electrolyte interface in the developed cell in comparison with the preliminary cell. A secondary phase in grain boundary regions was observed close to the cathode-electrolyte interface. The thickness of these regions were generally greater at the cathode-electrolyte interface than at the anode-electrolyte interface, as shown in figure 6.8. Also, an interfacial layer, identical in appearance to that observed at the anode in the preliminary cell, was observed at the cathode in the developed cell instead. Quantitative EDX spectroscopy data from points measured in the cathode-electrolyte interfacial region in the developed cell are presented in table 6.1 with corresponding locations identified in figure 6.9.

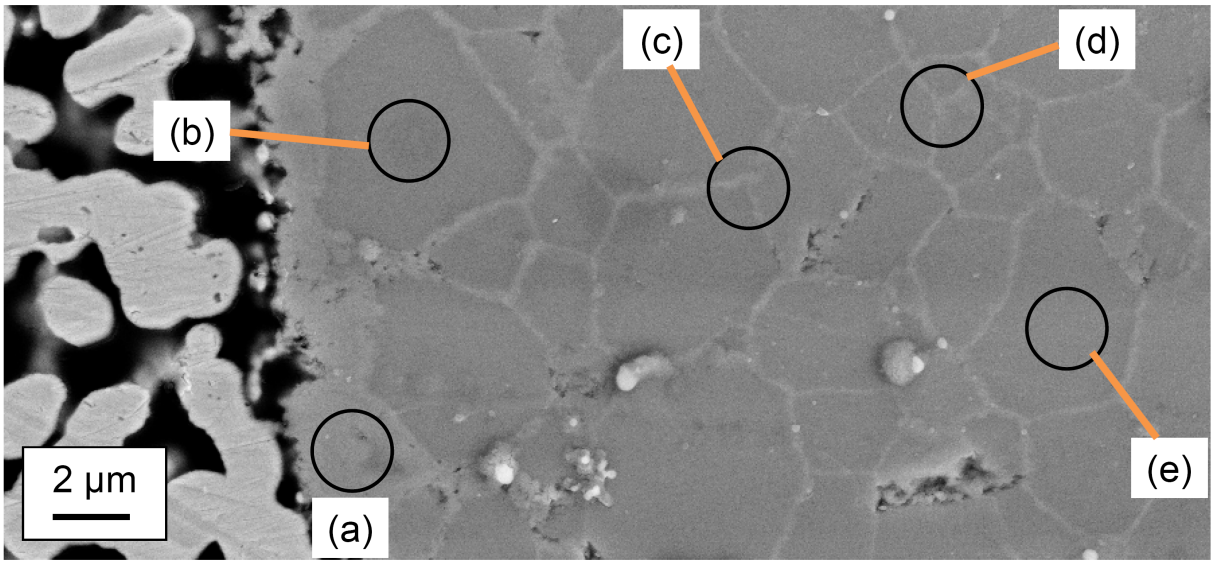



Figure 6.9: FEGSEM image of the cathode-electrolyte interfacial region with example EDX spectra measurement locations indicated as follows; (a) interfacial layer, (b) and (e) grain bulk, (c) and (d) grain boundary triple points. Circle diameters roughly indicate the area of primary electron interaction at the surface of the sample, however, it should be noted that the maximum cross sectional area of the primary electron interaction volume parallel with the surface of the sample is greater than this area.

| Location | Carbon | Barium | Cerium | Yttrium | Oxygen | Platinum |
|---|---|---|---|---|---|---|
| Grain Bulk | 24.6 (3.3) | 10.5 (0.6) | 9.3 (0.5) | 0.9 (0.3) | 54.6 (2.4) | 0.0 (N/A) |
| Grain Boundary Triple Points | 25.1 (2.3) | 7.8 (1.5) | 9.9 (1.0) | 1.3 (0.3) | 55.9 (2.4) | 0.0 (N/A) |
| Interfacial Layer | 26.3 (4.0) | 9.5 (2.2) | 6.5 (2.7) | 1.2 (0.4) | 54.1 (2.7) | 2.4 (1.4) |

Table 6.1: Average atomic % of elements detected using EDX spectroscopy measured at various locations corresponding with figure 6.9. Standard deviation values are quoted in brackets.

Incident electrons fired at the sample surface during EDX spectroscopy measurements interacted with unknown sub-surface microstructure. Therefore, errors in corresponding the atomic % values shown in table 6.1 with particular observed microstructural features on the surface of the sample are difficult to estimate. Multiple measurements in locations visually similar to the those indicated in figure 6.9 were conducted in several different sections of the cell to gain a greater degree of certainty. All results for a given location type were found to be similar to one another with trends in elemental atomic % ratios maintained with a high degree of regularity.

When analysing the results in table 6.1, it must be noted that samples were polished using a diamond suspension and therefore, the presence of embedded carbon in the surface of the sample is understandable. This does make drawing any conclusions from the atomic % carbon

values difficult, leaving the amount of carbon originally present within the sample, and hence the detection of any carbonate phases before polishing, uncertain. However, it was consistently found that the atomic % carbon values were higher (and atomic % oxygen lower) in interfacial regions (type (a) shown in figure 6.9) relative to the bulk of the sample. Bearing in mind the reported tendancy of carbonate formation in BCY10, it is possible that the interfacial layer contained carbonates formed during testing.

| Location | Ce:Ba Ratio |
|---|---|
| Grain Bulk | 0.88:1 |
| Grain Boundary Triple Points | 1.27:1 |
| Interfacial Layer | 0.68:1 |

Table 6.2: Ce:Ba ratios at various locations within the developed cell, calculated from average atomic % presented in table 6.1

Grain boundary triple point locations, had a higher cerium to barium atomic % ratio than stoichiometric for BCY10 and that found in the grain bulk (see table 6.2). A 1.27:1 cerium to barium ratio was found in grain boundary triple point regions in comparison to 0.88:1 found in the grain bulk (stoichiometric value is 0.9:1). Grain boundary triple point regions were found to contain hypo-stoichiometric amounts of barium. This correlates with the previous EDX spectroscopy results on the preliminary cell shown in figure 6.4 which indicated barium depletion from grain boundary regions in the electrolyte close to the anode. The average cerium to barium ratio in the interfacial layer found at the cathode in the developed cell was found to be 0.68:1. Hyper-stoichiometric quantities of barium were therefore found at the interfacial layer.

At this stage, only speculative comments can be made on the mechanisms of changes to the cell microstructure and local composition during testing. Barium, initially located within the grain bulk, could have diffused along grain boundaries to the anode-electrolyte interfacial region during testing. Subsequently, as EDX spectroscopy results from locations such as type (a) shown in figure 6.9 suggest, a build up of a perovskite phase with a hyper-stoichiometric barium content, or indeed barium oxide or barium carbonate occurred at the electrode-electrolyte interface. Alternatively, cerium may have diffused from the anode-electrolyte interface along grain boundaries towards the middle of the cell and remained in grain boundary regions. Since the ionic radius of cerium is less than barium, perhaps cerium is the more likely candidate for

the mobile species. However, it may well be that cerium, barium, oxygen and yttrium ions are all mobile to a certain extent. Suggested methods of further investigation are discussed in the following chapter.

Similar microstructural and compositional alterations occurred in the developed cell close to the cathode as in the preliminary cell close to the anode. The cause for this these alterations to be observed at opposite electrodes could have been due to differing sintering regimes used or differing operating conditions. Questionable sealing, indicated by low OCV values obtained during the preliminary cell testing, may have allowed the cathode and anode to be exposed to different atmospheric conditions than the developed cell during testing. Furthermore, the preliminary cell was not supplied with gas for significant periods of time during non-testing periods due to the laboratory safety protocols. Current was neither applied to, nor drawn from the cell during these time periods, but could still have effected the results found here.

## 6.3 Analysis of Cell with Anode Exposed to 66% $H_2$ Humidified to ≈3%

Cell testing was carried out in SOEC and SOFC mode using an increased concentration of hydrogen in the anode compartment as detailed in section 5.3. A 24 hour test was carried out using an applied voltage of 1.75 V (SOEC mode) at 600$^o$C to evaluate the performance stability under these conditions. The resultant current density recorded over time is presented in figure 6.10. The current density was found to increase by 0.4 mAcm$^{-2}$ over the 24 hour period. This represents a very minor improvement in SOEC performance and suggests that the cell is relatively stable under these conditions in SOEC mode.

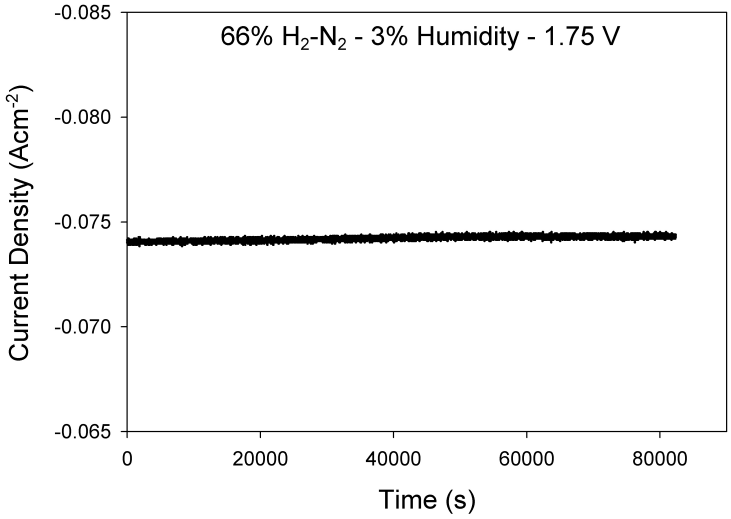



Figure 6.10: Change in current density over 24 hours with 1.75 V applied (SOEC mode)

Post test imaging of the cell cross-section and elemental analysis of the cell was carried out to see if similar microstructural alterations had occurred under these conditions, as with the cells discussed in section 6.2. Only very faint lines could be seen close to the cathode at grain boundaries in the electrolyte when the image contrast was increased significantly. Therefore, the same ionic mobility seen when using a lower concentration of hydrogen in the feed gas, was not observed here. This is also supported by the absence of an interfacial layer. However, another microstructural alteration was observed in this sample. 'Spots' varying in size from 1 to 4 $\mu$m were observed up to 80 $\mu$m from the cathode-electrolyte interface. These features may be spherical in shape and therefore, the apparent cross sectional area could be misleading in the determination of their size distribution. EDX spectroscopy was carried out on these 'spots' and in other locations for comparison, as shown in figure 6.11, and the corresponding results are shown in table 6.3.

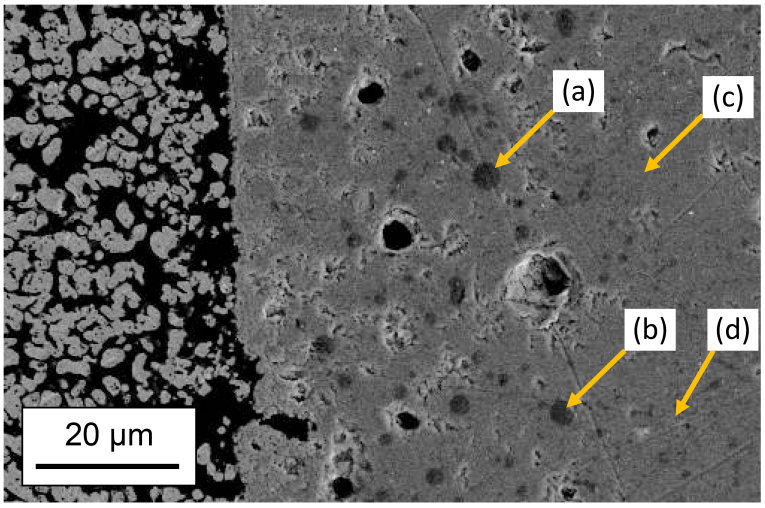



Figure 6.11: SEM image of the cathode-electrolyte interface showing 'spots' at sites (a) and (b) that were analysed using EDX spectroscopy. Sites in locations such as (c) and (d) were also analysed using EDX for comparison.

| Location | Carbon | Barium | Cerium | Yttrium | Oxygen | Ce:Ba Ratio |
|---|---|---|---|---|---|---|
| Dark 'Spots' | 43.3 (6.8) | 8.5 (1.6) | 6.6 (2.5) | 1.1 (0.7) | 40.5 (2.9) | 0.78:1 |
| Grain Bulk | 30.0 (4.5) | 13.1 (1.3) | 11.2 (0.9) | 1.6 (0.4) | 44.1 (2.6) | 0.85:1 |

Table 6.3: Average atomic % of elements detected using EDX spectroscopy, measured in dark 'spot' regions (eg: (a) and (b) figure 6.11) and grain bulk regions (eg: (c) and (d) figure 6.11). Standard deviation values are quoted in brackets.

Dark 'spots' present in locations (a) and (b) in figure 6.11, for example, were found to contain elevated concentrations of carbon and a sub-stoichiometric Ce:Ba atomic % ratio. EDX results therefore suggest that the dark 'spots' are areas where $BaCO_3$ had been formed. It is not clear why elevated concentrations of hydrogen in the anode gas supply would cause such features to be formed in the electrolyte close to the cathode. An increased flux of protons or oxygen ions through the electrolyte, as suggested by testing results under these conditions, could have effected the rate of hydrogen evolution, or of oxygen dissociation at the cathode. However, these occurrences would not have directly lead to barium carbonate formation in the electrolyte and further work is required to establish the composition of these 'spots' more definitively. Inhomogeneity is not desirable, since the ability of the material to uptake water and to conduct protons would be diminished. A decrease in the fuel cell or electrolyser performance would be anticpated under these conditions, should the formation of these features continue with operation.

## 6.4 Effect of Increased Humidity in Supplied Gas Feed on Cell Stability

An increase in humidity in the supplied gas feed should have allowed a greater concentration of protonic defects to have formed within the electrolyte during testing. Such conditions are anticipated for commercial operation of SOEC devices. The concentration of steam required to be supplied to the device, above which the hydrogen production rate becomes unaffected, is unknown. In this experiment, the supply gas was attempted to be humidified as much as practically possible so that an increased flux of protons across the cell could be induced. The stability of a cell operated only in SOEC mode with the supplied gas humidified to ≈83% was assessed. This was done by recording potentiodynamic data at the beginning and at the end of an experiment. Measurements began at 750$^o$C, followed by 600$^o$C and then 500$^o$C, before increasing the temperature back up to 750$^o$C and conducting the same measurements as initially. The resultant initial and final IV curves measured at 750$^o$C are shown in figure 6.12.

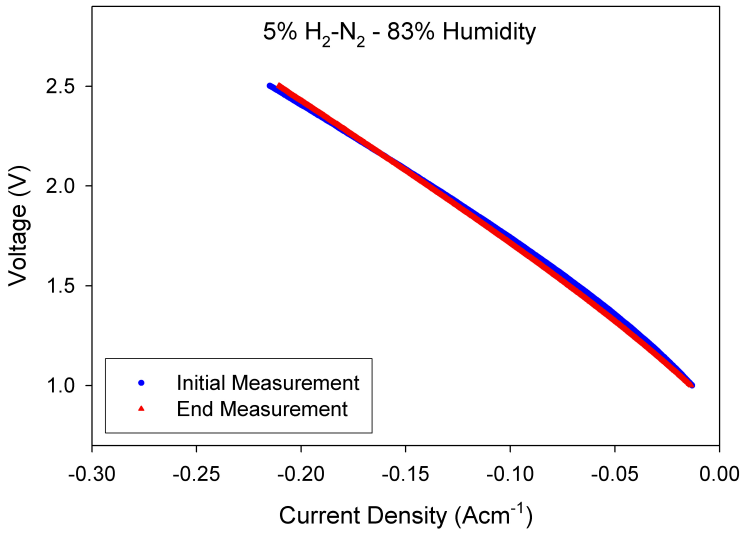



Figure 6.12: Potentiodynamic measurements made at the beginning and end of a test cycle, conducted using an anode gas supply feed of 5% $H_2$ balanced with $N_2$, humidified to ≈83%. Results show a slight change in SOEC performance during approximately 18 hours of testing at various temperatures and applied voltages.

Slight variances in activation polarisation and ASR values observed are indicative of potentially significant SOEC performance deterioration over longer periods of time. Voltage loss before the ohmic region of the IV curve was reached, was less at the end of the experiment than at

the beginning (0.70 V instead of 0.74 V), suggesting a certain amount of conditioning of active electrode-electrolyte sites had occurred. This was accompanied by a significant increase in ASR during the experiment from 3.10 $\Omega cm^2$ to 3.29 $\Omega cm^2$. Since typical device operation lifetime targets are in the thousands of hours and this experiment consisted of only 18 hours of cumulative operation, these data suggest that the stability of this cell is inferior to what is required. Even when the effects of temperature cycling are considered, to observe such an increase in ASR over such a limited period of operation is poor. The cell did not experience any operation in fuel cell mode so performance degradation cannot be attributed to this mode of operation or current cycling. Figure 6.13 is an SEM image showing the cathode-electrolyte interfacial region and locations where EDX spectroscopy data, shown in table 6.4, were collected.

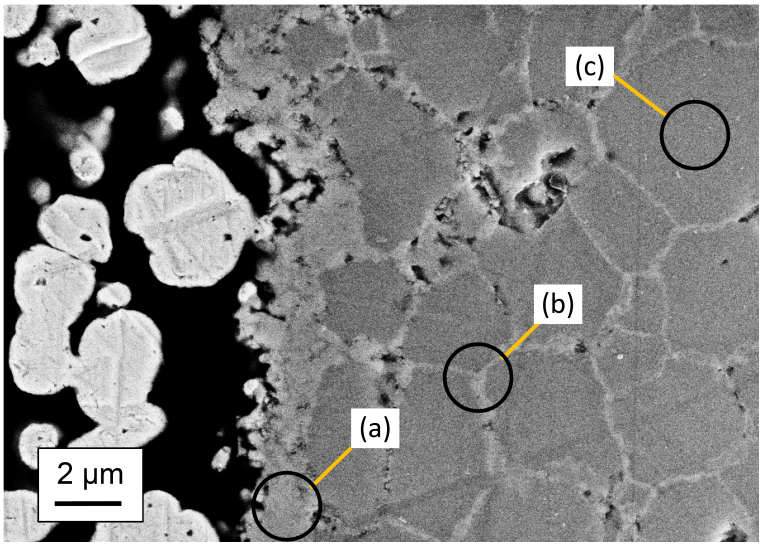



Figure 6.13: SEM image of the cathode-electrolyte interface of a sample after operation with approximately ≈83% humidity in the anode gas chamber

| Location | Carbon | Barium | Cerium | Yttrium | Oxygen | Platinum |
|---|---|---|---|---|---|---|
| Interfacial Layer | 37.4 (5.5) | 9.1 (2.0) | 3.15 (1.5) | 0.7 (0.3) | 46.6 (2.7) | 3.0 (1.3) |
| Grain Boundary Triple Points | 21.4 (2.1) | 8.5 (1.6) | 9.8 (0.9) | 1.3 (0.3) | 58.9 (2.5) | 0.0 (N/A) |
| Grain Bulk | 14.6 (4.0) | 11.5 (2.3) | 9.8 (0.6) | 0.9 (0.4) | 63.2 (3.1) | 0.0 (N/A) |

Table 6.4: Atomic % of elements detected using EDX spectroscopy measured at various points corresponding with figure 6.13

| Location | Ce:Ba Ratio |
|---|---|
| Grain Bulk | 0.86:1 |
| Grain Boundary Triple Points | 1.15:1 |
| Interfacial Layer | 0.34:1 |

Table 6.5: Atomic % of elements detected using EDX spectroscopy measured at various points corresponding with figure 6.13

As observed in the developed cell, tested in both SOEC and SOFC mode using 5% $H_2$ balanced with nitrogen humidified to 3% (section 6.2), an interfacial layer formed during operation at the cathode (location (a) in figure 6.13). EDX spectroscopy revealed that the interfacial layer had a similar composition as previously. A further similarity with the developed cell was the presence of distinctly lighter contrast in grain boundary regions, up to 20 $\mu$m from both electrode-electrolyte interfaces. In this instance the modification of grain boundary regions was observed to an equal extent at each interface, unlike previously observed. This suggests that perhaps either operation in fuel cell mode, or variation in humidity of the gas supplied to the anode, could have caused this effect to occur unevenly between anode and cathode interfacial regions. EDX spectroscopy results from locations of type (b) and (c) shown in figure 6.13 were similar to previously discovered, however a slightly lower cerium to barium atomic % ratio was found at grain boundary triple points in this sample than in the developed cell. This finding, along with the observed decrease in grain boundary modification distance from the electrodes (from 80 to 20 $\mu$m), indicates that degradation had not proceeded as far as with the developed cell. The developed cell discussed in section 6.2 was operated for a cumulative total of approximately 35 hours instead of 18 hours in this case. Shorter operation time therefore contributed towards the lesser degradation observed in this sample.

It appears as though the elevated humidity in the anode gas supply did not cause an increased rate of secondary phase formation at grain boundaries. However, the increased humidity does appear to have had a greater effect on the microstructure of the cell in the immediate vicinity of the anode-electrolyte interface, as shown in figure 6.14. A higher magnification image of the interface is presented in figure 6.15 where the distinctly altered microstructure can be seen in greater detail.

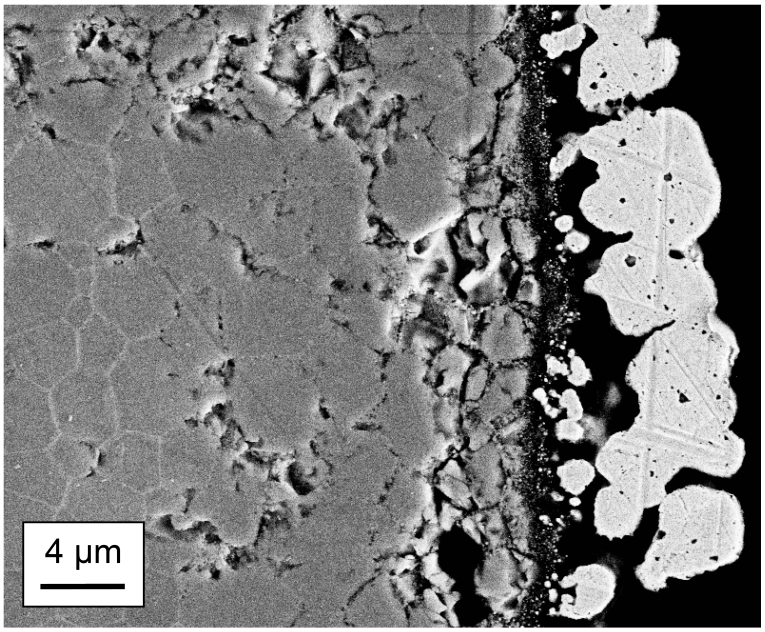



Figure 6.14: SEM image of the anode-electrolyte interface after 18 hours of operation in SOEC with an ≈83% humidity in anode gas feed

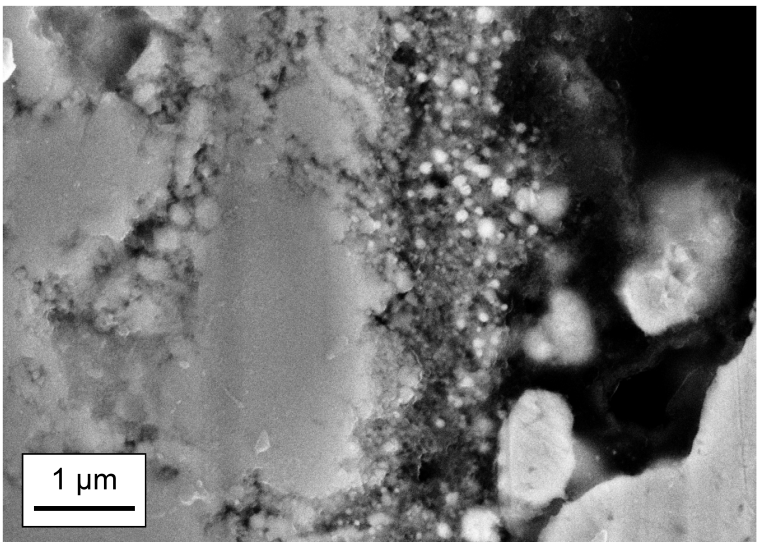



Figure 6.15: A high magnification SEM image of the anode-electrolyte interface showing detail of the interfacial layer containing nanoscopic particulates

An interfacial layer around 750 nm in thickness, of different appearance to that found at the cathode, can be seen in figure 6.15. Formation of this type of interfacial layer is not observed in other experiments, although the nanoscopic particulates observed at the anode in the developed cell are thought to be representative of the early stages of formation of this layer. It could not be confirmed that this interfacial layer consists of hydroxides as the presence of hydrogen cannot

be detected using EDX spectroscopy. Low concentrations of barium and cerium, and a high concentration of carbon, were able to be detected in this region. This finding suggests that the layer consists of a carbonaceous phase, with a low proportion of original electrolyte material present. The precise composition is unknown and further work is required to determine whether an increased humidity in the anode gas stream caused an increase in the rate of hydroxide formation, or indeed, if hydroxide formation occurred at all. Amongst this uncertainty remains the fact that the electrochemical performance of the cell has been shown to be compromised by the high levels of humidity used in this experiment over time. As discussed in section 2.10.2, very little work has been conducted on the stability of Y:$BaCeO_3$ in $H_2O$ containing atmospheres. However, Tanner and Virkar [132] found sintered samples of doped $BaCeO_3$ to be susceptible to hydroxide formation when exposed to atmospheres with high partial pressure of $H_2O$ below $900^oC$. Hydroxides may have formed in the following manner;

$$BaCeO_3 + H_2O \rightarrow Ba(OH)_2 + CeO_2 \tag{6.1}$$

This finding by Tanner and Virkar gives further cause for investigation into the presence of hydroxides at the anode-electrolyte interface, although EDX results suggest that carbonaceous species were also formed. The presence of hydroxides or carbonates at interfaces is likely to have had a negative effect on the ability of the material to dissociate water and absorb and conduct hydrogen and oxygen ions. With further operation under these conditions, it is probable that the formation of hydroxides and/or carbonates will prevent the device from electrolysing steam within a relatively short time-frame.

## 6.5 Summary

Observations of cell microstructure after electrochemical testing revealed conflicting results between the preliminary and developed cell. An interfacial layer, found to have high concentrations of barium and carbon, was discovered to be present at the anode in the preliminary cell but at the cathode in the developed cell. This was thought to be caused by a change in experimental setup allowing better sealing rather than any changes to the cell caused by differing sintering conditions. In both of these cells, electrochemical testing was not concerned with the assessment of cell durability. Therefore, suitable electrochemical data were not available to properly

assess how the performance of the cell changed over an appreciable period of time. Significant erosion of grain boundaries regions close the electrode-electrolyte interfaces was observed. EDX spectroscopy results are indicative of the formation of a secondary phase in these regions, possibly Y:$CeO_2$, observed as lighter contrast between grains. After having observed these samples post-test, it is believed that the electrochemical performance is highly likely to have been degraded over time due to the instability of the electrolyte material. Had testing continued over an extended period of time, it is probable that the cell would have undergone mechanical failure due to erosion in grain boundary regions.

A 24 hour test using a high concentration of hydrogen in the anode chamber gas feed revealed good electrochemical stability in SOEC mode over this time scale. Microstructural observations of the cell after testing found that the interfacial layer in the preliminary and developed cells had not formed. The presence of a reducing atmosphere may have prevented the formation of a secondary phase or phases. A high density of 'spots', appearing as darker areas of contrast up to 2 $\mu$m in diameter, were observed using SEM close to the cathode, only in the sample tested using a higher concentration of hydrogen. EDX spectroscopy revealed these regions to have elevated concentrations of barium and carbon, which suggests these areas contained barium carbonate and not the perovskite phase. The exact composition, and mechanism and cause of creation of these features in the sample during testing, is unknown and requires further investigation.

When BCY10 cells were operated using a higher humidity, nanoscopic particulates were found to have formed at the anode-electrolyte interface. Low concentrations of barium and cerium, and a high concentration of carbon, were able to be detected in this region suggesting the presence of a carbonaceous phase. However, further work is required to ascertain whether the nanoscopic particulates are barium hydroxide, as this seems to be a more likely composition. Electrochemical performance of the electrolyte material was shown to be compromised by operation under these conditions over time.

The main conclusions from this work and suggestions for further work follow.

# Chapter 7

# Conclusions and Further Work

Proton conducting solid oxide electrolysis cells are in the early stages of development and a great deal of work must be carried out in order for these devices to become commercially viable. Conclusions from this work are presented together with directly relevant discussions on further work. Some general points on the further work required and how experimental methods may be altered to achieve more detailed results are also made.

**Chapter 4 - Synthesis and Conductivities of Yttrium Doped Barium Cerate and Barium Zirconate**

- By sintering milled BCY10 powders 1500$^o$C for 10 hours, sufficiently dense samples for SOEC/SOFC experiments were able to be manufactured.
- BZY10 was found to require a 1 wt% dopant of ZnO in order to achieve similarly high densities using the same sintering regime as BCY10 samples.
- BCY10 sample conductivity data was in close agreement with the reported literature data.
- Conductivity data reported in the literature for BZY10 was found to be erratic with differing activation energies for conduction quoted.
- Zn doped samples were found to have conductivities within the bounds of the literature data. However, due to the large variances between these data, the affect of Zn addition on the total conductivity of BZY10 could not be concluded.

- Under humid conditions, the activation energies for both BCY10 and BZY10 above 400$^o$C were found to be significantly lower than below 400$^o$C. Therefore, the proton mobilities for these materials were found to be greater above 400$^o$C than below.

- BCY10 was found to have a conductivity approximately one order of magnitude greater than Zn-doped BZY10 over the entire temperature range studied.

- Pure BZY10 powder synthesised using a spray pyrolysis method was able to be sintered to a density of 90.6%TD. Powder synthesised using a combination of a high atomising frequency and a low solution concentration achieved this high density value. Other spray pyrolysis parameter sets yielded powders that sintered to density values no greater than 55%TD. The cause for such differences in sintered density is not clear and requires further investigation by use of particle size distribution analysis and microscopy techniques. Further amounts of powder using the successful parameter set is required to be synthesised in order to produce samples for conductivity and SOEC/SOFC testing purposes.

- The synthesis of BZY10 by spray pyrolysis could be investigated further by using a higher furnace temperature in an attempt to produce a more favourable particle size distribution for sintering.

- An average sintered density above 78%TD was not able to be achieved from pure BZY10 powders synthesised using the sol-gel method. It is probable that the method could have been optimised in order to synthesise powders capable of sintering to higher densities. Variables such as the molar ratios of citric acid to metal ions, and of citric acid to polyethylene glycol should be varied and the effects on the resultant powder sintering behaviour determined.

**Chapter 5 - Electrochemical Characterisation**

- Preliminary SOEC and SOFC results were improved upon by development of a test rig, apparatus set up and electrolyte capable of achieving higher power densities in fuel cell mode and lower ASR values in both SOFC and SOFC modes. Furthermore, activation polarisation losses were also reduced in this way.

- OCV measurements suggest that samples of BCY10 had an ionic transport number of less than unity. The electronic contribution to the total conductivity of these samples could be established using concentration cell measurements.

- Power densities in fuel cell mode were increased when an elevated hydrogen concentration in the anode gas feed was used.

- ASR values in electrolysis mode were lower when using an elevated hydrogen concentration in an anode gas feed with a humidity of ≈3%. However, when

- At 750$^o$C, the SOEC ASR was found to be lower when the anode compartment was humidified to ≈83% than to ≈3%, whereas below this temperature, ASR values were greater when using increased humidity levels. It was concluded that oxide ion conduction may be beneficial to the operation of a proton conducting SOEC.

- Potentiodynamic measurement cycles were carried out when using an anode supply gas of 100% $N_2$ humidified to ≈83% and a significant difference in current density beween increasing and decreasing voltage data was discovered. Such behaviour was observed at 500 and 600$^o$C but not at 750$^o$C and could be due to;

1. A residual concentration of protonic defects present from the device having recently operated at a higher voltage
2. Joule heating of the cell that took place when electrolysis is carried out above 1.4 V
3. An increase in the activation of the electrodes may have taken place when current was passed through the cell

- At a cell temperature of 500$^o$C a potentiostatic measurement at 2.25 V was carried out over a 20 minute period, and immediately afterwards, an OCV measurement was taken. It was found that the OCV value took almost an hour to stabilise and reach the original value measured. This is indicative of very slow kinetics of the cell at this temperature. The experiment was repeated with a cell temperature of 750$^o$C and it was found that OCV stabilisation occurred almost immediately. Therefore, the kinetics of the cell at this temperature were significantly improved at 500$^o$C.

- ASR values were found to be much lower in both SOFC and SOEC modes of operation at 750$^o$C for the BCY10 cell than Zn-doped BZY10 cell. Based on this data alone, the Zn-doped material is not conductive enough to compete with a BCY10 based cell. Further Zn-doped BZY10 cell test experiments are required to be carried out at other temperatures and under other atmospheric conditions. Effects of operation on microstructure and composition also need to be analysed. Furthermore, the ionic transport numbers of the Zn-doped BZY10 material are required to be determined.

Further experiments involving the direct measurement of gases are required in order to make more substantiated claims on the mechanisms of operation of a proton conducting SOEC device. Such experiments require a dual chamber testing rig to be constructed in order for the atmospheric exposure of both electrodes to be controlled. This would allow the measurement of the voltage required to produce hydrogen and the hydrogen production rate, as well as elucidate the effect of oxide ion conduction on the performance of proton conducting SOECs. Also, by increasing applied voltages in SOEC mode, the voltage value for concentration polarisation onset could be discovered allowing peak power consumption values to be determined.

**Chapter 6 - Post-Test Analysis of the Microstructure and Composition of Cells**

- Observations of cell microstructure after electrochemical testing revealed conflicting results between the preliminary and developed cell. An interfacial layer, found to have high concentrations of barium and carbon, was discovered to be present at the anode in the preliminary cell, but found at the cathode in the developed cell. The cause for this difference is unknown, however, it is more likely that changes in experimental setup are responsible rather than any changes to the cell caused by differing sintering conditions.

- Significant erosion of grain boundary regions close the electrode-electrolyte interfaces was observed. EDX spectroscopy results suggested the formation of a secondary phase in these regions, possibly Y:$CeO_2$, observed as lighter contrast between grains.

- Short term improvements in the electrochemical behaviour in both the preliminary and developed cells were observed and were thought to be related to protonic defect formation in the electrolyte.

- Electrochemical performance is highly likely to have been degraded over time due to the instability of BCY10. Had testing continued over an extended period of time it is probable that the cell would have undergone mechanical failure due to erosion in grain boundary regions.

- A 24 hour test using a high concentration of hydrogen in the anode chamber gas feed revealed good electrochemical stability in SOEC mode over this time scale. Microstructural observations of the cell after testing found that the interfacial layer found in the preliminary and developed cells had not formed. The presence of a highly reducing atmosphere may have prevented the formation of a secondary phase or phases.

- A high density of 'spots', appearing as darker areas of contrast up to 2 $\mu$m in diameter, were observed using SEM close to the cathode only in the sample tested using a higher concentration of hydrogen. EDX spectroscopy revealed these regions to have elevated concentrations of barium and carbon, which suggests these areas contained barium carbonate and not the perovskite phase. The exact composition, and mechanism and cause of creation of these features in the sample during testing, is unknown and requires further investigation.

- When the cell was operated using an anode feed gas composition; 5%$H_2$-$N_2$ humidified to $\approx$83%, a significant rate of ASR degradation was observed. This may have been due to the formation of some of the microstructural features discussed in the chapter such as the secondary phase at grain boundaries.

Further work is required to establish the mechanism by which the microstructure and composition of the BCY10 cell became altered and exactly how this effects the electrochemical behaviour of the material over time. Compositional changes that occurred at grain boundary and interfacial regions may be elucidated by FIB secondary ion mass spectrometry or transmission electron microscopy analysis. Similarly, the composition of crystallites and nanoscopic particulates could also be investigated in this manner. Longer term electrochemical tests under operating conditions are required in order to obtain a reliable quantitative indication of the cell durability so that estimates of the cell lifetime can be made.

**Final Comments**

Once electrochemical performance has been established in SOEC and SOFC modes of operation under various conditions for proton conducting electrolytes, the next step towards creating a commercially viable cell is to find suitable electrode materials. Platinum is an expensive catalyst and needs to be replaced with a less expensive, and preferably a more electrochemically beneficial alternative. There have been some attempts at developing electrodes for proton conducting SOFCs including work by Hibino *et al.* [90] who constructed a cell of the following configuration; Pd-loaded FeO ‖ $BaCe_{0.75}Y_{0.25}O_{3-\delta}$ (BCY25) ‖ $Ba_{0.5}Pr_{0.5}CoO_3$. The overpotentials of the electrodes used in the BCY25 based cell with the developed electrodes were proven to be four times less than with simply Pt electrodes. Also, Rauch and Liu [150] investigated $BaCuGd_2O_5$ and a $BaCuGd_2O_5$-$BaCe_{0.8}Gd_{0.2}O_{3-\delta}$ (30-70%vol.) composite as electrode materials for use with a $BaCe_{0.8}Gd_{0.2}O_{3-\delta}$ electrolyte. Conductivity measurements were carried out and it was found that the interfacial resistance of the $BaCuGd_2O_5$ material was 5 times less than when using silver electrodes, and the composite an interfacial resistance of 10 times less than silver electrodes. The composite material was found to have an excellent compatability with the electrolyte and was therefore identified as a viable electrode material. There has therefore been some success in initial experiments reported in the literature. However, there has been no work reported on the development of electrodes specifically designed to optimise the performance of proton conducting SOECs. There is therefore much required to be investigated in this area and such work must be carried out in order for commercially viable proton conducting SOEC devices to become reality.

**List of Papers Published as a Result of This Work**

P. A. Stuart, R. Ayres-Rocha, E. Djurado, S. J. Skinner, Sintering behaviour of $BaZr_{0.9}Y_{0.1}O_{3-\delta}$ powders prepared by spray pyrolysis, Journal of the European Ceramic Society, Volume 29, Issue 4, March 2009, Pages 697-702

P. A. Stuart, S. J. Skinner, J. A. Kilner, Solid oxide proton conducting steam electrolysers, Proceedings of the 8th Solid Oxide Fuel Cell Forum, July 2008.

P. A. Stuart, T. Unno, S. J. Skinner, J. A. Kilner, Solid oxide proton conducting steam electrolysers, Solid State Ionics, Volume 179, Issues 21-26, 15 September 2008, Pages 1120-1124

# Bibliography


[1] R. Hino, K. Haga, H. Aita, and S. Kenji, "Reasearh and development on hydrogen production by high temperature electrolysis of steam," *Nuclear Engineering and Design*, vol. 223, pp. 363–375, 2004.

[2] G. Ma, T. Shimura, and H. Iwahara, "Simultaneous doping with $La^{3+}$ and $Y^{3+}$ for $Ba^{2+}$ and $Ce^{4+}$ sites in $BaCeO_3$ and the ionic conduction," *Solid State Ionics*, vol. 120, pp. 51–60, 1999.

[3] R. C. T. Slade and N. Singh, "The perovskite-type proton conducting solid electrolyte $BaCe_{0.9}Y_{0.1}O_{3-\delta}$ in high temperature electrochemical cells," *Solid State Ionics*, vol. 61, pp. 111–114, 1993.

[4] W. Coors and D. Readey, "Proton conductivity measurements in yttrium barium cerate by impedance spectroscopy," *Journal of the American Ceramic Society*, vol. 85, pp. 2637–2640, 2002.

[5] N. Bonanos, B. Ellis, and M. N. Mahmood, "Oxide ion conduction in ytterbium-doped strontium cerate," *Solid State Ionics*, vol. 28, pp. 579–584, 1988.

[6] H. Iwahara, T. Yajima, and H. Ushida, "Effect of ionic radii of dopants on mixed ionic conduction ($H^+$ + $O^{2-}$) in $BaCeO_3$-based electrolytes," *Solid State Ionics*, vol. 70/71, pp. 267–271, 1994.

[7] W. Suksamai and I. Metcalfe, "Measurement of proton and oxide ion fluxes in a working y-doped $BaCeO_3$ sofc," *Solid State Ionics*, vol. 178, pp. 627–634, 2007.

[8] T. Norby and Y. Larring, "Concentration and transport of protons in oxides," *Current Opinion in Solid State and Materials Science*, vol. 2, pp. 593–599, 1997.

[9] K. D. Kreuer, "Proton conducting oxides," *Annu. Rev. Materials Research*, vol. 33, pp. 333–359, 2003.

[10] F. M. M. Snijkers, A. Buekenhoudt, J. Cooymans, and J. J. Luyten, "Proton conductivity and phase composition in $BaZr_{0.9}Y_{0.1}O_{3-\delta}$," *Scripta Materialia*, vol. 50, no. 5, pp. 655–659, 2004.

[11] H. G. Bohn and T. Schober, "Electrical conductivity of the high-temperature proton conductor $BaZr_{0.9}Y_{0.1}O_{2.95}$," *Journal of the American Ceramic Society*, vol. 83, no. 4, pp. 768–772, 2000.

[12] C. D. Savaniu, J. Canales-Vazquez, and J. T. S. Irvine, "Investigation of proton conducting $BaZr_{0.9}Y_{0.1}O_{2.95}$ : $BaCe_{0.9}Y_{0.1}O_{2.95}$ core-shell structures," *Journal of Materials Chemistry*, vol. 15, pp. 598–604, 2004.

[13] K. Katahira, Y. Kohchi, T. Shimura, and H. Iwahara, "Protonic conduction in zr-substituted $BaCeO_3$," *Solid State Ionics*, vol. 138, no. 1-2, pp. 91–98, 2000.

[14] N. Zakowsky, S. Williamson, and J. T. S. Irvine, "Elaboration of $CO_2$ tolerance limits of $BaCe_{0.9}Y_{0.1}O_{3-\delta}$ electrolytes for fuel cells and other applications," *Solid State Ionics*, vol. 176, no. 39-40, pp. 3019–3026, 2005.

[15] C. Holl, "Compression of witherite to 8 GPa and the crystal structure of $BaCO_3$," *Physics and Chemistry of Minerals*, vol. 27, pp. 463–467, 2002.

[16] H. Nowotny and G. Heger, "Structure refinement of strontium nitrate, $Sr(NO_3)_2$, and barium nitrate, $Ba(NO_3)_2$," *Acta Crystallographica Section C*, vol. 39, pp. 952–956, 1983.

[17] I. Levin, T. Amos, S. Bell, L. Farber, T. Vanderah, R. Roth, and B. Toby, "Phase equilibria, crystal structures, and dielectric anomaly in the $BaZrO_3CaZrO_3$ system," *Journal of Solid State Chemistry*, vol. 175, pp. 170–181, 2003.

[18] K. Takeuchi, C. K. Loong, J. W. Richardson Jr, J. Guan, S. E. Dorris, and U. Balachandran, "The crystal structures and phase transitions in y-doped $BaCeO_3$: Their dependence on y concentration and hydrogen doping," *Solid State Ionics*, vol. 138, no. 1-2, pp. 63–77, 2000.

[19] P. Pasierb, M. Wierzbicka, S. Komornicki, and M. Rekas, "Structural, electrical and transport properties of yttrium-doped proton-conducting strontium cerates," *Journal of Power Sources*, vol. 173, pp. 681–687, 2007.

[20] V. Kharton, I. Marozau, G. Mather, E. Naumovich, and F. J., "Transport numbers and oxygen permeability of $SrCe(Y)O_3$-based ceramics under oxidising conditions," *Electrochimica Acta*, vol. 51, pp. 6389–6399, 2006.

[21] R. Cervera, Y. Oyama, S. Miyoshi, K. Kobayashi, T. Yagi, and S. Yamaguchi, "Structural study and proton transport of bulk nanograined y-doped $BaZrO_3$ oxide protonics materials," *Solid State Ionics*, vol. 179, pp. 236–242, 2006.

[22] R. Cervera, Y. Oyama, and S. Yamaguchi, "Low temperature synthesis of nanocrystalline proton conducting $BaZr_{0.8}Y_{0.2}O_{3-\delta}$ by sol-gel method," *Solid State Ionics*, vol. 178, pp. 569–574, 2007.

[23] Z. Zhong, "Stability and conductivity study of the $BaCe_{0.9-x}Zr_xY_{0.1}O_{3-\delta}$ systems," *Solid State Ionics*, vol. 178, pp. 213–220, 2007.

[24] B. Lin, S. Zhang, L. Zhang, L. Bi, H. Ding, X. Liu, J. Gao, and G. Meng, "Protonic ceramic membrane fuel cells with layered $GdBaCo_2O_{5+x}$ cathode prepared by gel casting and suspension spray," *Journal of Power Sources*, vol. 177, pp. 330–333, 2008.

[25] E. Fabbri, A. D'Epifanio, E. Di Bartolomeo, S. Licoccia, and E. Traversa, "Tailoring the chemical stability of $Ba(Ce_{0.8-x}Zr_x)Y_{0.2}O_{3-\delta}$ protonic conductors for intermediate temperature solid oxide fuel cells (it-sofcs)," *Solid State Ionics*, vol. 179, pp. 558–564, 2008.

[26] J. T. S. Irvine, D. C. Sinclair, and A. R. West, "Electroceramics: Characterisation by impedance spectroscopy," *Advanced Materials*, vol. 2, pp. 132–138, 1990.

[27] W. Clark and J. Rifkin, "A green hydrogen economy," *Energy Policy*, vol. 34, no. 17, pp. 2630–2639, 2005.

[28] M. de Jong, A. H. Reinders, , J. B. Kok, and G. Westendorp, "Optimizing a steam-methane reformer for hydrogen production," *International Journal of Hydrogen Energy*, vol. 34, pp. 285–292, 2009.

[29] M. Grimston, V. Karakoussis, R. Fouquet, R. van der Vorst, P. Pearson, and M. Leach, "The european and global potential of carbon dioxide sequestration in tackling climate change," *Climate Policy*, vol. 1, pp. 155–171, 2001.

[30] W. Rice, "Hydrogen production from methane hydrate with sequestering of carbon dioxide," *International Journal of Hydrogen Energy*, vol. 31, pp. 1955–1963, 2006.

[31] A. Monzón, N. Latorre, T. Ubieto, C. Royo, E. Romeo, J. I. Villacampa, L. Dussault, J. C. Dupin, C. Guimon, and M. Montioux, "Improvement of activity and stability of nimgal catalysts by cu addition during hydrogen production by catalytic decomposition of methane," *Catalysis Today*, vol. 116, pp. 264–270, 2006.

[32] N. Q. Minh, "Science and technology of ceramic fuel cells," pp. 210–211, 1995. Book.

[33] A. S. Rahman, E. Croiset, and R. R. Hudgins, "Catalytic decomposition of methane for hydrogen production," *Topics in Catalysis*, vol. 37, no. 2-4, pp. 137–145, 2006.

[34] Y. Li, B. Zhang, X. Tang, Y. Xu, and W. Shen, "Hydrogen production from methane decomposition over $Ni/CeO_2$ catalysts," *Catalysis Communications*, vol. 7, pp. 380–386, 2006.

[35] R. Moliner, I. Suelves, M. J. Lázaro, and O. Moreno, "Thermocatalytic decomposition of methane over activated carbons: influence of textural properties and surface chemistry," *International Journal of Hydrogen Energy*, vol. 30, pp. 293–300, 2005.

[36] N. Muradov, F. Smith, C. Huang, and A. T-Raissi, "Autothermal catalytic pyrolysis of methane as a new route to hydrogen production with reduced $CO_2$ emissions," *Catalysis Today*, vol. 116, pp. 281–288, 2006.

[37] D. P. Harrison, "Sorption-enhanced hydrogen production: A review," *Industrial and Engineering Chemistry Research*, vol. 47, no. 17, pp. 6486–6501, 2008. 0888-5885.

[38] X. Vitart, A. Le Duigou, and P. Carles, "Hydrogen production using the sulfuriodine cycle coupled to a VHTR: An overview," *Energy Conversion and Management*, vol. 47, pp. 2740–2747, 2006.

[39] M. Ihara, H. Nishihara, K. S. Yoon, O. Lenz, B. Friedrich, H. Nakamoto, K. Kojima, D. Honma, T. Kamachi, and I. Okura, "Light-driven hydrogen prouction by a hybrid

complex of [ni-fe]-hydrogenase and the cyanobacterial photosystem i," *Photochemistry and Photobiology*, vol. 82, pp. 676–682, 2006.

[40] H. Ogino, T. Miura, K. Ishimi, M. Seki, and H. Yoshida, "Hydrogen production by anaerobes," *Biotechnology Progress*, vol. 21, p. 1786, 2005.

[41] S. K. Saxena, "Hydrogen production by chemically reacting species," *Int. J. Hydrogen Energy*, vol. 28, pp. 49–53, 2003.

[42] D. Das, "Recent developments in biological hydrogen production processes," *Chemical Industry and Chemical Engineering Quarterly*, vol. 14, no. 2, pp. 57–68, 2008. 1451-9372.

[43] A. Fujishima and K. Honda, "Electrochemical evidence for the mechanism of the primary stage of photosynthesis," *Bulletin of the Chemical Society of Japan*, vol. 44, pp. 1148–1150, 1971.

[44] A. Fujishima and K. Honda, "Electrochemical photolysis of water at a semiconductor electrode," *Nature*, vol. 238, pp. 37–38, 1972.

[45] M. Ni and M. Ni, "A review and recent developments in photocatalytic water-splitting using formula not shown for hydrogen production," *Renewable and sustainable energy reviews*, vol. 11, no. 3, pp. 401–425, 2007. 1364-0321.

[46] K. Raja, V. Mahajan, and M. Misra, "Determination of photo conversion efficiency of nanotubular titanium oxide photo-electrochemical cell for solar hydrogen generation," *Journal of Power Sources*, vol. 159, pp. 1258–1265, 2006.

[47] J. Chattopadhyay, H. Rok Kim, S. Bong Moon, and D. Pak, "Performance of tin doped titania hollow spheres as electrocatalysts for hydrogen and oxygen production in water electrolysis," *International Journal of Hydrogen Energy*, vol. 33, no. 13, pp. 3270–3280, 2008.

[48] M. Matsuoka, M. Kitano, M. Takeuchi, K. Tsujimaru, M. Anpo, and J. Thomas, "Photocatalysis for new energy production recent advances in photocatalytic water splitting reactions for hydrogen production," *Catalysis Today*, vol. 122, pp. 51–61, 2007.

[49] I. Paulauskas, J. Katz, G. Jellison Jr., N. Lewis, and L. Boatner, "Photoelectrochemical studies of semiconducting photoanodes for hydrogen production via water dissociation," *Thin Solid Films*, vol. 516, no. 22, pp. 8175–8178, 2008.

[50] K. G. Kanade, B. B. Kale, J. Baeg, S. M. Lee, C. W. Lee, S. Moon, and H. Chang, "Self-assembled aligned cu doped zno nanoparticles for photocatalytic hydrogen production under visible light irradiation," *Materials Chemistry and Physics*, vol. 102, pp. 98–104, 2007.

[51] Y. Liu, L. Xie, Y. Li, R. Yang, J. Qu, Y. Li, and X. Li, "Synthesis and high photocatalytic hydrogen production of $SrTiO_3$ nanoparticles from water splitting under uv irradiation," *Journal of Power Sources*, vol. 183, no. 2, pp. 701–707, 2008.

[52] H. Solar, "www.hydrogensolar.com," 15-06-2009.

[53] A. T-Raissi and D. Block, "Hydrogen: Automotive fuel of the future," *IEEE Power and Energy*, vol. 2.

[54] E. P. R. Institute, "Electric power research institute hydrogen briefing to the doe," $http://www1.eere.energy.gov/hydrogenandfuelcells/pdfs/epri_h2_market_study.pdf, 11-06-09$.

*[55] J. Martinez-Frias, A.-Q. Pham, and S. M. Aceves, "A natural gas-assisted steam electrolyser for high-efficiency production of hydrogen,"* Int. J. Hydrogen Energy*, vol. 28, pp. 483–490, 2003.*

*[56] J. I. Levene, M. K. Mann, R. M. Margolis, and A. Milbrant, "An analysis of hydrogen production from renewable electricity sources,"* Solar Energy*, vol. 81, pp. 773–780, 2007.*

*[57] Y. Shin, W. Park, J. Chang, and J. Park, "Evaluation of the high temperature electrolysis of steam to produce hydrogen,"* Int. J. Hydrogen Energy*, vol. 32, pp. 1486–1491, 2007.*

*[58] S. Fujiwara, S. Kasai, H. Yamauchi, K. Yamada, S. Maniko, K. Matsunaga, M. Yashino, T. Kameda, T. Ogawa, S. Momma, and E. Hoashi, "Hydrogen production by high temperature electrolysis with nuclear reactor,"* Progress in Nuclear Energy*, vol. 50, pp. 422–426, 2008.*

*[59] M. Abu-Khader, "Recent advances in nuclear power: A review,"* Progress in Nuclear Energy*, vol. 51, pp. 225–235, 2008.*

*[60] C. A. Linkous, "Development of solid polymer electrolytes for water electrolysis at intermediate temperatures,"* Int. J. Hydrogen Energy*, vol. 18, no. 8, pp. 641–646, 1993.*

*[61] M. Kato, S. Maezawa, and K. Sato, "Polymer-electrolyte water electrolysis,"* Applied Energy*, vol. 59, no. 4, pp. 261–271, 1998.*

*[62] D. L. Stojic, M. P. Marceta, S. P. Sovilj, and S. S. Miljanic, "Hydrogen generation from water electrolysis possibilities of energy saving,"* Journal of Power Sources*, vol. 118, pp. 315–319, 2003.*

*[63] M. H. Santos Andrade, M. L. Acioli, J. G. Silva Junior, J. C. P. Silva, E. O. Vilar, and J. Tonholo, "Preliminary investigation of some commercial alloys for hydrogen evolution in alkaline water electrolysis,"* Int. J. Hydrogen Energy*, vol. 29, pp. 235–241, 2004.*

*[64] "ITM power launches home hydrogen station,"* Fuel Cells Bulletin*, vol. 2008, no. 9, p. 8, 2008.*

*[65] S. H. Jensen and M. Mogensen, "Perspectives of high temperature electrolysis using soec,"* Hi2H2 Project*.*

*[66] K. Eguchi, T. Hatagishi, and H. Arai, "Power generation and steam electrolysis characteristics of an electrochemical cell with a zirconia or ceria based electrolyte,"* Solid State Ionics*, vol. 86-88, pp. 1245–1249, 1996.*

*[67] H. Iwahara, H. Uchida, and N. Maeda, "High temperature fuel and steam electrolysis cells using proton conductive solid electrolytes,"* Journal of Power Sources*, vol. 7, pp. 293–301, 1982.*

*[68] S. Chalk and J. Miller, "Key challenges and recent progress in batteries, fuel cells, and hydrogen storage for clean energy systems,"* Journal of Power Sources*, vol. 159, pp. 73–80, 2006.*

*[69] J. Baker, "New technology and possible advances in energy storage,"* Energy Policy*, vol. 36, pp. 4368–4373, 2008.*

*[70] S. Satyapal, J. Petrovic, C. Read, G. Thomas, and G. Ordaz, "The U.S. department of energy's national hydrogen storage project: Progress towards meeting hydrogen-powered vehicle requirements,"* Catalysis Today*, vol. 120, pp. 246–256, 2007.*

[71] *I. Hadjipaschalis, A. Poullikkas, and V. Efthimiou, "Overview of current and future energy storage technologies for electric power applications,"* Renewable and Sustainable Energy Reviews*, vol. 13, pp. 1513–1522, 2008.*

[72] *P. Edwards, V. Kuznetsov, W. David, and N. Brandon, "Hydrogen and fuel cells: Towards a sustainable energy future,"* Energy Policy*, vol. 36, pp. 4356–4362, 2008.*

[73] *R. Ströbel, J. Garche, P. T. Moseley, L. Jörissen, and G. Wolf, "Hydrogen storage by carbon materials,"* Journal of Power Sources*, vol. 159, pp. 781–801, 2006.*

[74] *Y. Zhao, Y. Kim, A. C. Dillon, M. J. Heben, and S. B. Zhang, "Hydrogen storage in novel organometallic buckyballs,"* Physical Review Letters*, vol. 94, p. 155504, 2005.*

[75] *M. Conte, A. Iacobazzi, M. Ronchetti, and R. Vellone, "Hydrogen economy for a sustainable development: state-of-the-art and technological perspectives,"* Journal of Power Sources*, vol. 100, pp. 171–178, 2001.*

[76] *S. Stoltz and C. Wagner, "Solubility of water vapor and hydrogen in solid oxides,"* Bunsengesellschaft fuer Physikalische Chemie*, vol. 70, no. 8, pp. 781–788, 1966.*

[77] *H. Iwahara, "Technological challenges in the application of proton conducting ceramics,"* Solid State Ionics*, vol. 77, pp. 289–298, 1995.*

[78] *K. D. Kreuer, "On the development of proton conducting materials for technological applications,"* Solid State Ionics*, vol. 97, pp. 1–15, 1997.*

[79] *K. H. Ryu and M. Haile, "Chemical stability and proton conductivity of doped $BaCeO_3$-$BaZrO_3$ solid solutions,"* Solid State Ionics*, vol. 125, pp. 355–367, 1999.*

[80] *K. D. Kreuer, "Aspects of the formation and mobility of protonic charge carriers and the stability of perovskite-type oxides,"* Solid State Ionics*, vol. 125, pp. 285–302, 1999.*

[81] *S. Yamaguchi, H. Yugami, and S. Ikeda, "Operation of hydrogen-air fuel cells based on proton conducting oxides and hydrogen storage metals,"* Journal of Alloys and Compounds*, vol. 330-332, pp. 911–915, 2002.*

[82] *T. Schober, "Tubular high-temperature proton conductors: transport numbers and hydrogen injection,"* Solid State Ionics*, vol. 139, no. 1-2, pp. 95–104, 2001.*

*[83] N. Bonanos, B. Ellis, and M. N. Mahmood, "Construction and operation of fuel cells based on the solid electrolyte Gd:$BaCeO_3$, journal = Solid State Ionics, volume = 44, number = 3-4, pages = 305-311, year = 1991,"*

*[84] T. Yajima, H. Iwahara, and H. Uchida, "Protonic and oxide ionic conduction in $BaCeO_3$-based ceramics - effect of partial substitution for Ba in $BaCe_{0.9}O_{3-\delta}$ with Ca,"* Solid State Ionics*, vol. 47, no. 1-2, pp. 117–124, 1991.*

*[85] W. Coors, "Protonic ceramic fuel cells for high-efficiency operation with methane,"* Journal of Power Sources*, vol. 118, no. 1-2, pp. 150–156, 2003.*

*[86] H. Iwahara, T. Esaka, H. Uchida, and N. Maeda, "Proton conduction in sintered oxides and its application to steam electrolysis for hydrogen production,"* Solid State Ionics*, vol. 3/4, pp. 359–363, 1981.*

*[87] H. Iwahara, "High temperature proton conducting oxides and their applications to solid electrolyte fuel cells and steam electrolyser for hydrogen production,"* Solid State Ionics*, vol. 28-30, pp. 573–578, 1988.*

*[88] H. Iwahara, T. Esaka, H. Uchida, T. Yamauchi, and K. Ogaki, "High temperature protonic conductor based on $SrCeO_3$ and its application to the extraction of hydrogen gas,"* Solid State Ionics*, vol. 18/19, pp. 1003–1007, 1986.*

*[89] T. Schober, "Applications of oxidic high-temperature proton conductors,"* Solid State Ionics*, vol. 162-163, pp. 277–281, 2003.*

*[90] T. Hibino, A. Hashimoto, M. Suzuki, and M. Sano, "A solid oxide fuel cell using y-doped $BaCeO_3$ with pd-loaded feo anode and $Ba_{0.5}Pr_{0.5}CoO_3$ cathode at low temperatures,"* Journal of the Electrochemical Society*, vol. 149, no. 11, pp. A1503–A1508, 2002.*

*[91] H. Matsumoto, M. Okubo, S. Hamajima, K. Katahira, and H. Iwahara, "Extraction and production of hydrogen using high-temperature proton conductor,"* Solid State Ionics*, vol. 152-153, pp. 715–720, 2002.*

*[92] T. Kobayashi, K. Abe, Y. Ukyo, and H. Matsumoto, "Study on current efficiency of steam electrolysis using a partial protonic conductor $SrZr_{0.9}Yb_{0.1}O_{3-\delta}$,"* Solid State Ionics*, vol. 138, pp. 243–251, 2001.*

[93] *J. T. S. Irvine, A. Kruth, C. D. Savaniu, and S. Tao, "Steam electrolysis,"* World Intellectual Property Organisation*, p. WO 2005/093130, 2005.*

[94] *A. S. Nowick, Y. Du, and K. C. Liang, "Some factors that determine proton conductivity in nonstoichiometric complex perovskites,"* Solid State Ionics*, vol. 125, pp. 303–311, 1999.*

[95] *P. Murugaraj, K. D. Kreuer, T. He, T. Schober, and J. Maier, "High proton conductivity in barium yttrium stannate $Ba_2YSnO_{5.5}$,"* Solid State Ionics*, vol. 98, pp. 1–6, 1997.*

[96] *H. Iwahara, T. Mori, and T. Hibino, "Electrochemical studies on ionic conduction in ca-doped $BaCeO_3$,"* Solid State Ionics*, vol. 79, pp. 177–182, 1995.*

[97] *K. D. Kreuer, W. Munch, M. Ise, T. He, A. Fuchs, U. Traub, and J. Maier, "Defect interactions in proton conducting perovskite-type oxides,"* Bunsengesellschaft fuer Physikalische Chemie*, vol. 101, no. 9, pp. 1344–1350, 1997.*

[98] *W. Munch, K. D. Kreuer, S. Adams, and G. Seifert, "The relation between crystal structure and the formation and mobility of protonic charge carriers in perovskite-type oxides: A case study of y-doped $BaCeO_3$ and $SrCeO_3$,"* Phase transitions*, vol. 68, no. 3, pp. 567–586, 1999. 0141-1594.*

[99] *K. D. Kreuer, E. Schonherr, and J. Maier, "Proton and oxygen diffusion in $BaCeO_3$ based compounds: A combined thermal and gravimetric analysis and conductivity study,"* Solid State Ionics*, vol. 70/71, pp. 278–284, 1994.*

[100] *G. Ma, H. Matsumoto, and H. Iwahara, "Ionic conduction and nonstoichiometry in non-doped $Ba_xCeO_{3-\delta}$,"* Solid State Ionics*, vol. 122, pp. 237–247, 1999.*

[101] *H. Iwahara, H. Uchida, and K. Morimoto, "High temperature solid electrolyte fuel cells using perovskite-type oxide based on $BaCeO_3$,"* Journal of the Electrochemical Society*, vol. 137, no. 2, pp. 462–465, 1990. 0013-4651.*

[102] *R. Davies and M. Islam, "Dopant and proton incorporation in perovskite-type zirconates,"* Solid State Ionics*, vol. 126, pp. 323–335, 1999.*

[103] *R. A. De Souza, J. A. Kilner, and C. Jeynes, "The application of secondary ion mass spectrometry (sims) to the study of high temperature proton conductors (htpc),"* Solid State Ionics*, vol. 97, pp. 409–419, 1997.*

*[104] K. D. Kreuer, S. Adams, W. Munch, A. Fuchs, U. Klock, and J. Maier, "Proton conducting alkaline earth zirconates and titanates for high drain electrochemical applications,"* Solid State Ionics*, vol. 145, pp. 295–306, 2001.*

*[105] W. Munch, K. D. Kreuer, G. Seifertli, and J. Majer, "A quantum molecular dynamics study of proton diffusion in $SrTiO_3$ and $CaTiO_3$,"* Solid State Ionics*, vol. 125, pp. 39–45, 1999.*

*[106] K. D. Kreuer, "On the complexity of proton conducting phenomena,"* Solid State Ionics*, vol. 136-137, pp. 149–160, 2000.*

*[107] C. Zuo, T. H. Lee, S. J. Song, L. Chen, S. E. Dorris, U. Balachandran, and M. Liu, "Hydrogen permeation and chemical stability of cermet [Ni-$Ba(Zr_{0.8-x}Ce_xY_{0.2})O_3$] membranes,"* Electrochemical and solid state letters*, vol. 8, no. 12, pp. J35–J37, 2005.*

*[108] K. D. Kreuer, T. Dippel, Y. M. Baikov, and J. Maier, "Water solubility, proton and oxygen diffusion in acceptor doped $BaCeO_3$: a single crystal analysis,"* Solid State Ionics*, vol. 86-88, no. 1, pp. 613–620, 1996.*

*[109] X.-T. Su, Q.-Z. Yan, X.-H. Ma, W.-F. Zhang, and C.-C. Ge, "Effect of co-dopant addition on the properties of yttrium and neodymium doped barium cerate electrolyte,"* Solid State Ionics*, vol. 177, pp. 1041–1045, 2006.*

*[110] K. S. Knight, "Powder neutron diffraction studies of $BaCe_{0.9}Y_{0.1}O_{2.95}$ and $BaCeO_3$ at 4.2 k: a possible structural site for the proton,"* Solid State Ionics*, vol. 127, no. 1-2, pp. 43–48, 2000.*

*[111] A. Kruth and J. T. S. Irvine, "Water incorporation studies on doped barium cerate perovskites,"* Solid State Ionics*, vol. 162-163, pp. 83–91, 2003.*

*[112] A. Kruth, G. C. Mather, J. R. Jurado, and J. T. S. Irvine, "Anomalous variations of unit cell parameters with composition in proton conducting, $ACeO_3$-type perovskite solid solutions,"* Solid State Ionics*, vol. 176, no. 7-8, pp. 703–712, 2005.*

*[113] K. S. Knight, "Structural phase transitions, oxygen vacancy ordering and protonation in doped $BaCeO_3$: results from time-of-flight neutron powder diffraction investigations,"* Solid State Ionics*, vol. 145, no. 1-4, pp. 275–294, 2001.*

*[114] T. Scherban, R. Villeneuve, L. Abello, and G. Lucazeau, "Raman scattering study of $BaCeO_3$ and $SrCeO_3$,"* Solid State Communications*, vol. 84, no. 3, pp. 341–344, 1992.*

*[115] T. Scherban, R. Villeneuve, L. Abello, and G. Lucazeau, "Raman scattering study of acceptor doped $BaCeO_3$,"* Solid State Ionics*, vol. 61, pp. 93–98, 1993.*

*[116] C. Loong, M. Ozawa, K. Takeuchi, K. Ui, and K. Nobuyuki, "Neutron studies of rare earth-modified zirconia catalysts and yttrium-doped barium cerate proton-conducting ceramic membranes,"* Journal of Alloys and Compounds*, vol. 408-412, pp. 1065–1070, 2006.*

*[117] R. C. T. Slade and N. Singh, "Systematic examination of hydrogen ion conduction in rare earth doped barium cerate ceramics,"* Solid State Ionics*, vol. 46, pp. 111–115, 1991.*

*[118] B. Zhu, X. Liu, and T. Schober, "Novel hybrid conductors based on doped ceria and BCY20 for itsofc applications,"* Electrochemistry Communications*, vol. 6, no. 4, pp. 378–383, 2004.*

*[119] A. Tomita, K. Tsunekawa, T. Hibino, S. Teranishi, Y. Tachi, and M. Sano, "Chemical and redox properties of a solid oxide fuel cell with $BaCe_{0.8}Y_{0.2}O_{3-\delta}$,"* Solid State Ionics*, vol. 177, pp. 2951–2956, 2006.*

*[120] A. Tomita, T. Hibino, and M. Sano, "Chemical and redox properties of a solid oxide fuel cell with $BaCe_{0.8}Y_{0.2}O_{3-\delta}$,"* Solid State Ionics*, vol. 1177, pp. 2951–2956, 2006.*

*[121] P. Babilo and S. Haile, "Enhanced sintering of yttrium doped barium zirconate by addition of zno,"* Journal of the American Ceramic Society*, vol. 88, pp. 2362–2368, 2005.*

*[122] T. Schober and H. G. Bohn, "Water vapor solubility and electrochemical characterization of the high temperature proton conductor $BaZr_{0.9}Y_{0.1}O_{2.95}$,"* Solid State Ionics*, vol. 127, pp. 351–360, 2000.*

*[123] P. Babilo, T. Uda, and S. Haile, "Processing of yttrium-doped barium zirconate for high proton conductivity,"* Journal of Materials Research*, vol. 22, pp. 1322–1329, 2007.*

*[124] A. D'Epifanio, E. Fabbri, E. Di Bartolomeo, S. Licoccia, and E. Traversa, "Design of $BaZr_{0.8}Y_{0.2}O_{3-\delta}$ protonic conductor to improve the electrochemical performance in intermediate temperature solid oxide fuel cells,"* Fuel Cells*, vol. 8, pp. 69–76, 2008.*

*[125] L. Chick, L. Pederson, G. Maupin, J. Bates, L. Thomas, and G. Exarhos, "Glycine-nitrate combustion synthesis of oxide ceramic powders,"* Materials Letters*, vol. 10, pp. 6–12, 1990.*

[126] *E. Djurado and E. Meunier, "Synthesis of doped and undoped nanopowders of tetragonal polycrystalline zirconia (tpz) by spray-pyrolysis,"* Journal of Solid State Chemistry*, vol. 141, pp. 191–198, 2008.*

[127] *A. Poirson, P. Decorse, G. Caboche, and L. Dufour, "A dilatometric study of the $La_{0.8}Sr_{0.2}MnO_3$ sintering behaviour,"* Solid State Ionics*, vol. 99, pp. 287–295, 1997.*

[128] *N. Menzler, D. Lavergnat, F. Tietz, E. Sominski, and E. Djurado, "Materials synthesis and characterisation of 8ysz nanomaterials for the fabrication of electrolyte membranes in solid oxide fuel cells,"* Ceramics International*, vol. 29, pp. 619–628, 2003.*

[129] *M. Bucko and J. Oblakowski, "Preparation of $BaZrO_3$ nanopowders by spray pyrolysis method,"* Journal of the European Ceramic Society*, vol. 27, pp. 3625–3628, 2007.*

[130] *H. Ding, B. Lin, D. Fang, Y. Dong, S. Wang, X. Liu, and G. Meng, "$BaZr_{0.1}Ce_{0.7}Y_{0.2}O_{3-\delta}$ proton-conducting electrolyte prepared by gel-casting for low-temperature solid oxide fuel cells,"* Journal of Alloys and Compounds*, vol. 474, pp. 364–369, 2008.*

[131] *S. Haile, G. Staneff, and K. Ryu, "Non-stoichiometry, grain boundary transport and chemical stability of proton conducting perovskite,"* Journal of Materials Science*, vol. 36, pp. 1149–1160, 2001.*

[132] *C. W. Tanner and A. V. Virkar, "Instability of $BaCeO_3$ in $H_2O$ containing atmospheres,"* Journal of the Electrochemical Society*, vol. 143, no. 4, pp. 1386–1389, 1996.*

[133] *A. K. Azad and J. T. S. Irvine, "High density and low temperature sintered proton conductor $BaCe_{0.5}Zr_{0.35}Sc_{0.1}Zn_{0.05}O_{3-d}$,"* Solid State Ionics*, vol. 179, no. 19-20, pp. 678–682, 2008.*

[134] *D. Johnson, "Zview/zplot version 2.9b copyright 19902005 scribner associates inc.,"*

[135] *A. Singh, H. Singh, S. P. Singh, and R. L. Sawhney, "Numerical calculation of psychrometric properties on a calculator,"* Building and Environment*, vol. 37, pp. 415–419, 2002.*

[136] *D. Johnson, "Cview/cware version 2.6 copyright 19902002 scribner associates inc.,"*

[137] *F. Karlsruhe, the National Institute of Standards, and Technology, "http://cds.dl.ac.uk/cds/datasets/crys/icsd/llicsd.html," 2009.*

*[138] B. V. L'vov, "Mechanism and kinetics of thermal decomposition of carbonates,"* Thermochimica Acta*, vol. 386, pp. 1–16, 2002.*

*[139] T. Scherban, W. K. Lee, and A. S. Nowick, "Bulk protonic conduction in yb doped $SrCeO_3$ and $BaCeO_3$,"* Solid State Ionics*, vol. 28-30, pp. 585–588, 1987.*

*[140] T. Scherban, Y. M. Baikov, and E. K. Shalkova, "$H^+/D^+$ isotope effect in y-doped $BaCeO_3$ crystals,"* Solid State Ionics*, vol. 66, pp. 159–164, 1993.*

*[141] M. Gaudon, E. Djurado, and N. Menzler, "Morphology and sintering behaviour of yttria stabilised zirconia (8-ysz) powders synthesised by spray pyrolysis,"* Ceramics International*, vol. 30, pp. 2295–2303, 2004.*

*[142] S. Tao and J. Irvine, "Conductivity studies of dense yttrium-doped $BaZrO_3$ sintered at 1325°C,"* Solid State Chemistry*, vol. 180, pp. 3493–3503, 2007.*

*[143] F. Iguchi, T. Yamada, N. Sata, T. Tsurui, and H. Yugami, "The influence of grain structures on the electrical conductivity of a $BaZr_{0.95}Y_{0.05}O_3$ proton conductor,"* Solid State Ionics*, vol. 177, pp. 2381–2384, 2006.*

*[144] W.-D. Yang, Y.-H. Chang, and S.-H. Huang, "Influence of molar ratio of citric acid to metal ions on preparation of $La_{0.67}Sr_{0.33}MnO_3$ materials via polymerizable complex process,"* Journal of European Ceramic Society*, vol. 25, pp. 3611–3618, 2005.*

*[145] T. Shimada, C. Wen, N. Taniguchi, J. Otomo, and H. Takahashi, "The high temperature proton conductor $BaZr_{0.4}Ce_{0.4}In_{0.2}O_{3-\delta}$,"* Journal of Power Sources*, vol. 131, pp. 289–292, 2004.*

*[146] M. Laguna-Bercero, R. Campana, A. Larrea, J. Kilner, and V. Orera, "High efficiency reversible solid oxide microtubular fuel cells,"* Electrochemical Society Transactions*, vol. 25, pp. 865–872, 2009.*

*[147] S. Yamanaka, K. Kurosaki, T. Maekawa, T. Matsuda, S. Kobayashi, and M. Uno, "Thermochemical and thermophysical properties of alkaline-earth perovskites,"* Journal of Nuclear Materials*, vol. 344, pp. 61–66, 2005.*

*[148] E. H. Kisi and C. J. Howard, "Crystal structure of zirconia phases and their interrelation,"* Key Engineering Materials*, vol. 153-154, pp. 1–35, 1999.*

*[149] Y.-Q. Wu, Y.-F. Zhang, G. Pezzotti, and J.-K. Guo, "Effect of glass additives on the strength and toughness of polycrystalline alumina,"* Journal of the European Ceramic Society*, vol. 22, no. 2, pp. 159–164, 2002.*

*[150] W. Rauch and L. Meilin, "$BaCuGd_2O_5$-$BaCeO_3$ composite cathodes for barium cerate-based electrolyte,"* Journal of the Electrochemical Society*, vol. 144, pp. 4049–4053, 1997.*